Kinetics of Gelation in Photoreversible Gels

by

Sanjoy Sircar

B.S. Chemical Engineering

Lehigh University, 2002

SUBMITTED TO THE DEPARTMENT OF CHEMICAL ENGINEERING IN PARTIAL FULFILLMENT OF THE REQUIREMENTS FOR THE DEGREE OF

Doctor of Philosophy

at the

Massachusetts Institute of Technology

September 2010

[February 2011]

Signature of Author .....
Department of Chemical Engineering
Sept 27, 2010

Certified by .....
T. Alan Hatton
Ralph Landau Professor of Chemical Engineering Practice
Thesis Supervisor

Certified by.....
Kenneth A. Smith
Gilliland Professor of Chemical Engineering
Thesis Supervisor

Accepted by .....
William M. Deen
Carbon P. Dubbs Professor of Chemical Engineering
Chairman, Committee for Graduate Students

Kinetics of Gelation in Photoreversible Gels

by

Sanjoy Sircar

Submitted to the Department of Chemical Engineering on September 27, 2010 in partial fulfillment of the requirements for the degree of Doctor of Philosophy in Chemical Engineering

ABSTRACT

Smart materials, or materials that respond to some stimulus by changing their properties, make up an active area of research in many fields. Light can be considered an especially attractive choice of stimulus because it can be applied with precise spatial and temporal control, and is non-invasive. This thesis explores light sensitive gels and colloids, which could be used as valves in microfluidics devices, as tunable templates for the production of nanoparticles, or as devices for capturing pollutants or delivering drugs. At the basis of the sensitivity to light is the azobenzene chemical group, which isomerizes from *cis* to *trans* under visible light and the reverse under UV light. When this group is embedded in the hydrophobic tail of a surfactant, the aggregation properties of the surfactant become light-sensitive. The *trans* form of the azobenzene surfactant is more likely to form micelles than the *cis*. When mixed with a hydrophobically modified polymer, these micelles can act as crosslinking sites for a gel network. Upon UV irradiation, the crosslinking is disrupted and the gel transitions to a solution state.

NMR methods were used to characterize the micelles and gels, and to understand the steps that control the kinetics in these photoreversible systems. The gelation process can be considered to consist of photoreaction, micelle formation, and possibly polymer relaxation. It was found that the photon flux through the material limits the rate of reaction, which then controls the remaining processes in the system. The photoreaction was studied under varying conditions, including concentration, light intensity, and wavelength. Due to their optical thickness, these materials are possibly better suited for use as thin films.

NMR experiments were also used to probe the interactions between the polymer and surfactant. In contrast to surfactant-only solutions, *trans*-dominated and *cis*-dominated micelles appeared equally likely to form aggregates with an appropriate polymer. The *cis*-rich aggregates failed to effectively crosslink the polymer and form a gel. This was confirmed by using diffusion measurements to monitor the size of crosslinked polymer clusters. This cluster growth correlated well with previous rheology results, but the high tendency of *cis* samples to form aggregates had not been anticipated. It is hypothesized that *cis*-dominated aggregates are too small and unstable to act as crosslinking sites.

In an effort to create a wider array of tunable colloids, the azobenzene surfactant was then mixed with a traditional surfactant of opposite charge. Solutions consisting of oppositely charged surfactants have been known to result in unilamellar vesicles, when prepared at appropriate concentrations and mixing ratios. The size, type and number density of the aggregates in this work were found to be controllable through the use of light. Depending on the light conditions, either nanodiscs or vesicles could be observed.

Thesis Supervisor: T. Alan Hatton
Title: Ralph Landau Professor of Chemical Engineering Practice

Thesis Supervisor: Kenneth A. Smith
Title: Gilliland Professor of Chemical Engineering

Acknowledgements

I must thank my thesis advisors, Alan Hatton and Ken Smith, for their support, guidance and patience throughout this work. It quickly became apparent to me why this pairing has been so productive throughout the years, as they complement each other well. Their technical expertise and problem-solving instincts were always valuable, as well as their encouragement when a project was not going well. Of course, sometime the needed encouragement was for moving on to the next topic. I would be remiss if I also did not note how enjoyable it is to work and chat with them; this certainly makes a difference.

I would also like to thank Professors Bob Cohen and William Deen for serving on my thesis committee and providing guidance from a fresh perspective over the years. I also note the Singapore-MIT Alliance for their generous funding.

I greatly enjoyed collaborating with Eduardo Marques, who spent one summer with us here in Cambridge. Through him I learned about another field of colloid science, and found a fun extension of my work.

As it happens, I did much of my experimental work outside the confines of the Hatton Lab. Many people have been generous in letting me use their instruments, as well as providing guidance. I must thank Chris Turner and Tony Bielecki at the Francis Bitter Magnet Lab for allowing me to invade their NMR facility once weekly for several months, and putting in considerable time to ensure my experiments would be successful. I am also indebted to Jerry Ackerman. At the eleventh hour I was left desperately scrambling for a location to finish certain experiments, and he graciously accepted a call from a total stranger and invited me to his facility at MGH. At MGH, Christian Farrar then took time out of his day in order to babysit me, and this was greatly appreciated. I was also a heavy user of the DCIF facility in the Chemistry Department, where Jeff Simpson and Anne Gorham provided advice and troubleshooting. Debby Pheasant's facility was an oasis of good cheer, on top of having a magical light scattering instrument that did not perturb my samples. Ben Wang, also a great friend outside school, was helpful with the rheometer at ISN. Finally, Arijit Bose at URI allowed us to use his cryogenic-TEM facilities, resulting in some fantastic images. In fact his students did all the work; I simply sat back and watched.

Within the Hatton group, I am thankful for the general spirit of camaraderie and helpfulness. In particular, Smeet Deshmukh, Huan Zhang, Brad Cicciarelli and Tiangang Shang were of great help, as we were working on related projects. Ted Lee got me started off, patiently answering the uneducated questions of a beginner. Many others, including Nathan Aumock, Harpreet Singh, Saurabh Tejwani, Fei Chen, Andre Ditsch, Asha Parekh and Lino Gonzalez have contributed both good companionship and thoughtful discussion. I might also recognize Michael Stern, on whose computer this is being typed, due to my own computer crashing at a somewhat inopportune time.

A series of undergraduate students have had the (mis)fortune of working under my care; I was always amazed by their enthusiasm and initiative. Among them were Szymon Leszczynski, Amanda Brisky and Dale Robinson. They did my experiments without complaint, and often had better ideas than I did. There was also one precocious high school student who pitched in, Muhammad Kandil. His task was particularly onerous, but he handled it well.

Socially, my time here was made greatly enjoyable by numerous friends among the graduate student body. I trust that many of these will be life-long relationships. I cannot possibly list all the significant people, but I will point out Theis Clarke, Kristin Ploeger and Jason Ploeger. Graduate school may not be the easiest phase of life, but they ensured that I would have some warm and fun memories. As for Jane

Rempel, without her loyal friendship and hospitality, I simply don't know what I would have done. She went above and beyond what could rightfully be expected of a friend.

I would like to thank my extended family both in the states and in India for their support, including Sayan Mitra who was here at MIT alongside me. Also the family friends who have stepped forward in times of need. I also thank my new family: Bruce, Linda and Andrew Deschere, for their support.

This brings me to the long-suffering people in my life who never stopped giving me love and patience, much more than I ever deserved. My parents, Shivaji and Shukla, have been generous with their love and have been waiting for this for quite some time. I thank them for everything they have done for me. Finally, my wife Cristina. We met here along the way, so I am leaving MIT having gained much more than just a degree. I am indebted to her for providing encouragement, motivation, assistance and unconditional love. Indeed she should be a co-author, given that some of the diagrams herein are her creations. I thank her for keeping faith that the frustrations of a long distance relationship with a graduate student, including missed birthdays and anniversaries, would someday be worth it. I hope that someday is now.

Table of Contents

List of Figures

Chapter 1

Introduction

1.1 Background and motivation

Smart materials, which are materials that are sensitive to changes in their environment, are attractive for use in a wide array of engineering applications. The ability to reversibly alter structures or material properties by using stimuli such as temperature, light, pH or electric field provides a level of control and flexibility not available in traditional non-responsive systems. The use of light is particularly powerful, as it can be applied non-invasively with great spatial control. One class of smart materials that has attracted recent attention is those that take advantage of self-assembly. Surfactants and certain polymers are known to spontaneously self-assemble into regular patterns or structures, due to hydrophobic, electrostatic or other intermolecular forces. Self-assembly can be exploited to easily create nano- or micro-scale structures, avoiding the need for complicated nanolithography methods. These systems can be made light-sensitive by incorporating an appropriate photoresponsive chemical moiety. The present work describes and develops various colloids and gels that can result from light-sensitive surfactants and their mixtures with polymers.

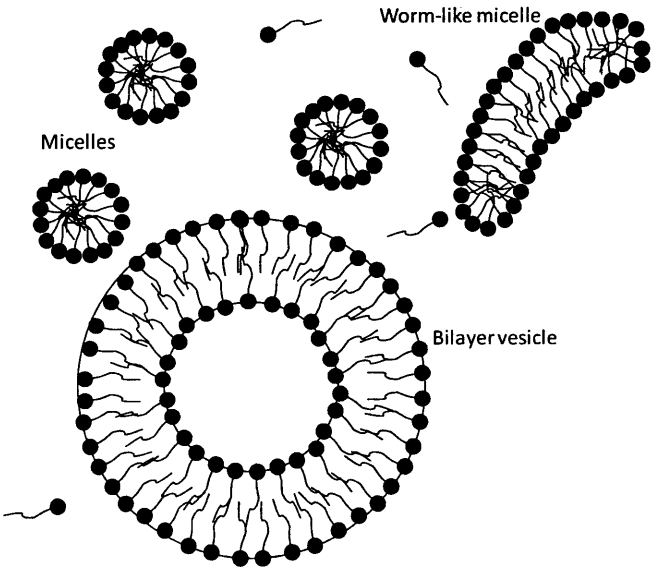

Figure 1-1 Selection of possible self-assembled structures. Shown are spherical micelles, a worm-like micelle and a vesicle. Vesicles have an aqueous core, which may be used to store hydrophilic substances. Factors

including the geometry and concentration of the surfactant, as well as concentration of any added salt, will determine which structure is formed.

Surfactant molecules can self-assemble into various colloidal structures, including micelles and vesicles (Figure 1-1). Micelles can be used to localize hydrophobic molecules, while vesicles can store either hydrophobic or hydrophilic molecules. Vesicles also occur naturally and are used within biological cells for the storage, transport and release of compounds. It has been suggested that these capabilities could be exploited for drug delivery [1-3], the storage and controlled release of perfumes [4], or for removing harmful compounds from contaminated water or soil [5, 6]. Certain block copolymers can also form micelles [7], and these have also been proposed for use in drug delivery [8-10]. Such colloids have also been used as reaction sites for the production of nanoparticles [11], or as templates for the production of more permanent structures such as silicate molecular sieves used as adsorbents and catalysts [12]. Many of these applications could be enhanced if the formation of the colloids could be triggered by an external stimulus.

Azobenzene is a moiety commonly used in light-sensitive smart materials. UV light is known to drive a *trans-cis* isomerisation reaction in azobenzene, while visible light initiates the reverse [13, 14]. When incorporated in a surfactant molecule, this change in conformation can alter the shape of any self-assembled aggregates, and also the propensity to form aggregates [15-18]. For example, the cationic photosurfactant 4-ethylazobenzene-4'-(oxybutyl)trimethylammonium bromide (azoTAB) is more likely to form micelles in the *trans* state than in the *cis* [16]. Other useful properties of surfactants can also be made tunable to light. The surface tension of azobenzene-surfactant solutions has been observed to change upon irradiation, which may be relevant to applications involving detergency and wetting [19, 20]. Surfactants are also used to stabilise emulsions, and these have been made light sensitive as well [21, 22]. UV irradiation has been demonstrated to affect the micellar solubilisation of organic molecules [23].

Based on these developments, it is apparent that photo-sensitive surfactants provide a promising avenue for achieving stimuli-responsive self-assembled systems. This work attempts to extend the field by developing novel photosensitive colloids, as well as describing the state of the self-assembled system during the irradiation process, at intermediate mixtures of *cis* and *trans*. Also provided is a quantitative description of the photoisomerization rate. The work is based on the azoTAB surfactant, first described by Hayashita et al [16].

There is also active research in the development of smart gels. Gels can be broadly defined as crosslinked materials that form three dimensional networks, swollen with some solvent. Polymers are generally a major component. Gels typically exhibit viscoelasticity, in contrast to the solvent which lacks any elasticity. If that solvent is water, the result is called a hydrogel. Swollen hydrogels can hold many times

their weight in water; this superabsorbency has been used commercially in diapers. Hydrogels have also found use in contact lenses, and as scaffolds for growing and implanting human tissue [24-26]. Gels can be classified by the type of crosslinking employed: chemical, where the crosslinks are formed by covalent bonds, or physical, where the crosslinking is based on non-bonding interactions. The network in chemically-crosslinked gels is permanent, but the gel can respond to external stimuli by reversibly swelling with solvent or collapsing. This is known as a volume phase transition, and can be triggered by temperature [27-29], pH [30, 31], light [32-34], or combinations thereof, such as local heating due to light absorption [35]. These externally controlled volume phase transitions serve as the basis of proposed actuators and valves for microfluidics [36-38]. pH-sensitive gels exhibiting volume transitions could also be used in oral drug delivery, whereby the gels respond to the acidic conditions in the stomach [30]. Hydrogels have also been designed to be sensitive to some chemical. For example, changes in glucose [39] or carbon dioxide [40] levels in the body have been used to modulate the rate of release of some drug from a hydrogel.

Unlike chemically-crosslinked gels, the networks in physical gels can be reversibly formed or dissolved. Lee et al have demonstrated such a gel that undergoes sol-gel transitions in response to light [41]. The system consists of the azoTAB surfactant and an oppositely charged amphiphilic polymer, hydrophobically-modified poly(acrylic acid) (HMPAA). After visible irradiation, which favors the *trans* isomer, azoTAB tends to form micelles which act as crosslinking sites for the polymer. A gel network thus forms. Under UV irradiation, the micelles break up and a gel-sol transition takes place. Other types of light-sensitive physical gels have been devised by incorporating the azobenzene group within pendant groups on the polymer itself [42-44].

Different practical applications can be imagined for such gels. The viscosity of the azoTAB-HMPAA system changes by three orders of magnitude upon the gel-sol transition. Systems with tunable viscosity have been commercialized as dynamically controllable dampeners in automobile suspensions [45]. In this case the applied external stimulus is a changing magnetic field, and is a feature in sports cars such as Audis and Corvettes [46]. Tunable viscosity systems could also be a means to control flow, for applications in oil recovery [47] or in microfluidics. Thermally-triggered sol-gel transitions have been proposed for usage in drug delivery; the material is injected while in the sol state and it then gels at the internal body temperature [48]. The gel then releases the drug compound at some appropriate sustained rate. Light may not be an ideal stimulus for in-vivo applications, but light-sensitive gels could be used for storage and release of reagents in microreactors. Tunable gel beds have also been proposed for use in molecular separations, such as capillary gel electrophoresis [49]. The separation resolution could be enhanced by selectively gelling or ungelling parts of the matrix medium.

In order to design and develop devices that use these light-sensitive gels, further characterization of the azoTAB-HMPAA system was attempted in the present work. Of particular interest was the rate of gelation, as well as the nature of the structures that form under different irradiation conditions. The time scale for the transition in the azoTAB-HMPAA system was described on the basis of rheological measurements to be on the order of minutes, but with some slow behavior extending to hours [41]. An understanding of this rate is a prerequisite for any successful design, so the various steps involved were investigated. These include the photoisomerization reaction, as well as the formation and dissolution of micelles.

Many previous studies of gelation have focused on the measure of rheological properties, such as viscosity and dynamic modulus [50-53]. While this provides observations relevant for certain applications, it does not give direct information regarding the molecular-scale structure of the gels. In this work, NMR spectroscopy was used to more directly observe the formation of aggregates, and the interaction between the surfactant and polymer. Some NMR techniques have been previously demonstrated on other surfactant and surfactant-polymer systems [54-56]. This would lead to a better understanding of the azoTAB-HMPAA system, as well as possibly demonstrating techniques relevant to other surfactant-polymer systems. Finally, many of the applications envisioned for the gel require an understanding of how solutes diffuse through the gel or the sol, so this aspect was also experimentally studied.

1.2 Photosensitive surfactant

1.2.1. Azobenzene

Any light-sensitive system must include some moiety that absorbs light and then reacts in some way. Azobenzene and stilbene are commonly used groups [57, 58]; both of these undergo a reversible isomerisation reaction upon the absorption of light. Other useful groups include triphenylmethane leucohydroxide, which dissociates into an ion pair upon UV irradiation [59].

The light-sensitive colloids and gels described in this work all exploit the properties of the azobenzene moiety. Azobenzene, pictured in Figure 1-2, can exist in either the *trans* (also called E, for *entgegen*) or *cis* (Z, *zusammen*) conformation about the N-N double bond. Conversion between the two forms is driven by the absorption of light; UV favors the formation of *cis*, while visible light favors *trans*. The *trans* isomer is more thermodynamically stable, so there is also a thermal reaction from *cis* to *trans*. A sample that has been left in the dark will eventually become entirely *trans*; this is known as the dark-adapted state. After prolonged irradiation, azobenzene eventually reaches some steady state composition

of *trans* and *cis*; this is known as the photostationary state. The photostationary state is a function of the irradiation wavelength.

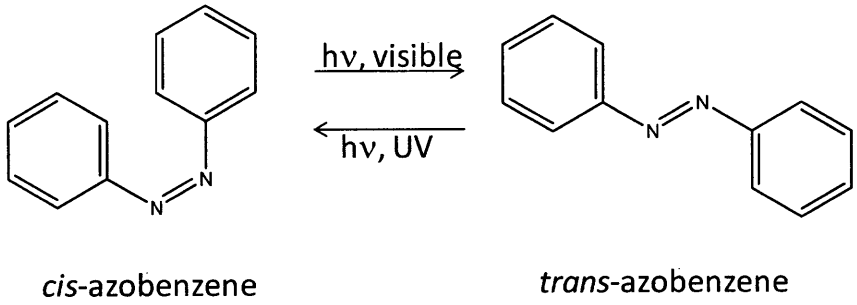

Figure 1-2 Isomers of azobenzene. The *trans* isomer is favored under visible irradiation, while the *cis* predominates under UV irradiation. Samples in the dark eventually revert to being entirely *trans*.

The photochemistry of azobenzene has been investigated for decades. The light-initiated reaction between the *trans* and *cis* forms of azobenzene was first observed in 1937 [14]. The nature of the reaction pathway remains unresolved in the literature; it is unclear whether the reaction takes place through an out-of-plane rotation or an in-plane inversion (see Figure 1-3). A further complication is that the reaction pathway may be dependent on the irradiation wavelength. [58, 60, 61]. Both computational [62-65] and experimental work [60, 66-68] continues on this matter to the present day.

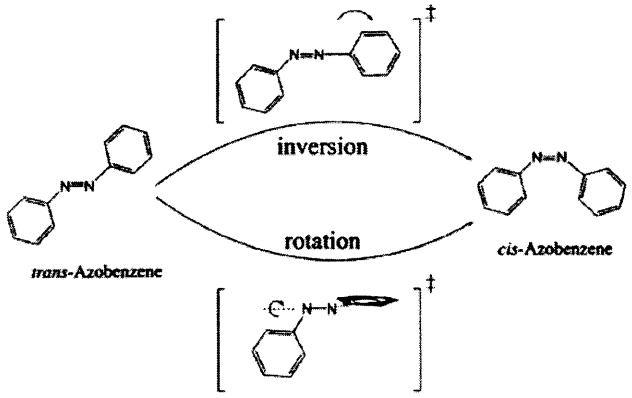

Figure 1-3 Possible mechanisms for the isomerisation reaction of azobenzene. Taken from Diau et al [63]

1.2.2. azoTAB surfactant

The azobenzene group has been embedded in various larger molecules for different purposes, such as optical storage of information and holography, as reviewed by Knoll and Rau [61, 69]. Azobenzene has also been located within surfactant molecules, such as azoTAB [16] (shown in Figure 1-4). The azoTAB

molecule was designed to be more soluble in water than the originally reported azobenzene surfactants [15]. The azoTAB surfactant is used throughout this work.

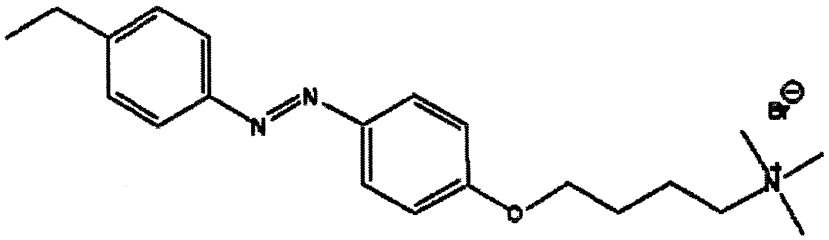

Figure 1-4 Structure of azoTAB, shown in the *trans* form

Surfactant molecules are amphiphilic, in that they include both a hydrophilic head and hydrophobic tail section. Amphiphilic molecules in aqueous solution tend to form aggregates such as micelles or vesicles (Figure 1-1) due to the entropically driven hydrophobic effect [70]. Interactions between water molecules are relatively strong, due to hydrogen bonding. In contrast, physical interactions between water and hydrophobic materials are weak. The water molecules will therefore continue to form hydrogen bonds with each other, even in the presence of the surfactant hydrophobic tail. In order to do so, there is some short-scale ordering of the water molecules around the tail, which results in an entropic penalty. This entropic cost is relieved if the hydrophobic tails are removed from contact with the water. This could occur through phase separation, whereby the hydrophobic molecules precipitate out of solution. However, the hydrophilic head groups of the surfactant do interact strongly with water, so the structures in Figure 1-1are favored instead.

The hydrophilic head of azoTAB is a charged trimethylammonium group, which is very commonly found in synthetic cationic surfactants. The azobenzene group is included in the hydrophobic tail, with an alkyl spacer group separating the head and the azobenzene.

azoTAB is attractive for use in colloid science because the *cis* form has been found to be less likely to form self-assembled aggregates than the *trans* form. This effect is partially due to differences in hydrophilicity; the *cis* isomer has a higher dipole moment than the *trans* (3.1 D and 0.5 D, respectively) [19]. Further, the kinked shape of *cis* would likely decrease its ability to pack efficiently into a regular micellar structure (see Figure 1-5).

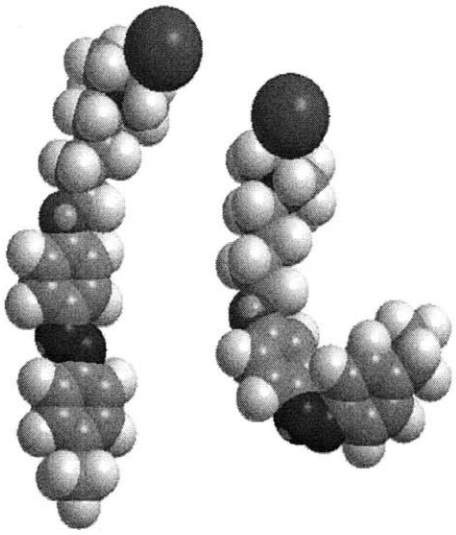

Figure 1-5 Space-filling models of the two isomers of azoTAB. The *cis* has a bent form that may discourage both micellar packing and any stabilizing π-π interactions.

This difference in the ability to form micelles makes it possible to induce micelle formation or dissolution with appropriate usage of light. These environmentally sensitive aggregates can be further used as cross-linking points for reversible polymer gels.

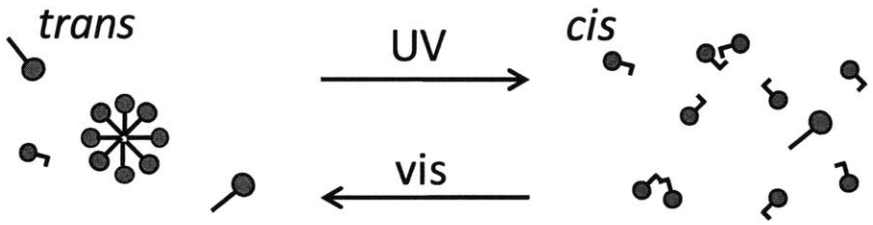

Figure 1-6 Expected effect of irradiation on micelle formation. Straight-tailed surfactants denote *trans*, while bent-tailed surfactants denote *cis*. UV light drives conversion to *cis*; visible light drives conversion to *trans*. The dark-adapted state is 100% *trans*. The surfactant is more able to form micelles when in the *trans* state.

1.3 Light-sensitive gels

Attempts to devise systems with photocontrolled rheology date to at least the 1980s. Irie et al were able to achieve modest changes in solution viscosity upon irradiation by incorporating light sensitive groups within a polymer [59, 71]. With azobenzene included in the main backbone chain of a polymer, the polymer coil contracted when the azobenzene was converted to the more compact *cis* form [71]. This was

accompanied by a 60% reduction in viscosity. Similar changes in viscosity resulted when incorporating a photo-ionisable moiety as a pendant group on a polymer [59], again due to a change in coil dimensions. There was no crosslinking or network formation in these early attempts.

A different class of photorheological fluid does not include polymer at all. The surfactant cetyltrimethylammonium bromide (CTAB) forms worm-like micelles in aqueous solution. At sufficient concentrations, these micelles become highly entangled, resulting in a viscoelastic gel-like system. When a photosensitive surfactant or some other photochromic molecule was added to the micellar solution, the micelles were disrupted after irradiation [72-74]. The original micelles were recovered upon irradiation with a different wavelength. These transitions resulted in a 3-4 order of magnitude change in viscosity.

Amphiphilic polymers can be used as a component in gel systems. Like smaller surfactant molecules, these polymers have both hydrophilic and hydrophobic sections. This can be accomplished by building block copolymers such as Pluronics, which consist of blocks of hydrophobic poly(propylene oxide) and hydrophilic poly(ethylene oxide). Pluronics can form micelle-like aggregates. Amphiphilic polymers can also be constructed by attaching hydrophobic pendant groups to some repeat units of an otherwise hydrophilic polymer. This process is known as hydrophobic modification. Such polymers can also form intra- or inter-polymer aggregates.

Deshmukh et al synthesized copolymers of hydrophilic dimethylacrylamide and a second repeat unit which included azobenzene as a hydrophobic pendant group. At sufficiently high concentrations in the visible photostationary state, infinite gel networks were formed due to aggregates formed by the pendant groups. These aggregates were disrupted upon UV irradiation, resulting in a 20-fold reduction in the zero shear rate viscosity [43].

The hydrophilic polymer poly(sodium acrylate) is commonly used as the foundation for hydrophobically-modified polymers. One such example is hydrophobically modified polyacrylic acid (HMPAA), demonstrated by Wang et al [75] and shown below:

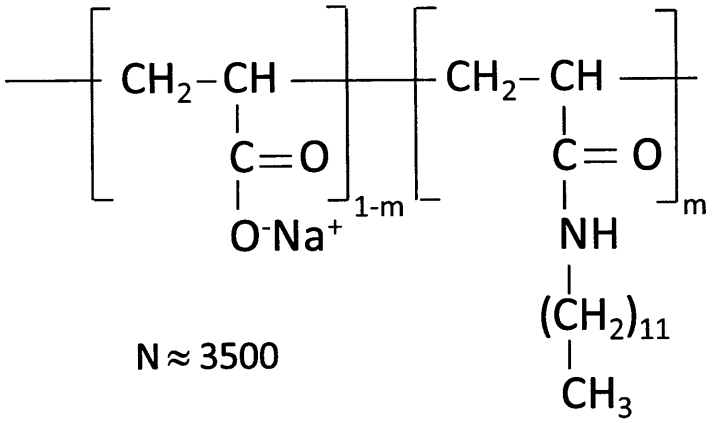

Figure 1-7 Structure of HMPAA as used in this work. 3% of repeat units are hydrophobically modified (m).

A hydrophobic alkyl chain is randomly grafted onto the original polymer. Mixtures of HMPAA and *trans* azoTAB were found by Lee et al to form viscoelastic gels [41]. It was hypothesized that the *trans* azoTAB micelles and the hydrophobic polymer grafts formed co-micelles, leading to crosslinking of the polymers. After conversion to *cis* under UV, the micelles were thought to break apart, causing the gel-sol transition. This transition was accompanied by a 3 order of magnitude change in the low shear rate viscosity. Further background on the subtleties of the interactions between surfactants and polymers is given in Chapter 4.

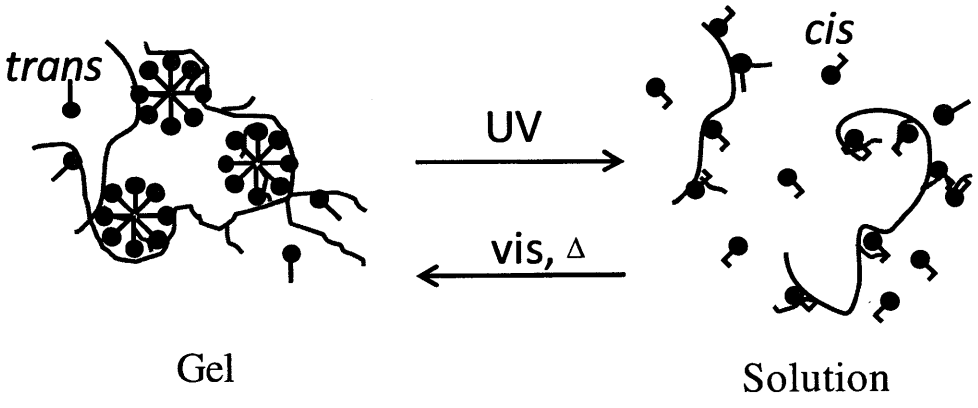

Figure 1-8 Possible mechanism for reversible gelation in azoTAB-HMPAA mixtures. Micelles are present in the dark-adapted or visible-adapted states; these micelles serve to crosslink the polymer coils into a network. These micelles break down when UV light is used to convert azoTAB to the *cis*.

Other workers have hydrophobically modified poly(sodium acrylate) with azobenzene pendant groups [44, 76]. Bovine serum albumin (BSA) [76] or typical surfactants [44] were added to supply crosslinking sites. Again, gels formed with the azobenzene in the *trans* state, but the polymer-surfactant or polymer-protein interactions were disrupted upon conversion to *cis*. The change in the low shear rate viscosity was 40-fold.

It is therefore possible to construct photoreversible gels by using mixtures of light-sensitive surfactant and insensitive polymer, or light-sensitive polymer and insensitive surfactant. The light-modulated effect may be stronger in the former case. That arrangement (azoTAB-HMPAA) was chosen for further study in this work.

1.4 Thesis Overview

The general goals of this research were to characterize the aggregates formed by the surfactant azoTAB under different light conditions, to use this surfactant to devise novel light sensitive colloids, to quantify the rate of gelation in light-sensitive gels, and to study the interaction between surfactant and polymer under different light conditions. As the photoisomerisation of azoTAB is central to all light-driven aspects of this work, this reaction is studied in detail in Chapter 2. The kinetics of the reaction are experimentally observed, and compared to models which were developed. This is needed to predict the isomeric composition of an azoTAB sample, as a function of irradiation intensity, wavelength and duration. Chapter 3 contains studies of micelle formation by azoTAB in aqueous solution. Included are observations of whether micelles form under different concentrations and isomer compositions, and if micelles are present, how many of the azoTAB molecules participate in them. These micelles act as crosslinking sites in azoTAB-hydrophobically modified polymer systems, which are described in Chapter 4. This Chapter describes NMR observations of the interaction between surfactant and polymer, the rate of isomerisation in these mixtures, and provides a linkage between molecular scale observations and rheological measurements. Also described is the diffusion of solutes through the polymer-surfactant matrix. Chapter 5 focuses on novel light-sensitive colloids that resulted from mixtures of azoTAB and another surfactant. This includes transitions between large vesicles, small vesicles, and discs.

1.5 Works Cited

1. Ostro, M.J. and P.R. Cullis, *Use of Liposomes as Injectable-Drug Delivery Systems.* American Journal of Hospital Pharmacy, 1989. **46**(8): p. 1576-1587.
2. Bombelli, C., L. Giansanti, P. Luciani, and G. Mancini, *Gemini Surfactant Based Carriers in Gene and Drug Delivery.* Current Medicinal Chemistry, 2009. **16**(2): p. 171-183.
3. Gershkovich, P., K.M. Wasan, and C.A. Barta, *A Review of the Application of Lipid-Based Systems in Systemic, Dermal/Transdermal, and Ocular Drug Delivery.* Critical Reviews in Therapeutic Drug Carrier Systems, 2008. **25**(6): p. 545-584.
4. Abe, M., K. Mizuguchi, Y. Kondo, K. Ogino, H. Uchiyama, et al., *Solubilization of Perfume Compounds by Pure and Mixtures of Surfactants.* Journal of Colloid and Interface Science, 1993. **160**(1): p. 16-23.
5. Kondo, Y., M. Abe, K. Ogino, H. Uchiyama, J.F. Scamehorn, et al., *Solubilization of 2-Phenylethanol in Surfactant Vesicles and Micelles.* Langmuir, 1993. **9**(4): p. 899-902.
6. Edwards, D.A., R.G. Luthy, and Z.B. Liu, *Solubilization of Polycyclic Aromatic-Hydrocarbons in Micellar Nonionic Surfactant Solutions.* Environmental Science & Technology, 1991. **25**(1): p. 127-133.
7. Alexandridis, P. and T.A. Hatton, *Poly(Ethylene Oxide)-Poly(Propylene Oxide)-Poly(Ethylene Oxide) Block-Copolymer Surfactants in Aqueous-Solutions and at Interfaces - Thermodynamics, Structure, Dynamics, and Modeling.* Colloids and Surfaces a-Physicochemical and Engineering Aspects, 1995. **96**(1-2): p. 1-46.
8. Kwon, G.S. and K. Kataoka, *Block-Copolymer Micelles as Long-Circulating Drug Vehicles.* Advanced Drug Delivery Reviews, 1995. **16**(2-3): p. 295-309.
9. Kazunori, K., K. Glenn S, Y. Masayuki, O. Teruo, and S. Yasuhisa, *Block Copolymer Micelles as Vehicles for Drug Delivery.* Journal of Controlled Release, 1993. **24**(1-3): p. 119-132.
10. Torchilin, V.P., *Structure and Design of Polymeric Surfactant-Based Drug Delivery Systems.* Journal of Controlled Release, 2001. **73**(2-3): p. 137-172.
11. Mann, S. and J.P. Hannington, *Formation of Iron-Oxides in Unilamellar Vesicles.* Journal of Colloid and Interface Science, 1988. **122**(2): p. 326-335.
12. Beck, J.S., J.C. Vartuli, W.J. Roth, M.E. Leonowicz, C.T. Kresge, et al., *A New Family of Mesoporous Molecular-Sieves Prepared with Liquid-Crystal Templates*Journal of the American Chemical Society, 1992. **114**(27): p. 10834-10843.
13. G. Zimmerman, L.-Y.C.a.U.-J.P., *The Photochemical Isomerization of Azobenzene.* Journal of the American Chemical Society, 1957. **80**: p. 3528-3531.
14. Hartley, G.S., *The Cis-Form of Azobenzene.* Nature, 1937. **140**: p. 281.
15. Shinkai, S., K. Matsuo, A. Harada, and O. Manabe, *Photocontrol of Micellar Catalyzes.* Journal of the Chemical Society-Perkin Transactions 2, 1982(10): p. 1261-1265.
16. Hayashita, T., T. Kurosawa, T. Miyata, K. Tanaka, and M. Igawa, *Effect of Structural Variation within Cationic Azo-Surfactant Upon Photoresponsive Function in Aqueous Solution.* Colloid and Polymer Science, 1994. **272**(12): p. 1611-1619.
17. Cicciarelli, B.A., J.A. Elia, T.A. Hatton, and K.A. Smith, *Temperature Dependence of Aggregation and Dynamic Surface Tension in a Photoresponsive Surfactant System.* Langmuir, 2007. **23**(16): p. 8323-8330.
18. Sakai, H., A. Matsumura, S. Yokoyama, T. Saji, and M. Abe, *Photochemical Switching of Vesicle Formation Using an Azobenzene-Modified Surfactant.* Journal of Physical Chemistry B, 1999. **103**(49): p. 10737-10740.
19. Shang, T.G., K.A. Smith, and T.A. Hatton, *Photoresponsive Surfactants Exhibiting Unusually Large, Reversible Surface Tension Changes under Varying Illumination Conditions.* Langmuir, 2003. **19**(26): p. 10764-10773.

20. Cicciarelli, B.A., T.A. Hatton, and K.A. Smith, *Dynamic Surface Tension Behavior in a Photoresponsive Surfactant System.* Langmuir, 2007. **23**(9): p. 4753-4764.
21. Porcar, I., P. Perrin, and C. Tribet, *Uv-Visible Light: A Novel Route to Tune the Type of an Emulsion.* Langmuir, 2001. **17**(22): p. 6905-6909.
22. Khoukh, S., P. Perrin, F.B. de Berc, and C. Tribet, *Reversible Light-Triggered Control of Emulsion Type and Stability.* Chemphyschem, 2005. **6**(10): p. 2009-2012.
23. Orihara, Y., A. Matsumura, Y. Saito, N. Ogawa, T. Saji, et al., *Reversible Release Control of an Oily Substance Using Photoresponsive Micelles.* Langmuir, 2001. **17**(20): p. 6072-6076.
24. Wichterle, O. and D. Lim, *Hydrophilic Gels for Biological Use.* Nature, 1960. **185**(4706): p. 117-118.
25. Peppas, N.A. and R. Langer, *New Challenges in Biomaterials.* Science, 1994. **263**(5154): p. 1715-1720.
26. Marler, J.J., J. Upton, R. Langer, and J.P. Vacanti, *Transplantation of Cells in Matrices for Tissue Regeneration.* Advanced Drug Delivery Reviews, 1998. **33**(1-2): p. 165-182.
27. Pelton, R.H. and P. Chibante, *Preparation of Aqueous Lattices with N-Isopropylacrylamide.* Colloids and Surfaces, 1986. **20**(3): p. 247-256.
28. Pelton, R., *Temperature-Sensitive Aqueous Microgels.* Advances in Colloid and Interface Science, 2000. **85**(1): p. 1-33.
29. Schild, H.G., *Poly (N-Isopropylacrylamide) - Experiment, Theory and Application.* Progress in Polymer Science, 1992. **17**(2): p. 163-249.
30. Brannonpeppas, L. and N.A. Peppas, *Solute and Penetrant Diffusion in Swellable Polymers .9. The Mechanisms of Drug Release from Ph-Sensitive Swelling-Controlled Systems.* Journal of Controlled Release, 1989. **8**(3): p. 267-274.
31. Philippova, O.E., D. Hourdet, R. Audebert, and A.R. Khokhlov, *Ph-Responsive Gels of Hydrophobically Modified Poly(Acrylic Acid).* Macromolecules, 1997. **30**(26): p. 8278-8285.
32. Mamada, A., T. Tanaka, D. Kungwatchakun, and M. Irie, *Photoinduced Phase-Transition of Gels.* Macromolecules, 1990. **23**(5): p. 1517-1519.
33. Irie, M., *Stimuli-Responsive Poly(N-Isopropylacrylamide) - Photoinduced and Chemical-Induced Phase-Transitions.* Advances in Polymer Science, 1993. **110**: p. 49-65.
34. Mudiyanselage, T.K. and D.C. Neckers, *Photochromic Superabsorbent Polymers.* Soft Matter, 2008. **4**(4): p. 768-774.
35. Suzuki, A., H. Suzuki, O. Sakashita, and H. Sakuyama, *Phase-Transition in Polymer Gels Due to Local Heating by Illumination of Light.* Phase Transitions, 1994. **47**(3-4): p. 161-181.
36. Hoffmann, J., M. Plotner, D. Kuckling, and W.J. Fischer, *Photopatterning of Thermally Sensitive Hydrogels Useful for Microactuators.* Sensors and Actuators a-Physical, 1999. **77**(2): p. 139-144.
37. Suzuki, H., *Stimulus-Responsive Gels: Promising Materials for the Construction of Micro Actuators and Sensors.* Journal of Intelligent Material Systems and Structures, 2006. **17**(12): p. 1091-1097.
38. Ji Young, P. and et al., *A Polymeric Microfluidic Valve Employing a Ph-Responsive Hydrogel Microsphere as an Actuating Source.* Journal of Micromechanics and Microengineering, 2006. **16**(3): p. 656.
39. Traitel, T., Y. Cohen, and J. Kost, *Characterization of Glucose-Sensitive Insulin Release Systems in Simulated in Vivo Conditions.* Biomaterials, 2000. **21**(16): p. 1679-1687.
40. Satav, S.S., S. Bhat, and S. Thayumanavan, *Feedback Regulated Drug Delivery Vehicles: Carbon Dioxide Responsive Cationic Hydrogels for Antidote Release.* Biomacromolecules. **11**(7): p. 1735-1740.
41. Lee, C.T., K.A. Smith, and T.A. Hatton, *Photoreversible Viscosity Changes and Gelation in Mixtures of Hydrophobically Modified Polyelectrolytes and Photosensitive Surfactants.* Macromolecules, 2004. **37**(14): p. 5397-5405.

42. Alvarez-Lorenzo, C., S. Deshmukh, L. Bromberg, T.A. Hatton, I. Sandez-Macho, et al., *Temperature- and Light-Responsive Blends of Pluronic F127 and Poly(N,N-Dimethylacrylamide-Co-Methacryloyloxyazobenzene).* Langmuir, 2007. **23**(23): p. 11475-11481.
43. Deshmukh, S., L. Bromberg, K.A. Smith, and T.A. Hatton, *Photoresponsive Behavior of Amphiphilic Copolymers of Azobenzene and N,N-Dimethylacrylamide in Aqueous Solutions.* Langmuir, 2009. **25**(6): p. 3459-3466.
44. Ruchmann, J., S. Fouilloux, and C. Tribet, *Light-Responsive Hydrophobic Association of Surfactants with Azobenzene-Modified Polymers.* Soft Matter, 2008. **4**(10): p. 2098-2108.
45. Rankin, P.J., J.M. Ginder, and D.J. Klingenberg, *Electro- and Magneto-Rheology.* Current Opinion in Colloid & Interface Science, 1998. **3**(4): p. 373-381.
46. America, A.o. *2011 Audi Tts Coupe, Explore the Audi Tts Coupe, Innovation.* 2010 [cited 2010; Available from: http://www.audiusa.com/us/brand/en/models/tts_coupe/explore/innovation.html.
47. Chang, F., Q. Qu, and M. Miller, *Fluid System Having Controllable Reversible Viscosity.* 2002: USA.
48. Jeong, B., Y.H. Bae, D.S. Lee, and S.W. Kim, *Biodegradable Block Copolymers as Injectable Drug-Delivery Systems.* Nature, 1997. **388**(6645): p. 860-862.
49. Deshmukh, S., *Responsive Polymers for Dynamic Modulation of Biomacromolecular Transport Properties*, in *Department of Chemical Engineering*. 2008, Massachusetts Institute of Technolog: Cambridge.
50. Allain, C. and L. Salome, *Gelation of Semidilute Polymer Solutions by Ion Complexation: Critical Behavior of the Rheological Properties Versus Cross-Link Concentration.* Macromolecules, 1990. **23**: p. 981-987.
51. Klaveness, T.M. and P. Ruoff, *Kinetics of the Cross-Linking of Polyacrylamide with Cr(Iii): Analysis of Possible Mechanisms.* J. Phys. Chem., 1994. **98**: p. 10119-10123.
52. Klaveness, T.M., P. Ruoff, and J. Kolnes, *Kinetics of the Cross-Linking of Poly(Acrylamide) with Cr(Iii). 3. Rheological Measurements of the Gelation.* J. Phys. Chem., 1995. **99**: p. 8255-8259.
53. Nijenhuis, K.T., *Viscoelastic Properties of Thermoreversible Gels*, in *Physical Networks: Polymers and Gels*, W. Burchard and S.B. Ross-Murphy, Editors. 1990, Elsevier: New York. p. 15-33.
54. Lindman, B., M.C. Puyal, N. Kamenka, R. Rymden, and P. Stilbs, *Micelle Formation of Anionic and Cationic Surfactants from Fourier-Transform H-1 and Li-7 Nuclear Magnetic-Resonance and Tracer Self-Diffusion Studies.* Journal of Physical Chemistry, 1984. **88**(21): p. 5048-5057.
55. Nilsson, S., K. Thuresson, B. Lindman, and B. Nystrom, *Associations in Mixtures of Hydrophobically Modified Polymer and Surfactant in Dilute and Semidilute Aqueous Solutions. A Rheology and Pfg Nmr Self-Diffusion Investigation.* Macromolecules, 2000. **33**(26): p. 9641-9649.
56. Brand, T., S. Richter, and S. Berger, *Diffusion Nmr as a New Method for the Determination of the Gel Point of Gelatin.* Journal of Physical Chemistry B, 2006. **110**(32): p. 15853-15857.
57. Gauglitz, G., *Photophysical, Photochemical and Photokinetic Properties of Photochromic Systems*, in *Photochromism: Molecules and Systems*, H. Duerr, Editor. 2003.
58. Rau, H., *Azo Compounds*, in *Photochromism: Molecules and Systems*, H. Duerr, Editor. 2003, Elsevier.
59. Irie, M. and M. Hosoda, *Photoresponsive Polymers - Reversible Solution Viscosity Change of Poly(N,N-Dimethylacrylamide) with Pendant Triphenylmethane Leucohydroxide Residues in Methanol.* Makromolekulare Chemie-Rapid Communications, 1985. **6**(8): p. 533-536.
60. Lu, Y.C., E.W.G. Diau, and H. Rau, *Femtosecond Fluorescence Dynamics of Rotation-Restricted Azobenzenophanes: New Evidence on the Mechanism of Trans -> Cis Photoisomerization of Azobenzene.* Journal of Physical Chemistry A, 2005. **109**(10): p. 2090-2099.
61. Knoll, H., *Photoisomerism of Azobenzenes*, in *Crc Handbook of Organic Photochemistry and Photobiology*, F.L. W. Horspool, Editor. 2004, CRC Press.

62. Monti, S., G. Orlandi, and P. Palmieri, *Features of the Photochemically Active State Surfaces of Azobenzene* Chemical Physics, 1982. **71**(1): p. 87-99.

63. Diau, E.W.G., *A New Trans-to-Cis Photoisomerization Mechanism of Azobenzene on the S-1(N,Pi*) Surface.* Journal of Physical Chemistry A, 2004. **108**(6): p. 950-956.

64. Tiago, M.L., S. Ismail-Beigi, and S.G. Louie, *Photoisomerization of Azobenzene from First-Principles Constrained Density-Functional Calculations.* Journal of Chemical Physics, 2005. **122**(9).

65. Conti, I., M. Garavelli, and G. Orlandi, *The Different Photoisomerization Efficiency of Azobenzene in the Lowest N Pi* and,Pi Pi* Singlets: The Role of a Phantom State.* Journal of the American Chemical Society, 2008. **130**(15): p. 5216-5230.

66. Nagele, T., R. Hoche, W. Zinth, and J. Wachtveitl, *Femtosecond Photoisomerization of Cis-Azobenzene.* Chemical Physics Letters, 1997. **272**(5-6): p. 489-495.

67. Fujino, T., S.Y. Arzhantsev, and T. Tahara, *Femtosecond/Picosecond Time-Resolved Spectroscopy of Trans-Azobenzene: Isomerization Mechanism Following S-2(Pi Pi*)<- S-0 Photoexcitation.* Bulletin of the Chemical Society of Japan, 2002. **75**(5): p. 1031-1040.

68. Fujino, T. and T. Tahara, *Picosecond Time-Resolved Raman Study of Trans-Azobenzene.* Journal of Physical Chemistry A, 2000. **104**(18): p. 4203-4210.

69. Rau, H., *Photoisomerization of Azobenzenes*, in *Photochemistry and Photophysics*, J. Rabek, Editor. 1990, CRC Press.

70. Tanford, *The Hydrophobic Effect: Formation of Micelles and Biological Membranes.* 1980: Wiley.

71. Irie, M., Y. Hirano, S. Hashimoto, and K. Hayashi, *Photoresponsive Polymers .2. Reversible Solution Viscosity Change of Polyamides Having Azobenzene Residues in the Main Chain.* Macromolecules, 1981. **14**(2): p. 262-267.

72. Wolff, T., C.S. Emming, T.A. Suck, and G. Vonbunau, *Photorheological Effects in Micellar Solutions Containing Anthracene-Derivatives - a Rheological and Static Low-Angle Light-Scattering Study.* Journal of Physical Chemistry, 1989. **93**(12): p. 4894-4898.

73. Sakai, H., Y. Orihara, H. Kodashima, A. Matsumura, T. Ohkubo, et al., *Photoinduced Reversible Change of Fluid Viscosity.* Journal of the American Chemical Society, 2005. **127**(39): p. 13454-13455.

74. Ketner, A.M., R. Kumar, T.S. Davies, P.W. Elder, and S.R. Raghavan, *A Simple Class of Photorheological Fluids:Â€‰ Surfactant Solutions with Viscosity Tunable by Light.* Journal of the American Chemical Society, 2007. **129**(6): p. 1553-1559.

75. Wang, K.T., I. Iliopoulos, and R. Audebert, *Viscometric Behavior of Hydrophobically Modified Poly(Sodium Acrylate)* Polymer Bulletin, 1988. **20**(6): p. 577-582.

76. Pouliquen, G. and C. Tribet, *Light-Triggered Association of Bovine Serum Albumin and Azobenzene-Modified Poly(Acrylic Acid) in Dilute and Semidilute Solutions.* Macromolecules, 2006. **39**(1): p. 373-383.

Chapter 2

Photokinetics

2.1 Introduction

A series of photoresponsive systems are described in this work. The sensitivity to light in each system is due to the azobenzene moiety. Azobenzene (Figure 2-1) can take either the *trans* or *cis* (Z, zusammen) conformation about its N-N double bond. Interconversion between the two forms is driven by the absorption of light; UV favors the production of *cis*, while visible light favors *trans*. The *trans* form is more stable, so there is also a thermal reaction from *cis* to *trans*; a sample left in the dark will eventually become entirely *trans*. This is known as the dark-adapted state.

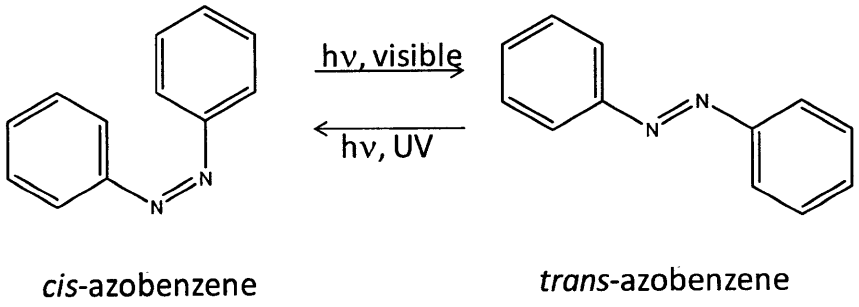

Figure 2-1 Isomers of azobenzene.

The azobenzene group is incorporated into a photosensitive surfactant, 4-ethyl-4'(trimethylaminobutoxy) azobenzene bromide (azoTAB), shown in Figure 2-2. This surfactant was first synthesized by Hayashita et al [1].

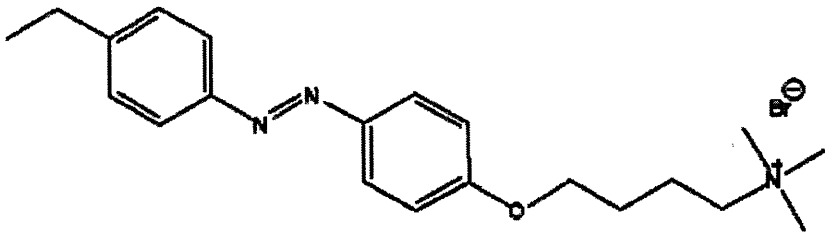

Figure 2-2 Structure of azoTAB, shown in the *trans* form

As discussed in Chapter 1, the *trans* isomer of azoTAB is more able to form micelles than the *cis*. This is due to packing constraints imposed by the kinked shape of *cis*, as well as the fact that the *trans* isomer is more hydrophobic. Using conductivity measurements, it has been demonstrated that there are concentrations at which a *trans*-dominated sample will form micelles, but a *cis*-rich sample will not [1]. This difference in the ability to form micelles makes it possible to induce micelle formation or dissolution with appropriate usage of light, as discussed in Chapter 3. These environmentally sensitive aggregates can be further used as cross-linking points for reversible polymer gels, as discussed in Chapter 4.

The equilibrium state of such a gel or colloidal system is determined in part by the isomer composition. The kinetics of any light-activated transition in such a system, such as gelation, can proceed no faster than the photoreaction itself. Therefore a complete description of the photochemistry is prerequisite for understanding the kinetics of the overall system and to design any applications. The rate of reaction and the steady state composition (photo-stationary state) should be known for any given set of irradiation conditions and azoTAB concentrations.

The photochemistry of azobenzene has been investigated for decades. The light-initiated reaction between the *trans* and *cis* forms of azobenzene was first observed in 1937 [2]. Knowledge of the exact mechanism is not required to adequately describe the kinetics, as was notably done by Zimmerman for azobenzene in isooctane [3], and followed by others [4, 5]. Zimmerman used UV-Vis spectroscopy to follow the reaction over time under various wavelengths of light, suggested a simple model that did not assume any specific mechanism, and was able make some limited inferences about the mechanism from the results. This approach has served as a blueprint for many workers in subsequent years. These published results are, however, insufficient for the present study. The behavior of azobenzene derivatives such as azoTAB can be expected to differ from azobenzene itself [6]. Solvent effects can also be expected to affect the absorption and reaction characteristics [7, 8]. Previous workers have characterized or used the azoTAB molecule in particular, though none have published a study of its kinetics [1, 9-11]. What follows is a description of such a study.

2.2 Experimental Section

2.2.1. Materials

The photosensitive surfactant 4-ethyl-4'(trimethylaminobutoxy) azobenzene bromide (azoTAB) was synthesized as previously described in the literature [1]. All reagents were used as received from Sigma-Aldrich. All solutions were prepared in deuterium oxide, obtained from Cambridge Isotope Laboratories (Andover, MA). The deuterated solvent is required for NMR studies, and was used in all other experiments as well to ensure consistency in the results.

2.2.2. Characterization

Isomer composition and photochemical kinetics were measured by both ^{1}H NMR and UV-Vis spectroscopy. The NMR data were collected using a Varian 500 MHz spectrometer and allowed direct computation of the isomer composition through integration of peak areas. The number of scans was set to ensure a signal to noise ratio sufficient for accurate integration (assessed qualitatively); at the lowest concentration (0.4 mM) this was 36 scans, requiring a total acquisition time of 10 minutes. Concentrations below 0.4 mM were not used to avoid overly long acquisition times. Fewer scans are required for a sufficient signal to noise ratio as the concentration increases, decreasing to a total acquisition time of 3 minutes used for 30 mM samples. Complete relaxation of the nuclei between each scan is required for the collection of quantitative peak areas [12]. It is recommended to wait for at least 5 times the nuclear relaxation time T_1 between scans, and this condition has been met by setting the delay time between pulses at 10 seconds. The free induction decay (FID) is the signal measured in the experiment; this was acquired in 3 to 5 seconds in each scan. Solutions were placed in quartz tubes (Wilmad Labglass) with an outer diameter of 5 mm and a sample volume of 0.6 mL. Quartz was used instead of the standard borosilicate glass as it is transparent across the wavelength range used to achieve photoisomerization (300 nm to 600 nm), thus allowing samples to be irradiated after loading in the tube.

Complementary UV-Vis absorbance data were acquired using an Agilent 8453 spectrophotometer, with sample temperature set to 25 C using a Peltier cell unless otherwise noted. Absorbance can be measured over the range 190 nm to 1100 nm. Quartz cuvettes were obtained from Starna Cells (Atascadero, CA). The cuvette path length was chosen to ensure that the absorbance remained below 2, and was generally below 1.5 for the peaks of interest. For concentrations between 0.005 mM and 0.08 mM, a standard rectangular cuvette with a 1 cm path length was used. For concentrations between 1 mM and 6 mM a path length of 0.01 cm was needed, as illustrated in Figure 2-3. In all cases, use of the Beer-Lambert Law allowed calculation of the isomer composition.

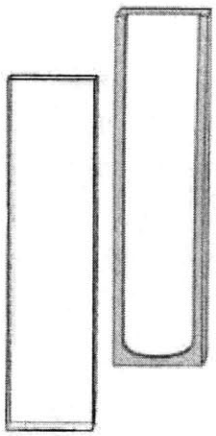

Figure 2-3 Reduced path length UV-Vis cell, used for concentrations of azoTAB above 1 mM (image from Starna). The solution is placed within the indented well seen on the part on the right. The flat piece on the left then covers and seals the well.

Photoisomerization of azoTAB was achieved using a 200 W mercury arc lamp (Osram, model 69198) and a variety of filters. The spectral lines of the lamp are shown in Figure 2-4; it must be noted that the available light is not uniform in intensity across the wavelength range of interest (300 nm to 600 nm). Bandpass filters (360 nm Oriel #59810, 330 nm #59800), long-pass filters (400 nm #51272) and narrow pass filters (350 nm #59640, 370 nm #59640, 400 nm #59280, 490 nm #59335) were used to isolate the desired wavelengths for any given experiment. Narrowpass filters typically have a full width at half maximum (FWHM) of 10 nm; the 330 nm bandpass filter and 360 nm bandpass filters have FWHM of 147 nm and 52 nm, respectively. Narrowpass filters thus yield more monochromatic light which simplifies any analysis, while the bandpass filters permit greater light intensity which allows faster photoconversion. The lack of strong Hg lines in the visible range does not permit use of visible monochromatic light of high intensity, so longpass filters are used in this range. In all cases an additional filter (Schott KG 4) was used to remove infrared wavelengths and prevent any heating they might cause. The intensity of UV light was measured using an Accu-Cal 30 radiometer; intensities varied from 0.15 to 8 mW/cm^2 at a distance of 1" from the lamp outlet, depending on the filter.

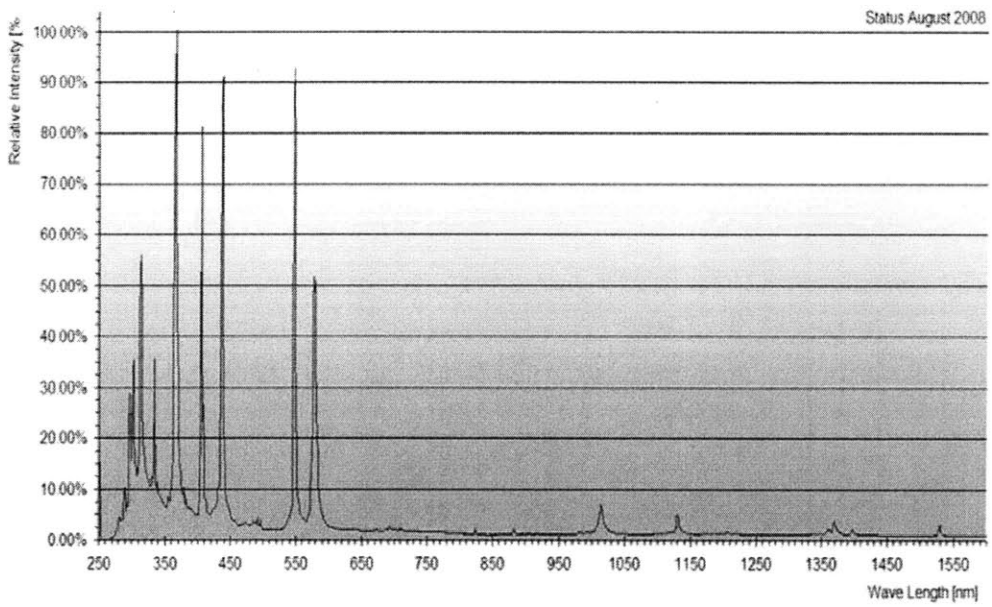

Figure 2-4 Spectral output of mercury lamp used in this work. Source: Sylvania.

Some supplementary data were collected using additional light sources of higher intensity. These are the Blue Wave 200 lamp (Dymax Corp, Torrington CT) for polychromatic UV light and an Argon ion laser operated at 1 W for 514 nm light. Both of these sources irradiate a smaller area than the Oriel lamp, but at a higher intensity. The Dymax lamp produces an intensity of 50 mW/cm^2.

All solutions were prepared in the dark from pure *trans* crystals and they remain 100% *trans* so long as they are stored in the dark. Photokinetics were measured by irradiating a sample (already loaded in cuvette or tube) for some length of time and then inserting into the appropriate spectrometer for measurement. The process is repeated on the same solution until the photostationary state is achieved. The intervening time between irradiation and measurement is less than one minute, over which time the isomeric composition is not expected to change (see Results). It has been found that the conversion at any total irradiation time is independent of how many stages of irradiation were used, e.g. ten seconds of UV light on an initially 100% *trans* sample brings about the same result as two five second doses of UV light on an identical sample (see Figure 2-5).

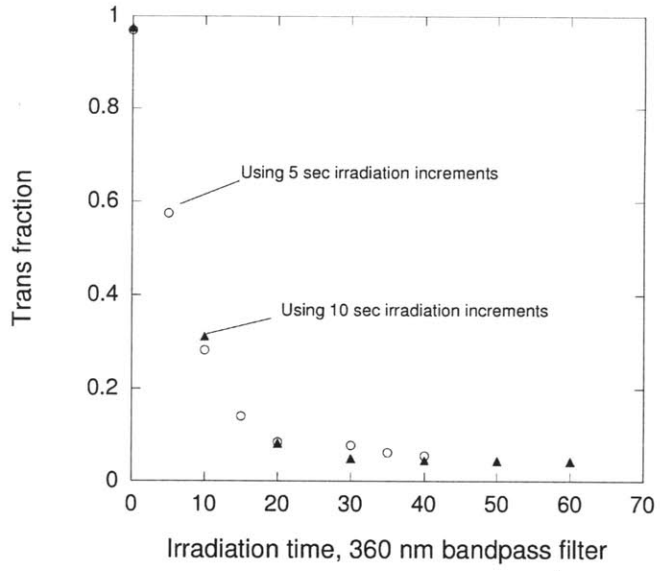

Figure 2-5 Effect of irradiation time increments on photoconversion rate. Measured by UV-Vis spectroscopy at azoTAB concentration of 0.04 mM and irradiance of 5.4 mW/cm^2 from mercury lamp with a 360 nm bandpass filter. Varying the irradiation increments does not significantly affect the amount of conversion. Methodology described in following section.

Irradiation of samples in UV-Vis cuvettes took place as pictured in Figure 2-6a. Magnetic stirring was using during irradiation for 1 cm path length cuvettes but is not possible with the shorter path length. A similar procedure was used for samples in NMR tubes, shown in Figure 2-6b. Stirring is not possible in the NMR tube. In all cases the entire sample volume fell within the illumination area, and the intensity was not found to vary greatly within that area. The temperature of the sample was not controlled during irradiation, but was generally not found to vary from room temperature.

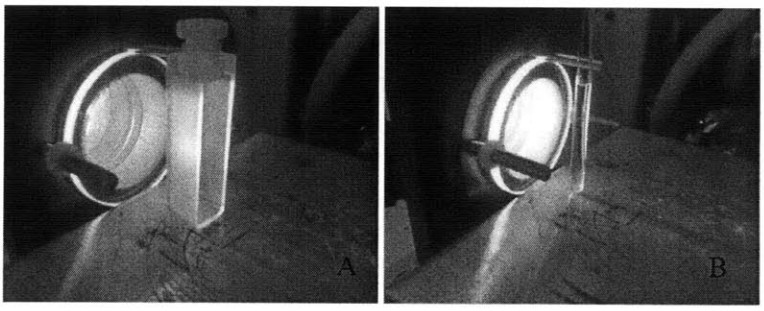

Figure 2-6 Experimental setup for sample irradiation. 8A, for UV-Vis cuvette. 8B, for NMR tube. Light exits lamp assembly through a filter with an outer diameter of 2 inches. Samples are placed 1" from the filter in a marked location, to ensure consistent irradiance.

2.3 Results and Discussion

Like any other azobenzene derivative, the azoTAB surfactant used here can undergo photoisomerization between *trans* and *cis* conformations upon absorption of light. UV wavelengths tend to drive conversion towards *cis* rich solutions, while visible wavelengths achieve the reverse. This conversion is useful in the case of azoTAB as the *trans* and *cis* isomers have different propensities to form micelles. *Cis* has a higher dipole moment so it can be expected to remain dispersed as monomers in water at concentrations higher than is possible for *trans*. Additionally the bent shape of the *cis* isomer does not lend itself to efficient packing within a micelle. This difference in the ability to form micelles is the basis for the photosensitivity of the materials described in this work.

As the balance between the two isomers controls the interesting aggregation behavior of the systems being studied, it is of vital importance to measure the isomeric composition at any given time and to be able to predict that composition over the course of some irradiation. Any change of properties in the studied system will be at least as slow as the photoreaction.

2.3.1. Determination of isomeric composition

A reliable technique to measure the isomer composition is prerequisite for studying photochemistry. It was found that both ^{1}H NMR and UV-Vis spectroscopy are adequate methods, though the use of UV-Vis requires some supporting data obtained by NMR. NMR is discussed first.

Shown in Figure 2-7 is the ^{1}H NMR spectrum of the nine protons in the three methyl groups arranged around the surfactant head. These nine are identical to each other in the NMR experiment and appear as a single singlet.

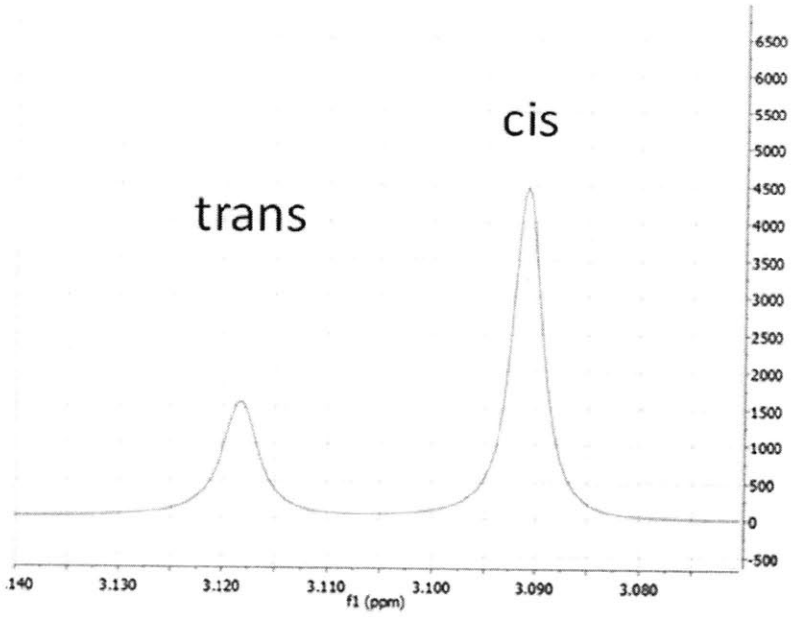

Figure 2-7 NMR (500 Mhz) spectrum of head group protons at 6 mM and 65 seconds of Dymax UV light. Peaks integrate to 29.5% trans.

Two distinct singlet peaks appear; the upfield triplet corresponding to *cis* and the downfield *trans*. The two isomers do not always appear in this relative order, so labeling must be done by following the peaks as they evolve from the dark adapted state, in which the sample is 100% *trans*. The isomer composition is simply determined by comparing the integrated peak areas of the two isomers. There are 11 different peaks in the proton spectrum and they yield isomer compositions which are in close agreement with each other. This agreement between all the peaks within a spectrum builds confidence in the measurement. The addition of polymer can obscure some azoTAB peaks, but the aromatic peaks of azoTAB are always well downfield of any polymer signal and thus integration is also possible with gel samples.

The appearance of two distinct peaks is a result of the relatively slow interconversion between *cis* and *trans* during the measurement. If exchange between the two isomers is longer than the millisecond time scale, the NMR experiment can resolve the two forms into two separate peaks [12]. The NMR data are collected in the dark, and it is shown later that the thermal conversion from *cis* to *trans* in the dark is much slower than that time scale, so this appearance of distinct peaks is consistent with expectations. Irradiation is performed prior to the NMR reading, but photoisomerization upon absorption of a photon is expected to be on the picosecond scale [13], so this step is assumed to be instantaneous and completed before the NMR acquisition.

Having established the usage of NMR to find isomer compositions, it becomes possible to also use UV-Vis spectroscopy to the same end. The basis of using UV-Vis absorbance to find the isomer composition lies in the Beer-Lambert Law, shown in derivative form:

$$dI = -\alpha C I dx \tag{2.1}$$

where dI is the reduction in light intensity due to absorption across a slab with thickness dx, I is the local light intensity (more properly 'irradiance'), C is the molar concentration of the absorbing species and α is some wavelength-specific constant. The basis for this expression is purely empirical.

Equation (2.1) integrates to

$$\ln \frac{I_0}{I_L} = \alpha \int_0^L C dx \tag{2.2}$$

where L is the path length, I_0 is the incident intensity and I_L the intensity at x = L. This expression simplifies to (2.3) if the concentration of the absorbing species is uniform throughout the sample volume:

$$\ln \frac{I_0}{I_L} = \alpha C L \tag{2.3}$$

It is common practice to use base 10 logarithms instead of the natural:

$$A = \log \frac{I_0}{I_L} = \varepsilon C L \tag{2.4}$$

where A is the absorbance and ε the molar absorptivity, which is wavelength-specific. UV-Vis instruments generally report the absorbance as defined in Equation (2.4). The previous constant α is related to ε by

$$\alpha = \varepsilon \ln(10) \tag{2.5}$$

The precision of the UV-Vis measurement becomes insufficient at absorbance values above 2. At a path length of 1 cm, this sets a concentration limit of 0.08 mM. Also, at higher concentrations, intermolecular interactions may influence the absorptivity and any large aggregates may cause scattering, so measurements in such regions must be carefully considered.

Guided by Equation (2.4), the absorbance at a series of different concentrations is measured for 100% *trans* samples. The path length is known, so the absorptivity can be calculated from the slope of the absorbance against concentration. The absorptivities for the 100% *trans* samples are shown below.

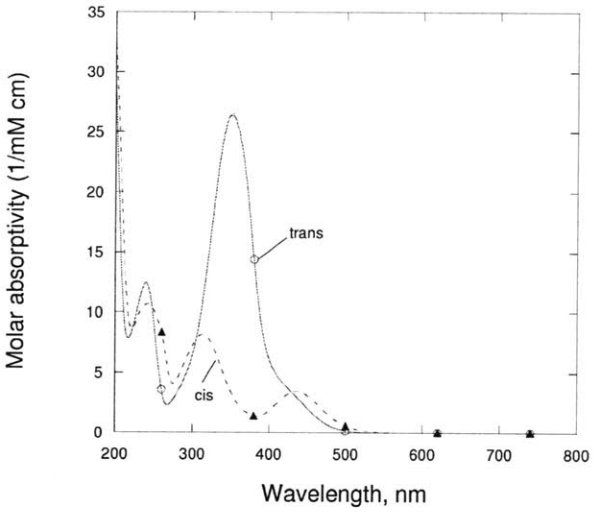

Figure 2-8 Molar absorptivities of *trans* and *cis* azoTAB, measured at concentrations between 0.01 and 0.08 mM using a 1 cm path length cell held at 25 C. *Trans* taken directly from slope of absorbance vs concentration; *cis* computed as described in the text.

It should be noted that while pure *trans* can be isolated, as confirmed by NMR, it is very difficult to obtain crystals or solutions of pure *cis* [3]. Instead, *cis*-rich solutions were prepared under UV light (97% *cis*, as measured by NMR), and the Beer-Lambert Law was used as written for two components:

$$A = \varepsilon_{trans} C_{trans} L + \varepsilon_{cis} C_{cis} L \tag{2.6}$$

It can be readily shown that the slope of absorbance versus concentration for this *cis*-rich solution will yield an apparent absorptivity ε_{UV}, from which the actual *cis* absorptivity ε_{cis} can be calculated:

$$\varepsilon_{cis} = \frac{\varepsilon_{UV} - \varepsilon_{trans} y_{trans}}{y_{cis}} \tag{2.7}$$

where y_{trans} and y_{cis} are 0.03 and 0.97 respectively, or the compositions of the UV-adapted solution. The mole fractions used here and throughout this work exclude the solvent. The molar absorptivities for *cis* shown in Figure 2-8 are thus calculated and not directly taken from the slope of A vs concentration. This approach for finding the *cis* absorptivities differs somewhat from that seen in the literature [3]. There are claims in the literature that 99% *cis* samples can be isolated by liquid chromatography [2, 3, 14], but this procedure was judged too unwieldy for the purposes of this work.

The absorptivities in Figure 2-8 are similar to those found by Lee for azoTAB in non-deuterated water [9], though they differ somewhat from pure azobenzene in ethanol (Figure 2-9). These differences may be due to both solvent and substituent effects [8]; the additional data required to distinguish between the

two effects were not collected. In particular, the azobenzene spectrum is significantly blueshifted in comparison to azoTAB. The azoTAB peak around 350 nm corresponds to the π-π^* transition to S_2, while that around 440 nm is assigned to n-π^* (S_1). The n-π^* transition is weak in *trans* as it is forbidden for that isomer [6], though it is rather stronger in azoTAB than in azobenzene. The π-π^* and n-π^* bands are much better separated in azobenzene than in azoTAB, in which they overlap significantly. The highest energy peak may correspond to the σ-σ^* peak. Vibrational fine structure is not observed.

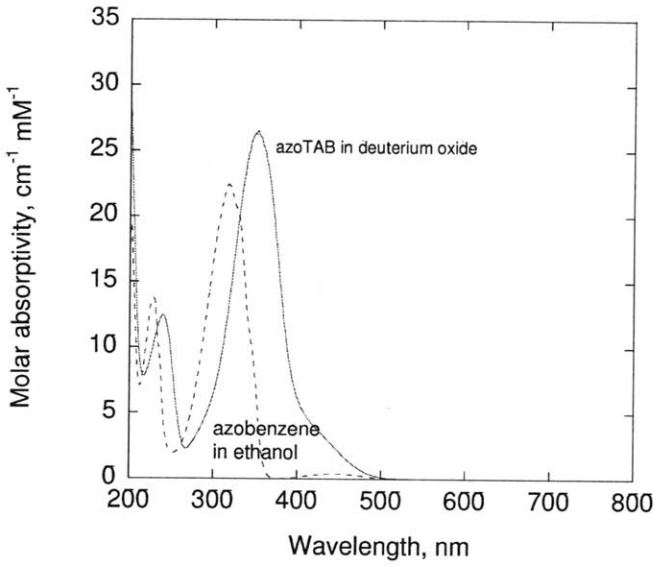

Figure 2-9 Effect of substituents and/or solvent on molar absorptivity. Solid line: 100% *trans* azoTAB in deuterium oxide (from Figure 2-8); broken line: 100% *trans* azobenzene in ethanol. Azobenzene data measured between 0.01 and 0.04 mM in 1 cm path length cell.

Some insights can be drawn from the absorptivities illustrated in Figure 2-8. The *cis* isomer shows well-separated π-π^* and n-π^* bands, with the former being blue-shifted in comparison with the *trans*. Irradiation in the π-π^* band should tend to cause conversion to *cis*, since *trans* absorbs much more strongly than *cis* over these (UV) wavelengths. Any *trans* present would have much opportunity to reach the excited states that enable the reaction. The absorptivities of the two isomers in the n-π^* band are more similar in magnitude. Visible irradiation would favor the formation of *trans*, but not as strongly as the converse. These inferences based on the absorptivities should hold unless one reaction (*cis*-to-*trans* or *trans*-to-*cis*) is somehow much more favourable than the other. The relative favourabilities of the two reactions can be assessed by comparing their quantum yields, which are discussed later in this chapter.

Having found the absorptivities, the isomeric composition of any solution can be found by fitting the absorbance predicted by the two-component Beer-Lambert Law to the measured absorbance by adjusting the isomer molar fractions. The appearance of consistent isobestic points (at 223, 248, 305 and 429 nm)

in Figure 2-8 and Figure 2-10 allows the assumption that there are only two absorbing species in the solution. The molar absorptivities of *cis* and *trans* are equal at those points and it would be a remarkable coincidence if a third component also had the same absorptivity at that wavelength.

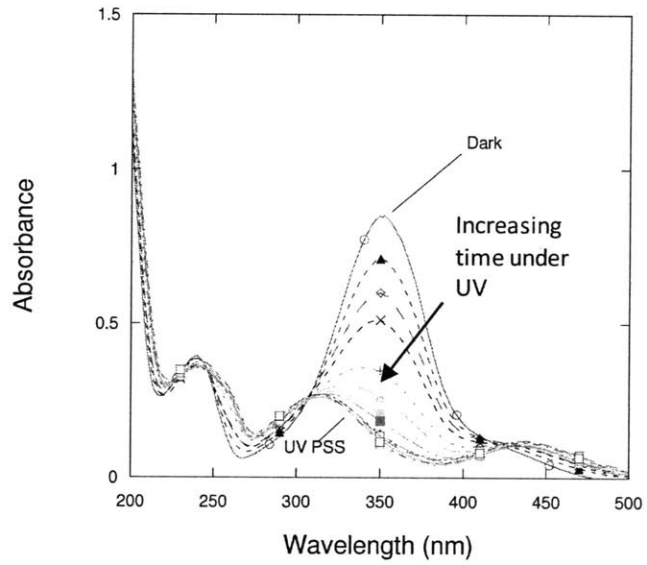

Figure 2-10 UV-Vis absorption spectra for 0.04 mM azoTAB solutions for different durations of irradiation at 370 nm. 400 seconds required to reach the UV photostationary state. Isosbestic points are clearly observed.

The fit was done by minimizing the sum of squared errors between the measured absorbance and the Beer-Lambert expression over the range from 280 nm to 450 nm. The fits are very good over this range of wavelengths; an example is shown in Figure 2-11.

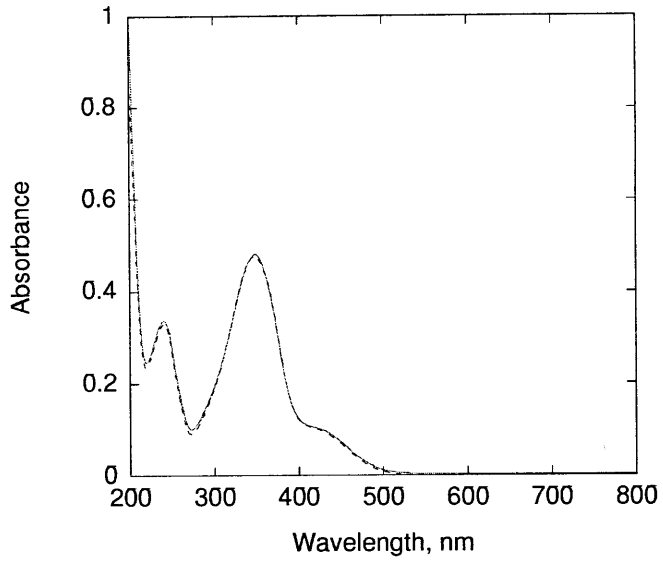

Figure 2-11 Comparison of measured absorbance (in red) and the absorbance using best fit isomer compositions (blue). Concentration of 0.028 mM and trans fraction of 0.587.

The isomeric compositions found from NMR and UV-Vis have been shown to be in close agreement, as seen in Table 2-1.

Table 2-1 *trans* fraction as measured by NMR and UV-Vis on the same samples. Details in text. Based on repeatability, the uncertainty range is about ± 0.02.

NMR	UV-Vis
1.00	1.00
0.97	0.92
0.69	0.70
0.38	0.40
0.24	0.26
0.06	0.09
0.05	0.04

This comparison between the two spectroscopic methods was complicated by the fact that the concentration ranges available for routine use in either instrument do not overlap. The maximum allowable concentration for UV-Vis using a standard 1 cm path length cuvette is 0.08 mM, which is

below the concentration range at which integrable spectra can be acquired using NMR in under 20 minutes. Therefore this experiment was performed by irradiating a large volume of 1 mM azoTAB solution with stirring. At various times the light was shuttered and a portion of the solution removed. Part of that portion was diluted to 0.04 mM for the UV-Vis measurement and the remnant was used directly for NMR. It was assumed that simple dilution would not cause any isomerisation.

The NMR method of determining the isomer composition is assumed to be more accurate than the UV-Vis, so NMR is used to corroborate results from UV-Vis when possible. The fitting procedure used in the UV-Vis method is sensitive to minor errors in the total surfactant concentration. When examining solutions known by NMR to be 3-4% *trans*, it was found that UV-Vis would return *trans* fractions between 1% and 6%. Formal error bars are not shown for isomer compositions in this work, but this range should guide an understanding of the uncertainty involved.

As the molar absorptivities seen in Figure 2-8 were measured at concentrations below 0.08 mM, it may be questioned whether those values apply at the higher concentrations used to make gels (1 to 30 mM), or whether the Beer-Lambert Law even applies at those concentrations. To check if the Beer-Lambert Law is applicable at higher concentrations, the molar absorptivities were measured again, at concentrations of 1 mM to 6 mM. A path length of 0.01 cm was used to find these values of ε_{trans}; they are very similar to those found at the lower concentrations, as shown below:

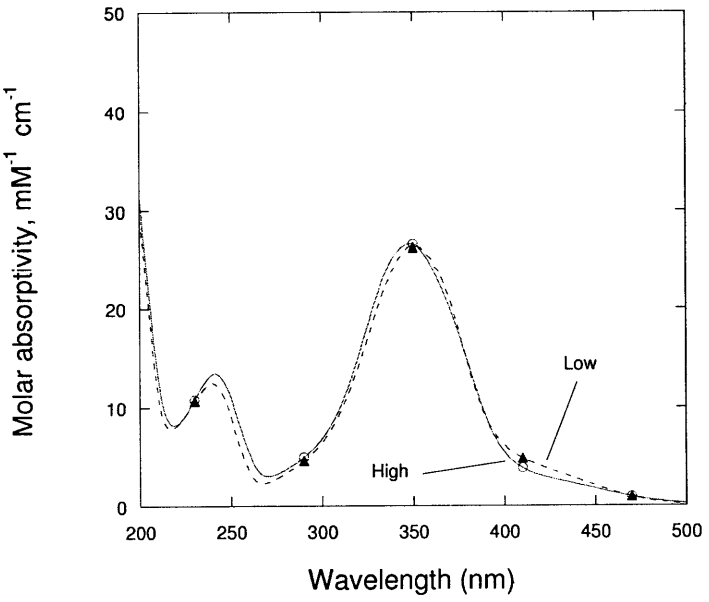

Figure 2-12 Molar absorptivities in the dark adapted state. "Low" measured between 0.01 and 0.08 mM; values taken from Figure 2-8. "High" measured between 1 and 6 mM using 0.01 cm path length cell. Absorptivities are comparable.

Not only are the absorptivities similar in the two concentration ranges, but the slopes of absorbance plotted against concentration are still very linear at the higher concentrations. This linearity confirms the applicability of the Beer-Lambert Law over that concentration range; distortions such as scattering due to any aggregates do not appear to take place.

2.3.2. Thermal Conversion

As the *trans* form of azobenzene is of lower energy than the *cis* (ΔH = 56 kJ/mol for azobenzene [6]), any *cis*-rich solution will revert to trans over time, even in the absence of light. This reaction is denoted as the thermal reaction. It could be inconvenient if it occurred quickly, because use of light would no longer be the only factor controlling the state of the system. It is therefore important to assess the rate of this reaction. Using UV-Vis spectroscopy to measure the changing isomeric composition while a sample is kept in the dark, the rate constant for this thermal reaction can be found.

The isomerisation is expected to follow a first order rate law:

$$\frac{dC_{cis}}{dt} = -k_t C_{cis} \tag{2.8}$$

A semi-log plot of $\frac{y_{cis}}{y_{cis,t=0}}$ against time would thus be expected to be linear, and as seen below, it is:

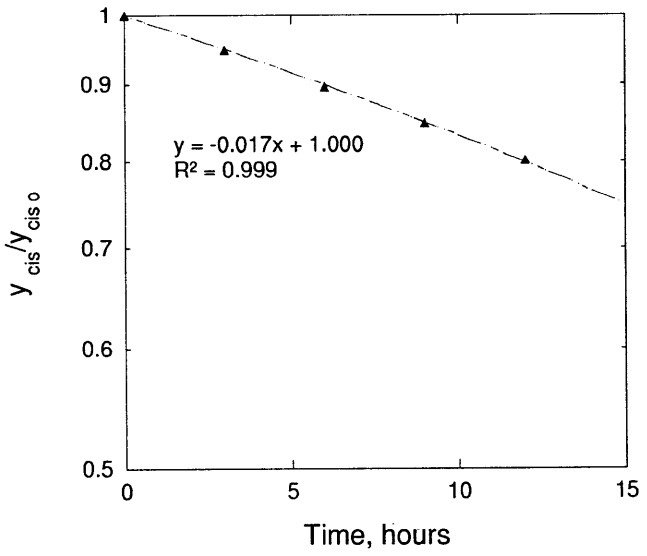

Figure 2-13 Plot to find first order rate constant for thermal isomerization, in 0.05 mM azoTAB solution at 25 C. Initially nearly entirely cis, so ordinate is approximately equal to the cis fraction.

The measured rate constant at 0.05 mM and 25 C, 0.017 1/hr, is comparable to that measured for azobenzene in isooctane, 0.008 1/hr [3]. The isomer composition changes slowly enough in the dark that this thermal reaction can be ignored at times up to one hour. There is currently insufficient data to quantitatively determine whether this rate constant applies at the concentrations more relevant to the systems described in this work (1-20 mM). A truly first order reaction would show no such concentration dependence. It has however been found with other azobenzene derivatives that tight packing reduces the thermal isomerization rate, due to steric hindrances [15]. It is therefore possible that this reaction rate is lower at the higher concentrations at which aggregates form. Any shift in the direction of a slower thermal reaction is considered to be favorable.

In order to emphasize the slow rate of reaction, the same data are shown again in Figure 2-14, with the expected *cis* fractions extended to long times. At 25 C, over a week may be required for a *cis*-rich sample to revert fully to the dark-adapted state. While the thermal isomerization rate has not been quantitatively measured over periods of such length, these time scales are consistent with informal observations. The slow rate of this reaction makes azoTAB favorable for use in practical applications, as its conformation will not appreciably change unless it is irradiated.

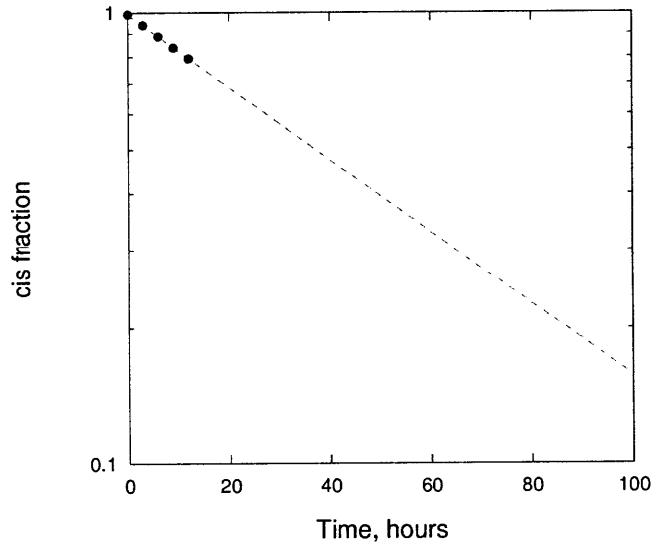

Figure 2-14 Measured *cis* fractions and expected cis fractions using first order rate law, extended to 100 hours.

The thermal isomerization rate measurements were repeated at 15 C and 35 C to find the activation energy. An Arrhenius plot is shown below:

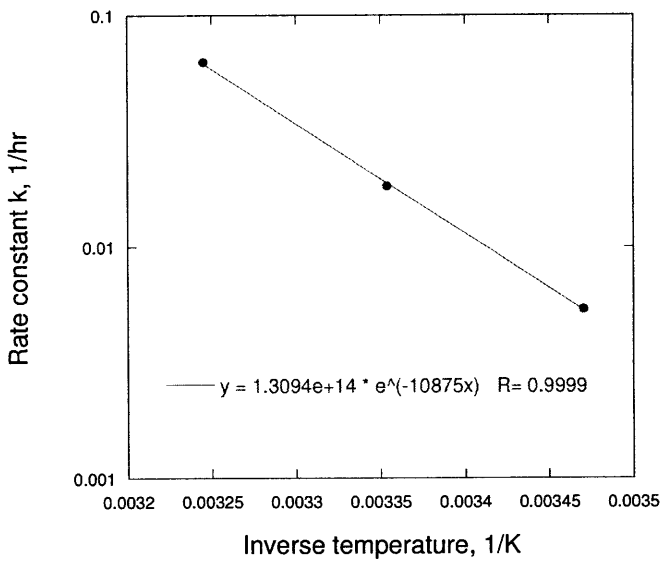

Figure 2-15 Arrhenius Plot to find Activation Energy, data at 0.05 mM and 15, 25 and 35 C

The activation energy is 90.4 kJ/mol, which falls into the range of literature values for azobenzene derivatives of 85 to 100 kJ/mol [6, 16]. Raising the temperature of the sample thus provides a secondary method for driving the solution towards *trans*, in addition to visible irradiation.

2.3.3. Photokinetics

Having established robust methods for determining the isomer composition, it becomes possible to study the photochemical reaction in some detail. At any given wavelength of irradiation, the isomer composition eventually reaches an equilibrium known as a photo-stationary state (PSS). The PSS has been found to be fairly independent of total concentration, though it is not achieved on reasonable time scales if the optical thickness is too great.

A range of different filters has been used with a mercury lamp to produce different photo-stationary states. These are summarized in the table below. This knowledge would be helpful in designing applications that use azoTAB; if it is desired to maintain the isomer composition at a certain value, one only has to choose the appropriate filter.

Table 2-2 Photostationary states at different wavelengths. Measured using either UV-Vis and/or NMR at various concentrations. Sample is irradiated until spectra stop changing.

Filter	PSS *trans* fraction
546 nm	0.98
510 nm and longer	0.93
514 nm	0.90
455 nm and longer	0.70
437 nm	0.54
400 nm and longer	0.47
400 nm	0.24
330, 350, 360 or 370 nm	0.03 to 0.04

The rate of conversion is related to the molar absorptivities at the irradiation wavelength, the total concentration, the intensity of irradiation, and the quantum yield (discussed below). The molar absorptivities at 500 nm and longer are very weak (Figure 2-8), so relatively higher photon fluxes are needed at those wavelengths in order to achieve conversion within a reasonable time frame. An argon ion laser is helpful in this regard, providing a high photon flux at 514 nm. Using the available mercury lamps for shorter wavelengths, conversion takes place on the time scale of minutes at the concentrations of interest, 1 mM to 20 mM (see Figure 2-16).

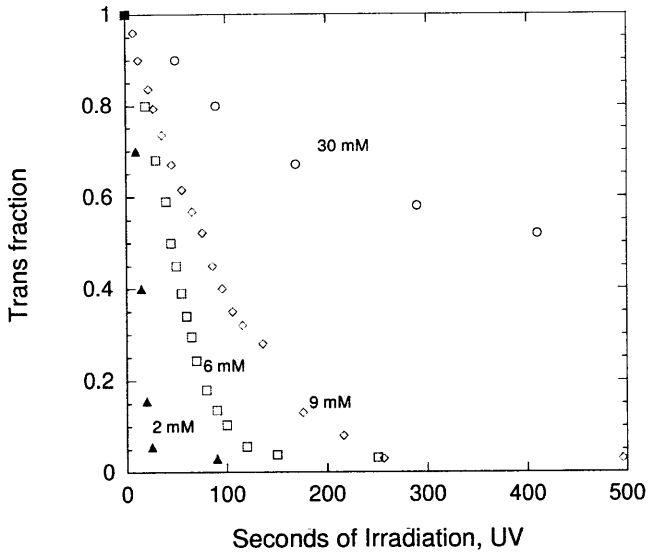

Figure 2-16 Reaction trajectories for azoTAB solutions in D_2O, initially at 100% trans, at 2, 6, 9 and 30 mM. Samples irradiated while in NMR tubes, inner diameter 4.9 mm. UV irradiation from Dymax lamp is used. Data should be taken as qualitative.

2.3.3.1. Well-mixed solutions: Model and experimental results

A kinetic model to describe the photoreaction would be helpful for describing and predicting the behavior of this system. Work towards this end was begun with well-mixed sample volumes, as this simplifies both the measurement and analysis of the reaction. A mathematical framework for describing the reaction in mixed solutions has been used in the literature for decades [3]; the derivation is repeated here. The sample volume is assumed to have a uniform cross-sectional area A_{cs}, as in a standard UV-Vis cuvette.

It is customary to define a term known as the quantum yield, which is specific to each component. For example, the quantum yield ϕ_{trans} is defined as the probability that a *trans* molecule will convert to *cis* upon absorption of one photon by that molecule. The rate of *trans* to *cis* reaction is equal to the rate of light absorption by *trans* multiplied by ϕ_{trans}. The quantum yield is generally taken to be independent of concentration. It can vary with wavelength, though it has been shown to be fairly constant within a given absorption band, e.g. π-π^* or n-π^* [3-5].

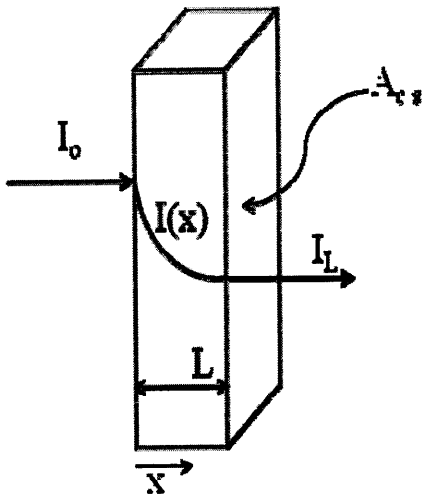

Figure 2-17 Schematic for light absorption across a sample. I_0 is the irradiance, and I_L is transmitted. $A_{c/s}$ is the cross sectional area.

The total rate of absorption in the control volume is equal to $A_{cs}(I_0 - I_L)$ as seen in Figure 2-17, where I_0 is the incident photon flux and I_L is the exiting flux. Assuming the concentrations are uniform throughout the volume and that the irradiation is monochromatic, the Beer-Lambert Law can be manipulated to show that this rate of absorption is equal to

$$A_{cs} I_0 \left(1 - 10^{-D}\right) \tag{2.9}$$

where D is the optical density or total absorbance:

$$D = \varepsilon_{trans} C_{trans} L + \varepsilon_{cis} C_{cis} L \tag{2.10}$$

This definition of quantum yield requires the rate of absorption by each individual isomer; again applying the Beer-Lambert Law, the volumetric rate of absorption by *trans* is

$$\frac{A_{cs} I_0 \left(1 - 10^{-D}\right) \varepsilon_{trans} C_{trans}}{\varepsilon_{trans} C_{trans} + \varepsilon_{cis} C_{cis}} \tag{2.11}$$

and a complementary expression is valid for *cis*.

The component balance then can be written as

$$A_{cs} L \frac{dC_{trans}}{dt} = -\frac{\phi_{trans} A_{cs} I_0 \left(1 - 10^{-D}\right) \varepsilon_{trans} C_{trans}}{\varepsilon_{trans} C_{trans} + \varepsilon_{cis} C_{cis}} + \frac{\phi_{cis} A_{cs} I_0 \left(1 - 10^{-D}\right) \varepsilon_{cis} C_{cis}}{\varepsilon_{trans} C_{trans} + \varepsilon_{cis} C_{cis}} + k_t C_{cis} A_{cs} L \tag{2.12}$$

which simplifies to

$$\frac{dC_{trans}}{dt} = -\phi_{trans} I_0 F \varepsilon_{trans} C_{trans} + \phi_{cis} I_0 F \varepsilon_{cis} C_{cis} + k_t C_{cis} \tag{2.13}$$

where F is a function of time known as the photokinetic factor:

$$F(t) = \frac{1-10^{-D}}{D} \tag{2.14}$$

As the optical density approaches zero, the photokinetic factor approaches the natural logarithm of 10, under which condition $F\varepsilon$ is equivalent to α. This simplification is not relevant here, but provides a link to the model described in Section 2.3.3.3 below.

It is unnecessary to repeat the exercise for *cis*, as at any given time, $C_{tot} = C_{trans} + C_{cis}$.

The irradiance I_0 must be expressed as a molar photon flux, whereas it is measured using a meter reporting in power per unit area. The power is converted to a photon flux by making use of the Planck relation, $E = h\nu$, to find the energy of a single photon at the given wavelength.

Equation (2.13) can be numerically integrated to find the expected $C_{trans}(t)$, provided the two quantum yields are somehow known. Best fit values of the quantum yields are found by comparing the model results with experimental results for $C_{trans}(t)$ in a well-mixed solution. In practice only one quantum yield need be fit, as solving Equation (2.13) at the photostationary state yields an expression relating the two values of ϕ:

$$\phi_{cis} = \frac{y_{trans,PSS}\varepsilon_{trans}}{y_{cis,PSS}\varepsilon_{cis}}\phi_{trans} \tag{2.15}$$

in which the compositions at the PSS are known. This expression assumes that the thermal reaction term is negligible in comparison to the photoreaction terms in Equation (2.13), which has been confirmed to be true under the conditions used to find values of the quantum yield.

UV-Vis was the method chosen for initially monitoring the photoreaction for the purpose of finding the quantum yields and assessing the applicability of the model described above. UV-Vis cuvettes allow stirring during irradiation and present simple planar geometry, as required by the model. As stated earlier, the use of 1 cm path length cells limits the concentration range to a maximum of 0.08 mM, which

is rather below the range of 1 mM to 30 mM which is relevant in the gels studied in this work. However, the quantum yields measured at the lower concentrations are expected to be valid at the higher concentrations. This assumption is tested in a later section.

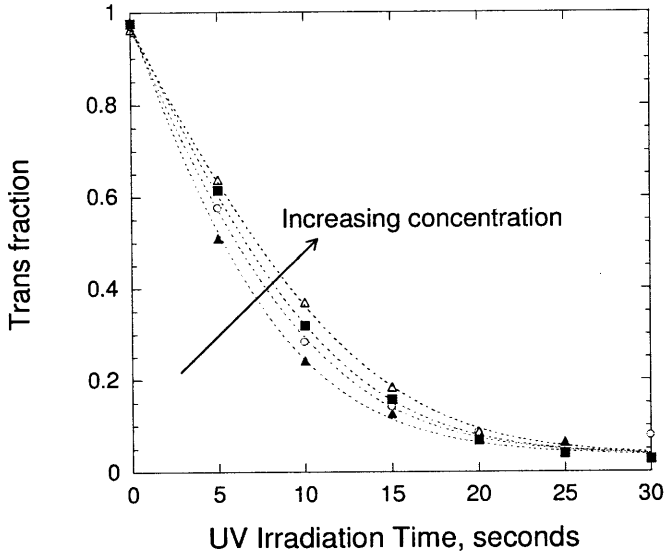

Figure 2-18 Test of the mixed model, including the predicted concentration dependence. Reaction results are shown for 0.03, 0.04, 0.05 and 0.06 mM azoTAB solutions, in a 1 cm path length cuvette with stirring. 5.43 mW/cm^2 irradiation used for each, using 360 nm bandpass filter. Shown with results from mixed-volume model, using quantum yield values fit separately for each concentration. Best fit values of ϕ_{trans}: 0.24, 0.24, 0.26 and 0.26 for 0.03 mM through 0.06 mM, in ascending order. Corresponding ϕ_{cis} : 0.10, 0.10, 0.10 and 0.11. ε_{trans} and ε_{cis} are 25.0 and 2.3 cm^{-1} mM^{-1}, respectively.

Some representative results are shown over a range of concentrations under 360 nm band pass irradiation in Figure 2-18. It is readily seen that the model given above adequately describes the observed rate of reaction, including the concentration dependence of the reaction rate. Values of the quantum yields were fitted separately for each individual concentration: ϕ_{trans} values range from 0.24 to 0.26. If it can be shown that these values are essentially equivalent, then the assumption that quantum yield is independent of concentration is justified.

The sensitivity of the model to quantum yield values is therefore demonstrated in Figure 2-19, using the 0.05 mM data from Figure 2-18. As the quantum yield increases, the reaction curve approaches the limiting case in which absorption always leads to reaction. The difference between the model-predicted conversion rates at ϕ_{trans} values of 0.24 and 0.26 is not absolutely negligible, but it falls within the uncertainty of any experimental measurement. The quantum yield is therefore taken to be independent of concentration, at least over the concentration range examined in Figure 2-18.

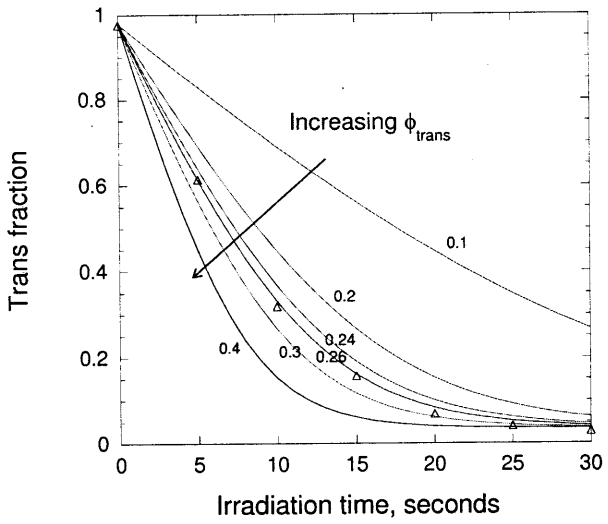

Figure 2-19 Sensitivity of reaction rate to quantum yield. Data is from Figure 2-18, 0.05 mM. Model curves for ϕ_{trans} values of 0.1, 0.2, 0.24, 0.26, 0.3 and 0.4.

A similar approach was used for other wavelengths; data collected at a concentration of 0.02 mM using 350 nm narrow band irradiation are shown in Figure 2-20. Due to the narrow band pass of the filter, the photon flux is much lower than that in the preceding examples. The time scale of the reaction is therefore much longer. The best fit values of the quantum yield are 0.34 and 0.08 for *trans* and *cis*, respectively. Fewer data sets were collected at this wavelength, so it is not apparent whether the observed difference in ϕ_{trans} between the 350 nm and 360 nm filters is significant, or due to some experimental uncertainty.

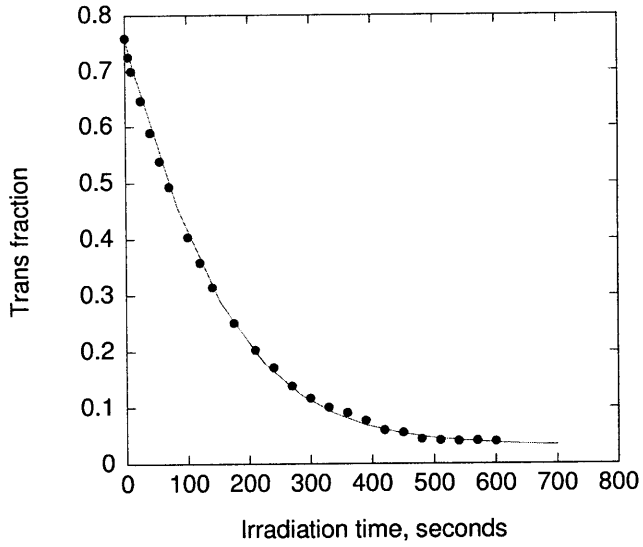

Figure 2-20 Photoconversion of azoTAB at 0.02 mM and 350 nm light, in stirred 1 cm path length cuvette. Incident intensity is 0.15 mW/cm^2. Solid line is model result using best fit value of quantum yield: ϕ_{trans} is 0.34 and ϕ_{cis} is 0.08. ε_{trans} and ε_{cis} are 26.3 and 3.4 cm^{-1} mM^{-1}, respectively. Initial and maximum absorbance at irradiation wavelength is 0.42.

Complicating the analysis of this reaction is the fact that the model was derived for monochromatic irradiation, whereas actual experimental conditions involve a distribution of wavelengths, particularly when a band pass filter is used. In each case, calculations were done assuming monochromatic conditions; from the results this approach appears reasonable. This issue is generally ignored in the literature, though an intensity-weighted average molar absorptivity has been suggested to account for the wavelength distribution [17]. Attempts to account for polychromaticity using this or any other method were unsuccessful due to insufficient data for the lamp's spectral radiance.

The quantum yields measured in the UV band are summarized in the table below:

Table 2-3 Measured quantum yield values, $\pi - \pi^*$ band

Wavelength, nm	Quantum yield, *trans* to *cis*	Quantum yield, *cis* to *trans*
330 nm (band pass filter)	0.36	0.06
350 nm	0.34	0.11
360 nm (band pass filter)	0.26	0.09
370 nm	0.23	0.07

Unfortunately it was not possible to measure the quantum yields in the visible wavelength range, due to poor quality measurements of the lamp's radiance in this range. However, it does appear very likely that the quantum yields in the visible range are higher than those in the UV. It is also possible to determine the ratio of the forward and reverse quantum yields, using Equation (2.15). Using this method, it can be seen that ϕ_{trans}/ϕ_{cis} is well above unity in the UV range (as shown above), about unity at 400 nm, and is about 0.5 at 514 nm. This wavelength dependence in the quantum yields suggests some complicated behavior in the potential energy surfaces of the system.

The importance of repeating these measurements for azoTAB despite the existence of published data for azobenzene is underscored by the differences in absorptivities as seen in Figure 2-9, and also the lack of agreement with reported quantum yields and photostationary states [3-5, 17]. Multiple authors have found in the π-π* band a ϕ_{trans} of 0.10-0.15 and a ϕ_{cis} of 0.35-0.41, in marked contrast to the results reported here.

2.3.3.2. Theoretical significance of the quantum yield

To this point, no assumptions have been made concerning the number or nature of intermediate steps or states in the overall reaction. Previous workers have attempted to shed light on the physical nature of the transition states using quantum chemical computation; this is beyond the scope of this work. Other workers have proposed plausible intermediate steps and have written rate laws, accordingly. Deshmukh [18] proposed the following mechanism:

$$A \underset{k_{rA}}{\overset{\varepsilon_A I}{\rightleftarrows}} A^* \xrightarrow{k_{dA}} B \tag{2.16}$$

with the corresponding reverse reaction

$$B \underset{k_{rB}}{\overset{\varepsilon_B I}{\rightleftarrows}} B^* \xrightarrow{k_{dB}} A \tag{2.17}$$

where A* and B* are excited states. On applying the quasi-steady state assumption for the excited states, it was found that $\phi_A = k_{dA} / (k_{rA} + k_{dA})$ and $\phi_B = k_{dB} / (k_{rB} + k_{dB})$. It was not possible to make any inferences about the values of the various rate constants introduced, but it is worth noting that in both this mechanism and others [3], the quantum yield is expected to be a constant with respect to concentration. This result would tend to justify the approach taken in this work, where no mechanism is proposed but the quantum yield is assumed constant over the course of a reaction.

Zimmerman did attempt to rule out another mechanism based on the empirically measured values of the quantum yield, but there is a possible error in that analysis. The mechanism in question is

$$A \underset{k_1}{\overset{\varepsilon_A I}{\rightleftarrows}} X^* \underset{\varepsilon_B I}{\overset{k_2}{\rightleftarrows}} B \tag{2.18}$$

and it was stated that this mechanism requires that $\phi_A + \phi_B = 1$. This is true if the quantum yield ϕ_A is defined differently, as the ratio of the rate of reaction from A to B to the rate of photon absorption by the entire system, both A and B. This is in contrast to the definition of quantum yield used in the rest of that work and that used here, which is the probability of reaction upon on absorption by a single species.

2.3.3.3. Unmixed systems: model

The assumption of a well-mixed solution may not be applicable to viscous gels, such as those formed when the appropriate polymer is added to azoTAB. For such gels, any analysis must allow for spatial gradients in concentration to develop. The rate of light absorption will be higher where the light enters the sample volume, so conversion there will initially occur more quickly than in the rest of the sample. The overall rate of reaction is thus limited by the photon flux.

The partial differential equations appropriate for this case have been previously described [18]. Using the Beer-Lambert Law, the light absorbed by species A in a differential slab with length dx is

$$dI_A = -\alpha_A I C_A dx \tag{2.19}$$

where I is the local light intensity, and α is the molar absorptivity as defined in Equation (2.3). The species conservation equation for the differential slice at some position x is thus

$$\left(\frac{\partial C_{trans}}{\partial t}\right)_x = -\phi_{trans}\alpha_{trans} I C_{trans} + \phi_{cis}\alpha_{cis} I C_{cis} + k_t C_{trans} \tag{2.20}$$

The attenuation of intensity with distance is described as

$$\left(\frac{\partial I}{\partial x}\right)_t = -I\left(\alpha_{trans} C_{trans} + \alpha_{cis} C_{cis}\right) \tag{2.21}$$

Solving Equations (2.20) and (2.21) simultaneously will provide $C_{trans}(x,t)$. The origin where x=0 is at the point where the light first encounters the sample (see Figure 2-17).

Some spatial profiles generated from the model are shown in Figure 2-21 to illustrate the gradients that can arise. The irradiation wavelength is 360 nm and the incident intensity is 4.2 mW/cm^2, equal to what is experimentally available.

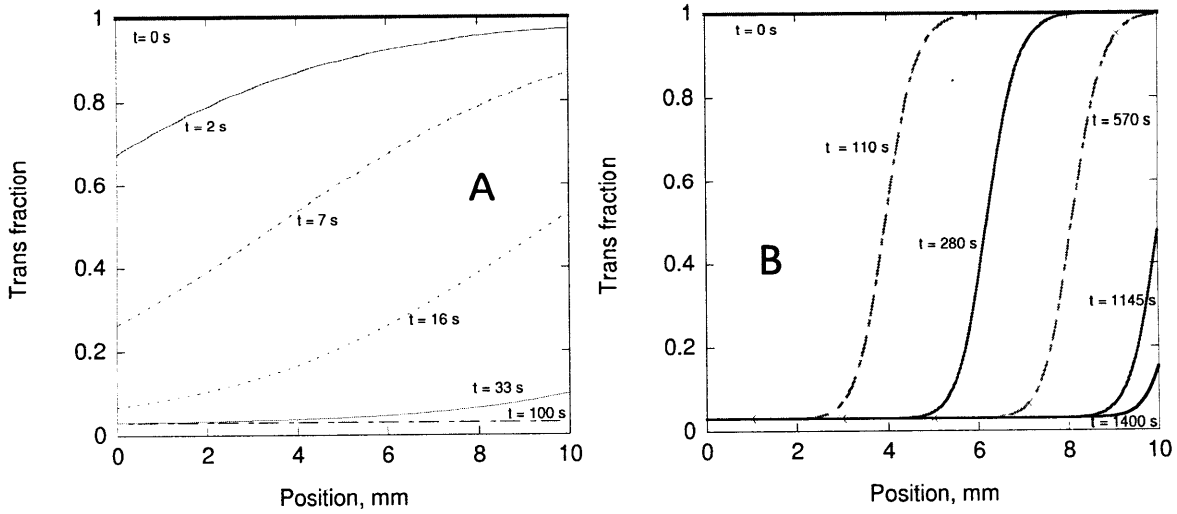

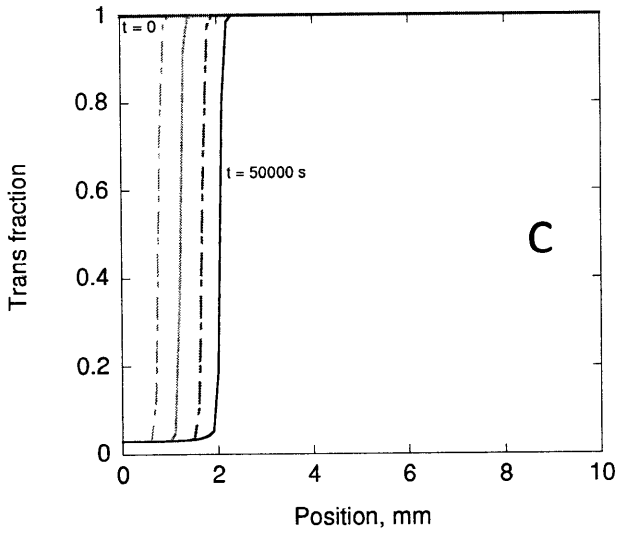

Figure 2-21 Predicted concentration gradients at various times. Total concentrations: Figure 2-21A, 0.05 mM; Figure 2-21Figure 2-21B, 0.5 mM; Figure 2-21C, 5 mM. Figure 2-21A, profiles shown at 0, 2, 7, 16, 33 and 100 seconds. B, profiles shown at 0, 110, 280, 570, 1145 and 1400 seconds. C: 0, 495, 2500, 12500 and 50000 seconds. Entire solution initially fully *trans* in each case. 360 nm light incident at x = 0 mm and 4.2 mW/cm^2. ϕ_{trans} is 0.26 and ϕ_{cis} is 0.09. ε_{trans} and ε_{cis} are 25.0 and 2.3 cm^{-1} mM^{-1}, respectively. Initial (and maximum) absorbance at irradiation wavelength is 1.25, 12.5 and 125 at 0.05, 0.5 and 5 mM, respectively.

As the concentration is increased, the concentration gradients become rather sharper and the penetration depth at any given time is reduced. This is due to the molecules at the front of the sample (low x) absorbing much of the light and converting much more quickly than molecules at high x. The width of the gradient part of the profiles roughly corresponds to the characteristic length $(\varepsilon C)^{-1}$. At high concentrations, the sample volume at high x may never achieve the true photostationary state.

The presence of these concentration gradients also causes the average concentration to deviate from that in the well-mixed case, as seen in Figure 2-22.

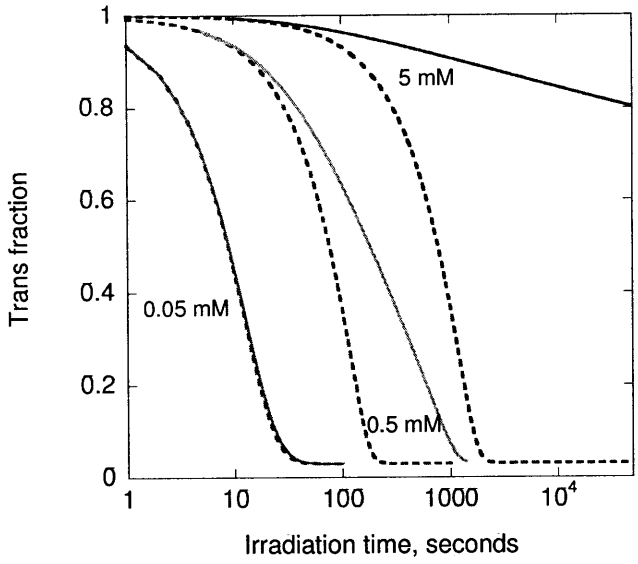

Figure 2-22 Comparison of models with and without mixing. Dotted lines from mixed model; solid lines from unmixed model. Spatially averaged composition at each time shown for unmixed model. Solutions initially at 100% *trans*. Irradiation wavelength 360 nm, intensity 4.2 mW/cm^2. Path length 1 cm.

At 0.05 mM where the total absorbance is at most 1.25, there is little deviation between the mixed and unmixed models. As the concentration is increased, any lack of mixing causes a dramatic decrease in the overall conversion rate. This decrease occurs because much of the incident light is being absorbed by the solution in a skin layer at the front of the sample, where the energy absorbed goes towards maintaining the photostationary state locally. With mixing, more of the energy absorbed goes towards net conversion, as opposed to maintaining a photostationary state.

The model results for unmixed samples should provide the slower limit for experimental results, as some diffusion on these time and length scales can be expected. The width of the concentration gradient in Figure 2-21c is about 0.4 mm, while the diffusivity of azoTAB can vary from $4*10^{-10}$ m^2/s for free monomers to $4*10^{-12}$ m^2/s for azoTAB bound to a polymer network (from Chapters 3 and 4). This leads to characteristic diffusion times of anywhere from 400 to 40,000 seconds. If any significant amount of unbound surfactant exists in the sample, the concentration profiles will not be as sharp as those seen in Figure 2-21c. Diffusion is considered more quantitatively in Chapter 4.

The kinetics in unmixed samples at high concentrations could be made faster by irradiating the sample from multiple directions, or increasing the intensity. The expected effect of increasing the incident intensity is seen in Figure 2-23.

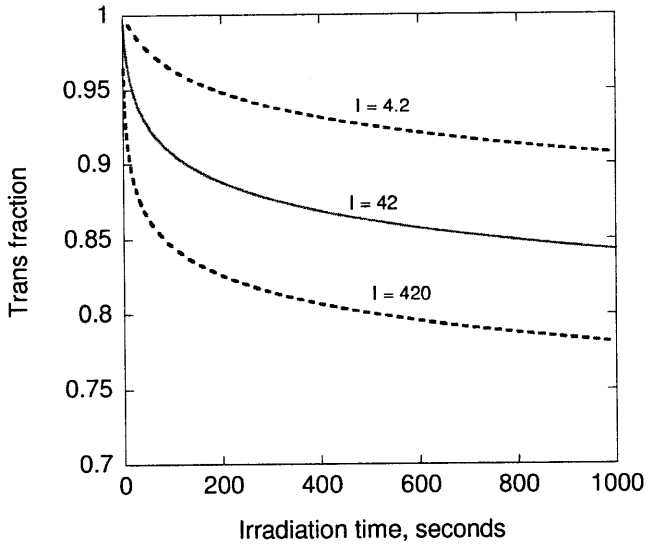

Figure 2-23 Predicted average *trans* fraction in unmixed samples at varying incident intensity: I_0 = 4.2, 42 and 420 mW/cm^2. All at 5 mM and 360 nm irradiation.

The increase in intensity does improve the overall kinetics in the unmixed sample by causing deeper penetration at any given time. 42 mW/cm^2 can be achieved using the Dymax BlueWave lamp mentioned earlier, while intensities of higher orders of magnitude can be achieved through use of a laser. A laser could be used for pinpoint irradiation, or some optics can be added to spread the light somewhat.

It is difficult to directly observe the spatial concentration gradients discussed above, but both UV-Vis (see Equation (2.2)) and NMR can give the spatial average of the concentrations, which can be compared to the spatial average of the model results.

2.3.3.4. Applicability of system

Concentrations on the order of 5 mM-10 mM azoTAB are most relevant for the applications explored in this work. Such concentrations are necessary for the formation of aggregates. As can be seen in the Figures above for unmixed samples, the rate of conversion at long path lengths can be quite slow at this concentration. This photon flux limitation will determine the maximum dimensions of a plausible device using azoTAB, if the material cannot be mixed.

The size limitation can be conveniently portrayed by calculating the penetration depth in Figure 2-21 as a function of time:

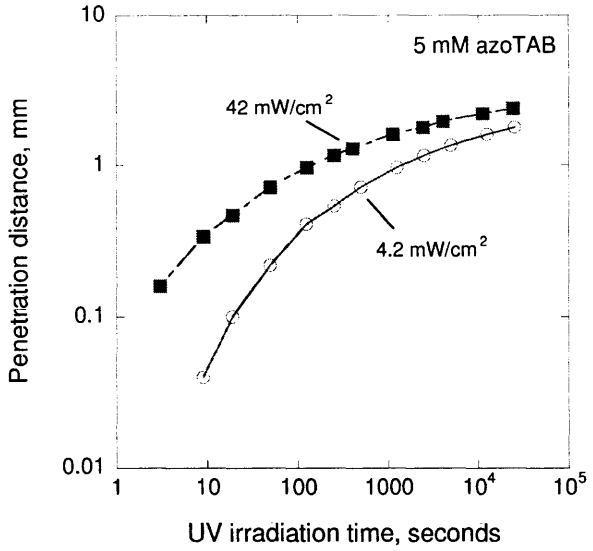

Figure 2-24 Position of penetration profile as a function of time, for two different UV irradiances. No mixing or diffusion effects are included. Both irradiances can be achieved using the equipment in this work; a laser could be used to produce higher intensities.

It is suggested that systems that depend on the reversible aggregation of azoTAB be limited to the micro-scale, unless mixing or irradiation from multiple directions is possible.

2.3.3.5. Reaction rate measurements using NMR

The experimental results shown above were limited by the concentration range accessible by using standard UV-Vis cuvettes (below 0.08 mM). The colloids and gels of interest in this work are prepared at higher concentrations (above 0.5 mM), so an alternative method of measuring the reaction rates is necessary. Given its successful use in measuring the isomer concentrations, NMR was chosen for this extension of the work. However, the geometry of the NMR tube (shown in Figure 2-6B) presents difficulties in the study of photochemistry. Irradiation along the axial dimension of the tube is inadvisable due to the long path length in that direction (about 5-6 cm). This path length, combined with the strong absorbance of azoTAB, would ensure strong axial concentration gradients and extremely slow conversion rates at the location of the NMR detector midway in the liquid height. It was therefore chosen to irradiate the samples from the side instead, as illustrated in Figure 2-6B. While this is experimentally more viable, it complicates the analysis. The models which have been developed assume rectangular geometry, whereas this experimental setup is cylindrical.

A rigorous model for this geometry would be written in two dimensions, but it is plausible that the rectangular model would provide qualitatively correct results if the average path length through the cylinder is used as an effective path length in the model. The outer diameter of the NMR tube is 5 mm, while the inner diameter is 4.92 mm. The average path length is $\frac{\pi R^2}{D}$, or 3.87 mm.

Initial NMR measurements were made on an azoTAB solution of 0.4 mM in order to demonstrate the feasibility of this approach. The relatively low concentration was used in order to avoid strong concentration gradients that would complicate this preliminary analysis. The experimental results were then compared to the model prediction using the *trans* quantum yield previously found for the 360 nm filter, 0.26. This comparison is seen in Figure 2-25 for both the mixed and un-mixed models.

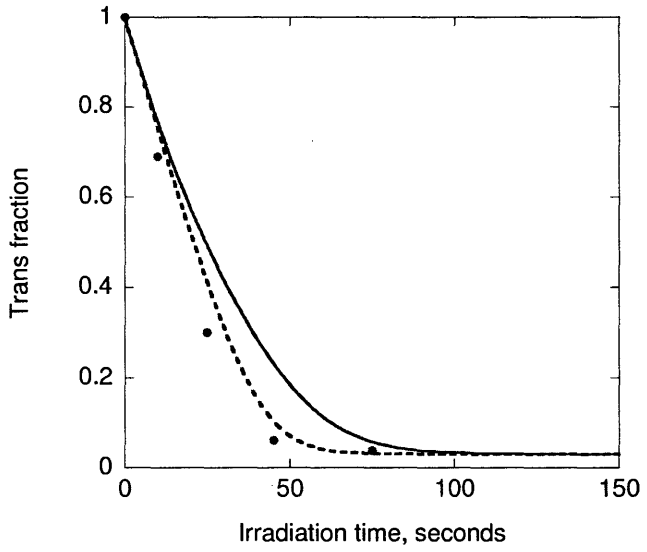

Figure 2-25 Measured and model results for 360 nm irradiation on a 0.4 mM solution in a NMR tube. Broken line used for mixed model, solid line for unmixed model. Incident intensity is 4.8 mW/cm^2. Quantum yields used as measured in previous experiments. Average length of the cylindrical tube (3.87 mm) is used in the rectangular model.

There is what can be described as a qualitative agreement between the data and prediction of the mixed model, while somewhat poorer agreement with the unmixed model. In the process of handling the sample, there was likely some agitation between scans. The sample is not particularly viscous, so this level of agitation likely ensured some mixing. It is therefore reasonable that the mixed-volume model applies. The agreement between model and experiment suggests that the geometric assumptions made in applying the model are valid.

Having verified the approach, similar experiments were then performed at higher concentrations and also with viscous gels. These results are also consistent with the models, and are discussed in Chapter 4. The data also show direct evidence of the spatial gradients discussed above.

2.3.4. Energy diagram of azoTAB

Some general aspects of the thermodynamics of azoTAB can be inferred from the experimental observations. The photoreaction has been shown to take place over the time scale of seconds, minutes or hours, depending on the light intensity. The thermal conversion of *cis* molecules to the more stable *trans* form occurs over the course of days, and under most conditions is dominated by the photoreaction. The difference in time scales between the thermal- and photo-initiated reactions suggests that the activation energy barrier for isomerization is not easily crossed in the ground state, but the barrier is either reduced or bypassed in the electronic excited state obtained on the absorption of light.

A hypothetical and simplified series of potential energy surfaces (PES) is shown in Figure 2-26 to illustrate this concept. The surfaces are plotted against an unspecified reaction coordinate; realistically the reaction coordinate would be multidimensional to allow for all the bond rotations seen in the rotation and inversion pathways pictured in Figure 1-3. In the ground state, a significant energy barrier to reaction is seen. Above the ground state are the excited states S_1 and S_2, corresponding to visible and UV absorption, respectively. Absorption will initially place the molecule on S_1 or S_2 along the dotted line, in accordance to the Franck-Condon principle. The excited molecule will then sample different configurations until it reaches a point where two PESs intersect, at which point it will jump to the lower energy electronic level. Such an intersection is known as a conical intersection (CI), and would be better represented on a multi-dimensional plot [19-21]. An actual intersection is not needed for radiationless relaxation, and is not explicitly shown in every instance in Figure 2-26, but quantum chemical calculations suggest that CIs are active in this system [14, 21-24]. It should be apparent that the energy from the absorption of light is used to overcome the energetic barrier to isomerization. It should also be noted that excitation need not lead to isomerization; the molecule can relax back to its original form.

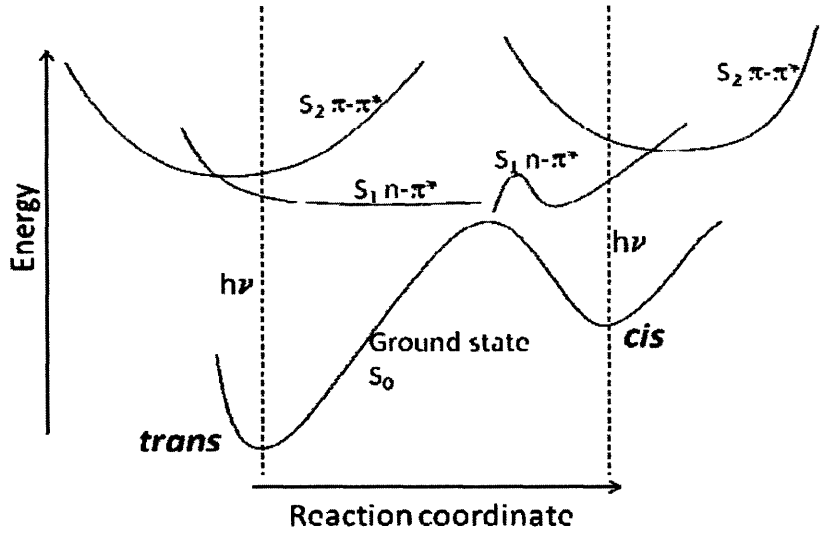

Figure 2-26 Hypothetical energy diagram of azoTAB system, only to illustrate basic concepts. Shown are possible potential energy surfaces for ground and excited states. See discussion in text.

2.3.5. Stability and sensitivity to ambient light

Degradation of azoTAB has not been observed in solution in deuterium oxide, even in samples which are three years old and have undergone dozens of photoreaction cycles.

Great care was taken throughout to limit exposure of azoTAB to the ambient light, but seconds of stray light will not cause significant photoconversion. In ten minutes under indoor fluorescent lighting, a 0.03 mM sample went from 93% to 79% *trans*. It can be inferred that at higher concentrations (1 to 10 mM), a momentary exposure to stray light will have little effect.

2.4 Conclusions

The characteristics of the light-initiated isomerization reaction of azoTAB have been comprehensively described over a range of conditions, including different concentrations and irradiation wavelengths. Experimentally, both UV-Vis and NMR spectroscopy can be used to follow the reaction over time. These observed reaction trajectories have been found to be consistent with appropriate models. This understanding will guide the design of practical applications which rely on the light-sensitive nature of the azoTAB molecule. For example, the models can be used to determine the required irradiation

wavelength and intensity for a desired conversion rate. The importance of photon flux limitations at high concentrations was also examined.

2.5 Works Cited

1. Hayashita, T., T. Kurosawa, T. Miyata, K. Tanaka, and M. Igawa, *Effect of Structural Variation within Cationic Azo-Surfactant Upon Photoresponsive Function in Aqueous Solution.* Colloid and Polymer Science, 1994. **272**(12): p. 1611-1619.
2. Hartley, G.S., *The Cis-Form of Azobenzene.* Nature, 1937. **140**: p. 281.
3. G. Zimmerman, L.-Y.C.a.U.-J.P., *The Photochemical Isomerization of Azobenzene.* Journal of the American Chemical Society, 1957. **80**: p. 3528-3531.
4. Gauglitz, G. and S. Hubig, Chemical Actinometry in the Uv by Azobenzene in Concentrated Solution: A Convenient Method. Journal of Photochemistry, 1985. **30**(2): p. 121-125.
5. Siampiringue, N., G. Guyot, S. Monti, and P. Bortolus, *The Cis-Trans Photoisomerization of Azobenzene - an Experimental Reexamination.* Journal of Photochemistry, 1987. **37**(1): p. 185-188.
6. Rau, H., *Azo Compounds*, in *Photochromism: Molecules and Systems*, H. Duerr, Editor. 2003, Elsevier.
7. Gauglitz, G., Photophysical, Photochemical and Photokinetic Properties of Photochromic Systems, in Photochromism: Molecules and Systems, H. Duerr, Editor. 2003.
8. Knoll, H., Photoisomerism of Azobenzenes, in Crc Handbook of Organic Photochemistry and Photobiology, F.L. W. Horspool, Editor. 2004, CRC Press.
9. Lee, C.T., K.A. Smith, and T.A. Hatton, Photoreversible Viscosity Changes and Gelation in Mixtures of Hydrophobically Modified Polyelectrolytes and Photosensitive Surfactants. Macromolecules, 2004. **37**(14): p. 5397-5405.
10. Lee, C.T., K.A. Smith, and T.A. Hatton, Photocontrol of Protein Folding: The Interaction of Photosensitive Surfactants with Bovine Serum Albumin. Biochemistry, 2005. **44**(2): p. 524-536.
11. Diguet, e.a., *Photomanipulation of a Droplet by the Chromocapillary Effect.* Angewandte Chemie, 2009. **48**: p. 9281-9284.
12. Derome, A., Modern Nmr Techniques for Chemistry Research. 1987.
13. Barrett, C., A. Natansohn, and P. Rochon, Thermal Cis-Trans Isomerization Rates of Azobenzenes Bound in the Side-Chain of Some Copolymers and Blends. Macromolecules, 1994. **27**(17): p. 4781-4786.
14. Monti, S., G. Orlandi, and P. Palmieri, Features of the Photochemically Active State Surfaces of Azobenzene. Chemical Physics, 1982. **71**(1): p. 87-99.
15. Takahashi, M., T. Okuhara, T. Yokohari, and K. Kobayashi, *Effect of Packing on Orientation and Cis-Trans Isomerization of Azobenzene Chromophore in Langmuir-Blodgett Film.* Journal of Colloid and Interface Science, 2006. **296**(1): p. 212-219.
16. Griffiths, J., *Photochemistry of Azobenzene and Its Derivatives.* Chemical Society Reviews, 1972. **1**: p. 481-493.
17. A. Gahr, L.W.a.R.N., *Polychromatic Actinometry with Filter Solutions.* Water Research, 1995. **29**(9): p. 2125-2137.
18. Deshmukh, S., L. Bromberg, K.A. Smith, and T.A. Hatton, Photoresponsive Behavior of Amphiphilic Copolymers of Azobenzene and N,N-Dimethylacrylamide in Aqueous Solutions. Langmuir, 2009. **25**(6): p. 3459-3466.
19. Levine, B.G. and T.J. Martinez, *Isomerization through Conical Intersections.* Annual Review of Physical Chemistry, 2007. **58**: p. 613-634.
20. Turro, N., et al, *Principles of Molecular Photochemistry.* 2009: University Science Books.
21. F. Negri, G.O., Electronic and Vibronic Spectra of Molecular Systems: Models and Simulations Based on Quantum Chemically Computed Molecular Parameters, in Computational Photochemistry, Olivucci, Editor. 2005, Elsevier.
22. Diau, E.W.G., A New Trans-to-Cis Photoisomerization Mechanism of Azobenzene on the S-1(N,Pi*) Surface. Journal of Physical Chemistry A, 2004. **108**(6): p. 950-956.

23. Tiago, M.L., S. Ismail-Beigi, and S.G. Louie, Photoisomerization of Azobenzene from First-Principles Constrained Density-Functional Calculations. Journal of Chemical Physics, 2005. **122**(9).
24. Conti, I., M. Garavelli, and G. Orlandi, The Different Photoisomerization Efficiency of Azobenzene in the Lowest N Pi* and,Pi Pi* Singlets: The Role of a Phantom State. Journal of the American Chemical Society, 2008. **130**(15): p. 5216-5230.

Chapter 3

Characterization of Micelles

3.1 Introduction

The photoisomerization of azoTAB between *cis* and *trans* forms was described in Chapter 2. In this chapter, the aggregation properties of azoTAB will be examined at various light conditions. Similar to any surfactant, azoTAB consists of a hydrophobic tail group and a hydrophilic head. In this case, the head is hydrophilic due to it being charged. There are no strong intermolecular interactions between the surrounding water and the hydrophobic tail, so water will prefer to interact with other water molecules through hydrogen bonding. The water molecules will order themselves around the intruding tail in order to maintain hydrogen bonding with each other. This ordering represents a decrease in entropy, which can be counteracted by segregating the hydrophobic tails such that they impose a minimum disruption on the surrounding water molecules [1]. This effect would result in a second liquid phase, as with oil and water, if not for the hydrophilic head group. Instead various structures such as micelles self-assemble such that the head groups are in contact with, and the tails are removed from, the solvent.

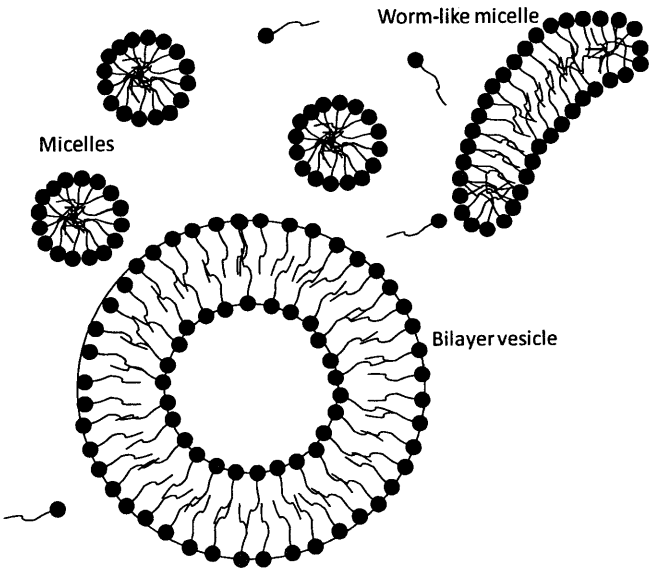

Figure 3-1 Selection of possible self-assembled structures. Shown are spherical micelles, a worm-like micelle and a vesicle. Factors including the geometry and concentration of the surfactant, as well as concentration of any added salt, will determine which structure is formed.

It is not always energetically favorable for these aggregates to form; it is generally observed that significant micelle formation only occurs above a certain concentration known as the critical micelle concentration (CMC). As the concentration is increased past that point, the additional surfactant molecules tend to go towards the formation of more aggregates. Further increases in concentrations may lead to transitions between the different types of aggregate shown in Figure 3-1.

.

The various applications of azoTAB discussed in this work are based on its aggregation properties and how these change under various light conditions. It may be expected that both forms of azoTAB, *trans* and *cis*, will form aggregates under appropriate conditions. A solution composed of both forms will contain mixed micelles, also composed of both forms. However, as discussed in Chapter 2, the *trans* form is more likely to self-assemble into micelles than the *cis* (see Figure 3-2). The use of irradiation to change the overall isomeric composition can then be expected to change the number, composition and size of the micelles. There is hence a strong motivation to carefully characterize and understand these behaviors.

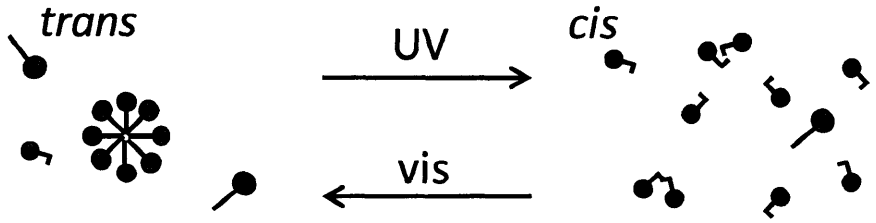

Figure 3-2 Expected effect of irradiation on micelle formation. Straight-tailed surfactants denote *trans*, while bent-tailed surfactants denote *cis*. UV light drives conversion to *cis*; the UV-adapted state is 96-97% *cis*. Visible light drives conversion to *trans*; visible-adapted states vary from 50-90% *trans*, depending on the irradiation wavelength. The dark-adapted state is 100% *trans*. At appropriate azoTAB concentrations, the dark- and visible- adapted states would be above the CMC, and micelles would form. The UV-adapted state would be below the CMC, and there would be no substantial micelle formation.

The work to characterize these aggregates started with the measurement of the CMC under various conditions. The formation of micelles can be experimentally detected by measuring any of a variety of properties, including conductivity, surface tension, viscosity, diffusion coefficient, NMR peak positions and the fluorescence of environment-sensitive probes. Each of these properties should exhibit some breakpoint at the CMC. Beyond the CMC, it may also be possible to study other aspects of micelles, such

as size, shape and composition. In this section the investigation is limited to NMR and fluorescence methods.

There have been many published studies of micelles using various NMR observations, such as the peak chemical shift [2-13], nuclear spin relaxation rate [11, 14-18] and the diffusion coefficient of the surfactant or counterion [19-23]. The field has been capably reviewed by Stilbs et al [24] so a complete overview will not be given here. Each method will be discussed briefly as needed for the analysis of the results. There has been some previous study of azoTAB using SANS [25] and fluorescence [26], and those results will be considered when relevant, but there is no report using the tools available through NMR. There is also apparently no prior work regarding the properties of mixed micelles at intermediate isomeric compositions. This work attempts to fill these gaps.

3.2 Experimental Section

3.2.1. Materials

The fluorescent dye nile red was used as received from TCI (Tokyo, Japan). The azoTAB surfactant was prepared as described in Chapter 2. Unless otherwise noted, all solutions were prepared in deuterium oxide from Cambridge Isotopes. This solvent was used as received, with no attempt to degas it.

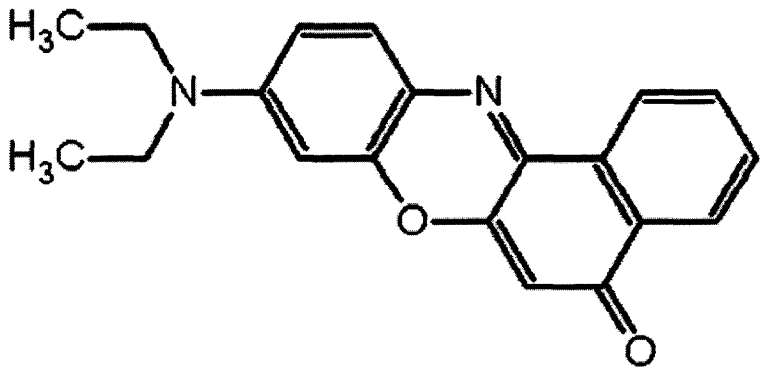

Figure 3-3 Structure of nile red.

3.2.2. Fluorescence Spectroscopy

The steady state fluorescence spectra of nile red in various solutions were measured using a QuantaMaster spectrofluorometer from Photon Technology International. It is standard practice to use

pyrene to study changes in environment such as micelle formation, but this is not possible here as pyrene and azoTAB are active at the same wavelengths. An alternative, nile red, was used instead as an environment-sensitive probe. Quartz cuvettes were obtained from Starna Cells (Atascadero, CA). The path length of the cuvettes was 1 cm and the volume of solution was 3.5 mL.

Nile red was used in a range of concentrations from 0.5 μM to 30 μM. It was not possible to directly add the requisite exceedingly small masses of nile red crystal to the sample solutions, so large volumes of nile red solutions in chloroform were made instead. The concentrations of these stock solutions were on the order of 10 mM, so the required mass of nile red could be obtained in an easily measured microliter portion of the stock solution. This portion was placed in a vessel, the chloroform was allowed to completely evaporate, and the sample solution was then added to the remaining nile red. After sufficient stirring to ensure uptake of nile red into the solution, the sample was loaded into the cuvette. The stock solution was kept sealed under refrigeration to minimize evaporation that would change its concentration, and fresh stock solution was made regularly.

The measured quantity in fluorescence experiments is the count rate of photons detected by a photomultiplier. This count rate is not a well-defined material property, but rather is highly dependent on experimental conditions. These conditions include the power of the excitation lamp, as well as the opening width of several variable shutters that control the amount and bandwidth of the exciting or emitted light. These settings are kept constant so that the measured emission intensities can be compared. This control of experimental conditions is sufficient for data collected within a single day, but is not always possible for data collected months apart. In that case a scaling factor is needed to directly compare the intensities from the different data series. A standard sample measured on each day was used to provide this scaling. The chosen standard was an acrylic block doped with rhodamine B; this choice avoids difficulties with evaporation. This block is excited at 560 nm and emits at 573 nm, roughly similar to nile red's excitation at 580 nm and emission at 650-660 nm in the solutions in this work. Comparisons against a standard solution of nile red in ethanol were used to demonstrate that the measured scaling factor is appropriate, despite the slight difference in excited and emitted wavelengths.

Three sets of fluorescence experiments were performed, all involving solutions of azoTAB and nile red in either water or deuterium oxide. In the first, the concentration of azoTAB was held constant while the concentration of nile red was changed. These results are not shown, but were used to ascertain what concentration of nile red is appropriate for use in the later experiments. In the second, the concentration of nile red was held constant as the concentration of azoTAB was varied from 0 mM to 11 mM. These data were collected for the dark-adapted, visible-adapted and UV-adapted states, and would show the

onset of micellisation. The visible light was produced with a 400 nm longpass filter, and the UV with a 360 nm bandpass filter (See Experimental Section, Chapter 2). The third experiment involved azoTAB solutions at concentrations above the *trans* CMC (4, 5, 6 and 7 mM) and the change in the nile red fluorescence intensity was monitored as the samples were gradually shifted from the dark-adapted state to the UV-adapted state through use of UV-irradiation.

As in similar UV-Vis experiments, the samples were well-stirred during irradiation, and the same solution was repeatedly shifted between the UV source and the fluorimeter until the photo-stationary state was achieved. At several points a microliter-scale sample of the solution was withdrawn and diluted to 0.01 mM, so that the isomeric composition could be measured using UV-Vis spectrometry with a 1 cm path length cuvette. The reduction in the solution volume over the course of the experiment due to this sampling was negligible. This combined dynamic fluorescence and UV-Vis experiment is thought to be novel.

3.2.3. NMR chemical shifts

The general experimental procedures were described in the previous chapter. Of particular importance in this section is the chemical shift reference. In order to compare peak positions between different samples, the absolute values of the chemical shifts must be known with precision. This precision is achieved by using some reference value for each sample. The primary reference used here is the chemical shift of the monodeuterated water peak (HDO) due to the solvent. Literature values exist for this peak position as a function of temperature [27]. Proper referencing is critical for this work, so this temperature dependence of the HDO reference was confirmed using sodium 3-(trimethylsilyl)propanesulfonate, which is accepted to define the 0 ppm point in aqueous samples. Additional experiments confirmed that the addition of azoTAB did not alter the chemical shift of HDO by any meaningful amount. Measured peaks should be taken to be precise within 0.002 ppm. The internal lock of the spectrometer to the solvent deuterium provided a secondary reference.

3.2.4. NMR relaxation times

NMR relaxation rates can also provide an indication of the molecular environment. Relaxation can occur through interactions with other nuclei; a surfactant molecule surrounded by other surfactants will relax faster than an isolated molecule. There exist separate experiments to measure the spin-spin relaxation time constant T_2 or the spin-lattice relaxation time T_1, but these were not performed in order to conserve time. Rather, T_2 can be inferred from the width of the 1-D NMR peaks [18, 28] using the expression

$$\Delta\upsilon_{1/2} = \frac{\pi}{T_2^*} \tag{3.1}$$

where $\Delta\upsilon_{1/2}$ is the full width at half maximum (FWHM), measured in hertz. The measured quantity T_2^* is not exactly the same as T_2, due to inhomogeneities in the spectrometer magnetic field [28]. These inhomogeneities can be mitigated by use of shimming, but differences may remain between different NMR probes and spectrometers. The presence of paramagnetic materials such as molecular oxygen will also enhance relaxation. Solvents used here were not degassed, so it is assumed that every sample had similar amounts of dissolved oxygen. Due to these limitations, the linewidth data are analysed qualititatively.

3.2.5. NMR diffusion

3.2.5.1. Background

NMR spectrometers can be used to measure diffusion coefficients by the pulsed-field gradient spin echo (PFG-SE) method, which is adequately described elsewhere [29]. The measured diffusivities are self-diffusion coefficients, indicative of stochastic motions in the absence of chemical potential gradients. The advantages of this technique are many: several components can be observed simultaneously, particularly if their diffusivities are of the same order of magnitude, and there is no need to add any isotopic labels or fluorescent markers. Either modification would involve cumbersome chemistry and could also change the properties of the material.

In general, PFG-SE methods involve the imposition of temporary gradients in the magnetic field in the spectrometer, as well as a number of radio-frequency pulses which are absorbed by the nuclei. The particular pulse sequence used in this work is known as the BPP-LED (bipolar pulsed-field gradient method with longitudinal eddy current delay) [30], and is depicted in Figure 3-4. The advantage of this sequence is that it minimizes the effects of mechanical and electronic distortions caused by applying a pulsed field gradient [29]. Applying the field gradient pulses may cause eddy currents in the electronics, which may then cause mechanical vibrations; the pairing of gradient pulses of opposite direction as seen in Figure 3-4 helps minimize such distortions. The diffusivity is related to the amplitude of the "spin-echo" signal observed in time AQ.

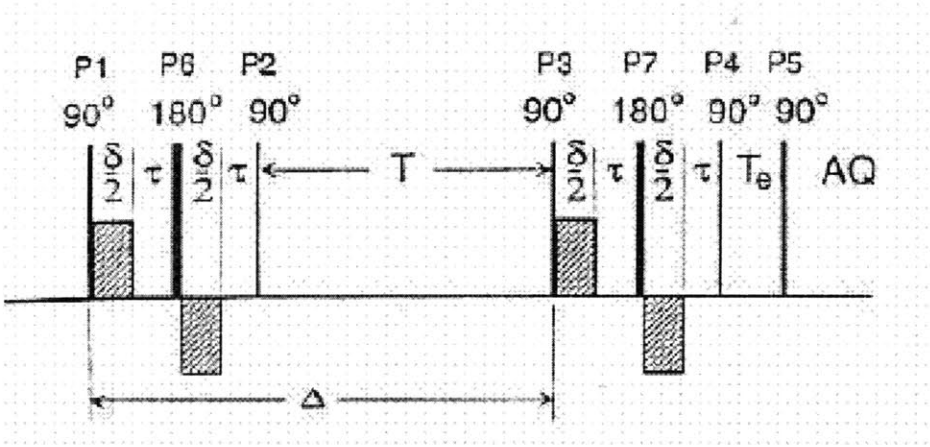

Figure 3-4 Pulse Sequence in the BPP-LED experiment. X-axis is time. Radiofrequency pulses are labeled P1, P2, etc. Filled grey boxes correspond to pulses of gradient magnetic field. Diffusion takes place over time Δ, typically from 100 to 3000 ms. δ is the gradient pulse width and may be varied from 2 to 5 ms. Measured quantity is the amplitude of the signal in time AQ. Taken from [30].

The relationship between the spin-echo intensity (S) and the apparent diffusion coefficient D is

$$S = S(0)\exp\left[-Dq^2\left(\bar{\Delta}-\frac{\delta}{3}-\frac{\tau}{2}\right)\right] \tag{3.2}$$

where

$$q = \delta\gamma G$$

and $\bar{\Delta}$, δ and τ are defined in Figure 1. In addition, γ is the gyromagnetic ratio of the nucleus in question, G is the magnitude of the applied field gradient, and $S(0)$ is the spin-echo intensity in the absence of field gradients. The gyromagnetic ratio for ^{1}H is $2.68*10^8$ rad s^{-1} T^{-1}. The magnitude of the spin echo is modulated by both diffusion and the nuclear spin relaxation rate; the effect due to relaxation is absorbed into $S(0)$. $S(0)$ decreases approximately exponentially as the time between P1 and AQ is increased. Within a single experiment, it is constant if $\bar{\Delta}$, δ and τ are held constant. In this work, the range of δ is 2 to 5 ms; $\bar{\Delta}$ can vary between 100 and 3000 ms, τ is always 0.1 ms, and G is varied from 0.6 to 57 G/cm (discussed below).

In general, the BPP-LED experiment is applied at a series of different field gradient strengths. As the gradient strength G is increased, the intensity of the spin-echo decreases. A "Stejskal-Tanner" plot of

ln S versus $q^2(\Delta - \delta/3 - \tau/2)$ should then yield a line with slope D. For convenience, the term on the abscissa of the plot shall be denoted as 'k'.

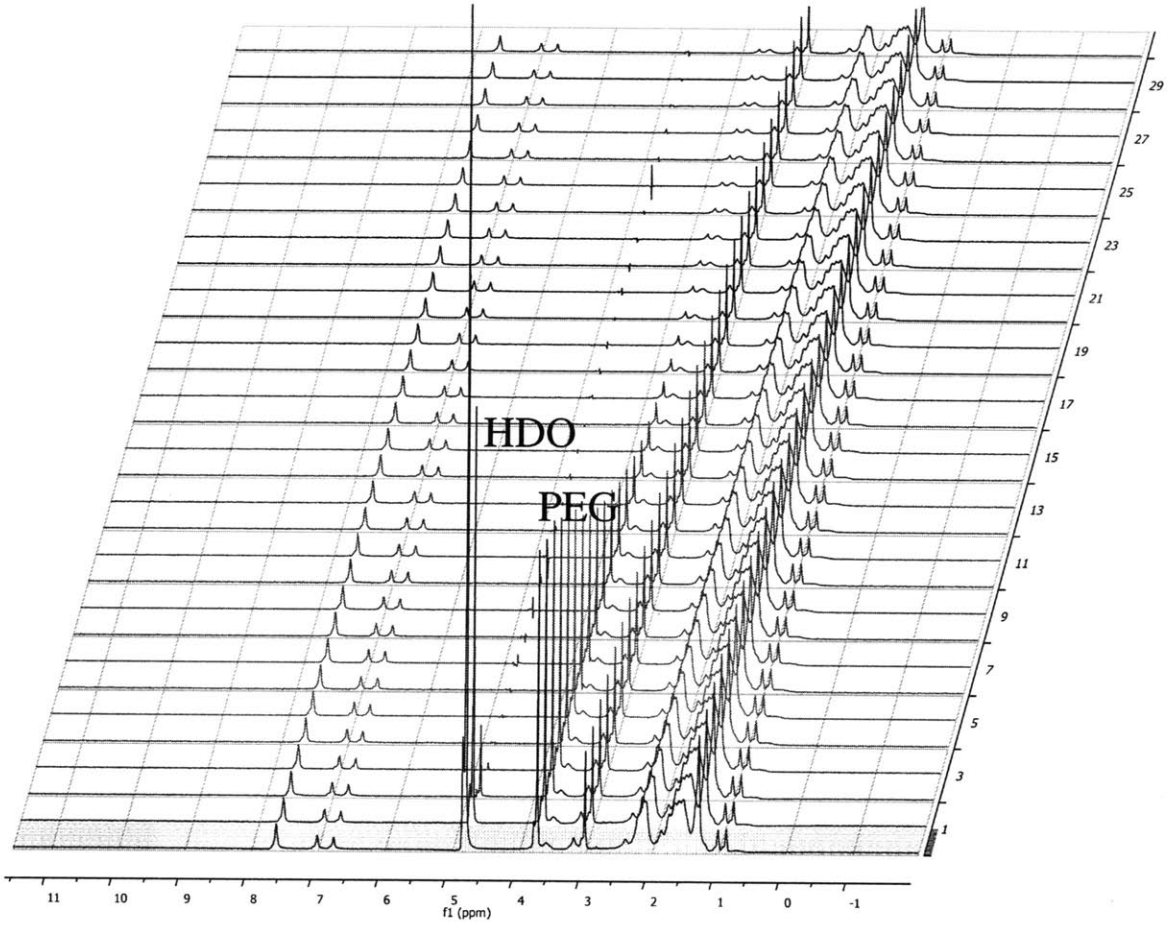

Figure 3-5 Spin-echo signals from diffusion experiment. Gradient strength increases from bottom spectrum to top (see text). Data shown for gelled mixture of azoTAB and HMPAA, with polyethylene glycol added as probe solute. Diffusion time is 500 ms. HDO attenuates fastest, then PEG; gel components (all other peaks) show little attenuation.

Faster moving components will show faster attenuation in the spin echoes with increasing gradient strength than slower components. This difference in attenuation can be seen in the example in Figure 3-5, taken of an azoTAB-HMPAA gel with polyethylene glycol (PEG) added as a solute. The strength of the field gradient increases from spectrum 1 to 29, from 3% to 93% of the maximum strength achievable in the instrument that was used. The increments in gradient strength are constant, but inspection of Equation (3.2) shows that the resulting increments in the Stejskal-Tanner abscissa 'k' are not. The peak due to fast-moving monodeuterated water, HDO, at 4.8 ppm quickly disappears; the PEG peak at 3.7 ppm persists somewhat longer, and the remaining peaks due to the slowly-moving gel are still visible at the

end of the experiment. HDO is observed by NMR because a small population of ^1H is present in the D_2O solvent, but there is insufficient ^1H to form significant amounts of H_2O.

In a Stejskal-Tanner plot, only the intensity at one particular frequency is shown; this frequency is usually the maximum of a peak. It is also valid to plot the integrated area of the peak, but only intensities are used in this work. An example plot is provided in Figure 3-6.

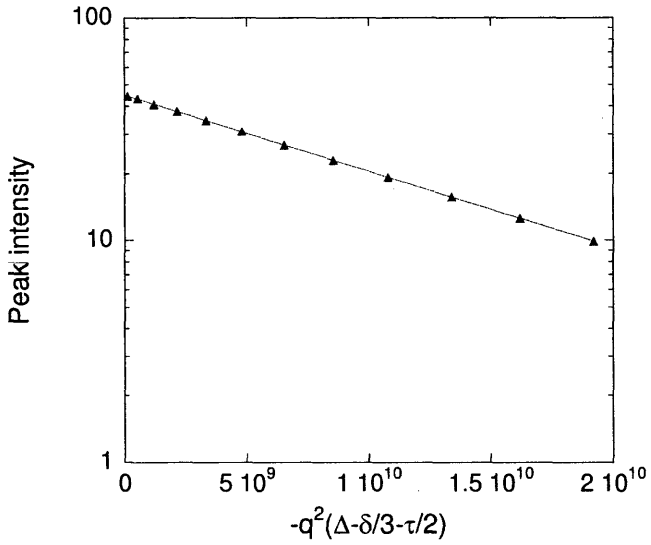

Figure 3-6 Example Stejskal-Tanner plot. Data shown for a phenyl ring proton in azoTAB at 30 mM. Δ is 0.5 seconds, δ is 2 ms. and the gradient strength is varied from 5 to 60% of the maximum. R^2 is 1.000, and the slope yields a diffusivity of $7.88*10^{-11}$ m^2/s.

The results are remarkably linear, and the same diffusivity is measured for every peak in the molecule. The mean diffusivity is $7.88*10^{-11}$ m^2/s, and based on the variance of measured values among the other protons, the 95% confidence interval is $1.9*10^{-13}$ m^2/s. The error on repeating the experiment is of course larger; any reported diffusivity should be considered accurate to two significant figures.

It is generally advisable to achieve intensity attenuation of at least one decade by varying the gradient strength in order to find reliable values for D. Therefore, particularly strong gradients would be necessary to study slow-moving components with confidence. Attenuation can also be increased by increasing δ or $\bar{\Delta}$, but there are physical limits on the δ that can be attained without burning out the coils used to apply the gradient, and $\bar{\Delta}$ cannot be so long that the nuclear spins totally relax before any spin echo is observed (as expressed by $S(0)$). Altering δ or $\bar{\Delta}$ changes $S(0)$, so even when a different value of δ or $\bar{\Delta}$ is used, the experiment to find D proceeds by incrementing the gradient field strength.

3.2.5.2. Multiple components

A common complication occurs when two components appear at the same frequency on the 1-D NMR spectrum, yet differ in their diffusion coefficients. This is often the case with surfactant molecules existing either as monomers or within micelles. If the observed proton can exchange between the two components (monomer or micelle) within the diffusion time scale $\bar{\Delta}$, the Stejskal-Tanner plot will still be linear. The observed diffusion coefficient will be a linearly weighted average of the multiple individual diffusion coefficients. Assuming that there are two possible components, then

$$D_{obs} = y_1 D_1 + y_2 D_2 \tag{3.3}$$

where y is the mole fraction in a given state.

If exchange between the two components is slow or impossible (as in the case of completely different chemical species that coincidentally appear at the same NMR chemical shift), then the Stejskal-Tanner plot will be non-linear. One has to consider the multiple distinct components in the original attenuation expression. Again assuming two components,

$$S = S_1(0)\exp[-D_1 q^2(\Delta - \frac{\delta}{3} - \frac{\tau}{2})] + S_2(0)\exp[-D_2 q^2(\Delta - \frac{\delta}{3} - \frac{\tau}{2})] \tag{3.4}$$

In such a case, D_1, D_2, $S_1(0)$ and $S_2(0)$ all must be fit from the Stejskal-Tanner plot. This topic is developed further in Chapter 4. Under certain circumstances, it may also be possible to find the mole fractions of the two components from the ratios of the S(0) values.

3.2.5.3. Measurement time

The time required for satisfactory results may vary from as little as seven minutes to as much as several hours. The longest parts of the pulse sequence are the time $\bar{\Delta}$, which is sometimes as long as 3 s, and the acquisition time, which is another 0.5 s. Each pulse sequence is repeated 16 times, in order to reduce artifacts from errors in the RF pulse lengths. It is also generally recommended to wait at least a second in between pulse sequences, to allow for nuclear spin relaxation and to reduce wear on the instrument. So, in order to simply measure the spin echo at a single gradient strength, about 35 seconds may be needed. In order to determine the diffusion coefficient, several gradient strengths must be used. If the Stejskal-Tanner plot is expected to be linear, 7 or 8 points may be sufficient, but at least 20 may be needed to fit two different D values from a curved plot. Then, for components at dilute concentrations, the number of scans must be increased from 16 to some multiple of 16, in order to improve the signal to noise ratio.

Most of the data shown here required ten to twenty minutes to acquire. This measurement time puts a limit on the temporal resolution possible for following a dynamic process, which reduced the incentive to irradiate the sample within the instrument.

3.2.5.4. Gradient calibration

In general, the directly controlled parameter is the gradient field strength, expressed as a fraction of the maximum strength that can be generated. In order to proceed, the absolute value of this maximum strength is required.

There are two basic methods for calibration: to use a reference sample of known diffusivity and back-calculate the gradient strengths, or to use a "phantom" tube. At present time, the only generally accepted reference sample is a mixture of H_2O and D_2O; the diffusion of the resulting HDO is measured. At 25 C, 1 mol percent H_2O in D_2O should yield a diffusion coefficient of $1.905*10^{-9}$ m^2/s [31, 32].

Figure 3-7 Phantom tube used for gradient calibration. Blue part is made of plastic. The annulus between the phantom and the NMR tube wall is filled with water.

A "phantom" tube (Figure 3-7) is a NMR tube with a cylindrical plastic insert. The hollowed-out gap in the middle of the insert is of known length. This gap is filled with water, a field gradient is applied, and a NMR signal is collected. The nuclear precession frequency is directly proportional to the strength of the local magnetic field

$$\omega = \gamma B \tag{3.5}$$

where ω is the frequency, γ is the gyromagnetic ratio and B is the local magnetic field.

If water protons at different points in the column are exposed to different fields, then they will be seen at different frequencies on the NMR spectrum.

The resulting NMR spectrum appears as follows:

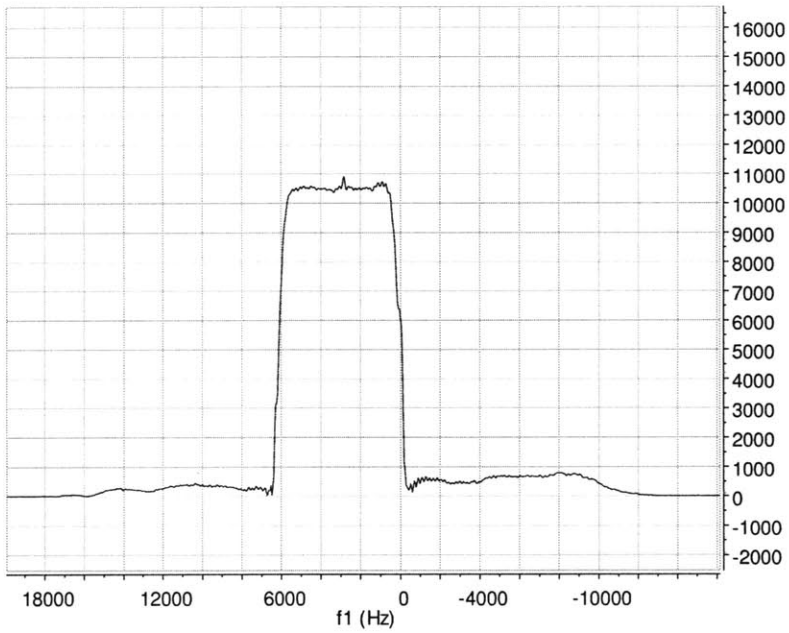

Figure 3-8 1-D NMR spectrum of phantom tube, as described in text.

One can clearly see the position of the water column, along with the small amount of water filling the narrow gap between the tube and the cylinder. The difference in field strength from top to bottom of the water column can be calculated from the difference in frequency from top to bottom, and then divided by the length of the water gap in order to find the magnitude of the field gradient.

Use of the phantom yields a maximum gradient strength of 61 G/cm, or 0.61 T/m, whereas the reference sample gives 62.8 G/cm with a standard deviation of 1.2 G/cm. It is difficult to assign more confidence to one method vs. the other. The value of 61 G/cm was assumed for this work. An error in the gradient strength will result in diffusion coefficients which are off by a factor of $\frac{G_{used}^2}{G_{actual}^2}$. Due to this calibration uncertainty, there may be up to a 5% systematic error in all measured diffusion coefficients.

With gradients of these magnitudes, diffusivities on the order of 10^{-9} through 10^{-11} m^2/s can easily be measured. Measurements of smaller diffusivities are possible, but a large decay in the observed intensity

might not be achieved. Specialized instruments with gradient strengths as high as 1000 G/cm are reported in the literature, but that capability was not available for this work.

Temperature was set to 25 C using conditioned airflow and heaters; the temperature was confirmed by use of the methanol "thermometer" [33, 34], in which the temperature is calibrated against the known temperature-dependence of the separation between the two proton peaks.

3.3 Results and discussion

3.3.1. Fluorescence methods

The onset of micellisation at the CMC has been studied at various isomeric compositions of azoTAB in solution. Shown in Figure 3-9 is the dependence of the fluorescence intensity of nile red on the concentration of azoTAB in deuterium oxide. Nile red fluoresces strongly when in hydrophobic domains, and is quenched in aqueous solution [35]. It also has poor solubility in aqueous solution, so it partitions to hydrophobic domains such as micelle cores. A sharp increase in fluorescence intensity is thus expected at the CMC, and is indeed observed for 100% *trans* (dark) and 50% *trans* (visible) solutions at 3.3 mM and between 4 and 5 mM, respectively. The fluorescence intensity continues to increase with azoTAB concentration until it reaches a plateau, at which point all available nile red has partitioned into the micelles.

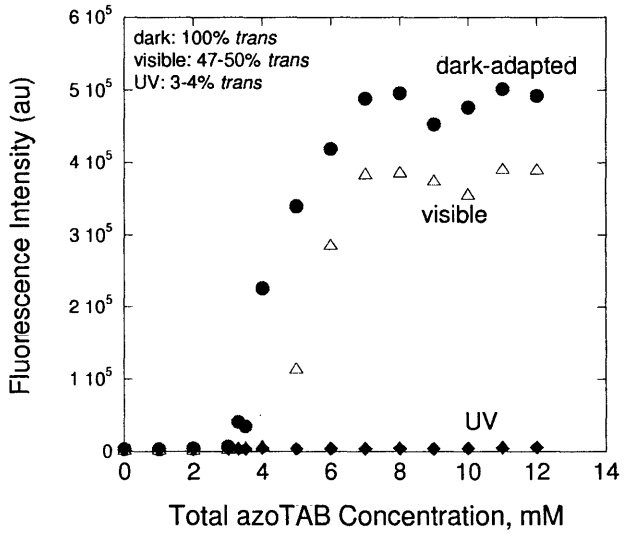

Figure 3-9 Fluorescence intensity of nile red in azoTAB solutions. Dark-adapted is 100% *trans*, visible is 50% *trans*, and UV is 3% *trans*. Solutions made in deuterium oxide. Nile red concentration is 13.5 micromolar. Mercury arc lamp used with 400 nm longpass filter to produce visible light; other filters can be used for more *trans*-rich visible photostationary states. 360 nm bandpass filter used for UV photostationary state.

Corresponding measurements in water indicate a CMC of 4.5 mM for 100% *trans* solutions, which is comparable to the literature value of 4.6 mM [36]. A slightly lower CMC for surfactants in deuterium oxide as compared to water has been previously noted [37, 38]. This isotope effect can be understood by considering that hydrogen bonding is stronger in deuterium oxide, thus enhancing the entropically-driven hydrophobic effect that leads to micelle formation.

There is no obvious breakpoint in the data for 97% *cis* solutions, which would indicate that either no significant amount of aggregation occurs at these concentrations, or that any aggregates are small or poorly formed and cannot solubilise the nile red probe. This finding is consistent with previous SANS results for *cis*-rich solutions, where it was found that small pre-micellar discs form instead of proper micelles [25]. In Figure 3-10 the fluorescence trend is shown in greater detail; there is some slight increase in intensity but it is nowhere near as strong as that seen in the *trans*-rich solutions.

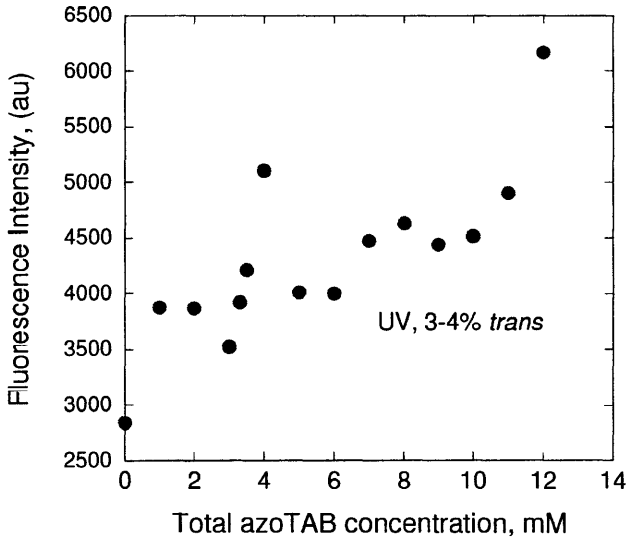

Figure 3-10 Fluorescence intensity of nile red in solutions of UV-adapted azoTAB. Same data as in Figure 3-9.

Nile red is also solvatochromic in that the wavelength of maximum emission is sensitive to the polarity of the environment [35, 39]. This effect is possibly due to a difference in polarity between the ground and excited states of nile red. The different states would be stabilized relatively differently by solvents of different polarities. This effect is illustrated in Figure 3-11, which shows a marked blueshift upon micelle formation.

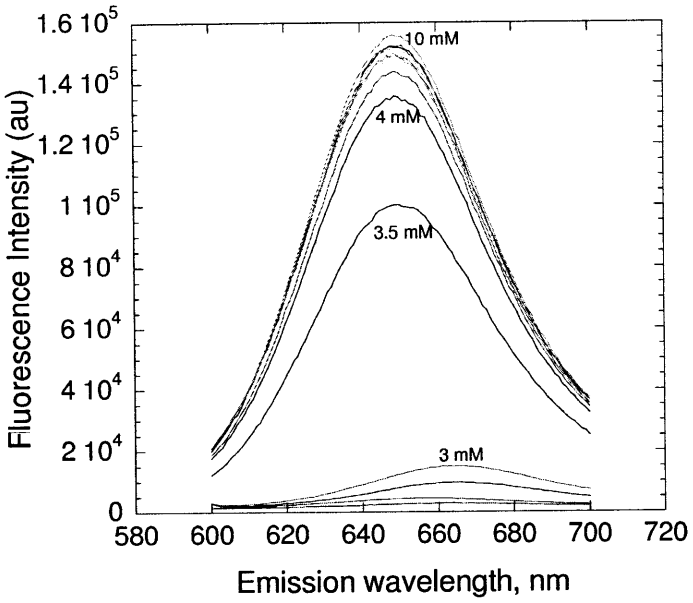

Figure 3-11 Emission spectra of Nile Red in dark-adapted azoTAB solutions. azoTAB concentrations are labeled. Blue-shift and intensity increase upon micelle formation are seen.

To provide context for this blueshift, the emission peak wavelength of nile red in solvents of different polarity is given below:

Table 4 Nile red emission wavelength in various solvents. From [35], but also also confirmed here, with the exception of ethylene glycol.

Solvent	Peak Wavelength	Dielectric Constant
Water	665	80
Ethylene glycol	652	37
Methanol	642	34
Ethanol	635	24
Acetone	615	21

The emission peak shifts from 665 nm to 650 nm on micelle formation, which is indicates that nile red sees an environment similar in polarity to ethylene glycol. This result indicates that some amount of water may penetrate into the micellar core, where nile red is expected to reside.

The schematic in Figure 3-12 summarizes these findings:

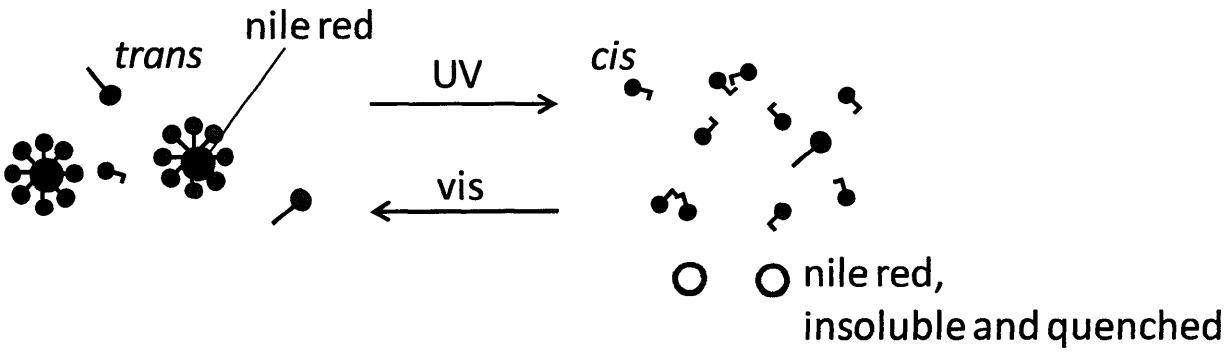

Figure 3-12 Effect of isomer composition on nile red fluorescence. Micelles in *trans*-rich solutions are able to solubilise the nile red. The nile red fluoresces strongly in these hydrophobic domains. In *cis*-rich solutions, the nile red is insoluble and emits only weak fluorescence emissions.

3.3.2. NMR methods with *trans* micelles, dark-adapted state

3.3.2.1. Chemical shifts, linewidths and diffusivities

Micelle formation can be detected through various NMR experiments, including measurement of the surfactant diffusivity [19, 20], chemical shift of the surfactant peak [3-5, 7, 9] and NMR relaxation rates [14-17]. For reasons to be discussed below, NMR measurements exhibit a single peak and a single diffusivity value which reflect both the monomeric surfactant and any micelles present in the solution. In general, this single measured value is related to the corresponding value for monomer and micelle through Equation (3.6)

$$p_{observed} = y_{monomer} p_{monomer} + y_{micelle} p_{micelle} \tag{3.6}$$

where p is the measured quantity (diffusivity, chemical shift or relaxation rate), $y_{monomer}$ is the fraction of azoTAB in the monomer form, $y_{micelle}$ is the fraction of azoTAB in the micellar form, and $p_{monomer}$ and $p_{micelle}$ are the values that would be measured if only monomer or only micelles were present. If this simple two-site model holds, then the observed value p would be expected to be constant at $p_{monomer}$ below the CMC, exhibit a breakpoint at the CMC, and then asymptotically approach $p_{micelle}$ as the concentration is increased beyond the CMC.

For the chemical shifts of the peaks in the dark-adapted state (100% *trans* solutions), such a pattern is observed for all azoTAB nuclei, as seen in Figure 3-13. The CMC appears around 3.3 mM, consistent with the fluorescent probe results. The breakpoint is somewhat obscured in this Figure, but will be more

apparent in later plots. The precise physical cause of the difference in chemical shift between monomer and micelle need not be determined for this analysis, but it can be noted that chemical shifts are generally related to the orientation and density of electrons near the nuclei. In the literature, the change in chemical shift has been attributed to the change from aqueous to hydrophobic environment [3, 6, 7], as well as changes in the bond angles in the surfactant tail [7, 22, 37]. In the latter interpretation, an increase in the population of *trans* conformers relative to *gauche* upon micelle formation is associated with downfield peak shifts. In contrast, all the nuclei in azoTAB exhibit strong upfield shifts upon micelle formation. Upfield shifts upon aggregation are seen in other systems with aromatic groups [12, 40-42], and are associated with a phenomenon known as the ring current effect [41, 43]. This effect is due to the strong interaction of aromatic π electrons with the magnetic field of the NMR instrument; as aromatic molecules engage in π-π stacking or form larger aggregates, the environment of the nuclei changes to result in easily measured variations in the chemical shift. This behavior is fortuitous, as it allows the study of azoTAB using ^{1}H NMR. Most NMR work on non-aromatic surfactant systems is based on ^{13}C or ^{19}F NMR, as the chemical shifts of these nuclei are more sensitive to changes in the environment.

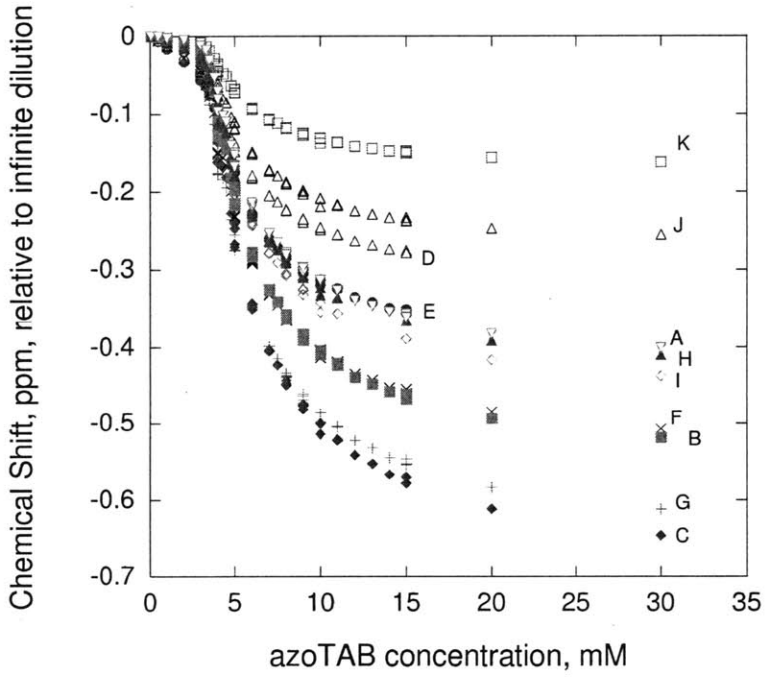

Figure 3-13 NMR chemical shifts of azoTAB, dark-adapted state, vs concentration. Shifts are shown relative to value at infinite dilution. Peak labels are defined in Figure 3-14. azoTAB is 100% *trans* in this state.

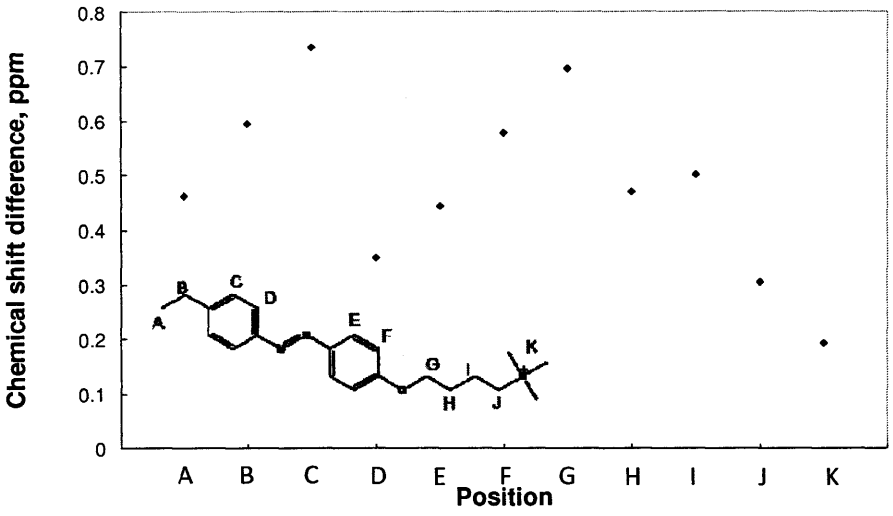

Figure 3-14 NMR peak assignment and the sensitivity of each peak to micelle formation. Peak labels correspond to Figure 3-13. Sensitivity expressed as the difference in chemical shift at infinite dilution δ_{mon} and high concentration asymptote δ_{mic}. Data collected in the dark-adapted state.

In Figure 3-14 the various protons of azoTAB are ranked by the magnitude of the chemical shift change upon micelle formation. The peaks of the protons in the hydrophobic tail are more sensitive to aggregation than those nearest the hydrophilic head. Regardless of the exact reason for the chemical shift changes due to micellisation, it is sensible that the headgroup sees a less dramatic change in environment than the tail.

Some indication of the exchange rate between the monomer and micellar forms can be inferred from the fact that the NMR spectra show a single combined peak that reflects both states. If a surfactant molecule were likely to remain in one or the other state during the time scale of the NMR experiment, the spectrum would show two distinct peaks. In this case, a single surfactant peak is observed, so the rate of exchange of individual molecules between bulk and micelle is fast compared to the relevant time scale, which is on the order of milliseconds.

NMR relaxation rates can also be used to detect changes in the aggregation state. There is more opportunity for intermolecular relaxation when a surfactant is localized in a micelle. Peak linewidths can be used as a proxy for the spin-spin relaxation rate. Such data are shown in Figure 3-15 for a phenyl proton. A possible breakpoint at the CMC is seen around 3 mM; the increased line broadening above this point signals increased relaxation rates. Qualitatively, line broadening is weakest for the head group protons and is particularly strong for the proton in position 'C'. This ordering is consistent with that seen

in chemical shift sensitivity, and may support the inference of rigid packing at position 'C', due to stacking interactions.

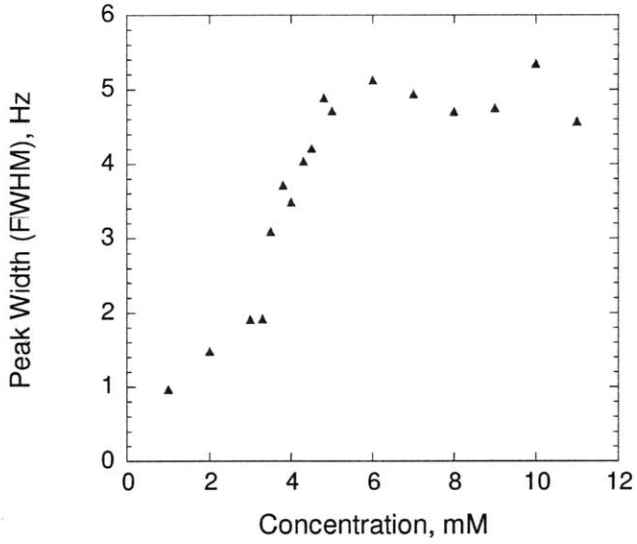

Figure 3-15 Peak width of *trans* azoTAB proton labeled 'E' in dark-adapted state.

Actual spectra are shown in Figure 3-16 in order to visually demonstrate both the chemical shift and linewidth dependences on concentration.

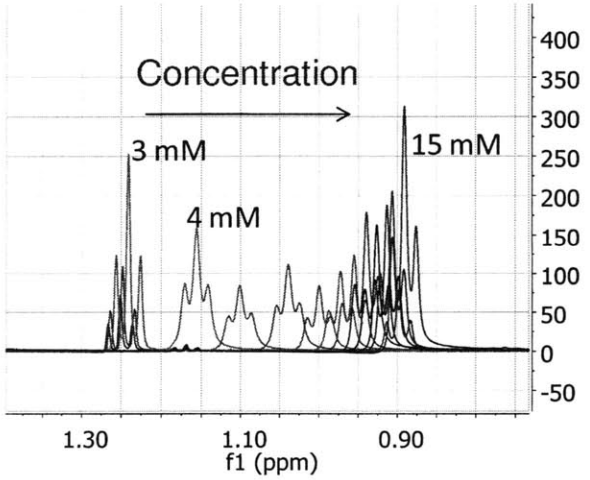

Figure 3-16 1-D NMR spectra of methyl protons in azoTAB (label 'A'). Several concentrations are superimposed. There is only one peak observed at each concentration. Data collected in the dark-adapted state, 100% *trans*. The peak moves upfield with increasing concentration, and it also becomes more broad.

Diffusion coefficients are also sensitive to micelle formation, and such measurements in dark-adapted solutions are shown in Figure 3-17. Because monomer and micellar azoTAB share the same NMR peak, NMR diffusometry cannot directly give distinct diffusivities for the two forms. However, the Stejskal-Tanner plot is linear as seen in Figure 3-6, so a single diffusion coefficient consisting of linearly weighted contributions of the two forms is observed. This observed diffusion coefficient should obey Equation (3.6), and this appears to be the case as seen in Figure 3-17. The linearity of the Stejskal-Tanner plot implies that the exchange rate between micelle and bulk is fast compared to the time of the measured diffusion, which in this experiment is 0.5 seconds. There again appears to be a breakpoint around 3.3 mM, indicating the CMC of azoTAB in the dark-adapted state.

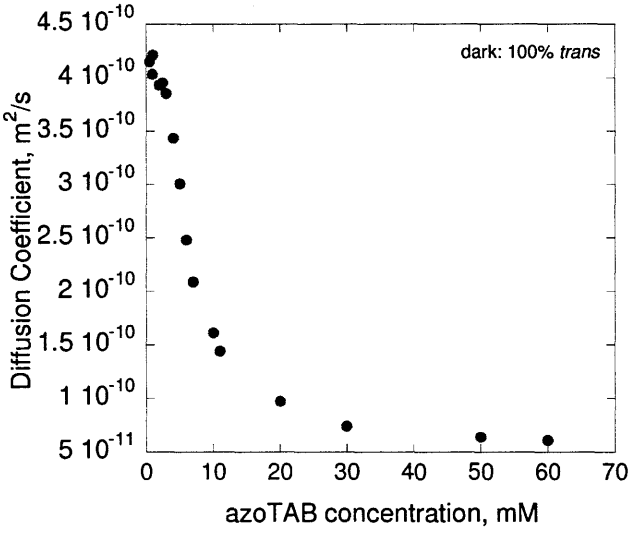

Figure 3-17 Diffusivity of azoTAB vs concentration. Measured at diffusion time of 0.5 s for solutions in deuterium oxide, dark adapted state.

Both the chemical shift data and diffusivities can be further analysed through application of the linear combination in Equation (3.6). The use of this relation would be greatly simplified if the chemical shifts and diffusivities of monomer and micelle, δ_{mon} , δ_{mic}, D_{mon} and D_{mic} could all be assumed constant throughout the entire concentration range. However, both chemical shift and diffusivity appear to vary with concentration below the CMC of 3.3 mM, where only monomers are expected. This variation may be due to the formation of dimers or other pre-micellar aggregates below the CMC. The slope of δ against concentration below the CMC is largest for the phenyl protons (peaks C-F) and the neighboring proton G, which may indicate the formation of dimers due to $\pi - \pi$ interactions. Further evidence for some sort of pre-micellar aggregation is apparent in the peak linewidth data of Figure 3-15, in which there is considerable line broadening even below the CMC.

Since the variation in δ or D below the CMC is small compared to the changes above the CMC, the changes below the CMC due to dimers are neglected as a first approximation. This is the usual practice in the literature; most authors do not explicitly mention this issue. The possibility of pre-micellization could be explicitly recognized by adding extra terms for dimers or other aggregates in Equation (3.6), and such a treatment has been previously attempted [44]. For azoTAB, the shape of the observed curves has been found to be consistent with the resulting three-site model, but that model was not adopted due to difficulties described in a later section.

The assumption of constant micellar and monomer values of δ and D implies further constraints. Above the CMC, any effect of the surrounding micelles on either monomers or micelles through electrostatic repulsion or obstruction would be neglected. It would also be assumed that the size and shape of the micelles are constant throughout the concentration range. Morphology changes, like a transition from spherical to wormlike micelles, would seem unlikely given the lack of additional breakpoints in chemical shift or diffusivity, but some level of micellar growth cannot be ruled out.

The linear combination of diffusivities or chemical shifts can be rearranged to provide Equation (3.7):

$$y_{mon} = \frac{\delta_{obs} - \delta_{mic}}{\delta_{mon} - \delta_{mic}} \tag{3.7}$$

which is used to calculate the fraction of azoTAB that is present in the monomer form at any given concentration. This fraction would be important to calculate, as it would indicate the extent of aggregate formation under the given conditions. To apply this equation, values of δ_{mon}, δ_{mic}, D_{mon} and D_{mic} are required. The monomer values are simply found through extrapolation to infinite dilution. The diffusivity and chemical shifts vary nearly linearly over the pre-CMC concentration range, so the extrapolation is straightforward. D_{mon} is estimated to be $4.2*10^{-10}$ m^2/s; this appears reasonable in comparison to literature values of other surfactants, such as $6.02*10^{-10}$ m^2/s for dodecyl trimethylammonium bromide (DTAB) [45]. DTAB is homologous to azoTAB, with the exception that it has a purely alkyl tail. The extended tail length of azoTAB is similar to that of a 12-carbon alkyl tail without an azobenzene moiety, as found in DTAB. Despite this similarity in length, it is plausible that the bulky azobenzene group would confer a lower diffusivity on azoTAB. The ratio of the diffusivities, 1.4, is equal to the inverse ratio of the molecular weights (also 1.4).

3.3.2.2. Pseudophase separation model, micelle size and monomer concentration

Determination of the micellar chemical shift and diffusivity δ_{mic} and D_{mic} was guided by application of the pseudophase separation model of micelle formation. In this model, it is assumed that the micelles constitute a distinct phase from the bulk solution. No micelles are expected below the CMC, and any surfactant added above the CMC is assumed to join the micellar phase. The size of the micelles is not considered in the model. Applying this assumption to Equation (3.6) results in the following expression:

$$\delta_{obs} = \frac{CMC}{C_{tot}}\left(\delta_{mon} - \delta_{mic}\right) + \delta_{mic} \tag{3.8}$$

as well as an analogous expression for diffusivity. If the assumptions built into this expression are appropriate, then a plot of the observed chemical shift or diffusivity against the inverse overall concentration should be linear above the CMC, with the intercept providing the pure micellar value δ_{mic} or D_{mic}. As seen in Figure 3-18 and Figure 3-19, such plots are indeed linear, providing confidence in the approach.

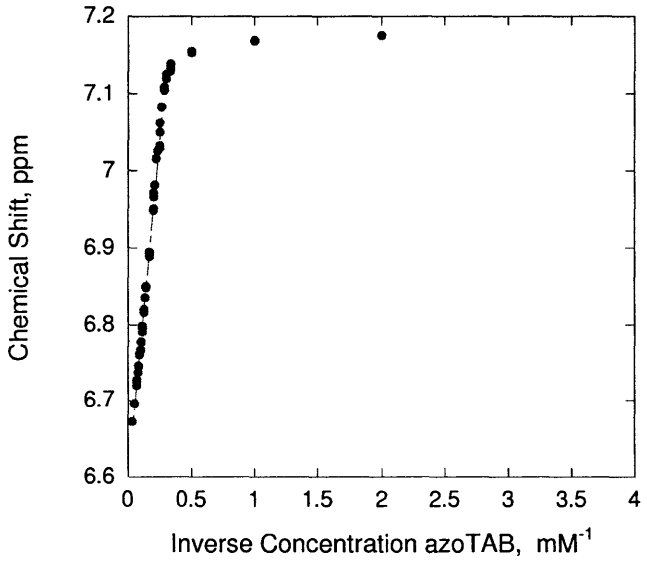

Figure 3-18 Chemical shift of phenyl proton ('F') vs inverse concentration, dark-adapted solutions. Plot is linear above the CMC. R^2 value is 0.995.

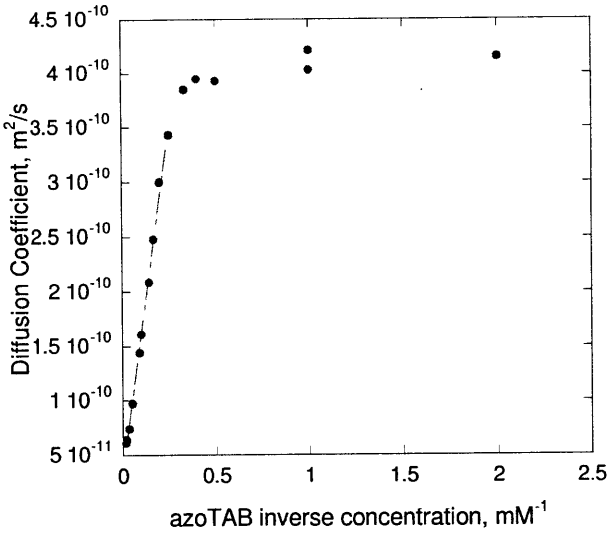

Figure 3-19 azoTAB diffusivity plotted against inverse concentration. Linear regression shown above CMC. $R^2 = 0.996$. Implied micelle diffusivity is $3.6*10^{-11}$ m^2/s, $\pm$ is $0.8*10^{-11}$ m^2/s, where the uncertainty limit is calculated from the 95% confidence intervals of the intercept.

The resulting value of the micelle diffusivity can be used to find the hydrodynamic radius R_h of the micelle through use of the Stokes-Einstein equation:

$$D = \frac{k_b T}{6\pi\eta R_h} \tag{3.9}$$

where k_b is the Boltzmann constant and η is the solvent viscosity. The viscosity of deuterium oxide was taken as 1.095 cp at the temperature of the diffusion measurements, 25 C [46]. The resulting value of the hydrodynamic radius, 5.5 nm, is rather higher than the fully-extended length of *trans* azoTAB, 2.2 nm. Applying the 95% confidence intervals on the extrapolated intercept, the minimum radius is 4.5 nm, which is still larger than expected.

This discrepancy can be attributed to several factors. The micelles may not be perfectly spherical. Recent SANS work with azoTAB suggested that oblate spheroid micelles form under visible light conditions [47]. The semi-major axis was reported to be about 3 nm, and the semi-minor axis about 1.9 nm. This result was considered plausible, as the minor axis is consistent with the fully-extended length of the surfactant tail. Unfortunately there are no SANS data available for azoTAB in the dark-adapted state, in which the micellar dimensions may differ.

The Stokes-Einstein equation has been modified for oblate spheroids [48]. The hydrodynamic radius is replaced by an effective radius:

$$\frac{\left(a^2-b^2\right)^{1/2}}{\tan^{-1}\left[\left(\frac{a^2-b^2}{b^2}\right)^{1/2}\right]} \tag{3.10}$$

where a and b are the lengths of the semi-major and semi-minor axes, respectively. If b is assumed to be 2 nm in accord with the fully extended tail length, then a would be 5.9 nm in order to achieve the lower estimate of the effective radius, 4.5 nm. While the aspect ratio may not be that extreme, it is likely that the azoTAB micelles are nonspherical and thus larger than what would be expected for a spherical micelle.

Furthermore SANS returns a radius of gyration, which would differ from the hydrodynamic radius. The hydrodynamic radius itself does not have an exact physical correspondence to the dimensions of the micelle, but it simply the radius of the hard sphere with an equivalent diffusivity. This radius may be expanded due to the Stern layer of tightly bound counterions or also possibly a shell of hydration.

There are other effects that might influence the apparent value of the micelle diffusivity, and thus the inferred micellar dimensions. The diffusivities of both monomer and micelle will not be constant over the entire concentration range, as both will be limited by obstruction due to the surrounding micelles. A very simple expression for the reduction in diffusivity due to obstructions is [49]

$$\frac{D}{D_o} = (1-\phi) \tag{3.11}$$

where D_0 is the unobstructed diffusivity and ϕ is micelle volume fraction. At the highest concentration used (60 mM), the volume fraction of micelles was estimated to be 0.02. This calculation was done by assuming the molecular volume of azoTAB to be 640 Å^3 [47]. Obstruction effects are thus not likely to be very significant, though electrostatic effects may be.

To the extent that some error is introduced by finding D_{mic} through extrapolation, it would not propagate strongly to the other calculations here. Because D_{mic} is much less than D_{mon}, Equation (3.7) is not very sensitive to uncertainty in D_{mic} except at very high concentrations (above 30 mM).

Other workers have tried to measure D_{mic} more directly by adding a highly hydrophobic solute to the solution [19, 22]. If nearly all the solute partitions to the micelle core, the diffusivity of the solute would be equal to that of the micelle. This technique was attempted with toluene and tetramethylsilane, which were reported to strongly partition into micelles, and which also have peaks that do not overlap with azoTAB. Unfortunately, enough of the solutes remained in the aqueous phase that their observed diffusivity was higher than that of azoTAB, making them unsuitable for probing the micelle in this way.

Having thus found δ_{mic} and D_{mic}, it is shown in Figure 3-20 that the shape of the curves in Figure 3-13 and Figure 3-17 can be well described using the pseudophase separation model as expressed in Equation (3.8):

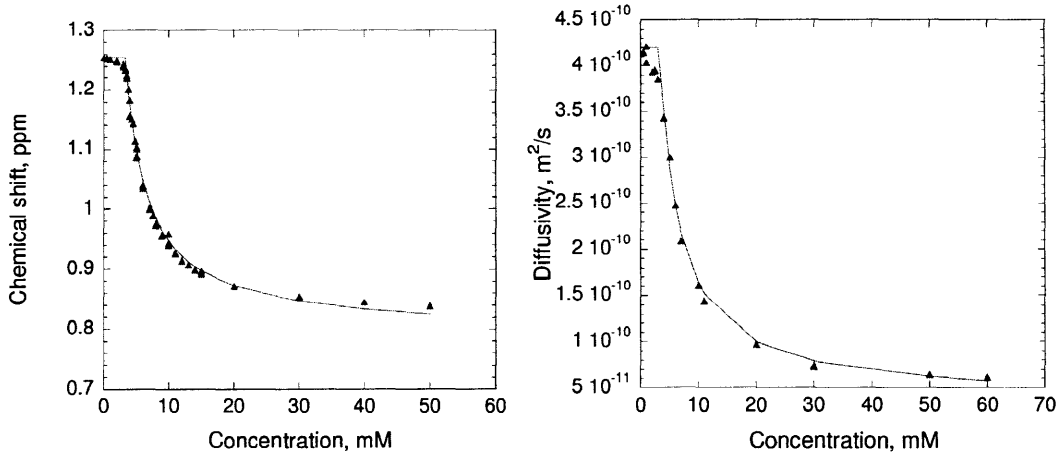

Figure 3-20(a) Chemical shift of methyl tail nuclei ('A') in dark adapted state vs concentration. Shown are measured values, and calculated values using Equation (3.8). (b): Corresponding chart for diffusivities.

As expected, the model fails to account for pre-micellar aggregation, but fits the remaining data quite well.

The pseudophase separation model was used to help evaluate the constants in Equation (3.7), but the derivation of the equation itself is entirely independent of that model. Calculated monomer concentrations can thus be used as an additional test of the applicability of the model. Results are shown in Figure 3-21, using both diffusivity and chemical shift data.

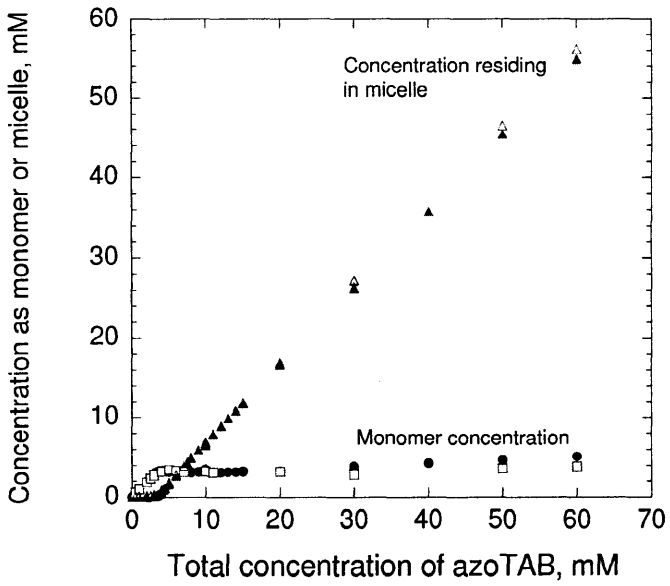

Figure 3-21 Concentration of azoTAB existing within micelles and as monomer. Calculated from chemical shift data using methyl peak 'A' (solid markers) and diffusivity (hollow markers). Dividing the micellar values by the aggregation number would yield the concentration of micelles.

The appearance of a sharp CMC and the relative constancy of the monomer concentration above the CMC justify the assumptions of the pseudophase separation model. There is a subtle maximum (seen more clearly in Figure 3-23) in the monomer concentration at the CMC, with the monomer concentration dropping slightly with increased concentration. The effect is weak enough that it cannot be ascertained whether it is real or a result of slight experimental error. The upwards drift in the monomer concentration above 30 mM is likely spurious and due to slight errors in the extrapolated values of δ_{mic} and D_{mic}. It is concluded that these two NMR methods can provide robust estimates of the how much surfactant is residing within aggregates. Such information is also useful for understanding the surfactant-polymer gel system, as discussed in Chapter 4.

3.3.2.3. Mass action model

The pseudophase separation model is attractive due to its simplicity, but its utility in describing characteristics of micelles is very limited beyond what was discussed above. An alternate view of micelle formation is the mass-action model. In this model, micelle formation can be described analogously to a chemical reaction:

$$nS_1 \rightleftarrows S_n \tag{3.12}$$

where n is the aggregation number, S_1 denotes the monomer, and S_n denotes the micelle. For simplicity, a single aggregation number is considered here, though polydispersity is possible. There is no presumption of a sharp CMC. The equilibrium constant for the process is written as:

$$K_n = \frac{[S_n]}{[S_1]^n} \tag{3.13}$$

Various attempts have been made to use this approach in conjunction with NMR to find the aggregation number of micelles. One basic approach has been to rearrange Equation (3.13) to the following form,

$$\ln n[S_n] = n \ln[S_1] + \ln nK_n \tag{3.14}$$

or some equivalent [2, 4, 5, 7, 11, 13]. Expressions relating the monomer concentration $[S_1]$ and the concentration of azoTAB residing in micelles $n[S_n]$ to NMR data are found using Equation (3.7) and substituted into the equation. A plot of $\ln n[S_n]$ vs $\ln[S_1]$ would then have slope n and intercept $\ln nK_n$. When prepared for azoTAB, this plot is anything but linear (see Figure 3-22).

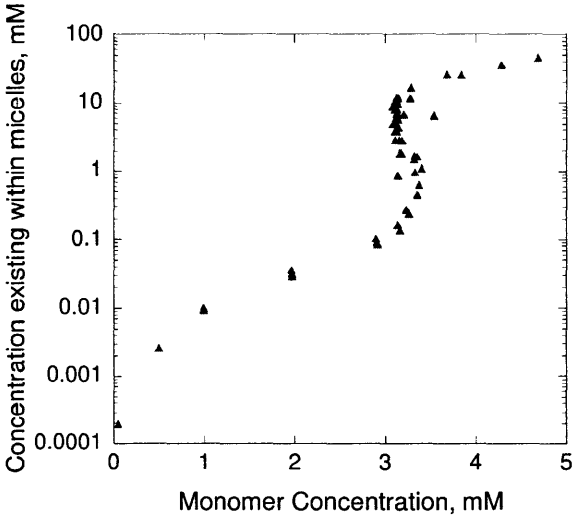

Figure 3-22 Plot that would provide the micelle aggregation number. Slope is nonlinear. See discussion in text. Data are the same as in Figure 3-21.

Similar plots in the literature often appear unconvincing as well; in one case arbitrary adjustments to δ_{mic} were required to produce a more linear result [4]. Another work observed that the method was not 'completely satisfactory' [9], but it is not clear whether the reasons for this have been anywhere discussed. That statement was made in 1979, and yet variations of this plot continue to appear.

On examining Equation (3.14) and Figure 3-22, it is apparent that the plot is not well-posed if the surfactant exhibits behavior similar to that of the pseudophase separation concept. Below the CMC, $n[S_n]$ is essentially zero, so nothing meaningful is plotted. Above the CMC, the monomer concentration is nearly constant, so the abscissa barely changes. In fact, if the monomer concentration decreases only slightly above the CMC, the slope becomes negative, as in Figure 3-22. While it has been recognized that the mass action model is not entirely suitable for ionic surfactants [10], these particular difficulties are related more to the method of analysis than the model.

The other basic approach to the mass action model [10, 17, 50, 51] has been to combine Equation (3.13) with the site balance $[S_1] + n[S_n] = C_{tot}$. This results in the following expression, or some equivalent:

$$nK_n[S_1]^n + [S_1] = C_{tot} \tag{3.15}$$

The monomer concentration is again related to NMR chemical shifts as previously discussed. The aggregation number, equilibrium constant, δ_{mon} and δ_{mic} are then fit by minimizing the error between the observed and calculated values of δ_{obs}. It has been generally observed that this fitting is difficult, as n and K_n are nearly covariant. Many pairs of values of the two parameters provide visually satisfactory fits. Elaborate schemes to find the global optimum have been devised, but accurate initial guesses of the aggregation number are required [51]. Also, the resulting aggregation numbers for ionic surfactants are often low compared to those measured using other techniques [10], so it was doubtful that this approach would be fruitful.

As expected, the covariance of n and K_n presented major difficulties. To demonstrate this, best fit values of K_n were found for various values of n. As shown in Figure 3-23, reasonable fits to data can be made at various values of the aggregation number. Increasing n generally results in more well-defined CMCs, but it is not obvious which value provides the best fit. The mass action model approaches equivalence with the pseudophase separation model as n approaches infinity, and any deviation from the pseudophase separation model in azoTAB is not well captured by the mass action model. Any aggregation number above 40 appears plausible. The best fit value of K_n for each n is shown in Figure 3-24.

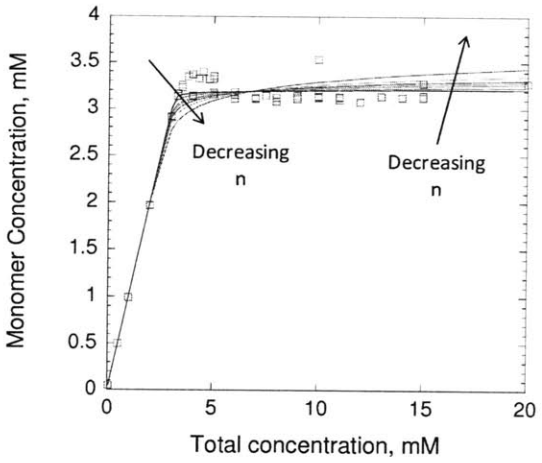

Figure 3-23 Demonstration of mass-action model. Model and experimental results for variation of monomer concentration with total concentration. Model results are shown for n = 20, 30, 40, 50, 60, 100 and 200.

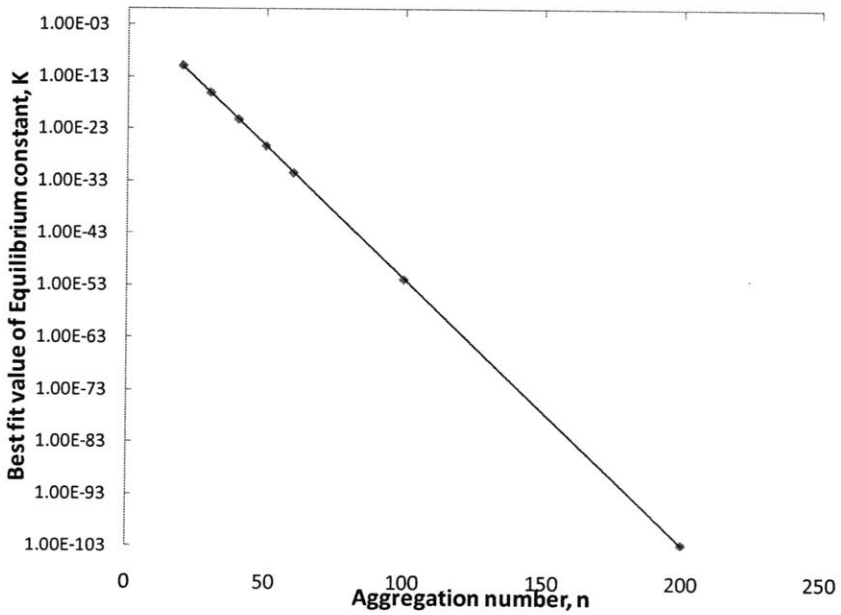

Figure 3-24 Relationship of aggregation number and best fit value of Equilibrium constant in mass action model. Above n = 40, any point on the line gives a reasonable fit to data.

In order to proceed, an aggregation number range of 70-100 has been adopted from SANS work in the literature [25], as well as geometric considerations.

The mass action model was also briefly considered in an attempt to describe the apparent pre-micellar aggregates observed below the CMC. In this case, the chemical shift would be expressed as a linear combination of three sites,

$$\delta_{obs} = y_{mon}\delta_{mon} + y_{pre}\delta_{pre} + y_{mic}\delta_{mic} \tag{3.16}$$

where the index 'pre' refers to the pre-micellar forms. A second equilibrium constant was invoked, in order to introduce the aggregation number n_{pre} of the pre-micellar clusters. However, this introduced three more parameters to fit: n_{pre}, K_{pre} and δ_{pre}. These parameters were also found to be covariant, and the fitting process was subject to multiple local minima. It was decided that little of value would result from this approach.

3.3.2.4. Summary of experimental results for micelles in dark-adapted state

A wide array of experimental results has been presented for micelles in the *trans* form. It has been comprehensively demonstrated that there is a clear CMC at approximately 3.3 mM. Above the CMC, the monomer concentration is relatively but not entirely constant. This latter result follows directly from NMR data, and requires the use of no model except for the basic concept expressed in Equation (3.6). Below the CMC, there is strong evidence of stacking interactions that result in pre-micellar aggregates.

Some inferences can be made about the nature of the micelles. According to fluorescent probe studies, there may be some degree of water penetration into the micelle core. NMR chemical shift data supports the reasonable possibility of stacking interactions within the micelles, causing some rigid packing in the vicinity of the phenyl rings. A robust estimate of the micellar size has not been possible, but NMR measurements to that end are at least consistent with previous SANS work.

Given the success of NMR chemical shift and diffusion data to characterize *trans* micelles, it appears likely that both techniques could be used to good effect in *cis-trans* mixed micelles and surfactant-polymer complexes. The diffusion coefficients of different components can be measured with a high level of accuracy, which would be helpful when studying gels, as in Chapter 4.

3.3.3. NMR methods with *cis* micelles, UV-adapted state

As in the fluorescence data, NMR methods do not show any obvious onset of micellisation in the UV-adapted state within the concentration range explored. Shown in Figure 3-25 are the chemical shifts of *trans* and *cis* azoTAB as a function of total concentration in the UV-adapted state. Data from the dark-adapted state are added for comparison. There is no obvious breakpoint in either the *cis* or *trans* series, in contrast to the clear CMC in the dark-adapted state at about 3.3 mM. Higher concentrations were not examined, due to the difficulty in achieving a photo-stationary state at high optical densities as discussed in the previous chapter. The absence of an observed UV CMC appears at first to be contrary to the

previous literature [36], in which the CMC in the UV-adapted state was measured to be 10.5 mM in water. However in that work the composition of the UV-adapted state was 84% *cis*, whereas here it is 96-97% *cis*. The additional *cis* content should raise the CMC further. Hayashita [36] did find that homologues of azoTAB with longer tails did have much lower CMCs in their UV-adapted state, so *cis* surfactants will form micelles more readily if the overall molecule is made more hydrophobic.

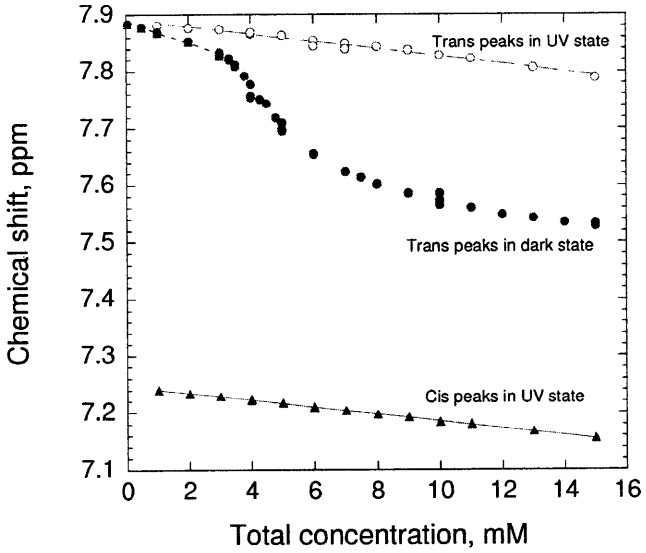

Figure 3-25 Chemical shift variation of *trans* and *cis* peaks in UV-adapted solutions, 96-97% *cis*. Also included are data from *trans* in dark-adapted solutions. The peak for phenyl proton 'E' is shown in all cases. Linear regression is shown for the entirety of the UV data; the slopes for *cis* and *trans* are -0.0061 ppm/mM and -0.0066 ppm/mM, respectively. Regression is also done for sub-CMC data in the dark-adapted state; slope is -0.019 ppm/mM.

While there is no breakpoint in the UV-state chemical shift data of Figure 3-25, there is a clear linear trend in both *cis* and *trans*. A similar trend was seen below the CMC in the dark-adapted data series. On the basis of corroborating diffusivity and peak linewidth data, this trend in the dark samples was ascribed to the formation of pre-micellar aggregates. It appears that similar behavior takes place in the UV-adapted condition. The presence of similar trends in both *cis* and *trans* in the UV-state implies that both isomers participate in these aggregates.

At infinite dilution the *trans* peak appears at about the same chemical shift, regardless of the light condition. The *cis* peak at infinite dilution appears at a markedly different chemical shift from the *trans*. Even in isolation from other surfactant molecules, the NMR environments within the *trans* and *cis* isomers differ from each other.

Diffusivity and linewidth data were collected in order to test these hypotheses about aggregate formation in the UV state. The UV-state diffusion coefficients in Figure 3-26A show no obvious breakpoint, but the *trans* diffusivity does drift downwards with increased concentration. The *cis* data are more ambiguous; there may be a reduction of about 11% between the diffusivity at 1 mM and the higher concentrations. As seen in Figure 3-26B, the linewidth data are similar. There is no apparent trend in the *cis* peak linewidths, but the peaks of the residual *trans* in the UV state do increase with concentration. The low concentration linewidths appear wider in the UV state than the dark-adapted, but the absolute values of these series should not be directly compared. The measurements were made on different NMR probes, and the differences in field inhomogeneities may affect the observed linewidths.

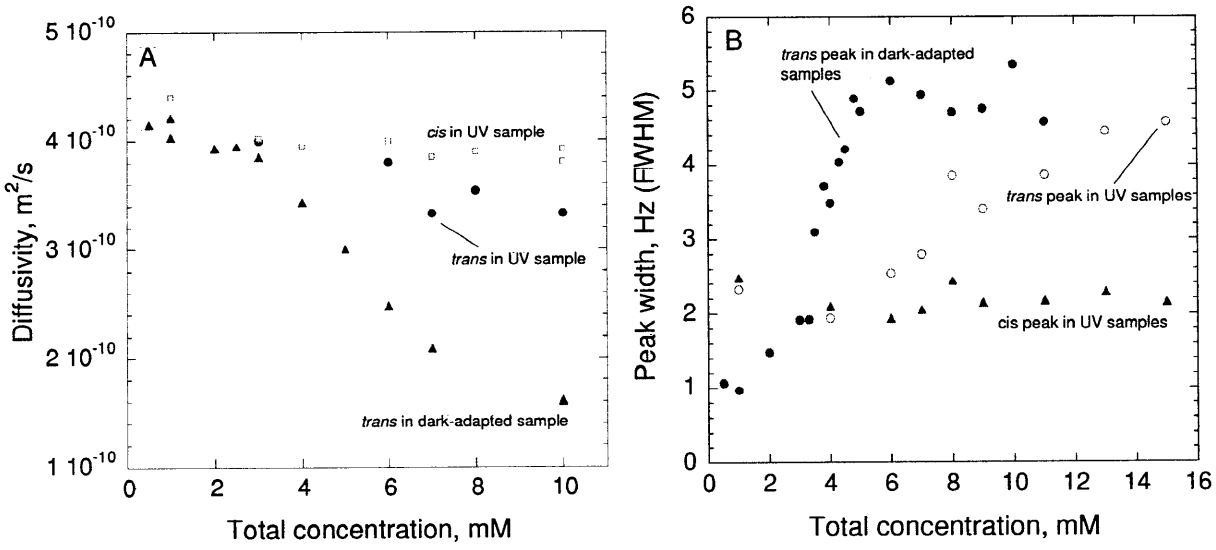

Figure 3-26: Comparison of azoTAB diffusion coefficients and peak linewidths in dark- and UV-adapted states. Residual *trans* in UV state also shown. Figure 3-26A: Diffusivities, B: linewidths. Absolute values of linewidth data cannot be directly compared between dark and UV samples, due to use of different NMR probe. Data in B from peak 'E'.

These chemical shift, diffusivity and linewidth data are not perfectly consistent, but they do suggest some pre-micellar aggregates in *cis*-rich solutions. On the basis of diffusion and linewidth data, *trans* surfactants may be more likely to participate in these structures, but chemical shift data indicate that *cis* do as well. It is possible that the *trans* isomers form relatively stable clusters due to stacking interactions, while the *cis* either form their own more loose clusters or pass transiently in and out of the *trans* dominated clusters. It is however not immediately obvious why the chemical shift and possibly the diffusivities of the *cis* exhibit a concentration dependence, while the peak linewidths do not.

Other possible explanations for the data in Figure 3-25 should also be considered. The chemical shifts and diffusivities could possibly be changing due to electrostatic interactions, as opposed to cluster formation. However at these concentrations, unassociated surfactants would on average be spaced further apart than the Bjerrum length in water, which is 0.7 nm. The electrostatics mechanism would also not explain the increasing linewidth in the *trans* form.

Recent SANS results support the conclusion that proper micelles do not form in the UV-adapted state [47]. The analysis suggested that pre-micellar aggregates with a disc-like structure were present instead, with aggregation numbers on the order of 5.

3.3.4. Mixed micelles

3.3.4.1. NMR chemical shift data

Any application of azoTAB will likely involve the use of two different wavelengths of light, one effecting a *trans*-rich photostationary state, and the other *cis*-rich. Choosing the photostationary states in this way will maximize the changes in physical properties that occur upon irradiation. During the irradiation process the system will go through all intermediate isomer compositions. In order to understand the characteristics of the system during photoreaction, these intermediate compositions should be studied in addition to the dark- and UV-adapted extremes. Mixed micelles consisting of both isomers are likely to form in this range. In the case of ideal mixing, the CMC of these mixed micelles is expected to be between the CMCs of pure *trans* and pure *cis* [52], though the CMC of pure *cis* has not been observed. These mixed compositions were investigated by starting with a sample of a given concentration in the dark-adapted state and repeatedly irradiating it with UV light until the UV photostationary state was reached. Shown in Figure 3-27 are plots of the observed chemical shift as the isomer composition is thus varied. A break appears in the chemical shift of both isomers, and is accompanied by a change in peak linewidths as well. This point is determined to be the CMC of the mixture. *Trans* and *cis* are presented on different scales, as the total variation in the *cis* chemical shift is very small as compared to that of *trans*. This either indicates that *cis* NMR peaks are relatively insensitive to the change in environment between bulk and micelle, or that very little *cis* takes part in the micelles. It is also possible that *cis* and *trans* form their own separate aggregates, with the *trans* micelles being larger and more stable. However if *cis* and *trans* were operating independently of each other, it would be unusual for them both to have the same CMC.

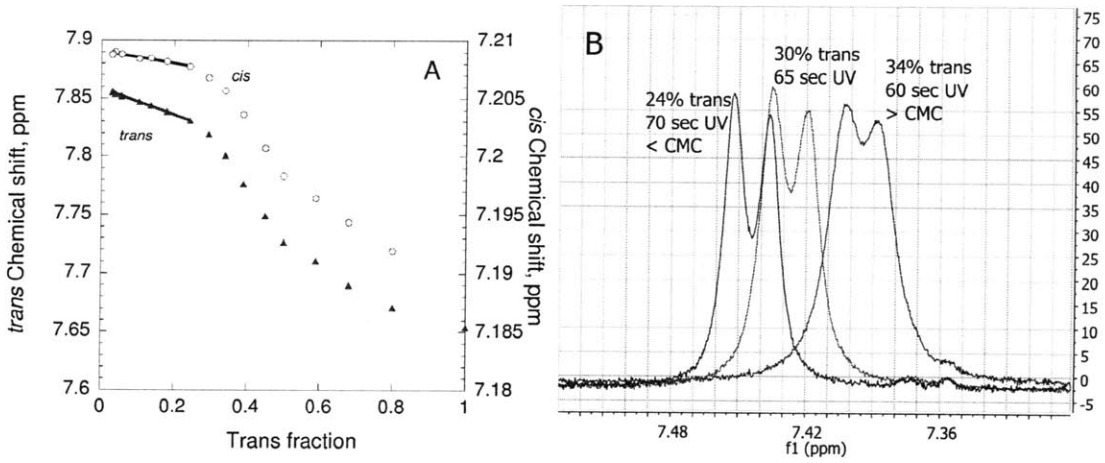

Figure 3-27 Chemical shift and peak widths as isomer composition is changed, at a total azoTAB concentration of 6 mM. A: Chemical shifts of both *trans* and *cis* peaks. Scale for *cis* is much narrower than for *trans*. Data measured by repeatedly irradiating initially dark sample until chemical shift becomes constant. Peaks shown for proton 'E'. Linear regression shown for data below the CMC. CMC is between 24% and 30% *trans*. B: Selected spectra showing peak 'C' of the *trans* isomer, as the CMC is crossed. NMR peaks are narrower below the CMC. Peak 'C' shows particularly strong changes in linewidth upon micelle formation. UV irradiation from high intensity Dymax lamp; see Chapter 2 Experimental Section.

Repetition of this experiment at different total concentrations yielded the CMC at a variety of isomer compositions. The *trans* chemical shifts are shown below:

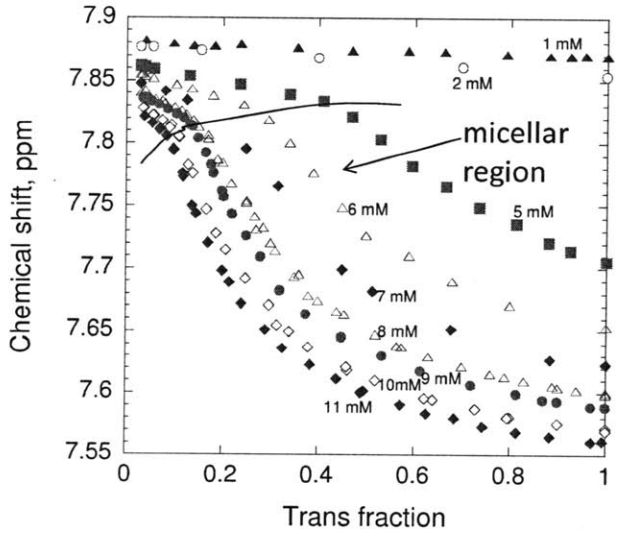

Figure 3-28 Chemical shifts of *trans* azoTAB at various total azoTAB concentrations and isomer compositions. Used to find CMC of mixtures. Shown are peaks of phenyl proton 'E'. Line is drawn to connect the breakpoints in each series, demarcating the CMC.

Figure 3-28 provides a helpful overview of the chemical shifts in this system. It acts as a phase diagram of the system, with the micellar region below the breaks in the curves. Along the right edge are data that

correspond to the dark-adapted results of Figure 3-13. If plotted against total concentration, the data along the left edge would reproduce the *trans* series shifts in the UV photostationary state from Figure 3-25. The series for 1 mM and 2 mM show no breakpoint, so no micelles are formed at those concentrations regardless of isomer composition. At higher total concentrations, the peak positions As the total concentration is increased, the CMC appears at lower *trans* fractions.

It would be instructive to apply Equation (3.6) to each of these curves. It would then be possible to find the monomer and micellar concentrations at every point on this plot. The changing composition makes this less straight-forward than the single component case; the appropriate values of δ_{mon} and δ_{mic} are not readily apparent at any given point. The issue is revisited in a later section.

3.3.4.2. NMR diffusion data

The same basic experiment was also performed using both NMR diffusometry and fluorescence spectroscopy. Shown in Figure 3-29 are diffusion results collected at 6 and 10 mM. The *trans* series at 10 mM shows a clear breakpoint at a *trans* fraction of about 0.11; micelles form above this point. The *cis* diffusivities trend only slightly downwards whereas the *trans* show significant shifts. This divergence between *cis* and *trans* again implies that the *cis* isomer participates in aggregate formation to a lesser extent than the *trans*. These data are analysed further below.

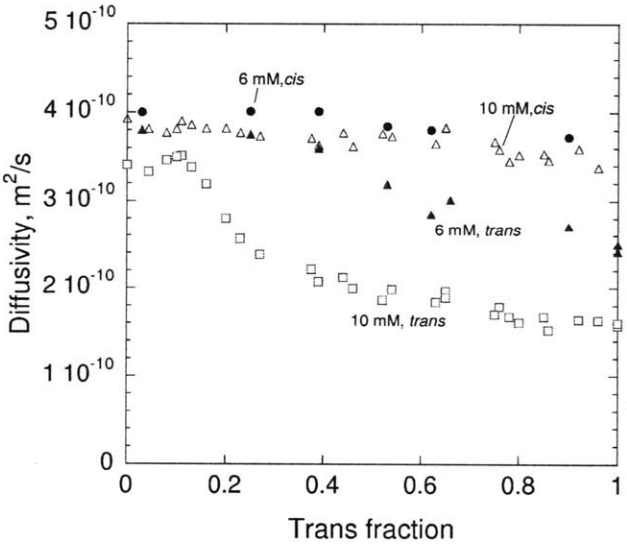

Figure 3-29 Diffusion Coefficients of *cis* and *trans* as a function of isomer composition. Hollow and solid markers correspond to data at 10 mM and 6mM, respectively. Red markers denote *trans*, and blue *cis*.

3.3.4.3. Fluorescence

The fluorescence intensity and emission wavelength of nile red in azoTAB solutions also show a sharp breakpoint at the CMC as the isomer composition is varied, as seen in Figure 3-30 for a total azoTAB concentration of 7 mM. The CMC appears at about a *trans* fraction of 0.26 at that total concentration. The fluorescence intensity then increases with increasing *trans* fraction as the number of micelles increases, and possibly also as the size or stability of the micelles increases. Nile red fluoresces at 650 nm in solutions with micelles, and at 660 nm in solutions without any available hydrodynamic domains. The intermediate wavelengths observed around the CMC could indicate relatively poorly formed micelles in this region, with a high level of water penetration into the aggregate. The intermediate wavelengths could also be the simple result of convolution between the emission spectra of nile red within and outside of micelles.

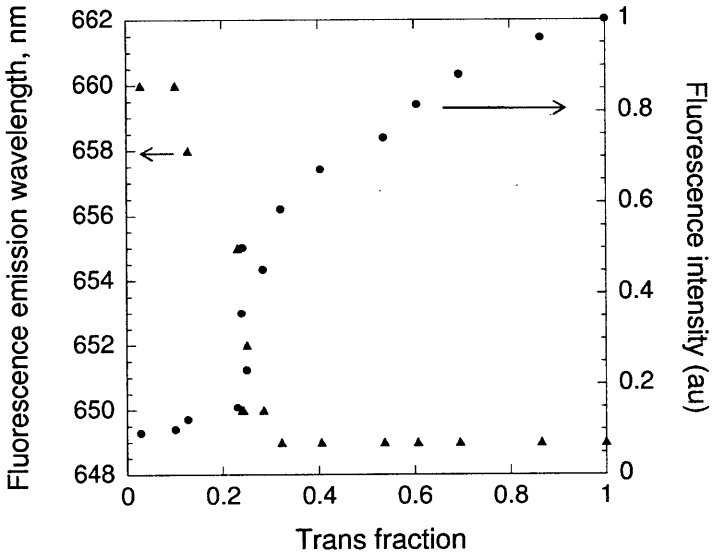

Figure 3-30 Fluorescence intensity and wavelength of Nile Red in azoTAB solutions as a function of isomer composition. Total azoTAB concentration is 7 mM, and nile red concentration is 0.54 μM. Isomer composition measured by using UV-Vis spectroscopy.

This experiment was repeated at several concentrations, as shown in Figure 3-31. The emission wavelength is plotted against irradiation time to provide a sense of the time scales in the experiment. The CMC is apparent in each curve.

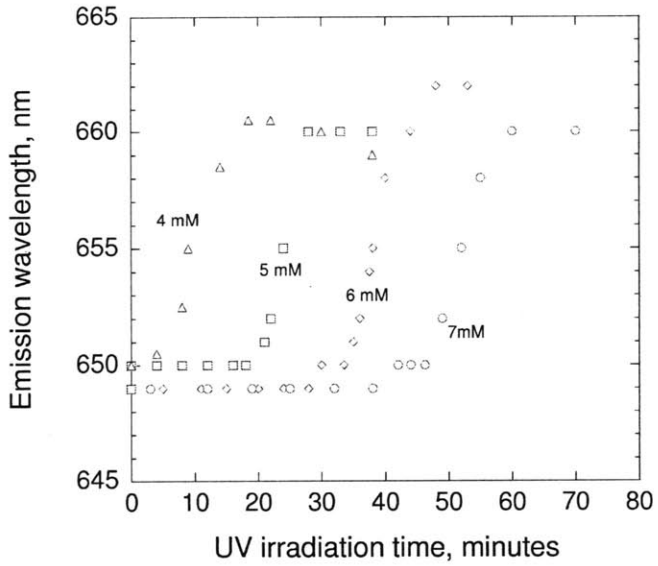

Figure 3-31 Fluorescence emission wavelength of nile red in azoTAB solutions, as a function of UV irradiation time. Repeated at total concentrations of 4, 5, 6 and 7 mM. Each solution was initially in dark-adapted state, 100% *trans*. Irradiation path length was 1 cm.

3.3.4.4. CMC of *trans*/*cis* mixtures

Combining all of the results above, the CMC of the azoTAB system can be plotted as a function of composition, as in Figure 3-32. The result is consistent with the previously reported *cis* CMC in a 84% *cis* solution [36]. Also shown is the CMC that would be expected if the *cis* isomer were completely invisible to the process: the concentration required at each composition for the concentration of *trans* to reach the CMC of pure *trans*. This expected CMC is clearly different from the measured values. While the experimental results presented thus far suggest that *cis* only plays a minor role in micelle formation, the presence of *cis* has a significant effect on the observed CMCs. In order to better understand this interaction between the two isomers, some simple models are considered.

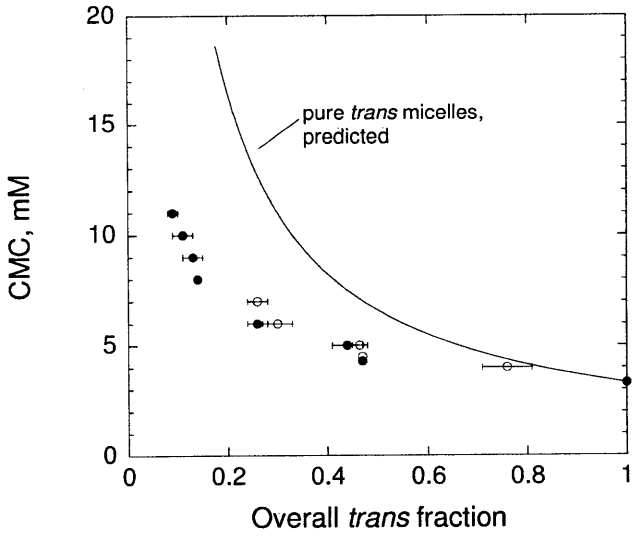

Figure 3-32 CMC for mixed micelles at various isomer compositions. Experimental points found using NMR (solid markers) and fluorescence (hollow markers). CMC values found from breakpoints in Figure 3-28, Figure 3-29 and Figure 3-31. Error bars indicate uncertainty due to sparseness of data points around the breakpoint. Also shown is curve at which *trans* concentration is equal to 3.3 mM, the CMC of pure *trans*.

3.3.4.5. Micelle composition: thermodynamic modeling and experimental results

The pseudophase separation model has been extended by Clint to mixed micelles in order to facilitate analysis of such results [52]. In this development the bulk phase is assumed to be an ideal solution, with the activity coefficient set to unity. The chemical potential of the surfactant monomer is written as

$$\mu_i^{mon} = \mu_i^{\dagger mon} + RT \ln C_i^{mon} \tag{3.17}$$

where the subscript i refers to the species *trans* or *cis*, μ_i^{mon} is the chemical potential of component i in the bulk, C_i^{mon} is the concentration of component i in the bulk (expressed as a molarity), and $\mu_i^{\dagger mon}$ is the Henry's law standard state chemical potential as used with units of molarity.

The micellar phase is also assumed to be ideal:

$$\mu_i^{mic} = \mu_i^{o\,mic} + RT \ln x_i \tag{3.18}$$

where μ_i^{mic} is the chemical potential of component i in the micelle, $\mu_i^{o\,mic}$ is the chemical potential in a micelle of pure i, and x_i is the molar composition of the micelle. In the single-component case C_i^{mon} is then set equal to the CMC of pure component i, consistent with the pseudophase separation model. These expressions eventually lead to (3.19) for predicting the CMC of the mixture:

$$CMC_z = \frac{1}{\frac{z_{trans}}{CMC_{trans}} + \frac{z_{cis}}{CMC_{cis}}} \tag{3.19}$$

where z_i is the molar fraction of azoTAB that is present as isomer i, and CMC_z is the CMC at that overall composition. It is difficult to apply Equation (3.19) as CMC_{cis} could not be measured, but the best-fit value of CMC_{cis} can be determined by using the experimental data found in Figure 3-32. This value is 12 mM. The resulting curve for CMC_z is shown in Figure 3-33 and it is apparent that this model is not very successful in *cis*-rich solutions. The agreement between model and empirical data is qualitatively reasonable over the rest of the composition range. The assumption of ideal mixing in the micelles, particularly in *cis*-rich solutions, is suspect due to the probable inefficiency of packing *cis* and *trans* together in the same micelle core. Electrostatic effects are also neglected when assuming ideality.

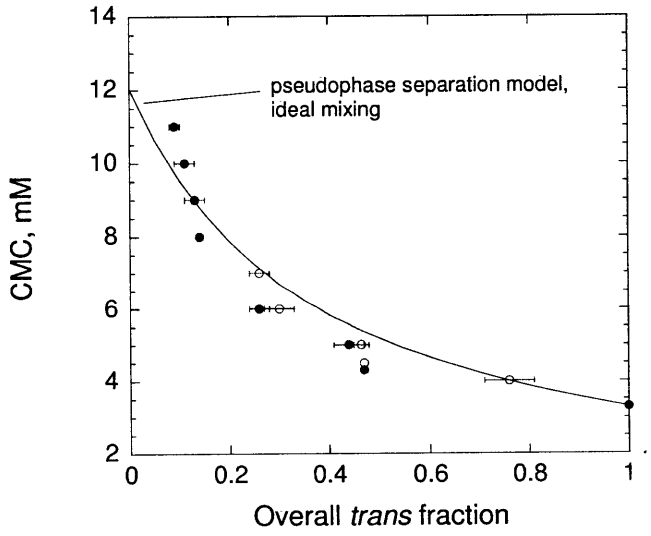

Figure 3-33 CMC of mixed micelles: Experimental points and curve using pseudophase separation model. CMC of pure *cis* micelles is fit using model form and data.

To account for such non-ideal behavior, an activity coefficient is inserted for the micellar phase.

$$CMC_z = \frac{1}{\frac{z_{trans}}{\gamma_{trans} CMC_{trans}} + \frac{z_{cis}}{\gamma_{cis} CMC_{cis}}} \tag{3.20}$$

Explicitly trying to describe the various non-idealities would add a good deal of complexity to the analysis. Instead it is common practice follow the treatment of Rubingh [53], who assumed regular solution behavior. In this case, the activity coefficient is expressed using a single-parameter Margules function:

$$\gamma_i = \exp(\beta x_j)^2 \tag{3.21}$$

where γ_i is the activity coefficient of component i, β is some empirically determined constant and x_j is the molar composition of the micelle due to the other component. Negative values of β are indicative of inter-isomer interactions that stabilize the micelle; no further meaning (if any at all) should be drawn from this crude parameter use. If β is negative the CMCs of the mixed micelles will be lower than those in the ideal mixing case, and can even be lower than the single component CMCs [52]. Activity models that actually describe the relevant physical interactions would in principle be preferable, but the Margules function is helpful for a first attempt.

Typically, values of β are found from measured values of CMC_z. If a single value of β can successfully be used to describe the entire range of measured CMC values, the choice of the Margules function is justified. With azoTAB, CMC_{cis} is also unknown so it is necessary to fit for both CMC_{cis} and β.

In order to use the regular solution approximation, an additional relation is needed to find the compositions within the micelles x_i. This expression is given by Rubingh for a binary mixture of i and j as:

$$\frac{x_i^2 \ln\left(\frac{z_i CMC_z}{x_i CMC_i}\right)}{x_j^2 \ln\left(\frac{z_j CMC_z}{x_j CMC_j}\right)} = 1 \tag{3.22}$$

The results of the fitting are seen in Figure 3-34; the best-fit values of β is -2.1 and that of CMC_{cis} 32 mM. The fit is reasonable, but the fitted values must be used with caution as there is insufficient data at

very high *cis* compositions to constrain the value of CMC_{cis} . The magnitude of β is plausible in comparison to values reported in the literature for other mixed micelles [53].

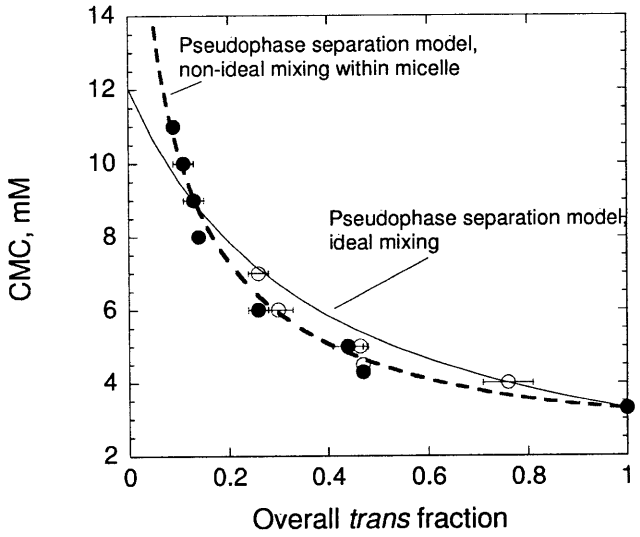

Figure 3-34 Pseudophase separation model for mixed micelles with non-ideal mixing in the micelle. CMC of pure *cis* solutions and single Margules parameter are fit. Ideal-mixing results of Figure 3-33 added for comparison.

Using the pseudophase separation models it is possible to predict a multitude of quantities at any given total concentration and composition, such as the concentration of each monomer and the micelle composition. These calculations are instructive, as these quantities are of interest when describing the mixed micelle system. They can also be compared to estimates from the experimental data in order to further confirm the utility of the model. Using the pseudophase separation [54] model, the monomer concentration of a single component can be written as:

$$C^{b}_{trans} = \frac{-(C_{tot}-\theta)+\left\{(C-\theta)^2+4z_{trans}C_{tot}\theta\right\}^{1/2}}{2\left(\dfrac{\gamma_{cis}CMC_{cis}}{\gamma_{trans}CMC_{trans}}-1\right)} \tag{3.23}$$

where

$$\theta = \gamma_{cis}CMC_{cis} - \gamma_{trans}CMC_{trans} \tag{3.24}$$

The composition within the mixed micelle is given as

$$x_{trans} = \frac{-(C_{tot} - \theta) + \left\{(C_{tot} - \theta)^2 + 4 z_{trans} C_{tot} \theta\right\}^{1/2}}{2\theta} \tag{3.25}$$

Equation (3.25) was used to calculate the micellar composition instead of Equation (3.22), merely out of computational convenience.

The behavior predicted by these models is illustrated in Figure 3-35 and Figure 3-36. Figure 3-35 shows how the monomer concentrations change with total concentration at a fixed overall composition z_{trans} of 0.50. It is important to note that the concentration of monomer is not fixed above the CMC, in sharp contrast to the pseudophase separation behavior of a single surfactant. There is some difference between the non-ideal and ideal mixing models. The mixed CMCs predicted by the two models diverged in the composition range inaccessible by experiment, but these differences in monomer concentrations appear under conditions that can be observed.

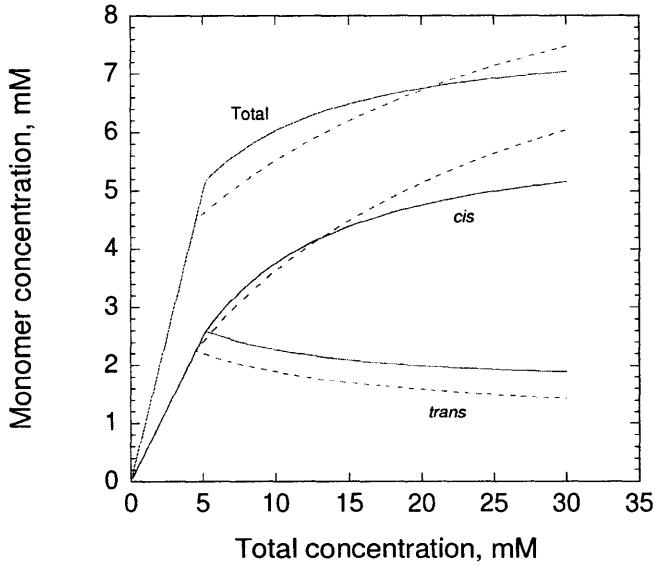

Figure 3-35 Concentrations of *trans* and *cis* monomer for an overall composition $z_{trans} = 0.50$. Solid lines calculated using ideal-mixing model, broken lines from non-ideal model. The CMC of the pure *cis* component is very different in the two cases.

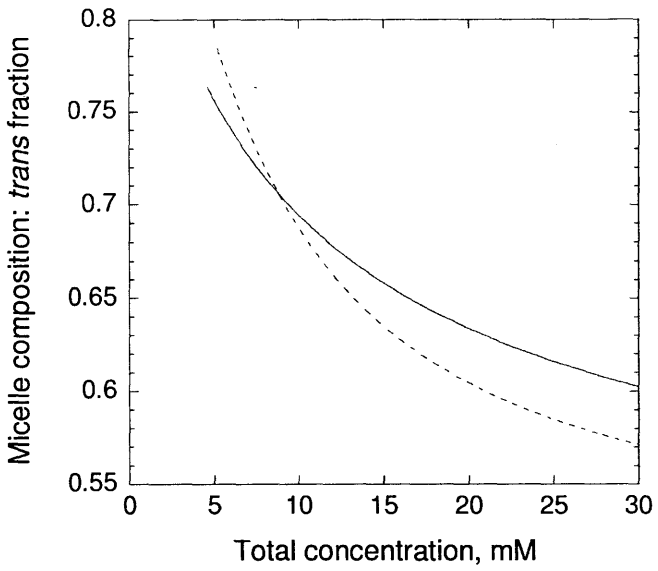

Figure 3-36 Composition of micelles as function of total concentration, calculated at $z_{trans} = 0.50$. Solid curve from ideal mixing model, broken curve from non-ideal model. No micelles are present below the CMC. Micelles are clearly *trans*-rich, particularly near the CMC.

Figure 3-36 shows how the micelle composition changes with increasing total concentration at a given overall composition, 50% *trans*. Compared to this overall composition, the micelle is enriched in *trans* at low concentrations. As the concentration is increased the micelle composition slowly approaches the overall composition.

It should be possible to extract some experimental estimates of the *trans* and *cis* monomer concentrations and the micelle composition from the data shown in Figure 3-28 and Figure 3-29. At any given data point, the following weighted averages must hold:

$$D_{trans}^{obs} = y_{trans}^{mon} D_{trans}^{mon} + y_{trans}^{mic} D^{mic} \tag{3.26}$$

$$D_{cis}^{obs} = y_{cis}^{mon} D_{cis}^{mon} + y_{cis}^{mic} D^{mic} \tag{3.27}$$

and

$$y_i^{mon} + y_i^{mic} = 1 \tag{3.28}$$

where D^{mic} is the diffusivity of the micelles present at that point, and y_i^{mon} is the fraction of component i that resides as monomer. It is assumed *cis* and *trans* form monodisperse mixed micelles. If D^{mon} and

D^{mic} are known, then the mole fractions can be found at any observed point. From here it is trivial to find the micelle composition.

Similar expressions can be written for the NMR chemical shifts:

$$\delta_{trans}^{obs} = y_{trans}^{mon}\delta_{trans}^{mon} + y_{trans}^{mic}\delta_{trans}^{mic} \tag{3.29}$$

$$\delta_{cis}^{obs} = y_{cis}^{mon}\delta_{cis}^{mon} + y_{cis}^{mic}\delta_{cis}^{mic} \tag{3.30}$$

Note that the micelle diffusivity D^{mic} is the same for the two isomers, but the micelle chemical shift is not.

Appropriate values for the bulk monomer can be found below the CMC. There is some difficulty here as the two-site model does not account for any pre-micellar aggregates. It is decided to entirely neglect the pre-micelles, and use diffusivities at infinite dilution as D_i^{mon} and δ_i^{mon}. Since the variations in chemical shift and diffusivity below the CMC are small compared to the change that occurs on micelle formation, this choice is not critical at higher total concentrations.

The micellar values present further difficulties. In the case of a single surfactant, it was reasonably assumed that the same size and type of micelle was present throughout the observed concentration range. The values of D^{mic} and δ^{mic} could therefore be taken as constants. In the case of mixed micelles, the size and composition of the micelles is expected to change as concentration and overall composition are changed. D^{mic} and δ^{mic} are no longer constants, nor is it immediately obvious how to evaluate them.

Some simplifying assumptions must be made in order to proceed. There have been a few similar attempts in the literature to quantitatively describe micelle formation from these NMR measurements. Fang, et al assumed that D^{mic} and the individual monomer concentrations C_i^{mon} were constant as total concentration was increased above the CMC at some fixed overall composition [55]. D^{mic} was then found by fitting against the data. As shown in Figure 3-35, the assumption of constant monomer concentrations above the CMC is inconsistent with models. Misselyn-Bauduin appeared to simply take D^{mic} as the diffusivity measured at high concentrations at the appropriate overall composition, assuming that the remaining monomers make a negligible contribution to the observed diffusivity [56]. This approach can introduce error because the monomer diffusivity is generally an order of magnitude less than the micelle diffusivity, so a small amount of monomer can still influence the observed diffusivity. Amato somewhat unsuccessfully attempted to extrapolate the chemical shift to high concentrations. The

chemical shifts were plotted against the inverse concentration at some fixed overall composition [57]. An extrapolated value of δ_i^{mic} is obtained from the intercept. This method is analogous to that done in this work for the 100% *trans* micelles in the dark-adapted state (Figure 3-18), but is not expected to be successful with mixed micelles. This can be understood by examining the following relation, derived directly from Equation (3.6):

$$\delta^{obs} = \delta_i^{mic} + \left(\delta_i^{mon} - \delta_i^{mic}\right)\frac{C_{mon}}{C_{tot}} \tag{3.31}$$

which can be written for either component, *cis* or *trans*. A plot of δ_{obs} vs $1/C_{tot}$ can be expected to be linear above the CMC if C_{mon} and δ_{mic} are constant as the total concentration is changed. These conditions held for a single component, but as shown in Figure 3-34, C_{mon} is not expected to be constant above the CMC in a mixture of different surfactants.

All of the above approaches from the literature also neglect the difference between the micelle composition and the overall composition; this difference was illustrated in Figure 3-36.

To take this latter effect into account, Inoue suggested an iterative approach [58]. The chemical shift was measured at some overall concentration and composition. An initial value of δ_i^{mic} was taken from observations at high concentrations at the same overall composition. Data were available at high concentrations, such that high concentration asymptotic values were directly used as δ_i^{mic}. A first-pass micelle composition was then calculated at each measured point. A new value of δ_i^{mic} was then found from high concentration observations at that composition. The process was repeated until it converged on some final value of δ_i^{mic}. This iterative method is more rigorous than the others outlined above, but does not seem to have been widely adopted. The iteration is cumbersome as it is not easy to automate, and a very wide range of experimental data is required.

In general, the study of azoTAB mixed micelles is somewhat easier than that in other surfactant pairs, as the use of light can be used to bring about different mixing ratios. The entire composition range at a given total concentration can be studied using a single solution; this is not possible with traditional mixed micelles. The use of light does impose some limitations, however. The previous work of Inoue made use of measurements at differing compositions in solutions of high concentration. These measurements provide limiting values of D^{mic} and δ^{mic}. It is difficult to do such work at very high concentrations of

azoTAB (above 30 mM), since the high total absorbance impedes the photoreaction. To mitigate this issue, samples were irradiated in vessels with low path length, but it appeared that the lack of stirring reduced the photoconversion rate. The Krafft point also limits the concentration range available; some precipitate appears over time in 60 mM solutions. Ultimately, a limited amount of diffusivity data and a wider range of chemical shift data were collected at 30 mM for possible use as limiting values of D^{mic} and δ^{mic} (see Figure 3-37).

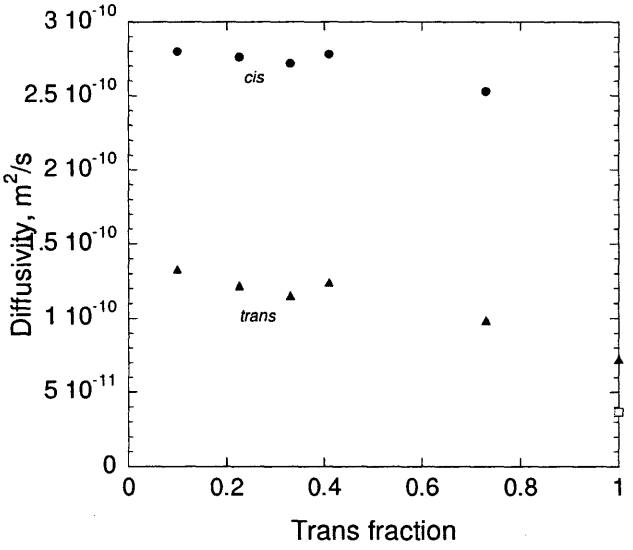

Figure 3-37 *Trans* and *cis* diffusivities measured in 30 mM azoTAB solution. *Cis* in blue, *trans* in red. Hollow marker for the previously extrapolated value of the *trans* micelle diffusivity.

The diffusion coefficients of both isomers are below the values typically seen below the CMC (about $4*10^{-10}$ m^2/s), so it appears that mixed micelles are present over the entire measured range. However the previously extrapolated micelle diffusivity from the dark-adapted state is significantly slower than the observed diffusivities; the monomer diffusivity is so much faster than the micelle that small amounts of monomer have an impact on the observed diffusion. It is thus decided to use the extrapolated dark-state diffusivity as the micelle diffusivity in all cases. This assumption introduces some error due to the possible dependence of micelle size on micelle composition. This error may be significant in any regime where the micelles are rich in *cis*. Using diffusion coefficients measured at 6, 10 and 30 mM over a range of light conditions (see Figure 3-29), micelle compositions were thus computed. These compositions were found by applying Equations (3.26) and (3.27) to each data point. Then, the concentration of *trans* and *cis* existing within micelles was found from $y_i^{mic} z_i C_{tot}$, where z_i is the fraction of azoTAB existing as isomer i. Finally, the composition within the micelle is

$$x_i = \frac{y_i^{mic} z_i C_{tot}}{\sum_j y_j^{mic} z_j C_{tot}} \tag{3.32}$$

The resulting micellar compositions are compared to model predictions in Figure 3-38.

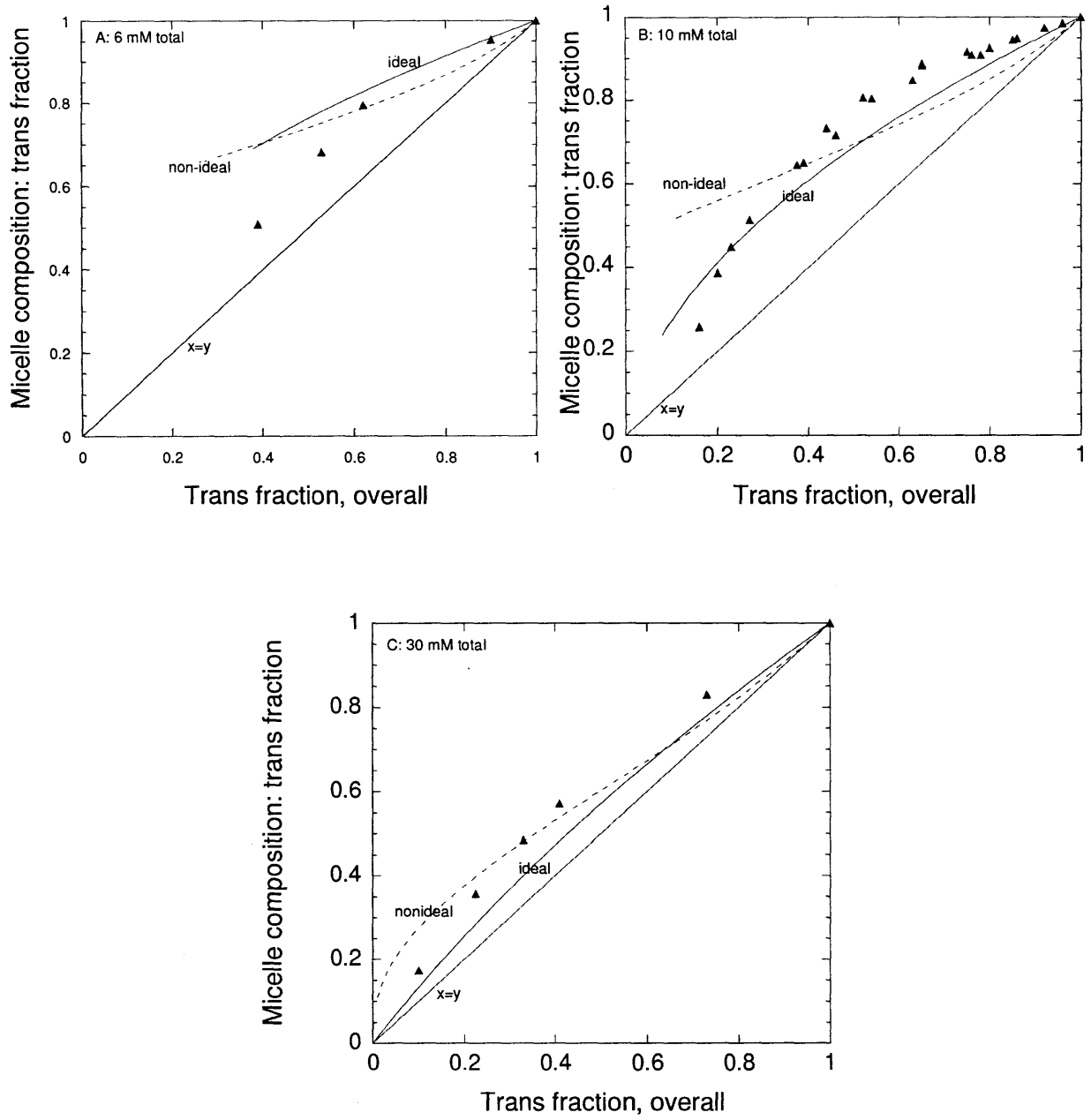

Figure 3-38 Composition of micelle as a function of overall isomer composition, at 6, 10 and 30 mM azoTAB. Measured points taken from diffusivity data as described in text. Line for y=x added to emphasize that micelles are *trans*-rich. Results of non-ideal mixing model shown as broken line, and ideal model as solid line.

In each case the micelle is enriched in *trans*, compared to the overall composition of the solution. Particularly at the higher concentrations, the results are in decent agreement with the model predictions. The ideal mixing model appears to describe the data better than the non-ideal model, so it will be adopted for the remainder of this work. The error due to the multiple assumptions involved likely causes the discrepancy between model and experiment at the lower concentration. At 6 mM, the monomer

diffusivity is of greater importance in the calculations, and so pre-micellar aggregates are relatively more important. Adding a third site for these clusters would be beneficial, but difficult due to reasons already discussed.

3.3.5. System kinetics

Some observations can be made about the overall kinetics of the surfactant system. The various diffusivities and chemical shifts reported above appear to be entirely dependent on the isomer composition and total concentration; the elapsed time after irradiation appears to have little effect. For example the irradiation time increments between the data points shown in Figure 3-28 can be as low as 5 to 10 seconds, with the NMR measurement itself requiring at least 4 minutes. The chemical shifts found in this manner are equal to those found in solutions of identical composition which have been at rest for longer periods of time. This equivalency suggests that there is no unusually slow response of the micelles to changes in isomer composition. The kinetics of micelle formation would not appear to be rate-controlling. The photoreaction rate in the system also appears to be unaffected by the presence of micelles, as shown in the previous Chapter. The rate law and parameters found below the CMC also appear to be valid above the CMC, though the presence or absence of convective mixing within the sample is critical. The effect of mixing is examined in Chapter 4.

3.4 Conclusions

The micelles that form in mixtures of *trans* and *cis* azoTAB have been characterized using a variety of experimental methods. The pseudophase separation model is found to be satisfactory in describing the characteristics of the pure *trans* system, particularly the dependence of monomer concentration on total concentration. The mass action model provided a lower limit on the micelle aggregation number. It has not been possible to isolate pure *cis* azoTAB, nor detect micelles in the UV photostationary state (3% *cis*). In both the dark- and UV-adapted states, pre-micellar aggregates are evident. The CMC has been found over a range of intermediate compositions, and the CMC values are reasonably well described by using the classical pseudophase separation model for mixed micelles. A multitude of observations suggest that any mixed micelles are particularly rich in *trans*, and these observations are consistent with the pseudophase separation model. Overall, it has been demonstrated that chemical shift and diffusivity data can be used to describe the state of the system, including monomer concentrations and the composition of any micelles. The application of these techniques to a mixed micelle system that can be internally altered by light may be novel. The tools developed will also be helpful in analyzing the interactions between azoTAB and polymers.

3.5 Works cited

1. Tanford, *The Hydrophobic Effect: Formation of Micelles and Biological Membranes.* 1980: Wiley.
2. Bossev, D.P., M. Matsumoto, and M. Nakahara, *F-19 Nmr Study of Molecular Aggregation of Lithium Perfluorooctylsulfonate in Water at Temperatures from 30 to 250 Degrees C.* Journal of Physical Chemistry B, 2000. **104**(2): p. 155-158.
3. Muller, N. and R.H. Birkhahn, *Investigation of Micelle Structure by Fluorine Magnetic Resonance .I. Sodium 10 10 10-Trifluorocaprate and Related Compounds,* Journal of Physical Chemistry, 1967. **71**(4): p. 957-&.
4. Muller, N. and F.E. Platko, *Investigation of Micelle Structure by Fluorine Magnetic Resonance .4. Fluorine-Labeled Nonionic Detergents,* Journal of Physical Chemistry, 1971. **75**(4): p. 547-&.
5. Fendler, J.H., E.J. Fendler, R.T. Medary, and O.A. Elseoud, *Proton Magnetic-Resonance Investigations of Formation of Alkylammonium Propionate Micelles in Benzene and in Carbon-Tetrachloride,* Journal of the Chemical Society-Faraday Transactions I, 1973. **69**(2): p. 280-288.
6. Drakenbe.T and B. Lindman, *C-13 Nmr of Micellar Solutions,*Journal of Colloid and Interface Science, 1973. **44**(1): p. 184-186.
7. Persson, B.O., T. Drakenberg, and B. Lindman, *Amphiphile Aggregation Number and Conformation from C-13 Nuclear Magnetic-Resonance Chemical-Shifts,* Journal of Physical Chemistry, 1976. **80**(19): p. 2124-2125.
8. Ulmius, J., B. Lindman, G. Lindblom, and T. Drakenberg, *H-1,C-13,Cl-35, and Br-81 Nmr of Aqueous Hexadecyltrimethylammonium Salt-Solutions - Solubilization, Viscoelasticity, and Counterion Specificity.* Journal of Colloid and Interface Science, 1978. **65**(1): p. 88-97.
9. Persson, B.O., T. Drakenberg, and B. Lindman, *C-13-Nmr of Micellar Solutions - Micellar Aggregation Number from the Concentration-Dependence of the C-13 Chemical-Shifts,*Journal of Physical Chemistry, 1979. **83**(23): p. 3011-3015.
10. Soderman, O., *On the Determination of Micellar Aggregation Numbers from the Concentration-Dependence of C-13 Nmr Chemical-Shifts,* Colloid and Polymer Science, 1987. **265**(1): p. 76-82.
11. Lee, Y.S. and K.W. Woo, *Micellization of Dodecyltrimethylammonium Bromide in D2o as Probed by Proton Longitudinal Magnetic-Relaxation and Chemical-Shift Measurements,* Bulletin of the Korean Chemical Society, 1993. **14**(3): p. 392-398.
12. Das, S., R.G. Bhirud, N. Nayyar, K.S. Narayan, and V.V. Kumar, *Chemical-Shift Changes on Micellization of Linear Alkyl Benzenesulfonate and Oleate,* Journal of Physical Chemistry, 1992. **96**(18): p. 7454-7457.
13. Ruso, J.M., D. Attwood, P. Taboada, V. Mosquera, and F. Sarmiento, *Light Scattering and Nmr Studies on the Self-Aggregation of Sodium N-Hexyl Sulfate in Aqueous Electrolyte Solution.* Langmuir, 2000. **16**(4): p. 1620-1625.
14. Lawson, K.D. and T.J. Flautt, *Measurement of Spin-Lattice Relaxation Times of Dimethyloctylamine Oxide through Critical Micelle Concentration,* Journal of Physical Chemistry, 1965. **69**(9): p. 3204-&.
15. Clifford, J., *Properties of Micellar Solutions .4. Spin Lattice Relaxation Times of Hydrocarbon Chain Protons in Solutions of Sodium Alkyl Sulphates,*Transactions of the Faraday Society, 1965. **61**(510P): p. 1276-&.
16. Odberg, L. and B. Svens, *Association of Short Chain Alkanoates as Studied by Nmr Methods,*Journal of Colloid and Interface Science, 1972. **41**(2): p. 298-&.

17. Wennerstrom, H., B. Lindman, O. Soderman, T. Drakenberg, and J.B. Rosenholm, *C-13 Magnetic-Relaxation in Micellar Solutions - Influence of Aggregate Motion on T1,* Journal of the American Chemical Society, 1979. **101**(23): p. 6860-6864.
18. Staples, E.J. and G.J.T. Tiddy, *Nuclear Magnetic-Resonance Technique to Distinguish between Micelle Size Changes and Secondary Aggregation in Anionic and Non-Ionic Surfactant Solutions,*Journal of the Chemical Society-Faraday Transactions I, 1978: p. 2530-2541.
19. Stilbs, P. and B. Lindman, *Determination of Organic Counterion Binding to Micelles through Fourier-Transform Nmr Self-Diffusion Measurements,*Journal of Physical Chemistry, 1981. **85**(18): p. 2587-2589.
20. Jansson, M. and P. Stilbs, *A Comparative-Study of Organic Counterion Binding to Micelles with the Fourier-Transform Nmr Self-Diffusion Technique,*Journal of Physical Chemistry, 1985. **89**(22): p. 4868-4873.
21. Jansson, M. and P. Stilbs, *Organic Counterion Binding to Micelles - Effects of Counterion Structure on Micellar Aggregation and Counterion Binding and Location,*Journal of Physical Chemistry, 1987. **91**(1): p. 113-116.
22. Li, P., M. Jansson, P. Bahadur, and P. Stilbs, *Nmr-Study of Organic Counterion Binding and Micellization of Decylammonium Dicarboxylate Surfactants,* Journal of Physical Chemistry, 1989. **93**(17): p. 6458-6463.
23. Lindman, B., M.C. Puyal, N. Kamenka, R. Rymden, and P. Stilbs, *Micelle Formation of Anionic and Cationic Surfactants from Fourier-Transform H-1 and Li-7 Nuclear Magnetic-Resonance and Tracer Self-Diffusion Studies,*Journal of Physical Chemistry, 1984. **88**(21): p. 5048-5057.
24. Soderman, O. and P. Stilbs, *Nmr-Studies of Complex Surfactant Systems,*Progress in Nuclear Magnetic Resonance Spectroscopy, 1994. **26**: p. 445-482.
25. C. Ted Lee, J., Kenneth A. Smith and T. Alan Hatton, *Small-Angle Neutron Scattering Study of the Micellization of Photosensitive, Surfactants in Solution and in the Presence of a Hydrophobically Modified Polyelectrolyte.* Langmuir, 2009. **25**: p. 13784–13794.
26. Lee, C.T., K.A. Smith, and T.A. Hatton, *Photoreversible Viscosity Changes and Gelation in Mixtures of Hydrophobically Modified Polyelectrolytes and Photosensitive Surfactants.* Macromolecules, 2004. **37**(14): p. 5397-5405.
27. Hugo Gottlieb, V.K.a.A.N., *Nmr Chemical Shifts of Common Laboratory Solvents as Trace Impurities.* J. Org. Chem, 1997. **62**: p. 7512-7515.
28. Derome, A., *Modern Nmr Techniques for Chemistry Research.* 1987.
29. Pelta, M.D., H. Barjat, G.A. Morris, A.L. Davis, and S.J. Hammond, *Pulse Sequences for High-Resolution Diffusion-Ordered Spectroscopy (Hr-Dosy).* Magnetic Resonance in Chemistry, 1998. **36**(10): p. 706-714.
30. Wu, D.H., A.D. Chen, and C.S. Johnson, *An Improved Diffusion-Ordered Spectroscopy Experiment Incorporating Bipolar-Gradient Pulses,*Journal of Magnetic Resonance Series A, 1995. **115**(2): p. 260-264.
31. Weingartner, M.H.a.H., *Calibration in Accurate Spin-Echo Self-Diffusion Measurements Using 1h and Less-Common Nuclei.* Journal of Magnetic Resonance, 1991. **92**: p. 115-125.
32. Weingartner, H., *Diffusion in Liquid Mixtures of Light and Heavy Water.* Ber. Bunsenges. Phys. Chem, 1984. **88**: p. 47-50.
33. Findeisen, M., T. Brand, and S. Berger, *A H-1-Nmr Thermometer Suitable for Cryoprobes.* Magnetic Resonance in Chemistry, 2007. **45**(2): p. 175-178.
34. Berger, S.a.B.S., *200 and More Nmr Experiments.* 2004: Wiley.
35. Sackett, D.L. and J. Wolff, *Nile Red as a Polarity-Sensitive Fluorescent-Probe of Hydrophobic Protein Surfaces,*Analytical Biochemistry, 1987. **167**(2): p. 228-234.
36. Hayashita, T., T. Kurosawa, T. Miyata, K. Tanaka, and M. Igawa, *Effect of Structural Variation within Cationic Azo-Surfactant Upon Photoresponsive Function in Aqueous Solution.* Colloid and Polymer Science, 1994. **272**(12): p. 1611-1619.

37. Shimizu, S., P.A.R. Pires, and O.A. El Seoud, *H-1 and C-13 Nmr Study on the Aggregation of (2-Acylaminoethyl)Trimethylammonium Chloride Surfactants in D2o.* Langmuir, 2003. **19**(23): p. 9645-9652.
38. Mukerjee, P., P. Kapauan, and H.G. Meyer, *Micelle Formation and Hydrophobic Bonding in Deuterium Oxide,*Journal of Physical Chemistry, 1966. **70**(3): p. 783-&.
39. Greenspan, P. and S.D. Fowler, *Spectrofluorometric Studies of the Lipid Probe, Nile Red.* Journal of Lipid Research, 1985. **26**(7): p. 781-789.
40. Stark, R.E., R.W. Storrs, and M.L. Kasakevich, *Nuclear Magnetic-Resonance Studies of Solubilization in Omega-Phenylalkanoate-Sds Mixtures.* Journal of Physical Chemistry, 1985. **89**(2): p. 272-277.
41. Landry, J.M., D.G. Marangoni, M.D. Lumsden, and R. Berno, *1d and 2d Nmr Investigations of the Micelle-Formation Process in 8-Phenyloctanoate Micelles.* Canadian Journal of Chemistry-Revue Canadienne De Chimie, 2007. **85**(3): p. 202-207.
42. Wang, T.Z., S.Z. Mao, X.J. Miao, S. Zhao, J.Y. Yu, et al., *H-1 Nmr Study of Mixed Micellization of Sodium Dodecyl Sulfate and Triton X-100.* Journal of Colloid and Interface Science, 2001. **241**(2): p. 465-468.
43. Mallion, J.A.N.F.G.a.R.B., *Aromaticity and Ring Currents.* Chem. Rev., 2001. **101**: p. 1349-1383.
44. Hada, S., S. Ishikawa, S. Neya, and N. Funasaki, *Dimerization and Alpha-Cyclodextrin Inclusion of Propantheline Bromide as Studied by Nmr and Molecular Modeling.* Journal of Physical Chemistry B, 1999. **103**(13): p. 2579-2584.
45. R. Atkin, V.S.J.C., E.J. Wanless and S. Biggs, *The Influence of Chain Length and Electrolyte on the Adsorption Kinetics of Cationic Surfactants at the Silica-Aqueous Solution Interface.* Journal of Colloid and Interface Science, 2003. **266**: p. 236-244.
46. Jones, G. and H.J. Fornwalt, *The Viscosity of Deuterium Oxide and Its Mixtures with Water at 25 Degrees C.* Journal of Chemical Physics, 1936. **4**(1): p. 30-33.
47. C. Ted Lee, J., Kenneth A. Smith and T. Alan Hatton, *Small-Angle Neutron Scattering Study of the Micellization of Small-Angle Neutron Scattering Study of the Micellization of Hydrophobically Modified Polyelectrolyte.* Langmuir, 2009. **25**: p. 13784–13794.
48. Cussler, E.L., *Diffusion: Mass Transfer in Fluid Systems.* 1984: Cambridge University Press.
49. Blanshard, A.H.M.a.J.M., *Diffusion in Gels.* Polymer, 1982. **23**: p. 1012-1026.
50. Boucher, G.D., A.C. MacDonald, B.E. Hawrylak, and D.G. Marangoni, *A Nuclear Magnetic Resonance Investigation of the Micellar Properties of Two-Headed Surfactant Systems: The Disodium 4-Alkyl-3-Sulfonatosuccinates. 1. Equilibrium Micellar Properties.* Canadian Journal of Chemistry-Revue Canadienne De Chimie, 1998. **76**(9): p. 1266-1273.
51. Chokappa, D.K. and S. Das, *Calculation of Micellar Aggregation Number from the Concentration-Dependence of Nmr Chemical-Shifts,*Indian Journal of Chemistry Section a-Inorganic Bio-Inorganic Physical Theoretical & Analytical Chemistry, 1994. **33**(9): p. 795-800.
52. Clint, J.H., *Micellization of Mixed Nonionic Surface-Active Agents,*Journal of the Chemical Society-Faraday Transactions I, 1975. **71**(6): p. 1327-1334.
53. Holland, P.M. and D.N. Rubingh, *Nonideal Multicomponent Mixed Micelle Model,*Journal of Physical Chemistry, 1983. **87**(11): p. 1984-1990.
54. Nishikido, N., *Thermodynamic Models for Mixed Micellization*, in *Mixed Surfactant Systems*, K.O.a.M. Abe, Editor. 1993, Marcel Dekker: New York.
55. Fang, X.W., S. Zhao, S.Z. Mao, J.Y. Yu, and Y.R. Du, *Mixed Micelles of Cationic-Nonionic Surfactants: Nmr Self-Diffusion Studies of Triton X-100 and Cetyltrimethylammonium Bromide in Aqueous Solution.* Colloid and Polymer Science, 2003. **281**(5): p. 455-460.
56. Misselyn-Bauduin, A.M., A. Thibaut, J. Grandjean, G. Broze, and R. Jerome, *Mixed Micelles of Anionic-Nonionic and Anionic-Zwitterionic Surfactants Analyzed by Pulsed Field Gradient Nmr.* Langmuir, 2000. **16**(10): p. 4430-4435.

57. Amato, M.E., E. Caponetti, D.C. Martino, and L. Pedone, *H-1 and F-19 Nmr Investigation on Mixed Hydrocarbon-Fluorocarbon Micelles.* Journal of Physical Chemistry B, 2003. **107**(37): p. 10048-10056.
58. Nakagawa, H.I.a.T., *Shift of Nuclear Magnetic Resonance Signal Caused by Micelle Formation. Ii. Micelle Structure of Mixed Surfactants.* J Phys Chem, 1966. **70**: p. 1108-1113.

Chapter 4

Photoresponsive Gelation

4.1 Introduction

Gels are materials that have attracted significant attention in recent years because of their possible applications in areas such as drug delivery, chemical sensors, contact lenses, electrophoresis, rheology modification and superabsorbency. A gel can be broadly defined as a polymer network of macroscopic dimensions, swollen with solvent. The network is formed when there is sufficient cross-linking between individual polymer coils such that the resulting structure spans distances that can be described as infinite, relative to the dimensions of the original coils. These crosslinks may be formed by covalent chemical bonds or physical interactions. Physical gels are of particular interest because the crosslinks can be designed to reversibly form or dissolve in response to external stimuli, such as heat, pH or light. The use of light is advantageous as it is chemically non-invasive and it offers a high degree of spatial control. The current work thus concentrates on a photoresponsive gel system. It consists of a mixture of a hydrophobically modified polymer and the photosensitive surfactant described in the previous chapters. The surfactant and the hydrophobic groups of the polymer form aggregates which can be formed or dissolved based on the wavelength of incident light. The aggregates serve to crosslink neighboring polymer coils, forming a network. NMR chemical shift and diffusion measurements are used to explore the nature of the polymer-surfactant interactions, the kinetics of the conversion between gel and solution states, and the transport of solute particles through the gel.

4.2 Background

4.2.1. Examples of chemically crosslinked responsive gels

Responsive gels are gels that respond in some way to changes in their environment. The most widely studied response is a change in the swollen volume of a chemically-crosslinked gel upon a change in temperature [1-3], pH [3-6] or light radiation [7-10]. A number of different applications have been proposed for responsive gels. These include use as actuators (such as artificial muscles), sensors, devices

for controlled drug delivery, optical switches, rheology modifiers, microfluidic valves, enhanced molecular separation systems, and tools for oil recovery.

The basis for many of these volume phase transitions is in the solution properties of the original polymer, prior to any crosslinking. For example poly N-isopropylacrylamide (pNIPAM) exhibits a lower critical solution temperature (LCST) in water, such that pNIPAM phase separates out of water at elevated temperatures and reenters into solution upon cooling [1, 2, 11]. Water remains a good solvent for crosslinked pNIPAM at low temperatures, so a swollen gel results. The gel then rejects solvent and collapses when heated above the phase transition temperature. The accompanying change in the mass of water retained by the gel can be several orders of magnitude. Similar transitions have been induced by changes in the solvent composition [12], or changes in temperature due to light irradiation [10].

Other classes of responsive gels can be built by crosslinking polymers comprised of weak acids, such as polyacrylic acid [5]. These gels expand and contract with changes in the pH, which modulates the ionization of the acid groups. The resulting variation in repulsive electrostatic forces between repeat units as well as changes in the osmotic pressure leads to swelling or collapse.

Stimulus-sensitive functional groups can also be incorporated into the chemical crosslinker. As discussed in previous chapters, azobenzene changes conformation upon light irradiation. When azobenzene is incorporated in the crosslinking agent, the entire gel expands or contracts under light, thus expelling or absorbing water [8].

4.2.2. Polymer-surfactant interactions

Mixtures of surfactant and polymer have been used in applications as diverse as paints, detergency, shampoos, foods, and oil recovery. The interactions between the two can also be exploited to design reversible gels. As discussed extensively in Chapter 2, surfactants in aqueous solution may form micelles when the surfactant concentration exceeds the CMC (critical micelle concentration). If polyelectrolytes are mixed with oppositely charged surfactants, analogous behavior may be seen. When surfactant is added at low concentrations, it will exist either free in solution or electrostatically bound to the polymer. This binding is not cooperative, meaning each surfactant molecule behaves independently of any others. As the surfactant concentration is increased past a critical aggregation concentration (CAC), the surfactants cooperatively form micelles that are enwrapped by the oppositely charged polymer [13-24]. The resulting complex can be envisioned as a necklace, with micelles acting as beads along the polymer string [16, 21, 25]. Evidence for this aggregation has been found using a variety of experimental

techniques, including light scattering [23], fluorescent probes [13, 17, 23], NMR [13, 26, 27], surfactant specific electrodes [28, 29] and neutron scattering [21]. The wrapping interaction between polymer and micelle may also lead to a reduction in polymer coil dimensions, as seen through a reduction in solution viscosity [30] and as measured using light scattering [31]. This change in dimensions can be observed in dilute polymer solutions.

Polymer-surfactant systems exhibit complicated phase behavior as the surfactant concentration is raised above the CAC. As the molar ratio of surfactant and polymer charged groups approaches 1:1, phase separation occurs and neutralized polymer-surfactant complexes exit the solution [13, 18, 21, 26]. This phase boundary is sometimes denoted as the charge neutralization concentration (CNC). Upon adding an excess of surfactant, a single isotropic phase is again observed. While it may be of use in other applications, phase separation should be avoided in the development of the reversible gels described in this work.

Surfactant aggregate formation is more favored in the presence of oppositely charged polymer than in solutions of surfactant alone. This difference is made clear by observations that the CAC is generally lower than the CMC, sometimes by as many as two decades [20, 21, 28, 32]. The extra electrostatic interactions in the polymer-surfactant system may help stabilise the micelles [33], but the low CAC is often interpreted as being at least in part an entropic effect [17-20, 23, 33]. Micelle formation is itself entropically driven, due to water molecules being more free to arrange themselves for hydrogen bonding when the surfactant hydrophobic tails are removed from contact with the water [34]. This gain in entropy upon micellization outweighs the accompanying entropy loss due to the segregation of surfactant from water, as well as the concentrating of surfactant counterions in the double layer around the micelle. The addition of polyelectrolyte makes micelle formation yet more entropically favorable because the polymer serves as a giant multivalent counterion for the surfactants. A large number of small counterions that were otherwise associated with surfactant or polymer are released into the bulk solution upon aggregation. There is some support for this interpretation, as the model due to Hansson which accounts for these effects is in qualitative agreement with experimental results [18]. The release of the polymer counterions into bulk solution has been directly observed through use of ion-specific electrodes [19, 20]. Titration calorimetry indicates that the aggregation process is at least in some cases endothermic, thus suggesting that entropic effects are important [19].

The CAC has also been observed to increase as the polymer concentration or the polymer charge density is raised [24, 35]. This effect is predicted by the model of Hansson [18], and is also interpreted in terms of entropy. At high polyelectrolyte concentrations, the released counterions of the polymer have a higher

final concentration in the bulk solution than in the case of dilute polyelectrolyte. This difference in bulk concentration corresponds with a reduction in the entropy gain due to the release of the counterions.

Polymer-surfactant interactions are not limited to those discussed above, as binding and micelle formation also occurs in systems with non-ionic polymer and ionic surfactant [14, 25, 36, 37]. The polymer is thought to reduce the interfacial tension between water and micelle by lessening the contact between the hydrophobic micellar core and the solvent [14]. Polar interactions should also stabilise the polymer-surfactant association. Hydrophobic interactions may also play a role, as association between cationic surfactants and non-ionic poly(ethylene oxide) (PEO) is observed only at higher temperatures, at which PEO has a more hydrophobic nature [36]. Other physical aspects of the system such as polymer chain flexibility can also affect aggregation and the CAC[21]. Polymers-surfactant systems are thus influenced by a subtle mixture of interactions that can be expected to change with the nature of the components and their concentrations.

4.2.3. Hydrophobically modified polymers

The polymer can be given further useful properties through hydrophobic modification. Hydrophobic groups are grafted onto the original water-soluble polymer as side chains. The resulting polymer is still soluble in water, but the side chains have a tendency to aggregate into micelle-like structures. These aggregates can be either intra- or inter-polymer in nature; the latter can result in a cross-linked gel. Hydrophobically modified polymers (HMP) are also known in the literature as associating polymers and polysoaps. Several different polymers have been modified in this way, such as polyacrylamides [38, 39], polyethylene glycol [40] and hydroxyethyl cellulose [41], but this work will focus on hydrophobically modified polyacrylic acid (HMPAA) [42], pictured in Figure 4-1.

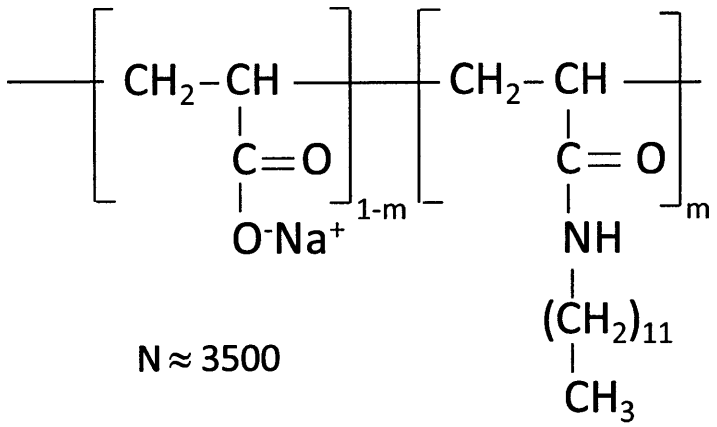

Figure 4-1 Structure of HMPAA as used in this work. 3% of repeat units are hydrophobically modified (m). On average each polymer coil has 3500 repeat units. The formula weights of unmodified and modified repeat units are 94 and 239 daltons, respectively. The unit formula weight in the original acid form is 72.

HMPAA is formed by grafting alkyl amines onto polyacrylic acid (PAA) through amidation; the side chains are typically chosen to be between 12 and 18 carbons in length. Anywhere from 1% to 10% of the PAA repeat units are modified, and the locations of the side chains are randomly distributed throughout the polymer coil [43]. HMPAA is often used with the remaining acid groups neutralized to the sodium salt form. The pK_a of PAA is 4.7 [44], so the sodium salt is easily achieved at neutral or higher pH through the addition of sodium hydroxide.

Aggregation of HMPAA is demonstrated through rheological measurements, in comparison to the sodium salt of unmodified polymer, Na-PAA [42]. At low concentrations, HMPAA solutions have a slightly lower viscosity than Na-PAA solutions. The slight reduction in viscosity is attributed to intra-coil aggregation, which causes to polymer coil to contract. Above some critical polymer concentration (~1-3 wt%), inter-coil aggregation becomes apparent and the viscosity of the HMPAA can be two to three orders of magnitude higher than that of Na-PAA. As the level of hydrophobic modification is increased, the viscosity at any given polymer concentration is also increased. Fluorescent probes have also been used to confirm the formation of these hydrophobic domains [45]. The solutions are shear-thinning, in that the physical interactions holding the polymers together are disrupted at high shear rates [3].

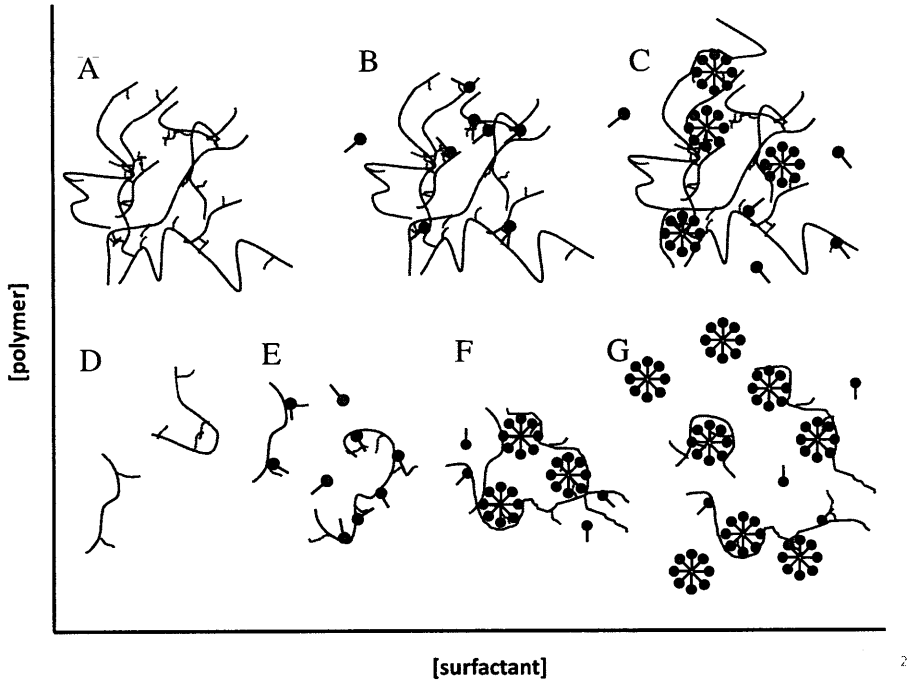

Figure 4-2 Possible arrangements in aqueous mixtures of hydrophobically modified polymer and oppositely charged surfactant. Hydrophilic polymer backbone shown in blue, and 'sticky' hydrophobic grafts in red. Possible variations in structure with changing polymer and surfactant concentration are shown. The length of the original polymer coils, the fraction of modified repeat units and the addition of other salts will also affect the observed structures. Not shown is phase separation possible in nearly equimolar mixtures of polymer and surfactant charged groups. See text for further discussion.

4.2.4. Mixtures of hydrophobically modified polymers and surfactants

The tendency of HMPs to form aggregates leads to interesting behavior in their mixtures with oppositely-charged surfactants. Some of the structures and domains that are possible in these mixtures are illustrated in Figure 4-2. In the absence of any surfactant, inter- and intra- polymer aggregates form in concentrated and dilute polymer solutions. These are shown in Figure 4-2A and D, respectively. As surfactant is added to the HMPAA solution, there is at first some non-cooperative binding. Individual surfactant molecules can bind to polymer, possibly preferentially at the side chains (Figure 4-2E). If the polymer concentration is high enough that the side chains have formed hydrophobic domains, the surfactant molecules may incorporate into those structures (B). Above a certain surfactant concentration (the CAC), cooperative aggregation sets in and mixed micelles dominated by surfactant molecules appear (Figure 4-2C and F). Similarly to systems with unmodified polymer, the CAC generally occurs below the CMC [45], but the transition may be less sharp when modified polymer is used [45]. Figure 4-2 also qualitatively reflects the elevation of the CAC with increasing polymer concentration.

The aggregation in such a system is driven by the same electrostatic, interfacial and entropic effects as in case with unmodified polymer, with the addition of the hydrophobic effect leading to the inclusion of side chains in the micelles. The polymer is cross-linked if each micelle on average incorporates side chains from more than one coil. As the surfactant concentration is further increased, the number of crosslinking micelles also increases, leading to an increase in viscosity and gelation.

Upon addition of sufficient surfactant, the number density of micelles can be so high that each micelle contains on average fewer than two polymer side chains. At this point, the micelles no longer serve as effective crosslinking sites and the polymer network breaks apart (Figure 4-2G) [31, 46]. Phase separation due to charge neutralization is also observed as the surfactant concentration is increased, though there is again a single phase when there is a molar excess of surfactant charge [26, 31]. Under conditions of excess surfactant, free micelles will observed in addition to those bound to the polymer (Figure 4-2G).

Rheological evidence for this progression of structures is available in the literature and an example is given in Figure 4-3 [46]. Interestingly there is evidence for polymer-surfactant interactions even when the polymer and surfactant have like charge. In this case, strong repulsive electrostatic forces are overcome by hydrophobic interactions to allow some degree of polymer-surfactant aggregation.

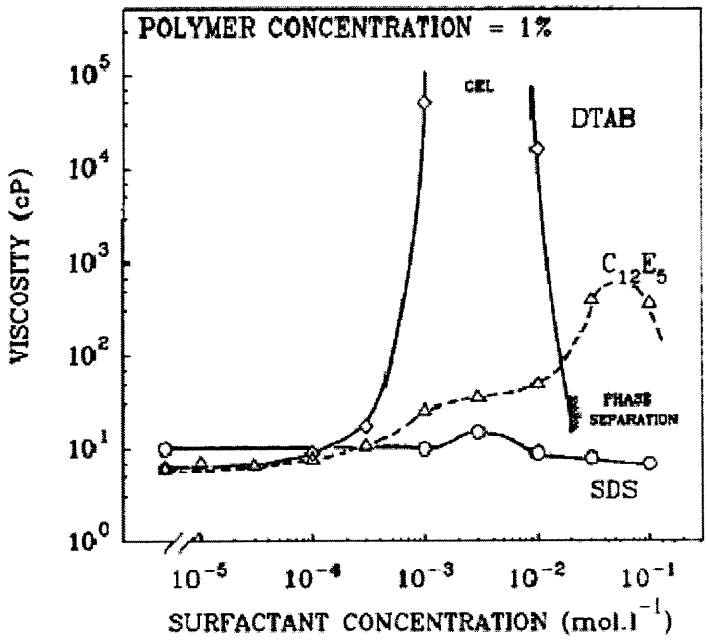

Figure 4-3 Viscosity of aqueous solutions of HMPAA with different surfactants: cationic (DTAB, dodecyltrimethylammonium bromide), nonionic ($C_{12}E_5$, pentaethylene glycol monodecyl ether) and anionic (SDS, sodium dodecyl sulfate). The polymer concentration is fixed. The original PAA has a molecular weight

of 150,000 daltons, which is smaller than that used in this work. The side chains have 18 carbons, and 1% of repeat units are modified. Taken directly from [46].

Similar behavior [47] has been demonstrated for aqueous mixtures of HMPAA and the photosensitive azoTAB surfactant [48] described in the previous chapters. azoTAB exists in two different isomers, *trans* and *cis*, and conversion between the two is achieved by irradiation. UV-irradiation favors the formation of *cis*, whereas visible light drives conversion towards *trans*. The *trans* form is also more stable, so samples isolated in the dark eventually revert to all *trans*. The *trans* form is more hydrophobic and packs more easily into micellar structures, so it has a lower CMC than the *cis* form. When mixed with HMPAA, the two isomers also exhibit different CACs. A mixture at appropriate concentrations can thus be switched between a viscous gel state and a relatively un-crosslinked solution state simply by use of light (see Figure 4-4).

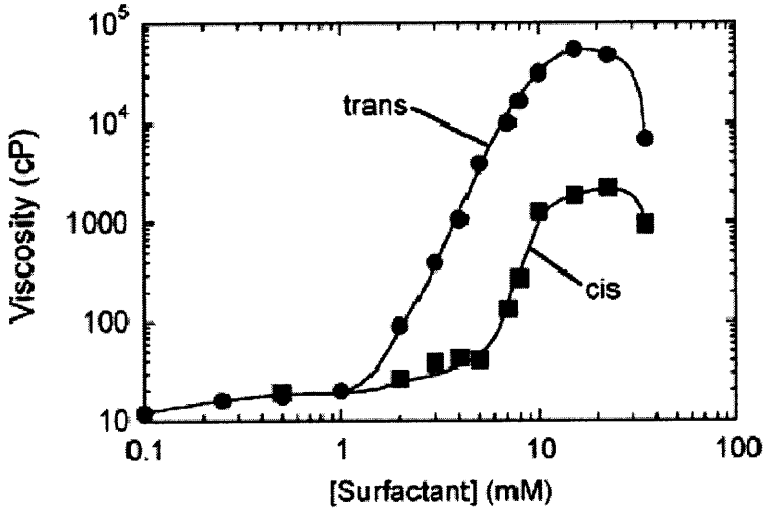

Figure 4-4 Viscosity of HMPAA-azoTAB system. HMPAA concentration is fixed at 2.5 wt%. Taken from Lee et al [47]

It can be seen in Figure 4-4 that the maximum viscosity in the *trans* form is higher than that in the *cis* form, suggesting that the *trans* micelles are more stable than the *cis*, leading to stronger micelles. The fully extended *trans* form of the surfactant is about the same length as the solubilized alkyl side chains, whereas the *cis* form is shorter. It has been shown that the formation of mixed micelles is enhanced when the constituents are of comparable length [49]. In addition, the packing of the surfactant molecules in micelles may be more efficient in the *trans* conformation, which would also make that form more stable.

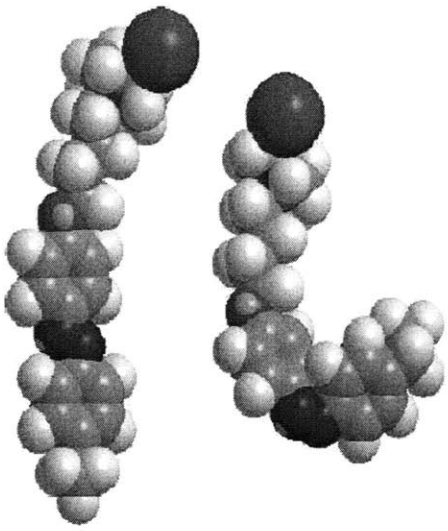

Figure 4-5 Space-filling models of *trans* and *cis* azoTAB. The kinked shape of the *cis* may prohibit efficient packing into well-ordered micelles.

The physical structures which may be present in the HMPAA-azoTAB system are summarized in Figure 4-6:

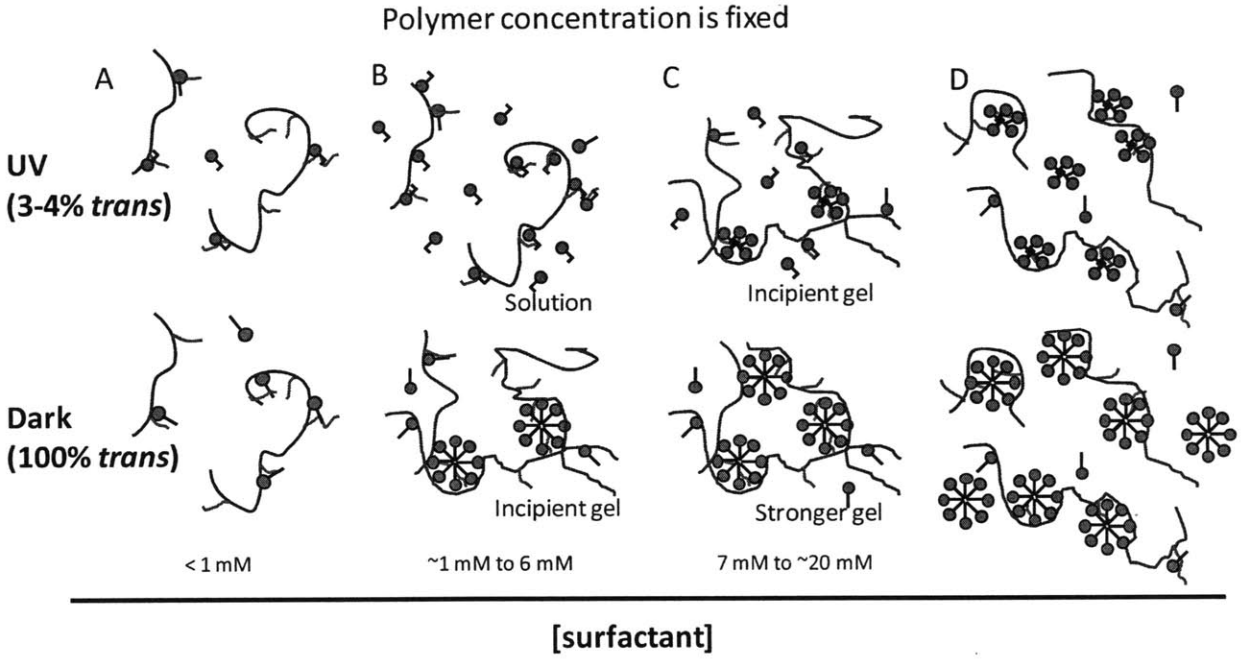

Figure 4-6 Possible configurations of azoTAB and HMPAA in aqueous solution, as understood before this work. Blue segments are the hydrophilic backbone of HMPAA. Red segments denote the hydrophobic side chains. Surfactants in green with straight tails are *trans* azoTAB; surfactants in blue with bent tails are *cis*. Progression of structures is similar to that illustrated in Figure 4-2, with the addition of an axis for isomeric

composition. See text for discussion. Recent SANS work suggests that the micelles are ellipsoid in either light condition [50]; this is not explicitly drawn for simplicity.

The progression of structures is similar to that illustrated in Figure 4-2, with the addition of an axis for isomeric composition. In section A, the system is below the CAC in either light condition. Section B corresponds to ~ 1 mM to about 6 mM. This region is above the CAC in dark-adapted samples, but below that for UV-adapted samples. Reversible gelation is thus initiated by use of light. In section C, the addition of further surfactant leads to more crosslinking and stronger gels in the dark-adapted state, as well as weak gels in the UV-adapted state. There will still be a difference in viscosity between the two light conditions, as seen in the 7 – 20 mM range in Figure 4-4. At higher concentrations, there are excess micelles in either isomer state, so the crosslinking becomes less effective.

There are other ways of incorporating photoresponsive moieties into physical gel systems. Azobenzene can be incorporated into branch units of the polymer which would then affect inter-polymer aggregation [51] or co-aggregation with oppositely charged micelles [52, 53]. Some photoresponsive polymers have also been formulated with azobenzene in the polymer backbone, as opposed to branch groups. Such a strategy has led to a polymer solution with photo-tunable viscosity [54, 55]. A gel was not actually formed, but the *trans* form of azobenzene led to a 60% higher bulk viscosity than the *cis* form. The more compact *cis* isomer resulted in more compact polymer coils, and thus lower viscosity.

4.2.5. Kinetics of gelation

In previous reported work, the time of sol-gel and gel-sol transitions in the azoTAB-HMPAA system was estimated to be on the scale of several minutes, though it required hours for the system to fully equilibrate [47]. The kinetics of this process thus appeared to have some complexity that would have to be understood before any practical applications are designed. A number of steps can be expected to be part of the process, and it is not a priori known which step would be rate limiting. The photoreaction initiates the process, and is controlled by light intensity, wavelength, path length and sample concentration (see Chapter 2). The photokinetics could also possibly be affected by steric hindrances in a gel system [56], though no such effect was observed in micellar azoTAB solutions. Subsequent to the photoreaction is the formation or dissolution of the micelles, which is typically on sub-second time scales [57], and finally any polymer relaxation.

When the gelation process has been experimentally monitored over time, it is often done by measuring changes in viscosity or elastic modulus [58-62]. This information is relevant if the applications of the gel are related to its rheological properties, but it does not directly provide insight on the molecular-level structure of the gel. Alternate methods to follow the kinetics are less frequently reported, but they include SANS (small angle neutron scattering) [63], NMR relaxation rates [62], and NMR diffusometry with probe solutes [64] and with the gelled polymer itself [65, 66]. It was felt that a NMR-based study of the kinetics of polymer-surfactant systems, particularly a light-activated one, would be beneficial.

4.2.6. NMR methods

The rheological results shown above provide some insight into the molecular architecture of the polymer-surfactant system, but NMR spectroscopy could be used to provide more direct observations regarding the characteristics of any aggregates. If the surfactant and polymer nuclei experience distinct electronic environments in each of the configurations illustrated in Figure 4-2, then these different states will have distinct NMR chemical shifts. If the chemical exchange between the various sites is fast compared to the NMR time scale, then the NMR spectrum will exhibit a single peak. The chemical shift of that observed peak will be a weighted average of the chemical shifts that would be expected for each individual site. The relevant time scale is on the order of

$$\frac{1}{\Delta\upsilon} \tag{4.1}$$

where $\Delta\upsilon$ is the difference between the peak frequencies of the various sites, in hertz.

In Chapter 2 it was shown that exchange of azoTAB between monomer and micellar environments is fast compared to this time scale, which is on the order of milliseconds. As such, only a single NMR peak was apparent for each azoTAB ^{1}H nucleus. The corresponding expression for this average chemical shift was given as

$$\delta_{obs} = y_{mon}\delta_{mon} + y_{mic}\delta_{mic} \tag{4.2}$$

where δ_{obs} is the measured shift, δ_{mon} and δ_{mic} are the shifts of surfactant in the monomer and micellar sites, and y_{mon} is the fraction of surfactant existing as monomer. This expression is written independently for *trans* and *cis* azoTAB.

The presence of the polyelectrolyte leads to additional possible surfactant sites, as illustrated in Figure 4-2. Surfactant monomer may be free in the bulk solution, or bound to the polymer chain through electrostatic and hydrophobic interactions. Likewise, micelles may be either free or enwrapped by polymer, with different numbers of polymer side chains possibly taking part in the micelles. Surfactant in each of these different sites could have different chemical shifts, adding terms to Equation (4.2). The NMR peaks of the polymer side chains may also be sensitive to these changes in environment, so the analysis could be repeated for that component. It would be infeasible to explicitly consider every possible distinct site for either polymer or surfactant, so simplifications must be made based on the observed results and physical assumptions.

If surfactant or polymer molecules do not exchange between the different sites on the NMR time scale, then distinct peaks will be observed for each environment. This slow exchange has been observed for the hydrophobic side chains in some previous NMR studies of HMPs [67, 68] (see Figure 4-7). In the case of slow exchange, the areas of these peaks can be integrated to give the relative fractions of side chain in various states.

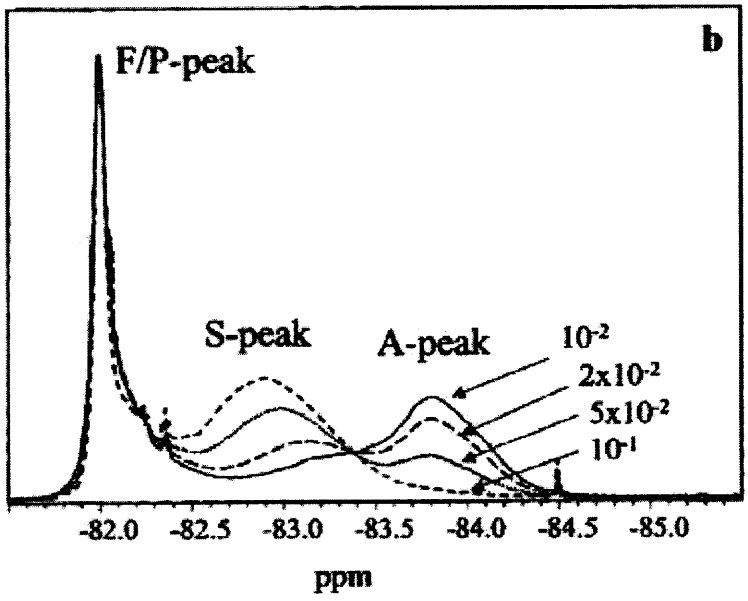

Figure 4-7 ^{19}F NMR spectra of a HMPAA mixed with different concentrations of sodium dodecyl sulfate. Shown is a series of peak corresponding to the side chain. The side chain consists of 8 carbons, and is perfluorinated. Polymer concentration is fixed at 5wt%. Peak F is attributed to unaggregated side chains; S to side chains incorporated in surfactant-rich micelles, and A to side chains aggregating with other side chains. Taken from [67]

4.2.7. Solute diffusion through polymer solutions and gels

Some of the applications envisioned for these reversible gels would require the rate of solute diffusion through the material to be dependent on the extent of gelation. With the azoTAB-HMPAA system, it can be imagined that the mesh through which a solute must diffuse will change in structure, based on the level of crosslinking present. Such an effect would enable these reversible gels to be used as tunable beds for electrophoresis or chromatography, for example.

The diffusion of solutes through hydrogels has been capably reviewed elsewhere [69, 70]. Solute mobility is generally reduced in polymer solutions and gels, as compared to the mobility in neat solvent. Various physical mechanisms have been developed to explain these effects. The polymer may simply decrease the free volume available for solute movement, it may cause increased hydrodynamic drag, or it may present impenetrable obstructions that lead to an increased path length for diffusion. Through consideration of these mechanisms, a multitude of equations have been developed to predict D / D_0, where D and D_0 are the solute diffusivities in gel and neat solvent, respectively. The key parameters in almost all of these relations are the polymer volume fraction ϕ_p and the radius of the solute r_s, but the form of the dependence of D on ϕ_p and r_s can vary widely. A sieving effect due to the mesh size of the polymer solution or gel has also been explicitly incorporated into the free volume theory. In this case, the expression for D / D_0 includes a factor such as

$$p = 1 - \frac{r_s}{\xi} \tag{4.3}$$

where p is the probability of a solute with radius r_s passing through a mesh of size ξ. Due to this effect, solute diffusion has been suggested as a complement to SANS for measuring ξ [71].

Polyethylene glycol (PEG) is often chosen as the probe molecule, as it should not bind to the substrate polymer through electrostatic or hydrophobic interactions. There is however some hydrogen bonding expected between PEG and PAA [72]. PEG also generally has a low polydispersity, allowing for simplified analysis, though some authors have quantitatively accounted for complications due to polydispersity [73]. Not all studies report that probe diffusivity is sensitive to gelation [69]. In gels formed by casein or whey, PEG diffusivity was actually found to increase upon gelation (induced by addition of rennet, or a change in temperature, respectively) [64, 73-76]. This effect was possibly due to larger voids appearing due to the coagulation process that let to gel formation. The diffusion coefficient

of PEG was also reported to be higher in carrageenan gels than in the corresponding solutions [77]. Those authors went on to enhance the gels with chemical crosslinking, and found no impact on solute diffusion. They hypothesized that such crosslinking would only affect solute diffusion if the addition of crosslinks changed the polymer volume fraction, unless the solutes were particularly large.

In contrast, gelation in 20 wt% dextran solutions, which occurred upon addition of potassium ions, was reported to decrease the diffusion coefficients of a range of small molecule solutes [78]. The diffusivity of acetone and water were reduced by 28% and 18%, respectively. Molecules as small as water were also found to respond to changes in the mesh size by Gibbs et al [79]. $R_s C / \xi$ was reported to be a good scaling parameter for the observed diffusivities, where C is the polymer concentration. Diffusion of proteins and hydrophobic fluorescein were also found to be reduced upon temperature-induced gelation in Pluronic-PAA copolymers [80]. The retardation of fluorescein was attributed to that molecule partitioning to the hydrophobic domains which act as crosslinkers for the gel. The effect on proteins was explained using the obstruction mechanism, through which the mean free path is increased as the gel forms.

Another dimension to solute mobility in gels is the dependence of the observed diffusivity on the time allowed for diffusion. Sometime no such dependence is found [73, 75, 78], in which case the diffusion can be taken as Gaussian and isotropic. If the apparent diffusivity decreases with increased diffusion time, the gel is likely inhomogeneous. On small length scales the diffusion may be relatively unhindered, but on longer length scales the probe may encounter some barrier. This situation is referred to as 'restricted' diffusion, and the distance between barriers can be inferred by studying the time dependence of the diffusivity. This has been done by using water to probe gellan gum gels [81], and PEG to probe chemically cross-linked PAA [82].

As should be apparent from this brief review, solute diffusion in gels is a complex topic. The diffusivity of solutes in polymer solutions is almost always found to decrease with increasing solute radius and polymer concentration. But it is rather difficult to predict exactly how the diffusivity will scale with those parameters, and even more difficult to predict how a solute will respond to gelation. Nonetheless such experiments shed light on the structure of the gel, and thus the gels in this work were probed using solutes of varying sizes.

4.3 Experimental section

4.3.1. Materials

All solutions in this section were prepared in deuterium oxide, used as received from Cambridge Isotope Laboratories. The azoTAB surfactant was synthesized as previously described [48].

The sodium salt of hydrophobically-modified poly(acrylic acid) (HMPAA) was prepared using an amide coupling reaction described by Wang [42]. Poly(acrylic) acid with an average molecular weight of 250,000 daltons is reacted with dodecylamine in the presence of dicyclohexylcarbodiimide. Anhydrous n- methylpyrrolidone is the reaction solvent. Enough amine is added to modify 3% of the polymer repeat units; the resulting polymer is denoted HMPAA 250k-3. The locations of amide coupling have been previously found to be randomly placed throughout the polymer coil [43]. The addition of sodium hydroxide results in the anionic polyelectrolyte shown in Figure 4-1. The pD of HMPAA solutions is about 8, which is well above the pK_a of PAA [83]. The purification procedure of Wang was modified in that excess sodium hydroxide was removed by dialysis, instead of using precipitation from methanol. Some supplementary experiments were performed using HMPAA with 5% of repeat units modified, denoted HMPAA 250k-5.

In some cases a solute was included in the sample. These were generally poly(ethylene glycol) (PEG) of different sizes, with the larger polymers labeled as poly(ethylene oxide) (PEO). All were used as received, and added such that the solute made up 0.06% or 0.03% of the samples on a mass basis. PEG or PEO with molecular weights of 600 and 100,000 daltons were obtained from Aldrich. PEG with weights of 6000, 12000 and 40000 daltons were obtained from Fluka respectively. Also obtained from Aldrich was a star PEO, with a molecular weight of 10,000 and 4 arms extending from a branch point. The samples obtained from Fluka were specified as standards for chromatography, and have low polydispersity (M_w / M_n of 1.1). Some additional experiments were done with small molecule solutes, dimethylformamide and pyridine. Both were used as obtained from the manufacturer.

4.3.2. Preparation of gels

Due to the difficulty in loading viscous samples, gels were prepared within the NMR tubes. Solutions of azoTAB and HMPAA were added from separate stock solutions to the tube and the gel forms as the two components mix. Any solute was added from a third solution. Some agitation was introduced by placing the NMR tubes upon a nutating mixer. The nutater gently gyrates the samples. To ensure sample

homogeneity, at least one month was allowed to elapse before any measurements are taken. No evaporation of solvent was evident during this period. When faster preparation was required, direct mixing was accomplished by manually agitating the sample with tube inserts available from Wilmad. These tube inserts were then left inside the NMR tube, in order to avoid removing any material.

Unless otherwise noted, the final polymer concentration was fixed at 2.5 wt %, inclusive of the sodium counterion. The mass of the surfactant or added solute was neglected in the calculation of the weight fraction. This polymer concentration is slightly above the overlap concentration (0.6 wt%), so the solutions are semi-dilute. The surfactant concentration was varied between 0 and 20 mM. The stock solutions of both surfactant and polymer are necessarily more concentrated than the final mixtures within the NMR tubes. HMPAA solutions are viscous and it becomes difficult to accurately transfer them into NMR tubes by pipette at concentrations above 6 wt%, thus putting a constraint on the possible concentration of the polymer stock solution. The solubility limit of azoTAB precludes surfactant stock solutions above 60 mM. Due to these limits, it was not easily possible to obtain polymer-surfactant mixtures at surfactant concentrations above 20 mM.

4.3.3. Measurement of ^{1}H NMR chemical shift

NMR spectra are taken with a 500 MHz Varian spectrometer, with settings and spectrum referencing as described in Chapter 2. Spectra were processed using the MestReNova software package.

Measurement of kinetics was done as described in Chapter 1, but using more concentrated samples (5 mM azoTAB). A sample within a NMR tube was irradiated with UV light for some increment of time, then inserted into the spectrometer and a ^{1}H spectrum was collected. The distinct *trans* and *cis* were integrated to find the fraction of each that was present. This cycle of irradiation and observation was repeated for the same sample until the photostationary state was achieved. The irradiation intervals ranged from 30 seconds to six minutes; the shorter intervals were used in the beginning of an experiment when the reaction rates were higher. 20 scans were found adequate for a satisfactory signal to noise ratio in each spectrum. Four minutes were required for to collect these 20 scans, and an additional 2-3 minutes were required for sample insertion and shimming before the spectrum could be collected.

The tubes were placed 1 cm away from the Oriel lamp described in Chapter 1, with a UV bandpass filter (Oriel 59810) installed. The irradiance at this distance was measured to be 4.7 mW/cm^2; the maximum intensity with this filter was at 360 nm. This filter had a full width at half maximum (FWHM) of 52 nm.

Kinetic experiments were done in two ways: avoiding agitation, and with intentional mixing. In the intentional mixing case, the sample tube was manually agitated before and after irradiation periods to ensure the sample volume was well mixed. When avoiding agitation, the sample was held as still as possible during transfer between the lamp and the spectrometer. The orientation of the tube with respect to the lamp was fixed, such that the same part of the sample volume was always nearest (or furthest) from the light source. This procedure was meant to allow composition gradients to build up within the tube, due to uneven absorption of light within the sample. It was impossible to ensure an entirely quiescent sample.

4.3.4. Diffusion measurements

Diffusivities of surfactant, polymer and solutes were measured using the pulsed field gradient spin-echo (PFG-SE) NMR method [84-86]. There exist a multitude of PFG-SE pulse sequences; the BPP-LED (bipolar pulsed-field gradient method with longitudinal eddy current delay) pulse sequence was chosen for this work [87]. Most measurements were performed in the Francis Bitter Magnet Lab at MIT using a 600 MHz spectrometer. The NMR probe was manufactured by Nalorac and can deliver a maximum field gradient of 61 G/cm. Some additional measurements were done at the Martinos Center of Massachusetts General Hospital using a 600 MHz Bruker instrument. The maximum gradient at this facility was 54 G/cm. In practice, neither probe could reliably produce linear gradients with these maximum magnitudes, so in practice the FBML probe was limited to 90% of the stated maximum value and the MGH probe was limited to 70%. The calibration of the gradients was described in the previous chapter.

The original and most simple PFG-SE pulse sequence is illustrated Figure 4-8, in order to demonstrate some basic concepts of the experiment. More rigorous discussions can be found in the literature [88]. An initial radiofrequency pulse rotates the spin magnetisation vector 90 degrees from the longitudinal axis to the transverse plane. From this time onwards, relaxation of this vector occurs exponentially with a time constant of T_2. At some time after the initial 90 degree pulse, a linear gradient in the background magnetic field is introduced for a duration δ. During this gradient pulse, the spatial locations of the different molecules in the sample are 'encoded'. After an interval Δ, another gradient field pulse is applied in order to 'decode' this information. The NMR signal at the end of the sequence is known as the spin-echo. If the molecules remain spatially fixed during Δ, the intensity of the spin echo will be simply that which is expected due to the aforementioned T_2 relaxation. Any movement of the molecules results in a weaker spin echo; relaxation and diffusion both independently attenuate the measured signal. Assuming all motion to be Brownian, mathematical expressions are available for relating the spin echo intensity to the diffusivity.

The BPP-LED pulse sequence used in this work is illustrated in Figure 4-9, with the governing relation provided in Equation (4.4). The sequence is different from the classical one shown in Figure 4-8 in some key respects. The imposition of field gradients can induce eddy currents which could distort the measurement. These eddy currents can be largely eliminated by following each gradient pulse with another gradient that is equal in magnitude but opposite in orientation. The BPP-LED sequence therefore splits each gradient pulse into bipolar pairs. BPP-LED is also an example of a stimulated echo sequence, in which the magnetisation vector is stored along the longitudinal axis for most of the experiment (during T and T_e of Figure 4-9). The nuclei in the sample will therefore relax mostly according to the longitudinal time constant T_1, instead of the shorter T_2. This feature is helpful for the study of polymers and immobilized molecules, as they tend to have fast relaxation rates as well as low diffusivities. For these slow-moving molecules, relatively long diffusion times (Δ) can be required for diffusion to cause an accurately measurable decrease in the spin echo intensity. Unfortunately the simultaneous attenuation of the spin echo due to relaxation can cause the signal to decay to imperceptible levels before the acquisition time. It is therefore beneficial to minimize the relaxation rate by selecting T_1 relaxation over T_2.

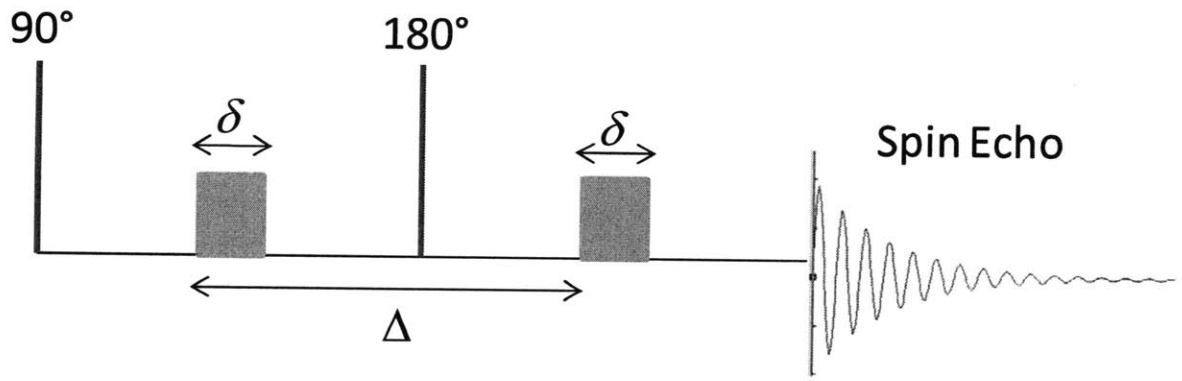

Figure 4-8 Pulse sequence of the classical Stejskal-Tanner PFG-SE experiment. Not used in this work, but shown for comparison with the BPP-LED sequence in Figure 4-9. X-axis is time, but is not drawn to scale. Radiofrequency pulses are shown as blue lines and are labeled with the flip angle. Grey boxes correspond to pulses of gradient magnetic field. The measured diffusion takes place over time and is the gradient pulse width.

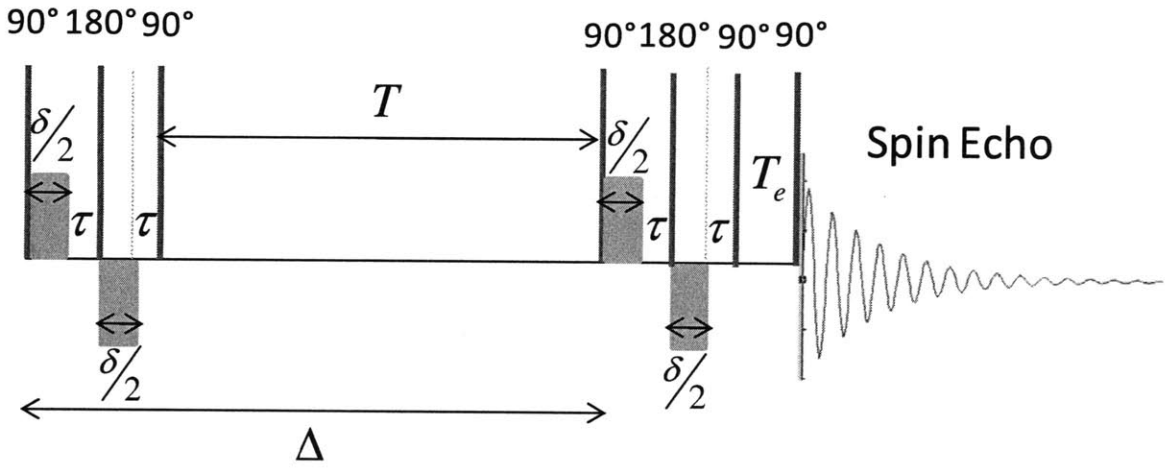

Figure 4-9 Pulse Sequence in the BPP-LED experiment. The temporal axis is again not drawn to scale. The measured diffusion takes place over time Δ, typically from 100 to 3000 ms. δ is the gradient pulse width and may be varied from 2 to 5 ms. τ is fixed as 0.1 ms, and the delay T_e at 50 ms. Measured quantity is the amplitude of the signal in time AQ. Rectangular gradient pulses are used, as shown.

The relationship between the observed spin echo intensity and the diffusivity in the BPP-LED sequence is as follows:

$$S = \frac{1}{2} S(0) \exp\left[\frac{-(T+T_e)}{T_1}\right] \exp\left[\frac{-(4\tau+2\delta)}{T_2}\right] \exp\left[-Dq^2\left(\Delta - \frac{\delta}{3} - \frac{\tau}{2}\right)\right] \tag{4.4}$$

where

$$q = \delta\gamma G \tag{4.5}$$

and Δ, δ, τ, T and T_e are defined in Figure 4-9. S is the intensity of the spin echo, and $S(0)$ is the signal intensity immediately after the initial radiofrequency pulse. The first two exponential decays account for the relaxation effects discussed above. D is the diffusion coefficient of the observed nucleus. The gyromagnetic ratio γ is a nucleus-specific constant, and is $2.68*10^8$ rad s^{-1} T^{-1} for ^1H. G is the strength of the magnetic field gradient.

To avoid having to explicitly account for the effects of relaxation, the various times T, T_e, δ and τ are generally held constant throughout a series of experiments. The terms due to relaxation can then be absorbed into S(0). The BPP-LED sequence is run at different values of the field

gradient strength G, and a semi-log plot of the resulting spin-echo intensities versus $q^2\left(\Delta-\frac{\delta}{3}-\frac{\tau}{2}\right)$ provides a slope equal to the diffusivity (see previous chapter). Such plots are commonly known as Stejskal-Tanner plots, and the abscissa is generally denoted as 'k'. In order to accurately determine the slope, the field gradient is varied such that there is about one decade of attenuation in the intensity values S. Due to the relatively weak gradient strengths available for this work, it can be difficult to attain this level of signal decay when studying polymers and other slowly-diffusing molecules. In such cases the signal attenuation is enhanced by setting the gradient pulse length δ to the maximum value of 5 ms; the equipment can be damaged if field gradients are applied for longer periods. The level of attenuation can be further increased by using large values of T, resulting in long diffusion times Δ. The maximum value of T is constrained by the rate of T_1 relaxation as discussed above; T was set as high as 2-3 seconds when measuring polymer diffusion.

An example Stejskal-Tanner plot for the simple case of dilute poly(ethylene glycol) diffusing in deuterium oxide is shown in Figure 4-10. The solute diffuses quickly enough that moderate values of δ and T are sufficient to obtain the desired level of decay in the spin echo.

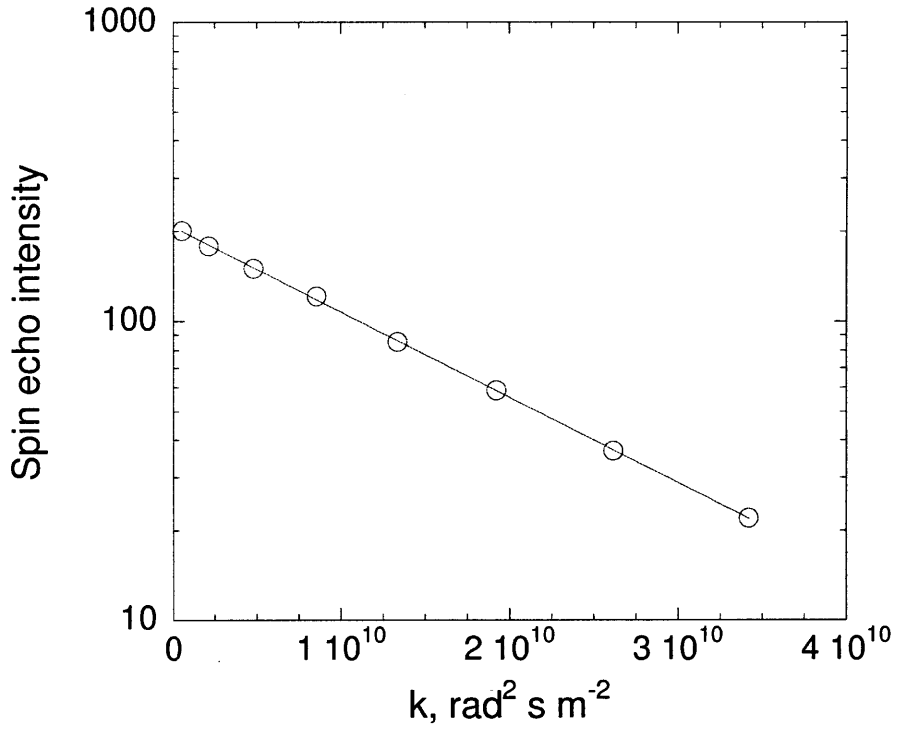

Figure 4-10 Example Stejskal-Tanner plot for 0.06 wt% PEG, molecular weight 12000, in deuterium oxide. Attenuation of signal is one decade. Parameters: δ, 2 ms; T, 500 ms. Field gradient varied from 0.061 T/m to 0.488 T/m. Diffusivity obtained from slope: $6.6*10^{-11}$ m^2/s. $R^2 = 0.9998$.

The spectra were analysed using the MestReNova package. The peak intensities were obtained by using the peak picking tool. Line broadening was applied to improve the signal to noise ratios, up to a maximum of 6 Hz.

There are further complications in this analysis when multiple species contribute to the NMR signal at a shared resonant frequency. This can occur when nuclei exchange rapidly between different environments, such as surfactant monomer and micelle. If the exchange is fast compared to the time scale given in Equation (4.1), then a single peak is observed according to Equation (4.2). The apparent diffusivity will also be a population-weighted average:

$$D_{obs} = \sum y_i D_i \tag{4.6}$$

where D_{obs} is the apparent diffusivity, found from the Stejskal-Tanner plot. D_i is the diffusivity of component i, and y_i is the fraction of nuclei existing as that component.

There are also cases in which two species share the same resonant frequency, but there is slow or no exchange of nuclei between the two forms. Under these conditions, a simple Stejskal-Tanner plot exhibits curvature. Equation (4.4) is re-written for the multiple components i:

$$S/S(0) = \sum_i \frac{1}{2} f_i \exp\left[\frac{-(T+T_e)}{T_{1i}}\right] \exp\left[\frac{-(4\tau+2\delta)}{T_{2i}}\right] \exp\left[-D_i q^2 \left(\Delta - \frac{\delta}{3} - \frac{\tau}{2}\right)\right] \qquad (4.7)$$

where f_i is the fraction of nuclei present in component i, T_{1i} and T_{2i} are relaxation time constants of species i, and D_i is the diffusivity of component i. Due to the overlap in the component peaks, it may not be possible to determine the relaxation time constants of each species. In this case, the relaxation terms cannot be considered explicitly, and are instead lumped into constants:

$$S/S(0) = \sum_i \frac{1}{2} f_i' \exp\left[-D_i q^2 \left(\Delta - \frac{\delta}{3} - \frac{\tau}{2}\right)\right] \qquad (4.8)$$

where f_i' is the product of the nuclear fraction and the relaxation terms. The term f_i' is equivalent to the nuclear fraction only if the various components i all have the same relaxation time constants. From measurements of the spin echo intensity S at various field gradient strengths, Equation (4.8) can be used to find the best-fit values of $f_i' S(0)$ and D_i. Additionally, if one component has a clearly lower diffusivity than the others, then only that slowest component contributes to the spin echo intensity at high gradient strengths. A Stejskal-Tanner plot may then appear linear at high values of $q^2\left(\Delta - \frac{\delta}{3} - \frac{\tau}{2}\right)$, with the slope corresponding to the diffusivity of the slowest component.

The time required to measure a diffusion coefficient prohibits the use of NMR diffusometry for following processes that occur on the time scale of minutes or less, unless they can be interrupted between measurements. After the sample is inserted into the spectrometer, ten minutes are required for allowing the sample to stabilise at the setpoint temperature (here, 25 C). Shimming of the gradient coils also takes place during this pause. Then, each individual spin echo measurement requires 0.5 to 3 seconds diffusion time, 1-2 seconds acquisition time, and 2 seconds of delay before the next measurement. Each measurement is done 16 times to complete the required phase cycling. Finally, spin echoes must generally be measured using at least 10 and sometimes over 50 distinct settings of gradient strength, in order to produce a usable Stejskal-Tanner plot. It can therefore take at least 25 minutes or well over an hour to measure the diffusion coefficients in any one sample tube.

As in the previous Chapter, the photoreaction of azoTAB is interrupted by applying the irradiation in intermittent pulses, with the NMR measurements done in between the pulses. Any remaining process that takes place on a time scale of minutes will not be observed.

4.4 Results: Polymer-surfactant interactions

4.4.1. ^{1}H NMR spectra

The ^{1}H NMR spectra of PAA, PAA-Na and HMPAA are shown in Figure 4-11, including peak assignments. The PAA spectrum is consistent with those reported in the literature [89, 90]. The multiplicity of the polymer backbone peaks is due to the tacticity of the chain. The orientation of the neighboring repeat units affects the chemical shift of each proton. The peaks can be integrated to show that there are about equal populations of racemo and meso diads, so the polymer is taken to be atactic. The modified polymer shows extra peaks attributed to the grafted side chains; a comparison of the integrated peak areas confirms that 3% of the repeat units are modified in HMPAA 250-3. This integration shows that the amide coupling reaction proceeds to full conversion and is thus controlled by the stoichiometry of the reagents.

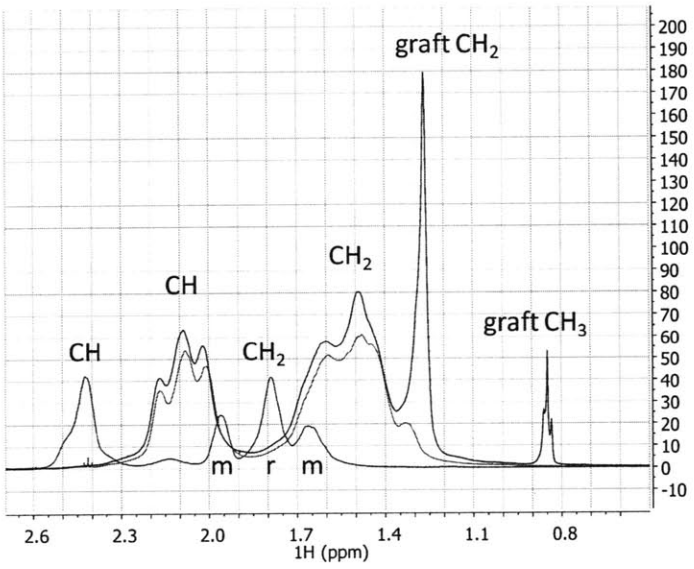

Figure 4-11 ^{1}H polymer spectra. In red, poly(acrylic) acid at low pH (PAA). In green, the sodium salt of PAA (PAA-Na). In blue, the sodium salt with hydrophobic modification (HMPAA). Peaks are shifted upfield upon addition of sodium hydroxide. Peaks due to tacticity of PAA are labeled; the resolution of these peaks is affected by the pH. All spectra are measured at a polymer weight fraction of 2.5% in deuterium oxide.

Characteristically for polymers, the ^{1}H peaks of HMPAA are broad and could obscure the signal from other components in the sample. Fortunately the aromatic proton peaks of azoTAB are located downfield

of the polymer and are clearly visible, as are the azoTAB peaks labeled 'G' and 'K' (see Figure 4-12). Likewise, the polymer peaks corresponding to the grafted chains and the CH groups of the backbone do not overlap with any surfactant peaks.

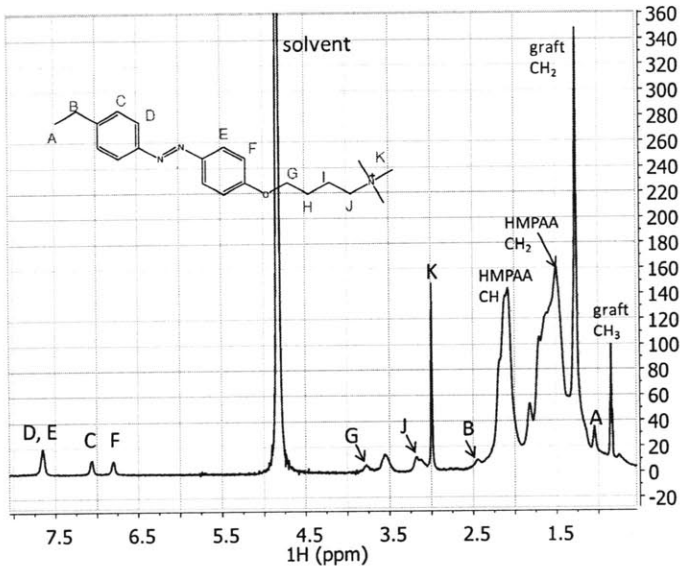

Figure 4-12 ^{1}H NMR spectrum of azoTAB-HMPAA mixture. Measured at azoTAB concentration of 3 mM and 2.5 wt% HMPAA in deuterium oxide. azoTAB molecule shown with labels for ^{1}H peaks. Surfactant nuclei H and I are obscured by the broad polymer chain CH_2 peak.

This lack of overlap allows both surfactant and polymer to be studied independently using ^{1}H. The *cis* and *trans* isomers of azoTAB again provide distinct ^{1}H peaks that can be integrated to provide the isomer composition. These features of the spectra of HMPAA-azoTAB mixtures allow the use of the techniques described in the previous chapter for the purpose of studying aggregation.

4.4.2. Surfactant chemical shifts

NMR spectra were collected in dark-adapted samples at a fixed HMPAA concentration and varying azoTAB concentrations. The superimposed spectra in Figure 4-13A show that only one peak is visible per proton at any given concentration, but the position of that peak is dependent on the concentration of azoTAB. This observation indicates rapid exchange of azoTAB molecules between at least two different sites, with the partitioning between those sites changing with concentration. An equation with a form like that of Equation (4.2) should apply for the chemical shifts. The concentration dependence of the chemical shifts is plotted in Figure 4-13B. The protons labeled 'G' and the aromatic protons are more sensitive to

changes in the environment than the headgroup protons 'K' (see Figure 4-12 for peak labeling). This ordering is similar to that shown in Chapter 2 for surfactant-only solutions. As discussed in that previous chapter, aromatic ring current effects [91] are likely causing enhanced changes in chemical shifts upon aggregate formation. In systems lacking aromaticity, the chemical shift is much less sensitive to aggregation. These ring current effects will generally be stronger in protons that are close to the aromatic rings, and are related to the orientation of the observed protons relative to the aromatic π electrons.

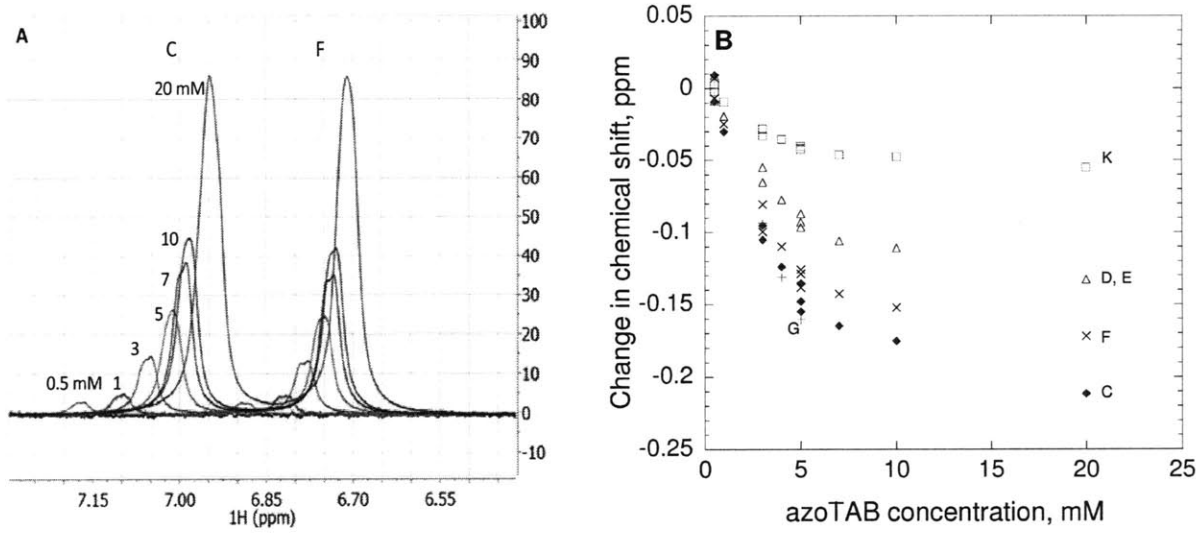

Figure 4-13 Dependence of peak position on azoTAB concentration in dark-adapted samples. Measured with 2.5 wt% HMPAA. Figure 4-13A: Overlaid spectra from various azoTAB concentrations, 0.5 mM to 20 mM. Shown are peaks 'C' and 'F'. Figure 4-13B: Chemical shifts of different protons, relative to the shift observed at 0.5 mM. Some surfactant peaks ('A', 'B', 'H', 'I') cannot be plotted because they are obscured by the polymer peaks.

The trends in Figure 4-13B are qualitatively similar to those seen in the absence of any polymer, but with some key differences. The data collected from surfactant-only solutions are shown in Figure 4-14A and are reviewed here. In dark-adapted samples, 100% of the surfactant exists in the *trans* form. There is a breakpoint in the dark-state chemical shift data at about 3.3 mM, indicating the *trans* CMC at which micelles begin to form. At concentrations above the CMC, the series asymptotically approaches the chemical shift of a surfactant residing within a micelle δ_{mic}, in accordance with Equation (4.2). If there were only non-interacting monomers below the CMC, then the chemical shift would be constant below 3.3 mM. There is however a slight slope to those data, indicating some level of pre-micellar aggregation.

In the UV-adapted state (circular markers in Figure 4-14A), 97% of azoTAB exists as the *cis* isomer, with the *trans* making up the balance. No breakpoint is apparent for either isomer; the trend throughout the observed concentration range suggests that only pre-micellar aggregates are formed. These results are

consistent with the hypothesis that the *cis* surfactant is less likely to form micelles than the *trans,* so it would have an elevated CMC. Fluorescent probe, NMR peak width and diffusivity measurements also confirm a lack of micelle formation in the UV-adapted samples, as discussed in the previous Chapter. Furthermore, SANS results suggest that *cis* azoTAB forms pre-micellar disc-like structures instead of proper micelles over this concentration range; the aggregation number of these discs is on the order of 5 [50]. In contrast, *trans* rich micelles in the dark- or visible- adapted states are likely to form ellipsoids with aggregation numbers in the range of 60-100. The *trans* isomer remaining in the UV state would tend to form micelles, but its prevalence is too low to allow micelle formation on its own. As suggested in the previous Chapter, if it were possible to extend the observations to higher concentrations, a CMC could become apparent in the UV photostationary state. However the experimentally accessible concentration range is limited by the difficulty of achieving a photo-stationary state in optically thick samples.

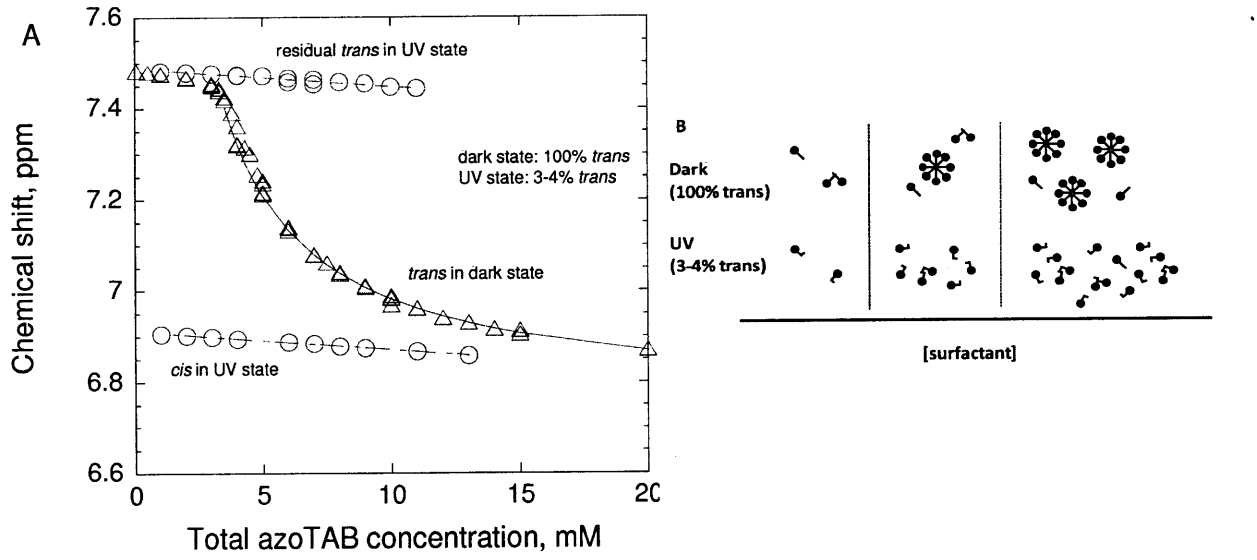

Figure 4-14 A: Chemical shift measurements for azoTAB peak 'C' in the absence of any polymer. Values for *trans* shown in red, *cis* shown in blue. Triangular markers are for the dark-adapted state; circles for the UV state. UV-adapted state measurements are limited to a lower concentration range due to the optical thickness of the samples. Linear trendlines are drawn for the UV data, and results of a simple pseudophase separation model are drawn for dark state data. See previous Chapter. B: Progression of aggregation under the different light conditions. *trans* azoTAB shown in green, with straight tail; *cis* shown in purple with bent tail. In dark-adapted state, some dimers or loose clusters can be expected below the CMC. As the concentration is increased above the CMC, the additional molecules form micelles. In the UV-state, only loose dimers or other pre-micellar aggregates are formed over the observed range. SANS work has suggested that these loose aggregates are disc-like, with aggregation numbers of about 5 [50]. Micelles dominated by *trans* appear to be ellipsoid, with aggregation numbers in the range of 60-100.

The chemical shifts at infinite dilution are also noteworthy because the effects of inter-surfactant interaction are excluded. The chemical shift of *trans* azoTAB converges on the same value at infinite dilution, regardless of the light condition. This convergence is expected, as the other surfactant molecules are too distant for their isomeric state to affect the environment of the observed *trans* molecule. There is however a large offset between the *cis* and *trans* peak positions at low concentrations, indicating that the NMR environments of the two isomers are inherently very different.

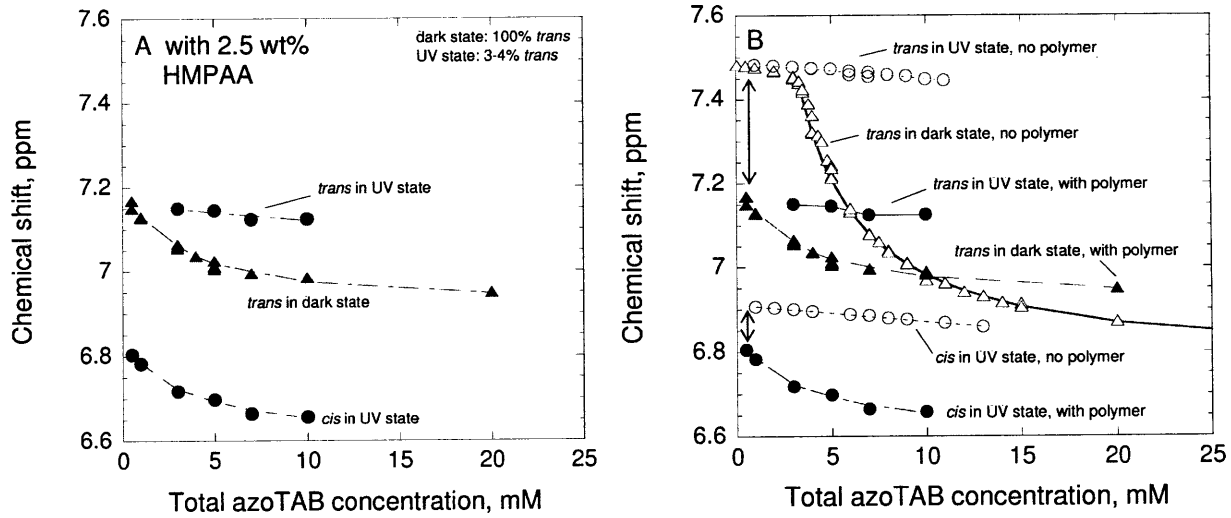

Figure 4-15 Chemical shift of azoTAB proton 'C' in different conditions. A: Aqueous solutions and gels with both azoTAB and HMPAA. B: with azoTAB solution data from Figure 4-14 added. Triangular markers: dark-adapted state, 100% *trans*. Circular markers: UV-adapted state, 3-4% *cis*. Solid markers: with 2.5 wt% HMPAA; hollow markers: no polymer. Red markers: *trans* isomer. Blue markers: *cis* isomer. Results of pseudophase separation model shown with *trans* data in azoTAB solution. Smoothed curves or linear trendlines added to guide the eye on other series. Minimum azoTAB concentration is 0.5 mM, limited by the sensitivity of the NMR experiment. Maximum azoTAB concentration in the UV-adapted state is again limited due to the optical thickness of the samples, which prevents complete photoconversion from being achieved throughout the sample. See text for discussion.

As illustrated in Figure 4-2, a larger array of possible sites must be considered for the azoTAB molecules upon the addition of HMPAA. At low surfactant concentrations, little cooperative binding of azoTAB is expected. Surfactant molecules will be either free in solution or individually bound to the polymer; this binding may tend to occur in the vicinity of the hydrophobic side chains. Cooperative aggregation should begin at the CAC, resulting in surfactant-rich micelles that incorporate some polymer side chains. As the azoTAB concentration is increased, the number of these micelles will increase and an increasing proportion of the surfactant will reside in the micelles. The azoTAB chemical shift observations in Figure

4-15A for both dark- and UV- adapted states with 2.5wt% HMPAA are qualitatively consistent with some of these expectations. The *trans* peaks in the dark-adapted samples (solid red triangles) and the *cis* peaks in the UV-adapted samples (solid blue circles) both asymptotically approach some value corresponding to the micellar state as the surfactant concentration is increased. This trend indicates an increasing extent of micelle formation as the azoTAB concentration is increased.

It is noteworthy that there is no obvious breakpoint in either the dark or UV series, whereas one would be expected if there were a sharp CAC within this concentration range. This is in marked contrast to the well-defined CMC observed in the dark-adapted samples in Figure 4-14A. Based on the shape of the curves, the CAC in either light condition is likely below the observed concentration range. However, rheological measurements suggest that the dark-adapted and UV-adapted CACs are approximately 1 and 6 mM respectively [47] (see Figure 4-4). This difference between dark- and UV- state CACs was interpreted to be the basis of the observed reversible gelation (illustrated in Figure 4-6). The chemical shift and rheology experiments are possibly consistent in the dark-adapted state, as it was infeasible to collect NMR data at sufficiently low concentrations to detect a CAC below 1 mM. The most dilute concentration observed was 0.5 mM. It is also likely that NMR will report a lower CAC than viscosity measurements, since a small population of micelles will strongly affect the observed chemical shift, but may not provide enough cross-linking to affect the observed viscosity.

There is however an apparent discrepancy between the rheological and NMR experiments in the UV-adapted state. The *cis* NMR peaks in the UV data (solid blue circles) follow much the same pattern as the *trans* peaks in the dark (solid red triangles). This similarity implies that roughly equal amounts of azoTAB are in micelles at any given concentration, regardless of the light condition. This is in contrast to the understanding derived from the viscosity measurements, in which the *cis*-rich samples are much less likely to form micelles than the *trans*-rich samples at concentrations between the two apparent CACs.

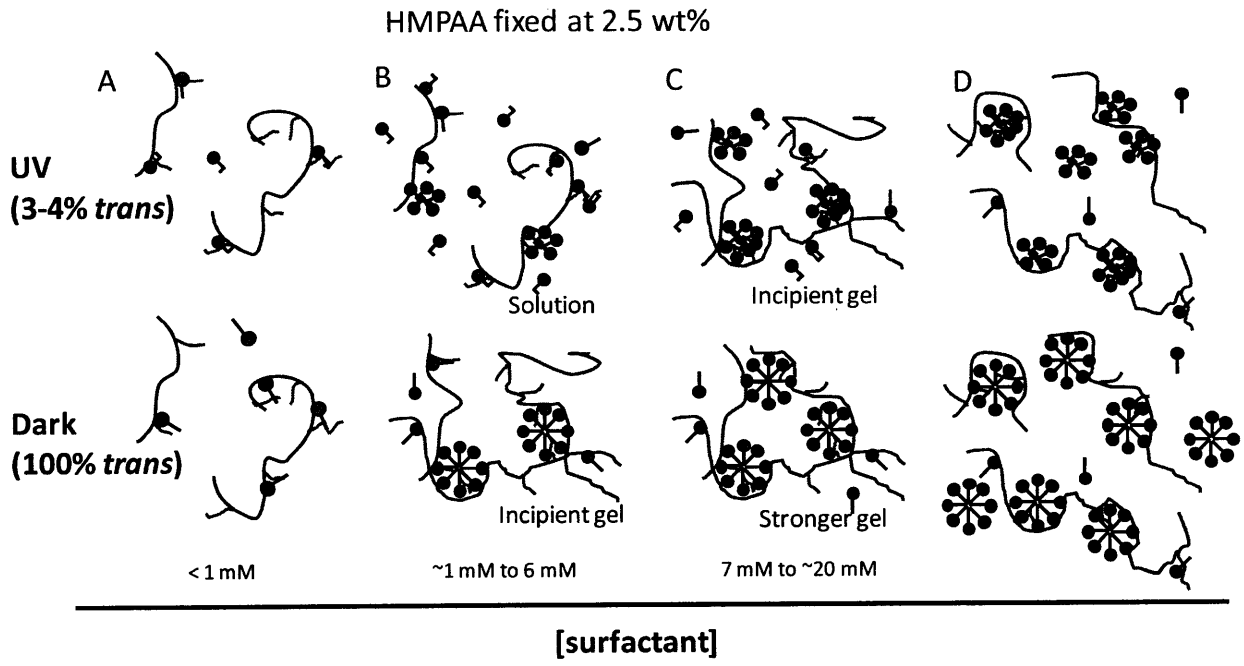

Figure 4-16 Possible structures in azoTAB-HMPAA system, upon consideration of NMR, SANS and viscosity results. Similar to Figure 4-6, but with amendments made for the UV-adapted state. Some sort of aggregation occurs in the 1-6 mM range, without leading to a substantial increase in viscosity. From about 7 mM onwards, crosslinking becomes apparent in the rheology results. It is possible that the aggregates of *cis* and the polymer side chains are small and weak, and on average provide less effective crosslinking than their *trans* counterparts. In this case, a higher number density of micelles is necessary in the UV state to achieve the same thickening effect observed in the dark state. It is also possible that the *cis* micelles grow in size as the surfactant concentration is increased, thus leading to better crosslinking.

It is possible that some weak aggregates are formed in the UV state at some CAC below 1 mM, but that these aggregates are not large or stable enough to provide effective cross-linking below 6 mM (see structures suggested in Figure 4-16). This hypothesis would reconcile the NMR and viscosity data. The weak *cis* micelle would be less likely to engage in elastically effective crosslinking than a *trans* micelle, so a higher number density is required in order to get the same thickening effect. Alternately, the *cis* micelles may grow as the surfactant concentration is increased, finally leading to a regime where they are large enough to promote crosslinking. Recent SANS results add some confidence to these hypotheses [50]. Guinier analysis was used to obtain an estimate of the micellar radius of gyration, as shown in Figure 4-17A. The *cis* dominated micelles are smaller than the *trans*, though they appear to grow somewhat as the surfactant concentration is increased. The extrapolated zero-angle scattering intensity is shown in Figure 4-17B. This value should be proportional to the micellar volume density and the micellar volume. These results indicate that while the *cis*-rich micelles are smaller than *trans*-rich micelles, micelles do indeed form in the UV-adapted state from ~ 1 mM. This is apparent because the scattering intensity rises smoothly with increasing surfactant concentration, with no apparent breakpoint at any CAC. Although these results were initially reported as being consistent with the hypothesis of the

different light conditions having different CACs, they appear to support the schematic proposed here in Figure 4-16. The CAC is around or below 1 mM, regardless of the light condition. However, the properties of the ensuing micelles are dependent on the isomer composition, and therefore the light condition has a strong influence over the observed viscosity.

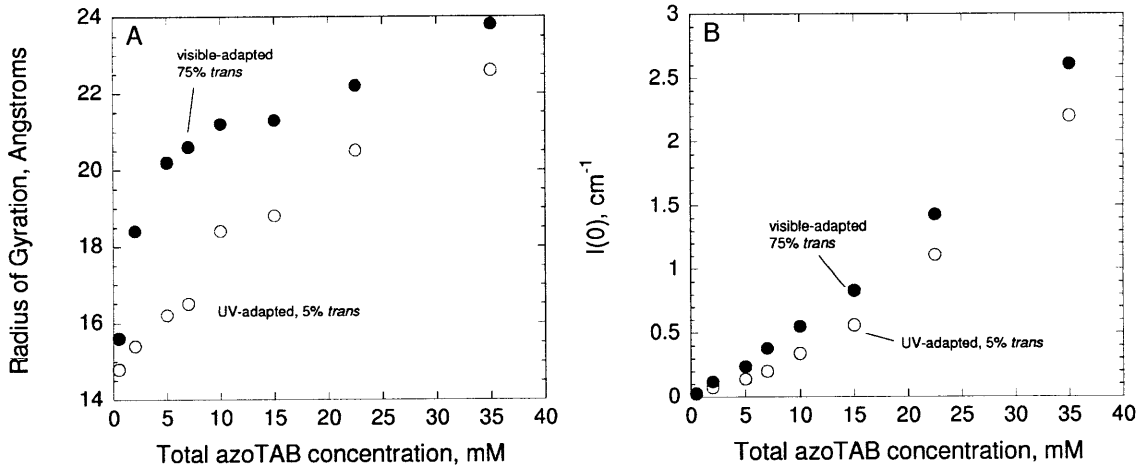

Figure 4-17 SANS results of Lee et al [50], for azoTAB-HMPAA mixtures. HMPAA concentration is fixed at 2.5 wt%. Shown are the UV-adapted state, and a visible-adapted state. Dark-adapted data are not available. The samples at higher concentrations (above 20 mM) may have a higher than expected *trans* content, due to the difficulty in reaching a photostationary state in optically thick samples. A: The micellar radius of gyration as found by Guinier analysis. B: The scattering intensity extrapolated to zero angle.

It should be noted that qualitative observations of the viscosity in the NMR tubes are consistent with the corresponding quantitative viscosity measurements. These judgments were made by observing the time required for a bubble to move through the material, and the time required for the material to creep down an inverted tube. This gives further confidence that the measured differences in gelation between UV- and dark-adapted states are real, despite the similarity in the chemical shift data.

Further insights can be gained by returning to Figure 4-15A. It does appear that the residual *trans* isomer in the UV-adapted samples does not participate significantly in the *cis*-dominated micelles. This segregation is implied by the very weak concentration dependence of the relevant chemical shift (red solid circles). Given that the fully-extended length of *trans* azoTAB is longer than the *cis*, the *trans* form would not be expected to pack well within *cis* micelles. However mixed micelles should be possible at other isomer compositions, as demonstrated using surfactant-only solutions in Chapter 2.

Comparisons can also be made between the samples with and without polymer (see Figure 4-15B). At low surfactant concentrations, the chemical shift in the absence of polymer (hollow markers) is that of

free azoTAB monomers, δ_{mon}. The azoTAB chemical shifts in the presence of polymer (solid markers) do not approach δ_{mon}, as indicated by the arrows in Figure 4-15B. This divergence could be partially due to some surfactant-rich micelles being present at the lowest measured concentration (0.5 mM), but it is likely also due to some individual molecules binding non-cooperatively to the polymer instead of remaining free in solution. The bound azoTAB would have some chemical shift δ_{bound}, while the free molecules should exhibit the same δ_{mon} as observed in the absence of polymer. The *cis* chemical shifts show less of this divergence than the *trans*, which may indicate that the more polar *cis* molecules are more likely to remain free in solution than the *trans*. The asymptotic chemical shifts at high azoTAB concentrations also differ between surfactant-only solution and surfactant-polymer mixture, indicating that the micellar environment is somewhat different when HMPAA is present.

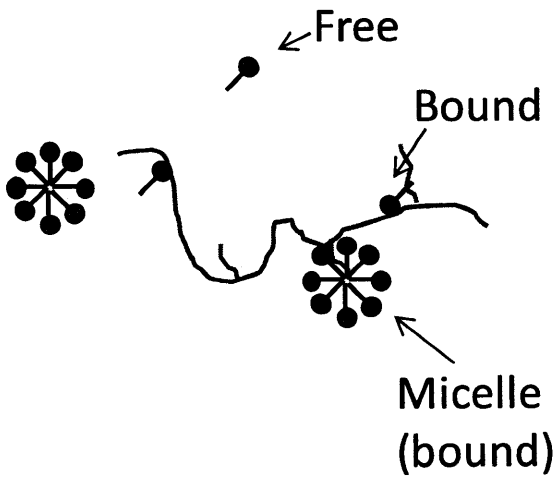

Figure 4-18 Different surfactant sites considered in the quantitative analysis presented here. Shown but not labeled is a free micelle; these are neglected in this section.

Equation (4.2) can thus be extended to account for surfactant that is non-cooperatively bound to the polymer:

$$\delta_{obs} = y_{mon}\delta_{mon} + y_{bound}\delta_{bound} + y_{mic}\delta_{mic} \tag{4.9}$$

This equation was used to find the amount of azoTAB that is residing in the aggregates. Combined with the aggregation number of the micelles, this information provides the number of cross-linking sites that are available for gel network formation. All of the terms of Equation (4.9) were initially unknown. The chemical shifts δ_{mon}, δ_{bound} and δ_{mic} are specific to the observed proton and the chosen photostationary state. Following the analysis of surfactant-only solutions, the micellar shift δ_{mic} for any given proton is found through extrapolation to high concentrations:

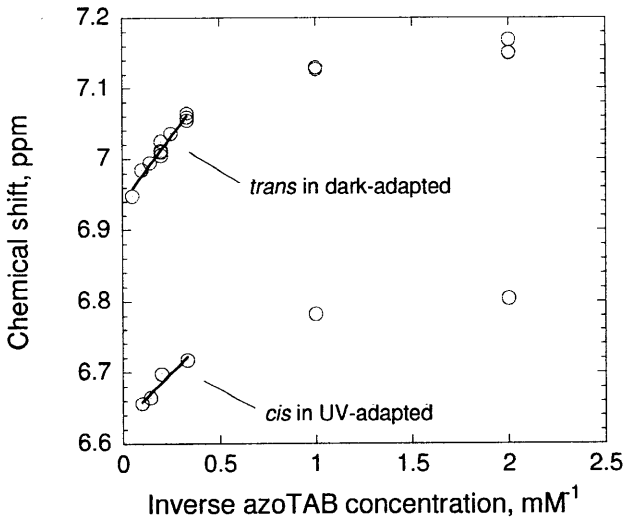

Figure 4-19 Chemical shift of an aromatic proton, 'C', plotted against inverse concentration. Linear regression is used to extrapolate to high concentrations; δ_{mic} is set equal to the intercept. Repeated for other aromatic ring protons D, E, F and headgroup protons K (not shown). The chemical shifts of D and E coincide in the dark-adapted state, while peaks C and F coincide in the *cis* in the UV-adapted state.

As a first approximation, micelles bound to the polymer and free micelles were assumed to have equivalent values of δ_{mic}. Even if this assumption is poor, relatively few free micelles are expected over this concentration range. The high concentration region of Figure 4-19 would be nonlinear if this simplification were inappropriate.

An independent estimate of the degree of surfactant binding was obtained by comparing the surfactant and polymer diffusivities (presented in the following section). In the dark photostationary state with 100% *trans* isomer, the amount of free surfactant is negligible and thus y_{mon} was set to zero. At low concentrations in the UV photostationary state (96-97% *cis*) , about 10% of the surfactant is free in solution, so in this case y_{mon} was set to 0.10.

With Equation (4.9) reduced to two terms for the dark-adapted state, only an estimate for δ_{bound} was left required to fully specify the system. Somewhat arbitrarily, the shift observed at 0.5 mM in the dark-adapted data was chosen to represent δ_{bound} for the *trans*. This selection in effect sets the dark-adapted CAC to 0.5 mM, so some error will be introduced at lower concentrations if the true CAC is much different from that. The choice appears reasonable because the observed shifts of the residual *trans* in the UV state also approach this *trans* δ_{bound} . Some dramatic shift in either *trans* series in the unobserved lower concentrations would be required to introduce a strong error.

The fraction of *trans* surfactant that is bound to the polymer but exists outside any micelle was therefore found by rearranging Equation (4.9):

$$y_{mic} = \frac{\delta_{obs} - \delta_{mic}}{\delta_{bound} - \delta_{mic}} \tag{4.10}$$

The analysis of the UV data requires consideration of all three sites labeled in Figure 4-18. The free surfactant chemical shift δ_{mon} was taken from dilute surfactant-only solutions. An estimate for δ_{bound} was then found by assuming there were no micelles at the lowest concentration (0.5 mM) and that 10% of *cis* surfactants were free at that concentration. It was then possible to estimate the remaining site populations, y_{mic} and y_{bound}.

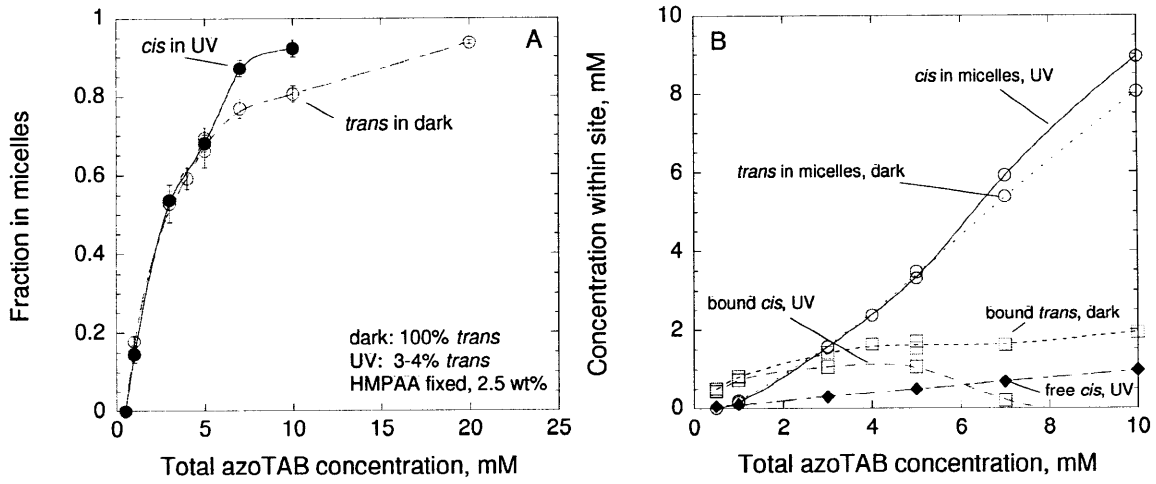

Figure 4-20 Surfactant populations. All data measured at a constant polymer content of 2.5 wt%. A: Fraction of azoTAB existing within micelles. Calculations are performed on data from the aromatic and the headgroup protons. Error bars show the 95% confidence intervals based on the spread of results from the different protons. Underlying assumptions add further uncertainty, especially for the UV state; see text. B: Concentrations of azoTAB as free monomer, bound monomer and in micelles. Dark samples are 100% *trans* while UV samples are 96-97% *cis*. The residual *trans* in the UV samples is not included in either plot. Curves are drawn to guide the eye.

The calculated surfactant populations are shown in Figure 4-20. These should be taken as semi-quantitative, due to the number of assumptions therein. In the dark-adapted state, the concentration of non-micellar *trans* surfactant remains in the range of 1-2 mM once the total azoTAB concentration exceeds 2 mM. This region of relatively constant monomer concentration is familiar from more

traditional micellar systems. It is also apparent that *cis* azoTAB in the UV samples and *trans* in the dark are similar in their propensity to form some sort of aggregate. However as discussed above, there are many indications that the crosslinking ability of these aggregates differ. Some of the other features of the UV-state curves may be artifacts of the method taken; the application of a constant free surfactant percentage of 10% may have led to unrealistic results.

4.4.3. Polymer chemical shifts

4.4.3.1. Polymer solutions

The hydrophobically-modified polymer also takes part in the self-assembly of aggregates; this interaction is necessary for cross-linking to take place. Like the surfactant chemical shift, the ^{1}H shift of the hydrophobic grafts should also reflect the multiple sites pictured in Figure 4-2. The grafts can be involved in intra- or inter polymer associations, they can form mixed micelles with azoTAB, and they can be entirely unassociated. Surfactant monomers can also bind to the polymer near the grafts without any cooperative aggregate formation.

Inter-polymer associations become more pronounced as the concentration of the amphiphilic polymer is increased, even in the absence of surfactant. ^{1}H NMR spectra of HMPAA solutions should therefore show some concentration dependence. No concentration dependence is seen for the backbone polymer peaks; the polymer backbone is not expected to participate directly in aggregate formation so this is as expected. A weak trend in the side chain chemical shifts is observed in Figure 4-21, and no additional peaks are apparent as the polymer concentration is increased. This behavior is consistent with fast exchange of side chains into and out of aggregates. These measurements are only reproducible within +/- 0.002 ppm, so the trend is barely strong enough to be observed. Since the chemical shift of the associated side chain cannot be found from these data, Equation (4.2) cannot be used to estimate the free and aggregated fractions. Previous publications indicated slow exchange in similar measurements [68, 92], but these used ^{19}F NMR instead of ^{1}H. Chemical shifts in fluorine NMR are more sensitive to environment changes than in proton NMR [93], so the difference in frequency between free and associated forms will be larger in fluorine NMR. According to Equation (4.1) , the NMR time scale will then be smaller in ^{19}F NMR than in ^{1}H NMR. Therefore the same chemical exchange can be slow in one NMR experiment, and fast in another. This result shows why similar experiments are often performed on fluoropolymers using fluorine NMR, as it is easy to calculate the population of grafts in different sites by integrating well-separated peaks. Fluorination was avoided in this work, as it alters the aggregation processes that are being examined.

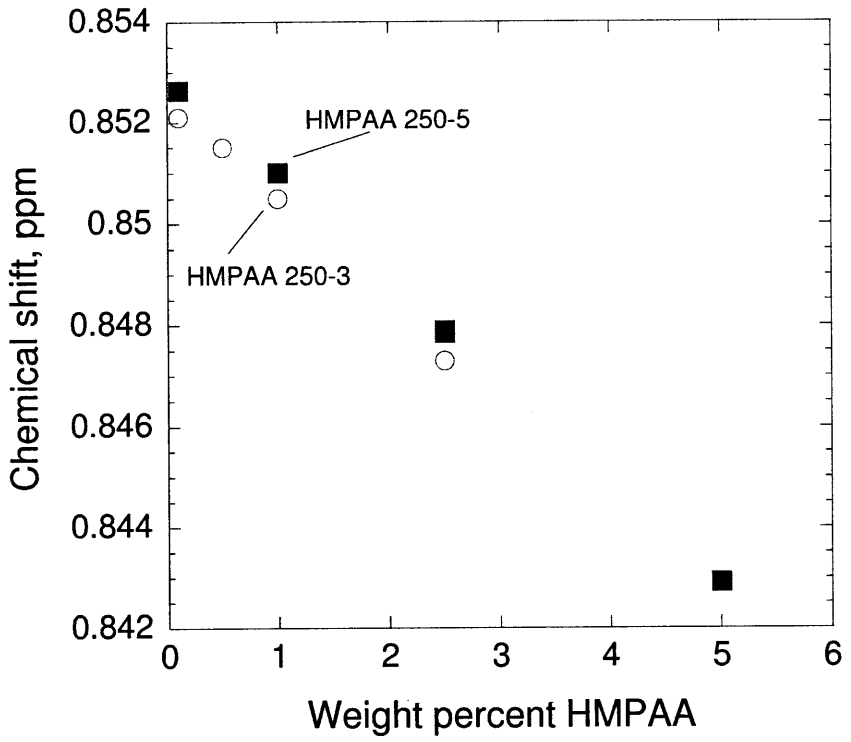

Figure 4-21 Chemical shifts of HMPAA hydrophobe, terminal methyl group. Change in shift with polymer concentration is indicative of interpolymer association. Hollow and solid markers: HMPAA with 3 and 5% of repeat units modified, respectively.

4.4.3.2. Polymer-surfactant mixtures

Upon the addition of surfactant, there are several distinct environments in which the hydrophobic side chains may be found, as illustrated in Figure 4-22.

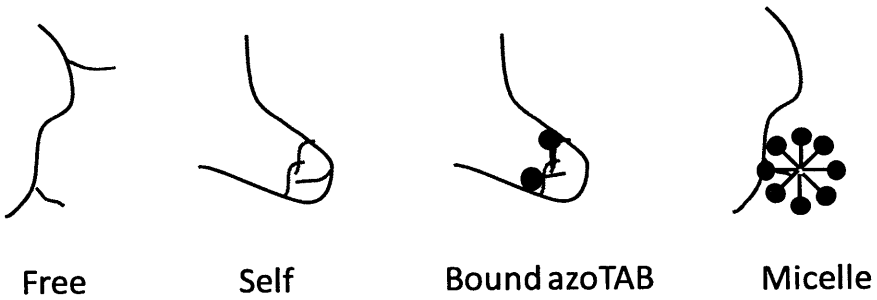

Figure 4-22 Possible sites for hydrophobic side chains (in red) in solutions with or without surfactant (green). "Free" denotes side chains that have not formed any sort of aggregate or complex. "Self" denotes side chains that have formed loose aggregates with other side chains; these aggregates may be intra- or intermolecular. The chemical shift data of Figure 4-21 reflect exchange between "free" and "self" sites. "Bound" refers to side chains located where surfactant has non-cooperatively bound to the polymer; this binding may take place where there were already "self" aggregation sites. "Micelle" denotes side chains incorporated in well-developed surfactant micelles.

If NMR were sensitive to the differences between these sites, then the side chain peaks would either shift (fast exchange), or entirely new peaks could be observed (slow exchange). Representative spectra in the dark adapted state are given in Figure 4-23.

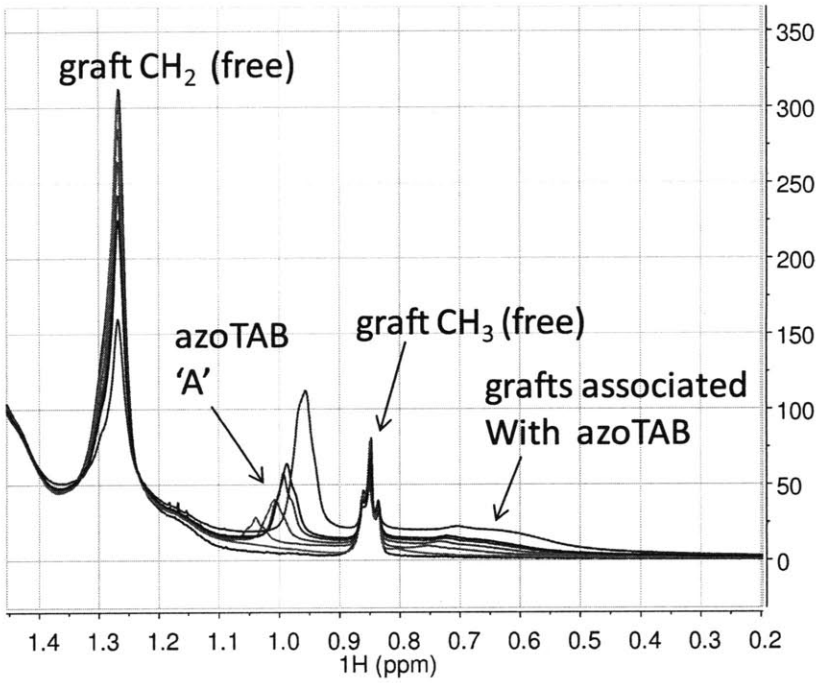

Figure 4-23 Portion of ^{1}H spectra of HMPAA-azoTAB gels in dark-adapted state. HMPAA is fixed at 2.5 wt %. Concentrations of azoTAB: 0 mM (red), 0.5 mM (gold), 3 mM (light green), 5 mM (green), 7 mM (light blue), 10 mM (dark blue), 20 mM (purple). Spectra are normalized such that HMPAA CH peaks are of equal intensity. Broad upfield peak is attributed to HMPAA grafts solubilised by azoTAB micelles, or associated with non-cooperatively bound azoTAB. The previously observed peaks for the grafted chains are labeled as 'free', but can also correspond to side chains aggregating primarily with each other.

The intensity of the azoTAB peak increases with the azoTAB concentration, as expected. The azoTAB peak also moves upfield, in accord with the other azoTAB peaks as shown in Figure 4-13B. These observations are consistent with fast exchange of the surfactant between the monomer and micellar states. The HMPAA hydrophobic groups show a different behavior. The peak positions do not appear to move, but the intensity of the graft CH_2 peak is greatly reduced with increasing azoTAB concentration. The missing peak area is likely appearing in the broad signal that appears between 1.1 and 0.4 ppm, overlapping with the graft CH_3 peak and the azoTAB peak. This broad signal may correspond to polymer grafts participating in azoTAB micelles, or are otherwise associated with bound azoTAB ("bound" in Figure 4-22). The original well-defined side chain peaks are attributed to unassociated HMPAA grafts or grafts aggregating loosely with each other ("free" or "self"). As the new surfactant-related peak is distinct from the original one, the exchange of side-chains into and out of the surfactant micelles is slow

compared to the NMR time scale. There should also be a reduction in the area of the graft CH_3 peak, but this is not as readily apparent because that peak overlaps with the broad micelle peak. The broad peak itself drifts upfield with increasing azoTAB concentration; this movement may be an indication that several different micellar environments are present, or of some balance between the "bound" and "micelle" sites. The spectrum in Figure 4-23 is qualitatively similar to that reported in the literature for another polymer-surfactant system (Figure 4-7), with the exception that the spectrum from this work does not show an obviously separate peak for side chain-dominated micelles.

It is noteworthy that the exchange of polymer side chains into and out of aggregates composed of side chains occurs more quickly than exchange into surfactant-rich micelles. In the absence of surfactant, the polymer side chains are unable to form aggregates that are as stable as surfactant micelles.

The fraction of hydrophobic grafts associated with azoTAB can be estimated from the reduction of the area of the graft CH_2 peak at 1.26 ppm in comparison to a sample without azoTAB. To allow this calculation, the spectra are first normalized (as seen in Figure 4-23) such that the polymer backbone CH peaks have the same absolute integrated area in each spectrum. The CH peak is chosen as the reference because it is apparently unaffected by the addition of azoTAB. The results for both dark-adapted and UV-adapted HMPAA-azoTAB mixtures are given in Figure 4-24. Just as the azoTAB appeared roughly equally likely to form micelles under either light condition, the polymer side chains are equally likely to associate with azoTAB regardless of the light condition.

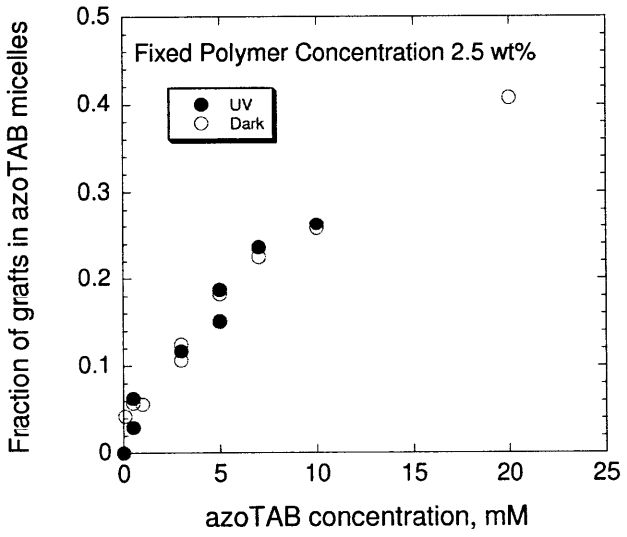

Figure 4-24 Fraction of polymer side chains that are incorporated in surfactant-rich micelles, or are otherwise associated with azoTAB molecules. Measurement at 20 mM in UV-adapted state is not possible due to the difficulty in reaching photostationary state at the thick optical density of that sample.

Despite this similarity between dark- and UV-adapted states, the spectra under the different light conditions have strong qualitative differences.

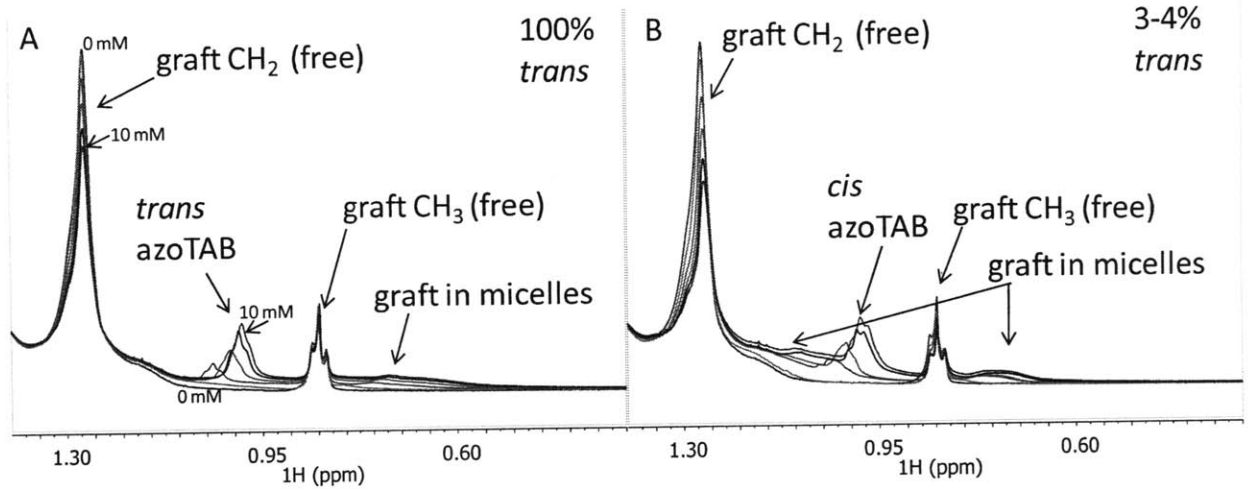

Figure 4-25 Portion of ^{1}H spectra of HMPAA-azoTAB gels in dark-adapted (A) and UV-adapted (B) states. HMPAA is fixed at 2.5 wt %. Concentrations of azoTAB: 0 mM (red), 0.5 mM (gold), 3 mM (light green), 5 mM (light blue), 7 mM (purple), 10 mM (light purple). Spectra normalized so that HMPAA CH peaks are of equal intensity. Terminal methyl azoTAB peak ('A') is visible, in addition to polymer side chain peaks. Well-defined polymer peaks that are present at 0 mM are assigned to un-aggregated (free) or loosely self-aggregated side chains (self). As surfactant concentration is increased, area is shifted from these well-defined peaks to broad peaks lying upfield, attributed to side chains incorporated in surfactant micelles or otherwise associated with bound surfactants. These broad peaks are different in position and appearance between the dark- and UV-adapted states, suggesting some difference in environment.

In both photostationary states, the area of the free side chain CH_2 peak decreases as the azoTAB concentration is raised. This area is shifted to very broad peaks that lie upfield, corresponding to side chains located in micelles. The free graft methyl peak is also reduced, but less noticeably due to the overlap with the broad peaks. However the characteristics of the broad peaks are strongly dependent on the light condition. In the dark-adapted state, the micellar peak is spread out between 1.1 and 0.4 ppm, whereas in the UV-state there appear to be two sets of somewhat narrower peaks. These differences between dark and UV spectra may reflect a different balance between the "bound" and "micelle" sites. The differences in peak width could also be related to relaxation effects. NMR line broadening occurs when the relaxation rate is high, which in turn occurs when molecules are relatively immobilized in close proximity to each other. This is because relaxation takes place through internuclear interactions; these interactions are more likely to take place when the molecules have close neighbors. Increased line broadening in the dark-adapted samples would indicate that the *trans*-rich micelles are more stable aggregates than the *cis*-rich micelles found in the UV state. This difference in stability would again be consistent with the idea that *cis*-rich micelles may indeed form and solubilise the polymer side chains, but

are not very effective crosslinkers with regards to rheological properties. These results are analysed further in the Discussion section.

4.4.4. Polymer diffusivity

4.4.4.1. General approach and results for unmodified polymer

The nature of the polymer network can also be characterized by measuring the polymer diffusivity under different conditions. This appears to be an underappreciated method for studying thickening or gelation in polymer-surfactant systems, though not it is not unprecedented [94]. The observed diffusivity should be a function of the size of the polymer coils or clusters. Clusters can form as a result of entanglements or crosslinking via the hydrophobic side groups and surfactant micelles. At any given combination of polymer and surfactant concentration, there will be some distribution of cluster sizes and correspondingly, a distribution of diffusivities. As the degree of crosslinking increases, larger and larger clusters will appear within this distribution, such that the observed diffusivities would be expected to decrease.

The diffusion coefficient can be related to the hydrodynamic radius of the polymer or cluster though the Stokes-Einstein equation:

$$R_H = \frac{k_b T}{6\pi\eta D} \tag{4.11}$$

where k_b is the Boltzmann constant, η is the solvent viscosity and D is the measured diffusivity. This relation is valid for a spherical particle that is larger than the surrounding solvent molecules, and is at infinite dilution. Deviations are expected due to interpolymer interactions at higher concentrations, as well as polymer-solvent interactions that might swell the polymer [95] and intra-polymer aggregation that could contract it. The hydrodynamic radius will be similar in magnitude to the radius of gyration; for NaPAA in dilute solution it was empirically found that [96]

$$\frac{R_H}{R_G} = 0.68 \tag{4.12}$$

which is comparable to theoretical predictions for linear polymers in a theta solvent [97-100]. A hydrodynamic radius can always be calculated using the Stokes-Einstein equation, but it would not always have a clear relationship to the radius of gyration like that given in Equation (4.12).

When multiple components appearing at the same NMR chemical shift have different diffusivities, the exchange rate of nuclei between the various components becomes relevant. If this exchange rate is fast compared to the diffusion time in the experiment, then the resulting Stejksal-Tanner plot is linear and a number-averaged diffusivity is observed (Equation (4.6)). If the observed nuclei do not exchange between components of different diffusivities during the time scale of the experiment, the Stejksal-Tanner plot will exhibit curvature as per Equation (4.7). Such a curvature was observed for the PAA and HMPAA used in this work (see example in Figure 4-26). The various diffusion coefficients can be extracted from the data though the use of Equation (4.8). To avoid overfitting, the analysis was done for only two modes of diffusion, one fast and one slow. In general, the fast mode could correspond to individual polymer coils, while the slow mode would be related to large crosslinked clusters. However, a successful fit of two diffusivities to the data does not necessarily mean that there is a strictly bimodal distribution of diffusivities. Also, crosslinking is not required for a distribution of diffusivities to be observed; the polydispersity of the original polymer and entanglements will also lead to a variety of diffusion modes.

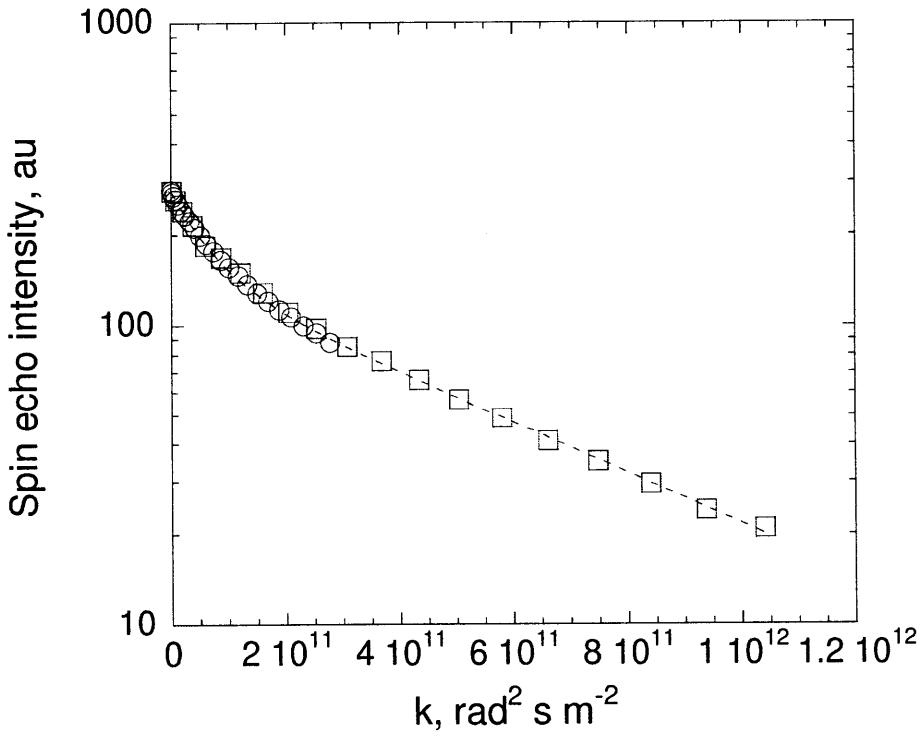

Figure 4-26 Stejskal-Tanner plot for 2.5 wt% NaPAA in deuterium oxide. Broken line is the fit to the 2 component diffusion model. Data are from the CH peak. δ is 5 ms. Circles, Δ is 505.2 ms. Squares, Δ is 2505.2 ms. The curvature of the plot signifies multiple diffusion coefficients. At high vales of k, the signal due to the faster components becomes negligible and the plot becomes linear. The slope of the linear section

can be taken as the slow component diffusivity. The spin echo intensities can be considered arbitrary units, so the curves have been adjusted vertically along the ordinate such that their magnitudes overlap. This adjustment does not impact the slopes. See text.

To allow reliable fitting of multiple components through Equation (4.8), the data must span a wide range of $q^2\left(\Delta-\frac{\delta}{3}-\frac{\tau}{2}\right)$ values (hereafter referred to as 'k'). This is easily possible using NMR probes specially purposed for diffusion studies; these can generate magnetic field gradients as large as 9 T/m [94]. Such a probe was not available for this work; the majority of experiments were done on a probe only capable of generating gradients up to 0.55 T/m. This instrument then failed and the experiments were completed with a maximum gradient of 0.34 T/m. In order to access the high k region by using these weak gradients (q is proportional to the gradient strength), diffusion times Δ as long as 2.5 or 3 seconds were required. These times are longer than what is generally used in NMR diffusion studies (100 to 500 ms), so experiments were also done at shorter times to judge whether the observed diffusivity was a function of the diffusion time. If the diffusion were hindered by certain physical barriers within a heterogeneous field, then the diffusivity would be dependent on the time allowed for motion. For example, a particle that is allowed to move freely within a box would have an apparent diffusivity that decreases as the observation time is increased. The true diffusivity would only be observed at short times when the particle would not be expected to encounter the boundaries imposed by the box.

A Stejskal-Tanner plot for NaPAA is presented in Figure 4-26, using diffusion times of both 0.5052 s and 2.502 s. The curvature in the plot is apparent in either case, and the trajectory of the two curves agree well over the span of k they have in common. This agreement suggests that the observed diffusivities are not strong functions of the diffusion time, so there should be little bias caused by using the longer times. It is also clear that additional information is collected through the use of the longer diffusion time; as discussed below the linear portion of the data at high k is required for accurately estimating the slow diffusivities.

It should be noted that this plot has curvature, despite NaPAA lacking any hydrophobic side chains. The slower components of NaPAA therefore cannot be attributed to a physically crosslinked cluster. In this case, a distribution of diffusivities may be expected due to the polydispersity of the polymer. The slower components may be due to the larger coils, as well as entangled coils. The weight fraction used here (2.5 wt%) is estimated to be somewhat above the overlap concentration, so some entanglements are expected in this semi-dilute solution. The combined effects of polymer polydispersity and mild entanglements

would not necessarily be expected to result in a bimodal distribution of diffusion coefficients, so in this case the 2-component fit may not be entirely appropriate.

Nilsson et al attempted to account for such polydispersity by assuming a log normal distribution of polymer diffusivities and then also fitting the width of the distribution [94]. Hansen et al fit three diffusivities to the data, with the fast and medium modes bounding the effects of polydispersity and the slow mode corresponding to the growing polymer network (though the authors did not explicitly make the latter connection) [65]. Hansen followed that analysis by replacing the fast and medium modes with a Raleigh distribution, in which the median diffusivity and the width of the distribution were fit. It is felt here that fitting yet another parameter from these data, whether a third diffusivity or the width of some distribution, is not strongly justified and would result in overfitting. It is also difficult to know what shape distribution is most appropriate for the faster modes. Some indication of the effect due to polydispersity could be had from DLS measurements in dilute solution, but that distribution would not be expected to hold as entanglements and crosslinking occur at higher polymer concentrations and as surfactant is added.

At high values of k in Figure 4-26, the signal due to the fast component becomes negligible, and the remaining linear section represents the slow component. Simply finding the slope in this region would yield the value of the slow diffusivity. In this case, this is $1.88*10^{-12}$ m^2/s, with 95% confidence intervals of +/- $1.49*10^{-13}$ m^2/s. This value could then be fixed when fitting the fast diffusivity by using Equation (4.8). Alternately, both diffusivities could be fit. Results of this optimization are given in Table 4-1, obtained through multiple methods.

Table 4-1 Fast and slow components of diffusion for NaPAA, 2.5 wt%. Results of different fitting methodologies are shown. Values are fit from bi-exponential data, unless denoted as 'fixed'. Fixed values are obtained directly from the linear portion of curve in Figure 4-26.

Diffusion time, ms	505.2	505.2	2505.2	2505.2	Combined data	Combined data
Fast, m^2/s	$1.70*10^{-11}$	$1.28*10^{-11}$	$1.27*10^{-11}$	$1.14*10^{-11}$	$1.52*10^{-11}$	$1.26*10^{-11}$
Slow, m^2/s	$2.59*10^{-12}$	$1.88*10^{-12}$ (fixed)	$1.94*10^{-12}$	$1.88*10^{-12}$ (fixed)	$1.95*10^{-12}$	$1.88*10^{-12}$ (fixed)

Either of the curves measured at different diffusion times can be analysed independently, or the two curves can be combined into a single series and then processed. As might be expected, the slow component cannot be accurately found by using the shorter diffusion time data alone. This finding underlines the necessity for using long diffusion times. The other best fit values in Table 4-1 for the slow component are within the margin of error of the value found by calculating the slope of the linear portion of the curve in Figure 4-26.

There is some scatter among the fitted diffusivities of the fast component. Given the relative magnitudes and prevalence of the fast and slow modes, it was found through use of synthetic data that it is necessarily more difficult to extract accurate values for the fast mode. As a result of these factors, an uncertainty of at least 20-30% can be expected to apply to the fast mode diffusivity. The physical significance of the magnitude of the fast diffusivity is discussed in the following section.

Analysis on all other samples was done by combining all the data measured at different diffusion times, and then fitting both modes (as in the second-to-last column in Table 4-1). This method was chosen because it maximizes the range of 'k' used in the fit. Combining different spin echo intensity curves requires the scaling of each curve by some factor, such that they all overlay on each other. The effect of this adjustment is merely to shift the curves vertically on the Stejskal-Tanner plot; the slopes are unaffected. It is unclear whether this method has been previously reported in the literature, so any limitations must be considered. The method would be invalid if there were resricted diffusion causing different apparent diffusivities to be observed at different diffusion times; this would cause the shapes of the curves to be dependent on the diffusion time. As discussed above, this possibility is discounted because the curves actually do overlay fairly well. Another requirement for combining the data in this manner can be derived from Equation (4.7). The curves measured at different diffusion times can only be expected to overlay well on each other if the nuclear relaxation rates of fast and slow component are equivalent. The peak linewidths in the spin echo spectrum provide some qualitative indication of the spin-spin relaxation time T_2, and these linewidths do not change as the signal due to the fast component decays away, leaving behind only the slow component. However it is difficult to assess whether the spin-lattice relaxation time T_1 varies among the fast and slow components. Because of these limitations, the other methods of estimating diffusivities were also monitored, to ensure they were broadly consistent with that reported here.

4.4.4.2. Comparison of modified and unmodified polymer

The physical relevance of the fitted diffusivities is clarified somewhat by comparing the unmodified polymer NaPAA to the modified HMPAA:

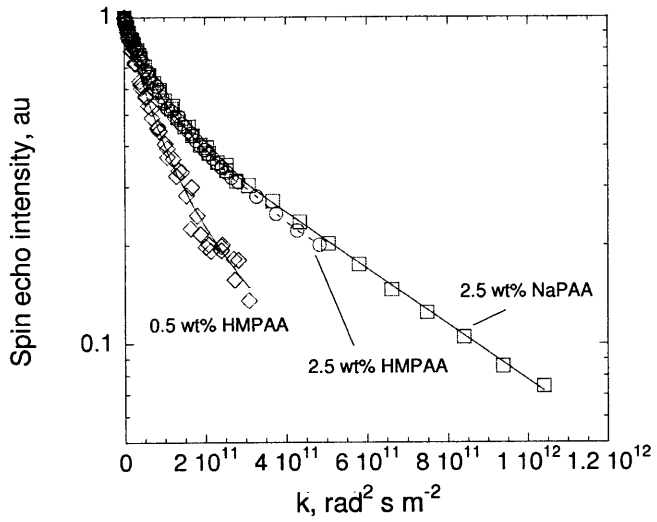

Figure 4-27 Stejskal-Tanner curves for 2.5 wt% NaPAA, 2.5 wt% HMPAA and 0.5 wt% HMPAA. 2.5 wt% is semidilute, while 0.5 wt% is dilute. Lines denote best fit to 2-component model. Diffusion times used: 505 and 1005 ms for HMPAA samples; 505 and 2505 ms for PAA samples. Poor signal/noise at the lower concentration precluded measurements at higher k values. Observation of 2.5 wt% HMPAA at higher k would have been desirable, but was prevented by failure of the instrument.

The spin echo attenuation curve for 2.5 wt% HMPAA is very similar to that of 2.5 wt% NaPAA. This indicates that the diffusion coefficients in either sample are similar, despite the fact that HMPAA is able to aggregate via its hydrophobic side chains and NaPAA is not. In contrast, the diffusion of 0.5 wt% HMPAA is markedly faster, and the decay curve is approaching linearity. The latter concentration is below the estimated overlap concentration, so fewer entanglements are expected.

These results suggest that at 2.5 wt%, there is insufficient interpolymer crosslinking in the modified polymer to create polymer clusters larger than what already effectively results from simple entanglements. Also, much of the slow diffusion component in the 2.5 wt% samples can be attributed to entanglements, as opposed to larger coils from the originally polydisperse polymer.

In samples shown above, the fast diffusivity was on the order of $1*10^{-11}$ m^2/s to $2*10^{-11}$ m^2/s. This range corresponds to hydrodynamic radii of 10-20 nm, or using Equation (4.12), radii of gyration between 15 and 30 nm. These values are consistent with the hydrodynamic radius obtained from dynamic light scattering on dilute polymer samples, 17 nm. An extrapolation from literature values for NaPAA yields an expected hydrodynamic radius of 18 nm [96], also consistent with the estimates here. The extrapolation was based on the hydrodynamic radius scaling with molecular weight as $R_h \sim MW^{0.56}$, as determined from the data given by the source. The fast component is thus attributed to individual

polymer coils; the broad range in the calculated fast diffusivities is due to both polydispersity and the difficulty in isolating the fast component contribution to the spin echo data.

4.4.4.3. HMPAA-azoTAB mixtures: HMPAA

Interaction with *trans* azoTAB has dramatic effects on the observed HMPAA diffusivities, as seen in dark-adapted samples, Figure 4-28:

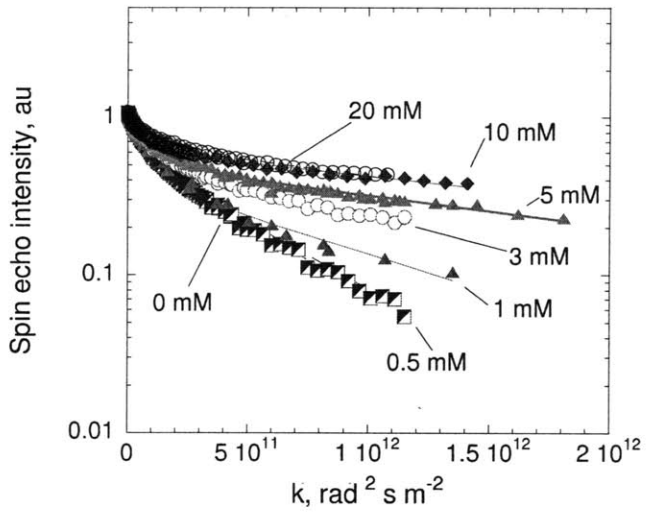

Figure 4-28 Stejskal-Tanner plots for HMPAA backbone CH group, in mixtures with azoTAB in deuterium oxide. Faster decay of the spin echo indicates faster diffusion. All samples are in the dark-adapted state, so azoTAB is 100% *trans*. HMPAA concentration is fixed at 2.5 wt%. azoTAB concentration varies as labeled in the plot. Data points for 0 mM (no azoTAB) are entirely obscured by 0.5 mM azoTAB series. Lines are drawn for best-fit results of the two-component model. Data are collected at δ of 5 ms and a variety of diffusion times ranging from 0.5 s to 3 s; data from different diffusion times are combined as described in previous section.

As in the previous section, there will be some distribution of polymer diffusivities in these samples with azoTAB. At 0 mM azoTAB, it was determined that this distribution is due to the presence of both entangled and free polymer coils, as well as the polydispersity of the original polymer. There appears to be little change from this configuration at the lowest observed azoTAB concentration, 0.5 mM. Even if azoTAB is aggregating into micelles at 0.5 mM, there would be too few of them at this concentration for there to be much crosslinking. As the azoTAB concentration is raised above 0.5 mM, there is a marked decline in the observed diffusivities. In this range, the formation of micelles leads to crosslinked clusters of polymers; the sizes of these clusters increase as the number density of the micelles increases.

For a quantitative analysis of these data, Equation (4.8) is again used to determine two diffusivities representative of the variety of clusters in the samples. It would be ideal if data could be collected at

higher k values in order to better constrain the slower components, but the available NMR probe was limiting in this respect. However, the differences between the different decay curves in Figure 4-28 are stark enough that the resulting trends should be reliable, even if there is some uncertainty in the magnitude of the slow component.

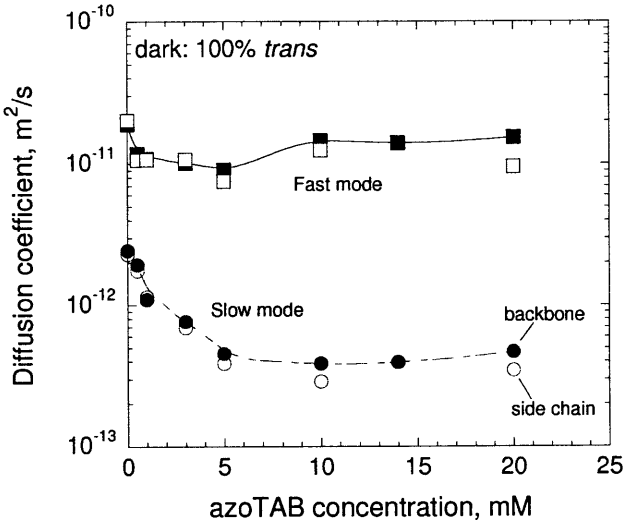

Figure 4-29 Best fit values of polymer diffusivities in dark-adapted HMPAA-azoTAB mixtures, using 2-component model. Fast mode corresponds to individual polymer coils and small clusters. Slow mode is attributed to large well crosslinked polymer clusters. Solid markers: signal from polymer backbone CH groups. Hollow: signal from terminal methyl group of hydrophobic side chains. Smoothed lines drawn to guide the eye. HMPAA fixed at 2.5 wt%.

Upon fitting the two diffusion coefficients (Figure 4-29), the fast component remains within the range of $1*10^{-11}$ m^2/s to $2*10^{-11}$ m^2/s obtained in the absence of any surfactant. This diffusion mode is thus still identified with individual polymer coils of various sizes and smaller clusters, based on the expected hydrodynamic radius of those forms. The slow component however responds strongly to the addition of surfactant, and the shape of this concentration dependence is strongly reminiscent of the corresponding chemical shift data of *trans* azoTAB in dark-adapted mixtures (Figure 4-15). Taken together, the surfactant chemical shift and polymer diffusivity data indicate a CAC somewhere below 1 mM, with crosslinking micelles forming as the azoTAB concentration is increased. These results are also consistent with the viscosity measurements of Figure 4-4. The viscosity data also show a maximum around 15 mM in the dark-adapted state; the slow diffusion coefficients exhibit a corresponding minimum which is made more apparent in a later figure.

The minimum slow diffusivity was found to be about $3.9*10^{-13}$ m^2/s, from 10 mM to 14 mM. While the Stokes Einstein equation may not be entirely applicable in this regime, it can be used to give an effective

hydrodynamic radius. This radius is about 500 nm, and presumably the actual dimensions of the cluster are commensurately large. This is well larger than an individual polymer coil, and it approaches macroscopic dimensions. Such dimensions are an indication that a gel, defined as a crosslinked network with macroscopic dimensions, is formed in these mixtures.

The diffusion coefficients have thus far been interpreted as describing the translation of a polymer coil or cluster, moving as a single unit. Rotations and undulations through which one part of a polymer moves relative to another section have been neglected. This assumption was assessed by consideration of the translational distances being observed. Using $\sqrt{2D\Delta}$ as the length scale of the movement with a diffusion time Δ of 2.5 seconds, the minimum diffusivity corresponds to motion of about 1.4 microns. This distance is over twice the effective hydrodynamic radius of those largest clusters. The fast diffusivities correspond to diffusion lengths of 5 microns. The fast mode can certainly be ascribed to pure translation. The slow mode is also mainly translational in nature, but other motions may also be relevant in the most highly crosslinked samples. The diffusivities of both the polymer backbone and the side chains were given in Figure 4-29, and the side chain slow mode diffusivities tend to be lower than those of the backbone. This effect is stronger in the more strongly gelled samples, 10 mM and above (see Table 4-2). It is possible that the side chains appear to diffuse more slowly because they are somewhat anchored in the intermolecular crosslinks.

Table 4-2 Slow mode diffusion coefficients of HMPAA, in dark-adapted samples. Data at 14 mM was too noisy to allow analysis of the side chain signal.

[azoTAB], mM	Slow diffusion coefficient Backbone CH , m^2/s	Slow diffusion coefficient Side chain CH_3 , m^2/s	Ratio of D, side chain/backbone
0	2.44E-12	2.3E-12	0.94
0.5	1.94E-12	1.75E-12	0.90
1	1.1E-12	1.15E-12	1.05
3	7.66E-13	6.95E-13	0.91
5	4.56E-13	3.87E-13	0.85
10	3.87E-13	2.88E-13	0.74
14	3.95E-13		
20	4.67E-13	3.48E-13	0.74

There are fewer polymer diffusivity measurements available in the UV-adapted state, but it is apparent that smaller clusters are present in the UV state, as indicated by the faster diffusion coefficients:

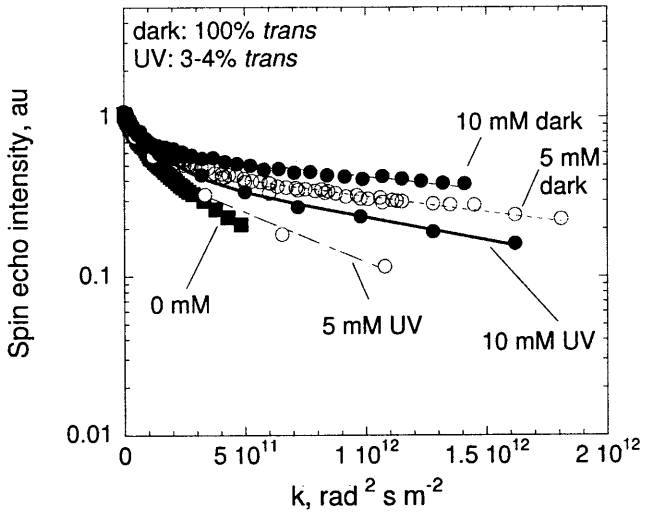

Figure 4-30 Stejskal-Tanner plots for HMPAA backbone groups in mixtures with azoTAB in deuterium oxide, in dark-adapted (red) and UV-adapted (blue) conditions. azoTAB concentrations: 5 mM (hollow markers) and 10 mM (solid markers). Polymer concentration is fixed at 2.5 wt%. Black squares: HMPAA without azoTAB. Lines are the results of fitting to the two component model. Faster decay indicates higher diffusion coefficients.

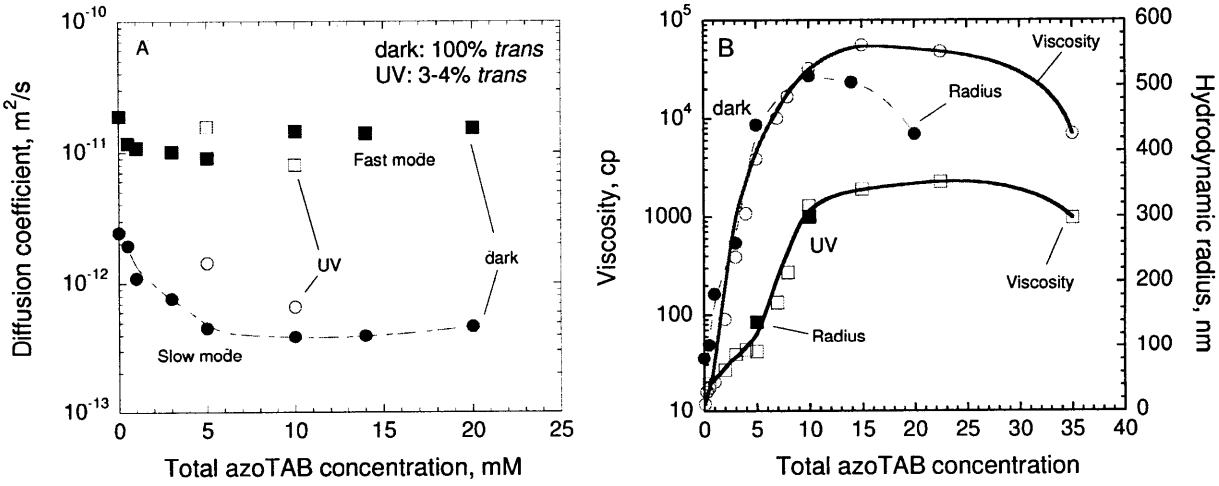

Figure 4-31 Polymer diffusivity and viscosity of HMPAA-azoTAB mixtures at different azoTAB concentrations and in both the dark- and UV-adapted states. HMPAA fixed at 2.5 wt%. A: Fitted diffusion coefficients using two component model, calculated using CH groups of HMPAA backbone. Solid markers: dark-adapted state. Hollow markers: UV-adapted state. B: Hollow markers: corresponding low-shear viscosity measurements, of Lee et al [47]. Solid markers: the effective hydrodynamic radius calculated from the slow diffusion mode, plotted on secondary ordinate. All lines drawn only to guide the eye.

The spin echo signals decay faster in the UV state than in the dark-adapted state for any given azoTAB concentration (Figure 4-30). On applying the two-component model, the slow component diffusivities are clearly faster in the UV state (Figure 4-31A). The differences between the light conditions are consistent with those seen in the viscosity measurements. The Stokes-Einstein equation was used to calculate the effective hydrodynamic radius for the slow diffusion mode. This radius scales with concentration similarly as the logarithm of viscosity, though the radius goes through a maximum somewhat earlier than the viscosity (Figure 4-31B). This relationship provides a bridge between macroscopic dynamic measurements like viscosity and the molecular level information provided by NMR. These results also confirm that photo-reversible gelation can occur at the appropriate concentrations of azoTAB.

In addition to the diffusion coefficients themselves, fitting the experimental data against Equation (4.8) also yields the fraction of polymer chains within each diffusion mode. This calculation is only valid if the nuclear relaxation times T_2 and especially T_1 are the same for both the fast and slow diffusing polymer components. As discussed above, assuming this equivalence appears to be reasonable.

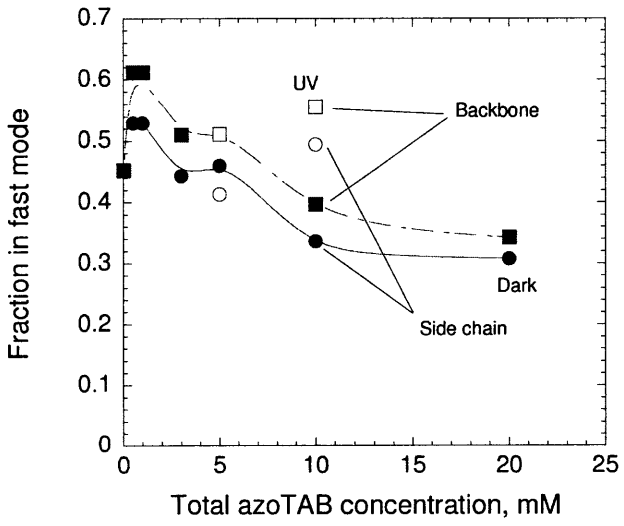

Figure 4-32 Proportion of polymer chains existing in the fast diffusion mode. Dark-adapted state shown in solid red markers. UV in hollow blue. Polymer backbone denoted by squares; side chains by circles. Interpretation is ambiguous, see text. Smoothed curves drawn to guide the eye.

In the dark-adapted state, the fraction of polymer existing in the slow mode (larger crosslinked clusters) generally increases as the azoTAB concentration is increased. This result is expected, as more of the polymer coils should participate in the formation of networks as the crosslink density is increased. These values however lack strong quantitative physical meaning. A strict bimodal size distribution of polymer

clusters is not expected; the analysis was only done in this way for convenience. The physical nature of what is identified here as the slow component is also changing over the observed concentration range. When few crosslinking micelles are present, the slow component might be identified with entangled polymers. As the number density of micelles increases, the slow component becomes more strongly related with crosslinked clusters.

Previous workers have partially addressed this issue by allowing a log-normal distribution of diffusivities for the fast component, and a single diffusivity for the slow component [94]. It is felt that this adds complexity without necessarily better approaching physical reality, and that any assumptions about the shape of the size distributions should come from independent measurements or theory. Such an exploration was outside the scope of this work, so these population fractions should be taken as qualitative, at best.

4.4.4.4. HMPAA-azoTAB mixtures: azoTAB

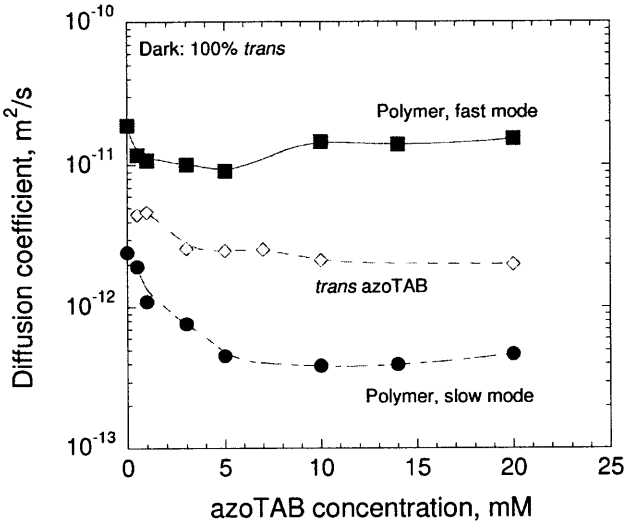

Figure 4-33 Diffusion coefficients of both azoTAB and HMPAA in mixtures of 2.5 wt% HMPAA and varying azoTAB concentration, in the dark-adapted state.

The diffusion of the surfactant also can be followed to provide insight on the nature of the surfactant-polymer mixture. The variety of possible sites for the surfactant in Figure 4-2 must again be considered. The surfactant may be found free in solution, bound non-cooperatively to the polymer, in free micelles, or micelles bound to the polymer. Further, the diffusion coefficient of the bound surfactant would depend

on the size of the polymer cluster to which it was attached. To reduce the number of possible sites somewhat, in can be assumed that it is irrelevant whether a polymer-bound surfactant is in a micelle or not; its diffusivity will be set by the size of the associated polymer cluster.

The Stejskal-Tanner plots for azoTAB were linear, as expected given that it was already determined that the exchange of surfactant between the various sites is fast. The measured diffusivity (see Figure 4-33 for dark-adapted samples) is thus a population-weighted average of the diffusivity of each site, per Equation (4.6). With the assumptions being made here, this average can be expressed as

$$D_{obs} = y_{free} D_{free} + y_{mic} D_{mic} + \int y_i D_i dD \tag{4.13}$$

where D_{obs} is the measured diffusivity, y_{free} is the fraction of surfactant free in solution, y_{mic} is the fraction of surfactant in free micelles, D_{free} is the diffusivity of the free surfactant and D_{mic} the diffusivity of free micelles. The integral is written for the surfactant bound to the polymer, with the index i referring to each value within the distribution of polymer diffusivities.

Given that no attempt is being made to describe that polymer distribution in a rigorous way, the bound surfactant term can be rewritten in terms of the two-component assumption for the polymer.

$$D_{obs} = y_{free} D_{free} + y_{mic} D_{mic} + (1 - y_{free} - y_{mic})\left[f_{fast} D_{fast} + f_{slow} D_{slow} \right] \tag{4.14}$$

where f_{fast} and f_{slow} are the fraction of polymer in the fast and slow modes, and D_{fast} and D_{slow} are the corresponding polymer diffusion coefficients. The polymer fractions will not be entirely physically realistic due to the reasons given in the previous section.

The diffusion coefficient of free surfactant was measured in Chapter 3 to be $4.2*10^{-10}$ m^2/s. This was measured for dilute azoTAB in aqueous solution, and is denoted D_0. However even free surfactant in polymer solutions will have diffusion more restricted than this, due to obstruction effects or increased drag (see Solute diffusion section for further discussion). A molecule with the size of azoTAB can be expected to have its diffusivity reduced to about $0.7 D_0$ due to the 2.5 wt% polymer around it. The free surfactant diffusivity is thus taken to be $2.9*10^{-10}$ m^2/s. Likewise the diffusivity of a micelle was found to be $3.66*10^{-11}$ m^2/s, and the reduction factor D / D_0 is estimated to be about 0.55. This results in a value of $2*10^{-11}$ m^2/s for D_{mic}, which is indistinguishable from D_{fast}. Free micelles are anyway only expected

to exist in significant numbers at high surfactant concentrations, beyond the maximum in viscosity, so the free micellar term shall be neglected. As a result, the working expression for the surfactant diffusivity is

$$D_{obs} = y_{free} D_{free} + (1 - y_{free})\left[f_{fast} D_{fast} + f_{slow} D_{slow} \right] \tag{4.15}$$

The free surfactant diffusion coefficient D_{free} is an order of magnitude higher than D_{fast} and at least two orders higher than D_{slow}. An upper limit for y_{free} can thus be calculated by assuming that the polymer-bound terms are negligible. This upper bound is 1-2% throughout the concentration range observed in the dark-adapted state, so it is apparent that very little *trans* surfactant will exist free of the polymer. The variation in azoTAB diffusivity in Figure 4-33 is dominated by the changing size distribution of the polymer.

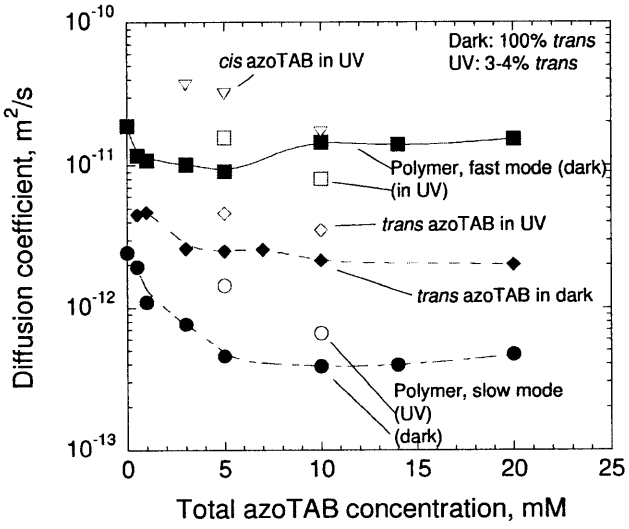

Figure 4-34 Diffusion coefficients of both surfactant and polymer, in both dark- and UV-adapted states. See figure for labels, and text for discussion. Smoothed curves drawn to guide the eye.

The corresponding data for the UV-adapted state are markedly different. The observed diffusivity for *cis* azoTAB is greater than either polymer mode. For this to be possible, some fraction of surfactant must be free in solution. The upper bound for the fraction of free *cis* surfactants is calculated to be about 12%. However the residual *trans* surfactant in the UV state remains almost entirely attached to the HMPAA, as

it was in the dark state. This difference in the propensity of *trans* and *cis* to bind to the polymer was previously inferred from the chemical shift data in Figure 4-15; it is now independently confirmed.

The difference in *trans* azoTAB diffusivity between the dark- and UV- adapted states is yet another indicator of the difference in gelation extent between the two photostationary states.

4.5 Kinetics

4.5.1. Average rate of conversion

The gelation process consists of multiple steps, including the light-initiated isomerisation of azoTAB and the resulting formation or dissolution of crosslinking micelles. The extent of the isomerisation reaction can be directly monitored using ^{1}H NMR. The spectra consist of distinct peaks for the *trans* and *cis* isomers of azoTAB (Figure 2-7); the areas of these peaks can be integrated to provide the isomer composition. Meanwhile the concentration of azoTAB existing inside or outside of micelles can be estimated by following the positions of those ^{1}H peaks as they move upfield or downfield in accordance with Equation (4.9).

The kinetic rate of conversion due to UV irradiation was measured for 5 mM azoTAB samples, both with and without 2.5 wt% HMPAA. Additionally, the experiment with only surfactant in solution was repeated with and without manual agitation between irradiation intervals. When there was evidence of composition gradients (discussed below) the average composition in the sample volume was calculated for each time.

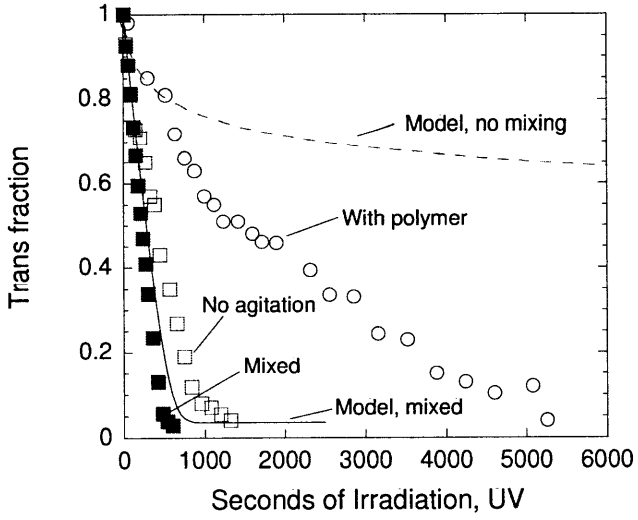

Figure 4-35 Photoreaction trajectory for 5 mM azoTAB samples under UV irradiation. Samples were initially in the dark-adapted state. Sample with 2.5 wt% HMPAA, hollow circles. Surfactant-only solutions denoted by squares; with mixing (solid) and without mixing (hollow). The given composition is averaged over

the entire sample volume, in the case of composition gradients. Irradiance was 4.73 mW/cm^2 for the experiments with polymer and the unmixed surfactant solution, and 4.59 mW/cm^2 for the well-mixed sample. This difference in intensity should have negligible impact. Broken and solid lines: model prediction for unmixed and perfectly mixed sample volumes, respectively.

In Figure 4-49 it is apparent that the conversion from *trans* to *cis* under UV was much slower in azoTAB-polymer gels than in well-mixed surfactant-only solutions. This result was anticipated through application of the models presented in Chapter 2. At azoTAB concentrations of this magnitude, much of the incident light is absorbed by a skin layer of molecules at the front of the sample. Conversion is fast in this layer, but is much slower at longer path lengths due to the reduced photon flux. This uneven absorption of light leads to composition gradients. Using the Beer-Lambert law to estimate of the thickness of this layer in a 100% *trans* 5 mM sample, 99% of the incident light is absorbed within 0.16 mm. Even in a hypothetical sample of 100% *cis*, 99% of the incident light would be absorbed within 1.3 mm. In the NMR samples used here, the maximum path length is 4.92 mm and the average is 3.87 mm, so these volumes are optically very thick at 5 mM azoTAB. If there were no convective mixing, the average composition would thus change very slowly. However if the sample were actively mixed, each molecule would on average absorb light at the same rate. The rate of conversion would be higher than in the unmixed case. Two photochemistry models were developed for the limiting cases of a perfectly mixed sample (Equation 2.13) and an entirely unmixed sample (Equations 2.20 and 2.21). For simplicity, only one spatial dimension was considered in the model, so the average path length was used in the model. Results from the unmixed model (Figure 2.21C) showed that in a 5 mM azoTAB sample under a similar UV intensity, many minutes or hours could theoretically be required before any substantial conversion is observed at a path length greater than 2 mm.

The rate of conversion in the intentionally mixed surfactant solution agrees well with the prediction of the well-mixed model (solid line in Figure 4-35). The average conversion is slower in the surfactant solution in which agitation was avoided, though it was impossible to maintain a perfectly quiescent sample while transferring it between the lamp and the spectrometer, and inserting it into the spectrometer. Agitation was also avoided for the gelled sample, but its higher viscosity better helped prevent mixing that would have smeared out any composition gradients. The apparent reaction rate in the gel was therefore much slower than in the surfactant solutions, though still not as slow as the prediction for a perfectly unmixed sample (broken line). In principle it would have been possible to reduce agitation further by irradiating the samples *in situ* in the spectrometer [101], but this additional step was left outside the scope of this work. Nonetheless, the apparently slow reaction kinetics in the gel can be entirely explained by the lack

of mixing. While it is not specifically excluded, there is also no need to invoke other mechanisms, such as steric hindrance reducing the reaction rate in polymer-bound surfactant.

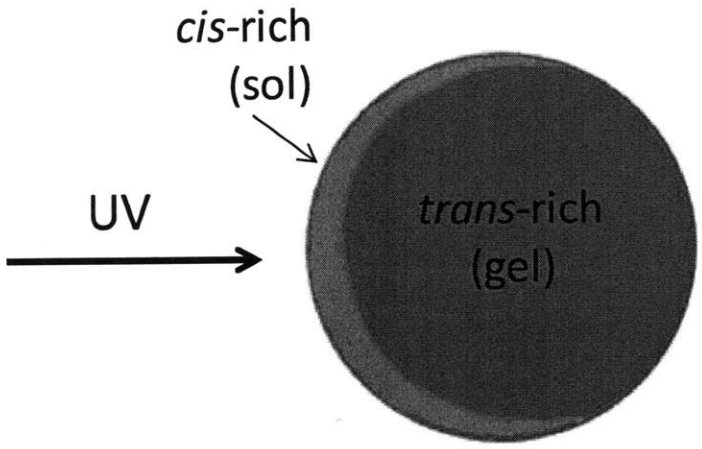

Figure 4-36 Cross section schematic of NMR tube with azoTAB-HMPAA mixture, assuming no convective mixing or diffusion. View: looking down along the axis of the tube. If the sample is initially in the dark-adapted state, it will initially be in a gel. Conversion to the sol will proceed from the side of the tube nearest the light source. The interface between gel and sol will slowly move across tube. It is drawn here as being a sharp interface; diffusion or mixing would cause more gradual gradients.

4.5.2. Composition gradients

Direct evidence for the composition gradients expected to arise in unmixed samples was found by examining the NMR spectra. Selected spectra from the three different kinetics experiments at 5 mM azoTAB are shown in Figure 4-37. Featured are the protons on the azoTAB aromatic rings.

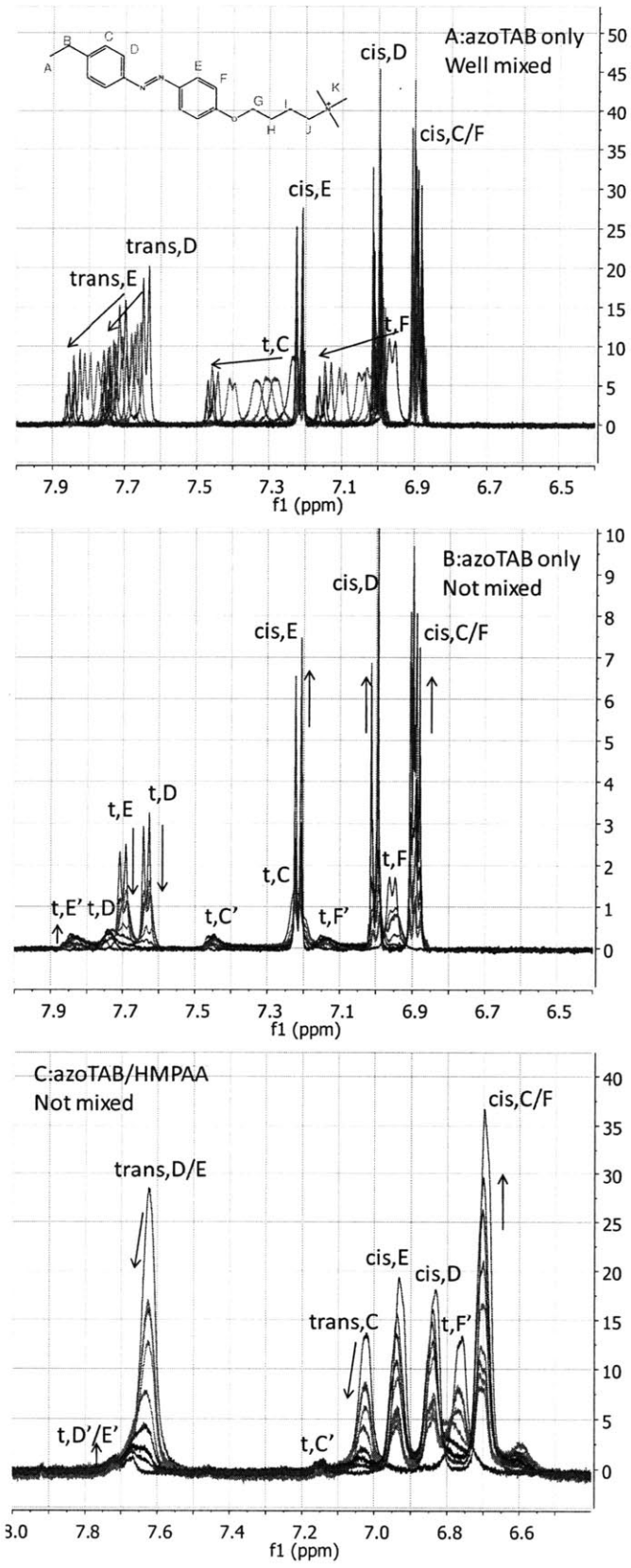
A:azoTAB only
Well mixed
cis,D
cis,C/F
cis,E
trans,D
trans,E
t,C
t,F
f1 (ppm)
B:azoTAB only
Not mixed
cis,D
cis,E
cis,C/F
t,E
t,D
t,C
t,F
t,E' t,D'
t,C'
t,F'
f1 (ppm)
C:azoTAB/HMPAA
Not mixed
cis,C/F
trans,D/E
cis,E
cis,D
trans,C
t,F'
t,D'/E'
t,C'
f1 (ppm)

Figure 4-37 ^{1}H HMR spectra of the aromatic region protons. Surfactant concentration fixed at 5 mM azoTAB. Panel A: azoTAB solution only, well-mixed. B: azoTAB only, not mixed. C: gel with 2.5 wt% HMPAA. Key for peak labels shown in Panel A. Samples were initially dark-adapted, 100% *trans*, and then irradiated with UV light. Arrows denote movement, growth or decay of peaks with irradiation. Overall compositions shown, expressed as *trans* fraction: Panel A, 1.00, 0.81, 0.74, 0.67, 0.53, 0.41, 0.23, 0.13, 0.03. Panel B: 1.00, 0.81, 0.73, 0.65, 0.55, 0.43, 0.27, 0.12, 0.04. Panel C: 1.00, 0.81, 0.72, 0.66, 0.55, 0.40, 0.24, 0.13, 0.04. These spectra were chosen such that the range of spectra in each panel would be comparable.

In the well-mixed surfactant-only sample (panel A), at any given time there is only one *trans* and one *cis* doublet for each proton. As the sample was irradiated, these peaks shifted downfield. This downfield movement is due to the dissolution of micelles as the sample became rich in *cis*. The positions of the *trans* peaks are much more sensitive to this dissolution than the *cis*, though the *cis* peaks also reflect the transition from micelle to monomer or pre-micellar aggregate (Figure 3-24).

The peaks in the unmixed surfactant solution showed a different behavior (panel B). A *trans* peak remained for some time at approximately the same frequency as that in the initial dark-adapted sample. As the intensity of this peak decayed, a second *trans* peak appeared and grew at a downfield location (denoted E', D', C' and F'). These downfield peaks correspond to monomer or pre-micellar *trans*, while the original upfield peaks are strongly influenced by micellar *trans*. The positions of these peaks are plotted in Figure 4-38. This observation of separate peaks is consistent with the presence of a fairly sharp composition gradient within the sample volume (as predicted in Figure 2-21C). The azoTAB molecules near the front of the sample were converted to the UV photostationary state, which was below the CMC. The residual *trans* in the UV state appeared as the downfield peak. The azoTAB molecules further away from the light source remained in the dark-adapted state, staying above the CMC and causing the upfield peak. The gradient between the two regions was fairly steep, so at least at early times, there was no substantial intermediate peak. Inadvertent mixing and diffusion evened out this gradient over time, eventually resulting in a smeared out *trans* peak.

The gel spectra (panel C) were similar in nature to the unmixed surfactant, with two *trans* peaks simultaneously appearing for any given proton. Again this suggests a composition gradient within the sample.

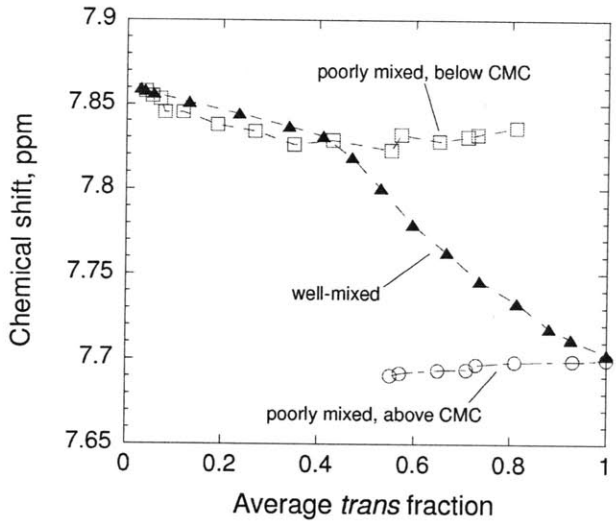

Figure 4-38 Position of *trans* peak 'E' in both well-mixed and poorly-mixed 5 mM azoTAB solutions. In several of the spectra for the poorly-mixed samples, two separate *trans* peaks appear. One peak is due to the part of the tube that is locally above the CMC, and the other below the CMC. The CMC is at about 40% *trans*, as seen in the breakpoint in the well-mixed series. The 'above CMC' peak is not tracked after it becomes very broad, indicating that the composition gradient became more gradual. Lines drawn to guide the eye.

In all of the aromatic proton peaks above, there was only a single *cis* doublet visible for each proton. It was not possible to separately resolve the peaks from the parts of the sample that were above and below the CMC. With the headgroup singlets it was easier to resolve two distinct peaks for the *cis* as well, in the poorly mixed surfactant solutions:

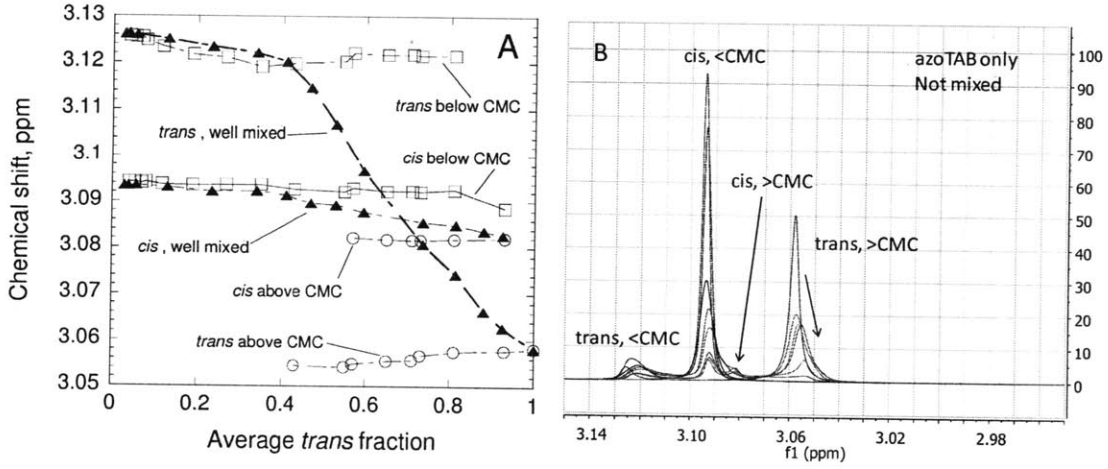

Figure 4-39 A: Position of the headgroup proton peak (K) in well-mixed and poorly-mixed 5 mM azoTAB solutions. Similar to the previous Figure, except the *cis* peak also shows two distinct peaks in the poorly-mixed solution. Lines are drawn merely to guide the eye. B: Superimposed spectra from the poorly-mixed sample. Shown at the same times and average compositions as Figure 4-37. Arrows indicate direction of growth or movement of peaks with UV irradiation.

However in the gel spectra, it was again not possible to resolve separate peaks for the *cis*:

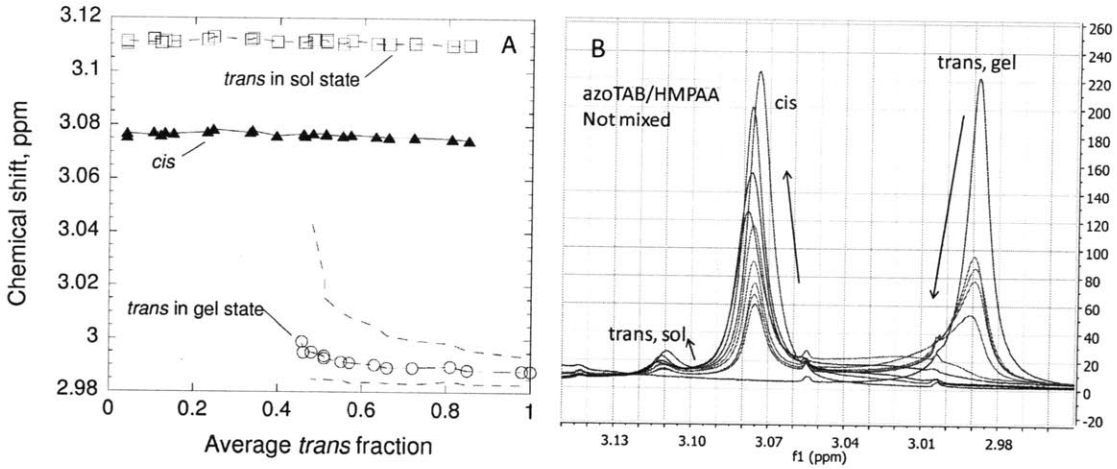

Figure 4-40 ^{1}H NMR spectra for the azoTAB headgroup protons 'K'. 5 mM azoTAB with 2.5 wt% polymer. Sample initially dark, then irradiated with UV to drive conversion to *cis*. A: Plot of peak frequencies. Distinct peaks seen for *trans* from the gel and sol parts of the tube. Width of gel peak increases with UV irradiation; broken lines show frequencies at half-maximum. This indicates the composition gradient becoming less sharp. Other lines are drawn to guide the eye. B: The spectra, superimposed. Arrows indicate direction of growth or movement of peaks with UV irradiation. Shown at the same times and average compositions as Figure 4-37.

This use of ^{1}H NMR to directly observe composition gradients in a photoreactive system may be novel. It could be further extended by using not only *in-situ* irradiation in the spectrometer, but also a NMR imaging probe. Such a probe could be used to directly image the variations over space, similar to an MRI. This additional step was left outside the scope of this work.

4.5.3. 2-dimensional photochemistry model

As illustrated in Figure 4-35, the photoreaction in a NMR tube is an inherently two-dimensional problem. The path length through the tube varies across the tube cross section. Thus far, it has been assumed that a one-dimensional model would be sufficient, with the average path length being used as the length of the modeled field. To check this assumption, some calculations were done using the full two-dimensional field. The model equations were not modified for this purpose; rather they were simply solved for each point in a two-dimensional grid instead of a one-dimensional grid. As diffusion is not yet considered, (see next section), there is no interaction between parts of the sample in a direction orthogonal to the passage of light. Parallel to the light beam, there is of course attenuation of the light intensity. Solving

the 2-D model is thus equivalent to solving several parallel 1-D models with different sample lengths, and then stacking the results.

When applied to a cylindrical NMR tube, Cartesian coordinates may appear inappropriate. There is however no angular symmetry in the system, so it would remain a two-dimensional problem in cylindrical coordinates as well. Additionally, the attenuation of the light intensity is most easily described in Cartesian coordinates. Therefore, the original Cartesian coordinate system was maintained.

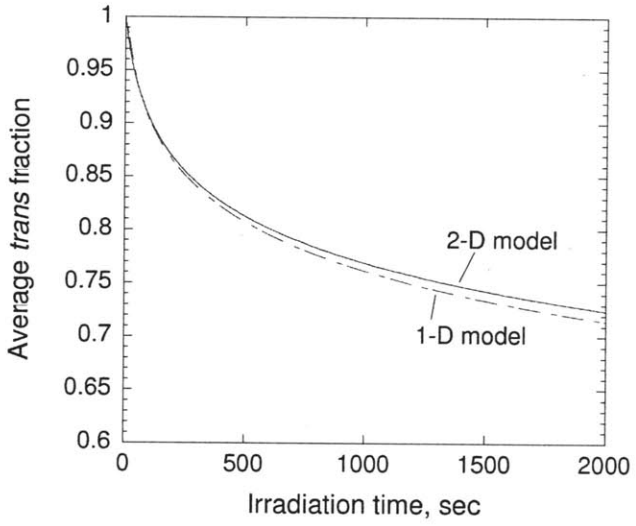

Figure 4-41 Conversion of *trans* to *cis* in the one- and two-dimensional models, with no mixing or diffusion. Irradiance is 4.73 mW/cm^2 at a wavelength of 360 nm. 1-D model uses a length of 3.87 mm, while the 2-D model uses the actual NMR tube inner diameter of 4.92 mm. Total concentration is 5 mM.

From the model comparison in Figure 4-41, it appears that reducing the problem of photoreaction in a NMR tube to a single spatial dimension is reasonable.

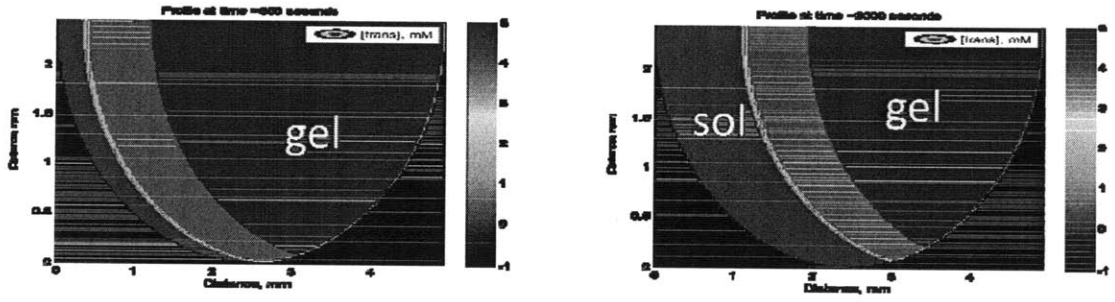

Figure 4-42 Example profiles from 2-D model. Same settings as in Figure 4-41. Shown is a half of the cross section of a cylindrical NMR tube, viewed along the axis of the tube. Dark blue denotes area outside the NMR tube. Light is incident on the left boundary of the tube. At 500 seconds and 2000 seconds of UV irradiation. Contour plots of the *trans* concentration, in mM. Colorbar is somewhat deceptive; see next Figure for better representation of the gradient.

The shapes of the resulting profile can be seen in Figure 4-42. As in the un-mixed 1-D model, there is a sharp gradient between a region that is UV-adapted, and a region that is essentially unreacted. In surfactant only solutions, the region in red would have *trans*-rich micelles, while the region in blue would have only monomers and pre-micellar aggregates. In surfactant-polymer mixtures, the region in red would be gelled, while the region in blue would be sol. The gradient between the regions is seen more clearly in Figure 4-43:

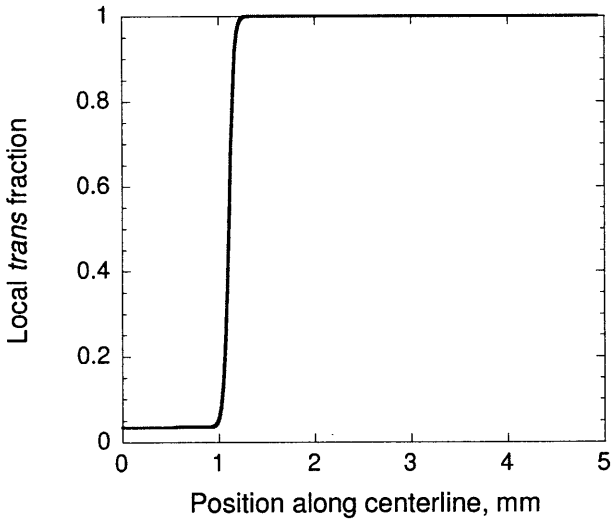

Figure 4-43 Profile of the *trans* fraction along the centerline of the NMR tube, after 2000 seconds of irradiation in the 2-D model, with no mixing or diffusion. The origin of the spatial axis is placed where light is incident on the sample.

In this Figure is the composition profile at the widest part of the NMR tube. The same profile would be found by solving the 1-D model with a sample length of 4.92 mm.

The additional computational burden of solving the two-dimensional model does not appear to be justified in a substantial change in the results.

4.5.4. Model with diffusion

In Chapter 2, two different photochemistry models were developed. One assumed a perfectly mixed sample volume, while the other assumed no diffusion and no convective mixing. Even in an experimental apparatus which eliminated convection, diffusion would still be present. There is therefore a need to extend the un-mixed model to include diffusion.

In the un-mixed sample model of Chapter 2, the rate of change of the *trans* concentration at any given position x was (Equation 2.20)

$$\left(\frac{\partial C_{trans}}{\partial t}\right)_x = -\phi_{trans}\alpha_{trans}IC_{trans} + \phi_{cis}\alpha_{cis}IC_{cis} + k_t C_{trans}$$

where ϕ_{trans} is the quantum yield of the *trans* to *cis* photoreaction, ϕ_{cis} is the quantum yield of the reverse photoreaction, I is the local light intensity and k_t is the first order rate constant for the thermal conversion of *trans* to *cis*. The concentration of *cis* was found by the conservation of species, $C_{tot} = C_{trans} + C_{cis}$. The molar absorptivities α_{trans} and α_{cis} are defined in the Beer-Lambert Law (Equation 2.19),

$$dI_A = -\alpha_A IC_A dx$$

where I_A is the light absorbed by some component A. As discussed in Chapter 1, this absorptivity is defined somewhat differently from that which is often presented in the literature.

The local light intensity is described by Equation 2.21:

$$\left(\frac{\partial I}{\partial x}\right)_t = -I(\alpha_{trans}C_{trans} + \alpha_{cis}C_{cis})$$

This model was extended to include diffusion as follows:

$$\left(\frac{\partial C_{trans}}{\partial t}\right)_x = -\phi_{trans}\alpha_{trans}IC_{trans} + \phi_{cis}\alpha_{cis}IC_{cis} + k_t C_{trans} + D_{trans}\frac{\partial^2 C_{trans}}{\partial x^2} \qquad (4.16)$$

and

$$\left(\frac{\partial C_{cis}}{\partial t}\right)_x = \phi_{trans}\alpha_{trans}IC_{trans} - \phi_{cis}\alpha_{cis}IC_{cis} - k_t C_{trans} + D_{cis}\frac{\partial^2 C_{cis}}{\partial x^2} \qquad (4.17)$$

It becomes necessary to solve separate conservation equations for *trans* and *cis* because the local total concentration C_{tot} may vary if the two species have different diffusivities, which they do. No flux boundary conditions were used at both ends of the modeled volume.

For surfactant-only solutions, the appropriate diffusivities were described in Chapter 2. At a total concentration of 5 mM, D_{cis} is about $4*10^{-10}$ m^2/s, while D_{trans} varies from $3*10^{-10}$ m^2/s in the dark-adapted state to $4*10^{-10}$ m^2/s in the UV-adapted state. These diffusivities are averaged over monomers, pre-micellar aggregates and micelles. The diffusivities in polymer-surfactant mixtures were described earlier in this Chapter; D_{cis} can be taken as $3.2*10^{-11}$ m^2/s while D_{trans} varies from $2.6*10^{-12}$ m^2/s in the dark-adapted state to $4.6*10^{-12}$ m^2/s in the UV-adapted state. For a first approximation, the variation of

the diffusivities with the extent of photoreaction was neglected in this model, and the dark-adapted values of D_{trans} were applied. It must be noted that the diffusivities being applied here are self-diffusion coefficients, describing Brownian motion in the absence of any concentration gradients. These values are not necessarily equivalent to the mutual diffusivities appropriate for use in Fick's Law and the above model. The two types of diffusion coefficients can however be expected to be similar for the surfactant, given that the solutions are dilute in surfactant.

The equations were not non-dimensionalised, but it is still possible to discuss characteristic time scales. The diffusion time scale is L^2 / D. Taking the characteristic length as 3.87 mm, or the average path length in the NMR tube, this time scale ranges from 10-14 hours in the surfactant solutions and is even longer in the polymers-surfactant mixtures. However, this is not the most appropriate characteristic length. Rather, diffusion would be expected to take place across the width of the composition gradient that arises due to uneven absorption of light. As discussed in Chapter 2, this width is on the order of $(\varepsilon C)^{-1}$, where ε is an alternate molar absorptivity defined in Equation 2.5 as

$$\alpha = \varepsilon \ln(10)$$

Using the molar absorptivity of *trans* azoTAB at the appropriate wavelength (360 nm), 2500 m^2/mol, the width of the gradient is thus about 0.08 mm. This brings the diffusion time scale to about 20 seconds in surfactant solutions and 40 minutes in gels. Based on the reaction times shown in Figure 4-35, it can be concluded that it is important to include the effects of diffusion. Meanwhile, the characteristic time of the thermal reaction is $1/k_t$, which is about 50 hours. The thermal reaction is negligible where the photoreaction goes to conversion quickly, but at locations in an optically thick sample where the local light intensity is very low, the thermal reaction can become relatively more important.

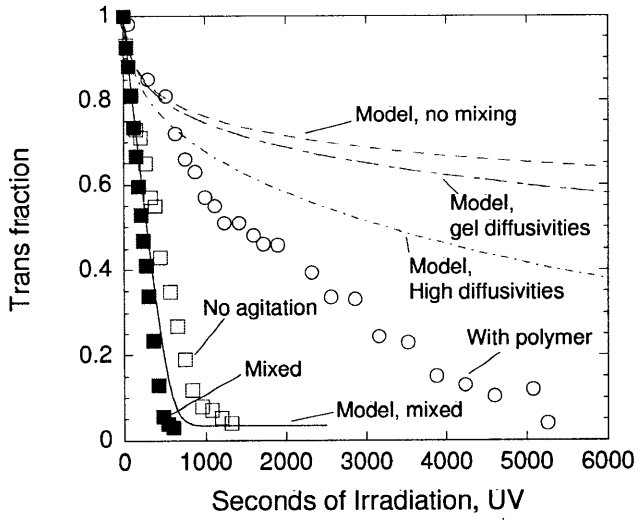

Figure 4-44 Comparison of model and experimental results for photoconversion of *trans* to *cis* in a NMR tube. Same as Figure 4-35, with the addition of models that include diffusion. "Gel diffusivities" taken from measurements in azoTAB-HMPAA mixtures; "high diffusivities" taken from measurements in surfactant-only solutions.

The results of the diffusion model are given in Figure 4-44. Using the diffusivities obtained from the surfactant-polymer mixtures, the rate of conversion is somewhat higher than in a perfectly unmixed system. Using the diffusivities from surfactant solution, the conversion is substantially faster. The observed reaction rate in the surfactant-polymer mixture was still faster than either of these however, so there must have been some convective mixing during that experiment. It is somewhat curious that this experimental series follows the model results at early times, up to 520 seconds. The viscosity of the gel would have been at a maximum at these times, so the gel would have been more impervious to agitation over this span. Beyond that time span, the sample would have undergone the gel-sol transition, and the viscosity would have decreased.

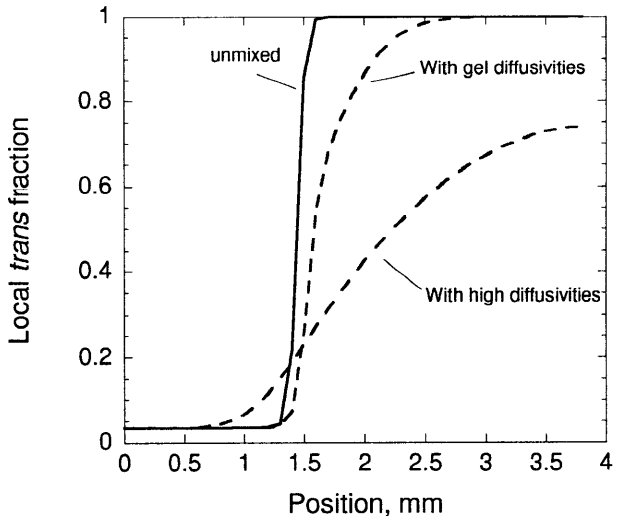

Figure 4-45 Composition profiles from unmixed and diffusion models, after 6000 seconds of UV irradiation. Shown are the local *trans* fractions. The average trans fractions are 0.64 in the unmixed model, 0.58 in the diffusion model with gel diffusivities and 0.38 using surfactant solution diffusivities.

An example of how diffusion affects the composition gradients is given in Figure 4-45. Even with the low diffusion coefficients in the gel, the sharp composition gradient is smoothed out substantially. The mole fractions are calculated based on the local total azoTAB concentration. Due to the different diffusivities of *cis* and *trans*, this local total concentration changes from 5 mM. The region at the front of the sample, near the light source, becomes rich in *cis* as the initially dark-adapted sample is exposed to UV light. This *cis* was assigned a higher diffusion coefficient than the *trans*, so this region becomes depleted in azoTAB.

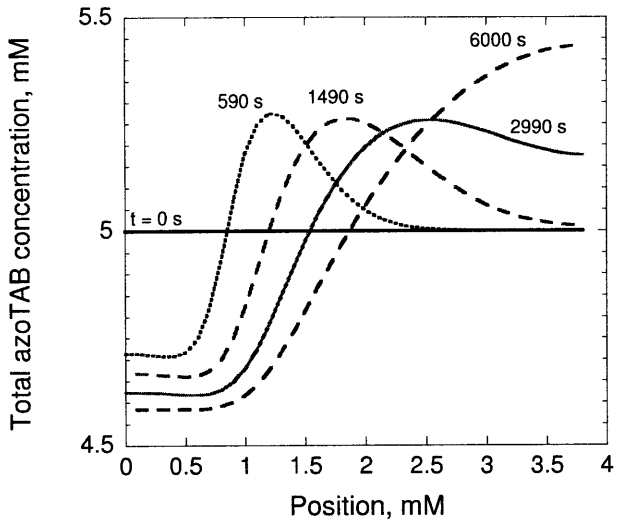

Figure 4-46 Profiles of the total azoTAB concentration, calculated from the diffusion model using surfactant solution diffusivites. The overall concentration is 5 mM, but this can change locally due to diffusion because *trans* and *cis* are treated as distinct components with different diffusivities. The front of the sample is rich in *cis* due to higher absorption of UV light. Because *cis* was given a higher diffusivity, that region then becomes depleted in total azoTAB.

These effects may be somewhat exaggerated in the model because the observed increase in *trans* diffusivity with UV irradiation was not included in the model. However, an increase in the local total azoTAB concentration in the deeper parts of the sample may explain the upfield drift in the micellar *trans* peak seen in Figure 4-40. As seen in Figure 4-13, the azoTAB peaks move upfield as the total concentration is increased.

4.5.5. Predicted NMR spectra

The shape of a NMR peak is generally described as being Lorentzian [102], which is alternately known as the Cauchy distribution. This distribution is defined as follows:

$$f_x = \frac{1}{\pi}\left[\frac{\gamma}{(x-x_0)^2+\gamma^2}\right] \tag{4.18}$$

where f_x is the value of the function at position x, γ is the peak half-width at the half-maximum (HWHM), and x_0 is the position of the peak center. With this quantitative description of the lineshape, predicted NMR spectra can be created from the results of any of the models. The predicted spectra can then be compared to the spectra that were observed in the presence of composition gradients.

The azoTAB headgroup peak was chosen for this analysis, because it returns a simple singlet peak. The synthetic spectrum for the headgroup peak was then simply built by taking a number-weighted sum of the predicted signals due to *trans* and *cis*:

$$f_x^{combined} = y_{trans} f_x^{trans} + y_{cis} f_x^{cis} \tag{4.19}$$

In the case of the diffusion or unmixed models, where the isomer composition varied over the sample volume, Equation (4.19) was applied for each grid point. The final spectrum resulted from taking a summation over all grid points.

As previously discussed, the peak position x_0 varies with the local isomer composition and the total azoTAB concentration. This variation is strong for *trans* and weak for *cis*. In all cases here, the total concentration was fixed at 5 mM. The values of x_0 used to build the predicted spectra were then interpolated from the observed peak positions in well-mixed 5 mM samples (Figure 4-39A). Such data were only available for surfactant-only solutions, so this analysis was not attempted for the gel samples.

The HWHM peak widths γ also vary with the isomer composition, as the NMR peaks are wider when micelles are present than when only monomer is present. The observed widths would also vary from spectrometer to spectrometer and even measurement to measurement, because line widths are affected by the quality of the shimming applied in order to achieve homogeneous magnetic fields. It was decided to keep the values of γ fixed for each isomer, as a simplification. 0.95 Hz was used for *trans*, and 0.8 Hz for *cis*. In any given spectrum, the observed linewidths may be slightly wider or narrower.

The predicted lineshapes were tested against those observed in well-mixed samples:

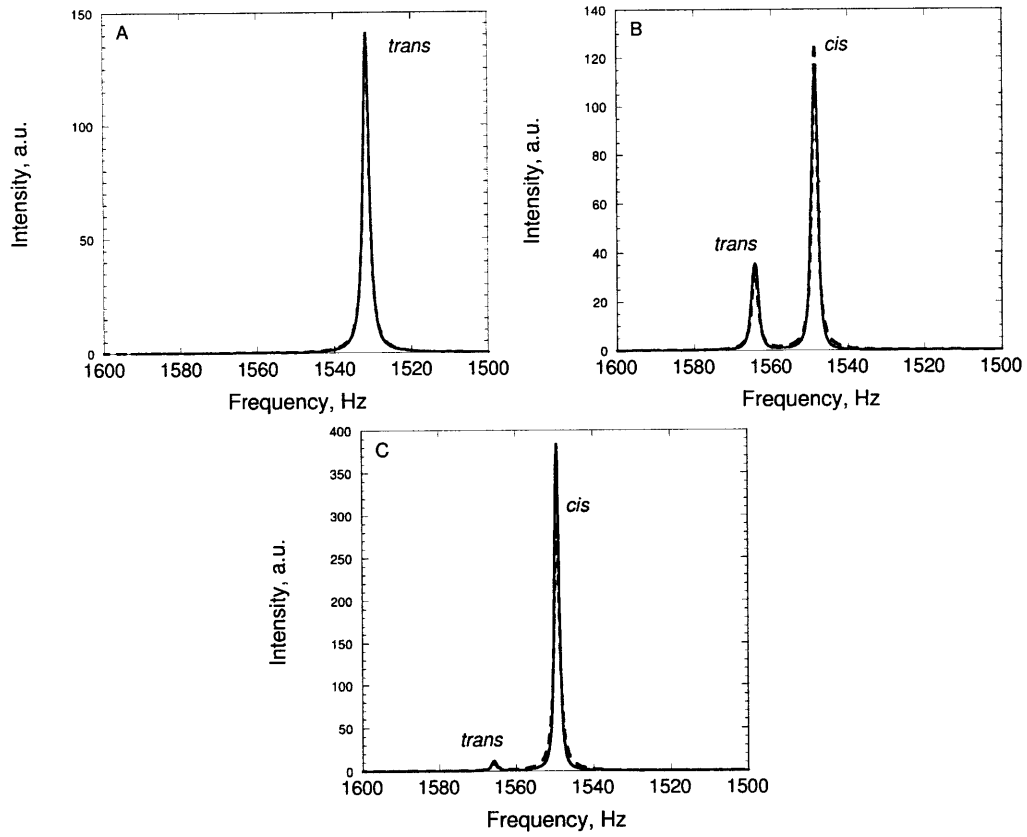

Figure 4-47 Predicted and observed NMR spectra for well-mixed sample volumes, for 5 mM azoTAB solutions. Predicted: Broken blue; Observed: solid black. A: dark-adapted state, 100% *trans*. B: 23% *trans*, or after 360 seconds of UV irradiation. C: UV adapted state, 3% *trans*.

The Lorentzian line shape fit the observed peaks reasonably well, with some error due to the unaccounted for changes in the linewidths.

Such a good agreement between model prediction and observation would not be expected in the azoTAB-HMPAA samples, given that none of the models correctly predict the observed rate of conversion. There was likely some convective mixing that would lead to unpredicted composition profiles. Despite this difficulty, a comparison was attempted.

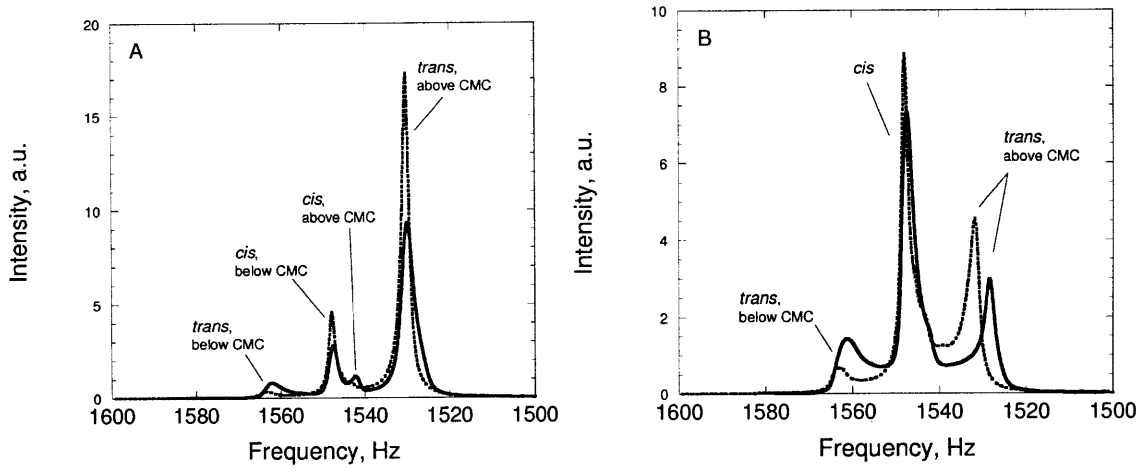

Figure 4-48 Observed (solid black) and predicted (broken blue) NMR spectra in poorly mixed 5 mM azoTAB only solutions. Diffusion model was used to generate the spectra, using diffusivities observed in surfactant solutions. A: Overall *trans* fraction is 0.81, achieved after 90 seconds of UV irradiation in the experiment, and 270 sec in the model. B: Overall *trans* fraction is 0.55, achieved after 390 seconds in the experiment, and 2450 sec in the model.

The experimental NMR spectra from the poorly-mixed samples were compared to the results of the diffusion model, such that the observed and predicted spectra had the same spatially-averaged isomer composition. There is not a strong agreement between observation and prediction, but the prediction does confirm that multiple *trans* peaks can be expected in a poorly-mixed sample.

4.5.6. Overview of kinetics

It was found that the photoreaction models underpredict the rate of photoconversion from *trans* to *cis* in the surfactant-polymer mixtures, but this is most likely due to convective mixing in the sample tube. In the absence of convection or diffusion, the rate of reaction at high optical depths is expected to be very slow. Therefore convection and diffusion are extremely important to the reaction rate.

There are no obvious indications that the time required for micelle formation or dissolution is limiting. Micellar kinetics are characterized by two different time scales, τ_1 and τ_2 [103]. The first is related to the rate of exchange of individual surfactant molecules between a micelle and the bulk, and is typically on the microsecond scale [104]. In this case, it is directly observed that the rate of exchange of individual surfactant molecules between the monomer and micelle states is at least as fast as the millisecond scale, and is thus not limiting in any way to the gelation process. This was found from the fact that there are not separate micelle and monomer NMR peaks in a well-mixed sample. The second time scale is related to

the lifetime of the micelle, or the rates of micelle formation and dissolution. This is typically on the millisecond scale, but can be longer in special cases such as Gemini surfactants [104]. In this system, these rates also seem to be fast compared to the photoreaction. This is inferred from the fact that the NMR peaks shift upfield and downfield appropriately, signaling that micelles are forming or breaking in response to irradiation as expected.

It therefore appears that the photon flux through the material is the rate controlling feature of the system. Upon absorption of light, the photoreaction takes place quickly, and then any micellar aggregation responds quickly to the change in isomer composition. The effect of low photon flux at high optical lengths can be mitigated by stirring the sample, such that all molecules are on average exposed to the same irradiance. What was not measured was the changing viscosity or polymer diffusivity during the irradiation process. This work was inspired by a report that [47] that the viscosity dropped upon UV irradiation on the time scale of minutes, and then within minutes recovered part way upon visible irradiation. For unstated reasons, the remaining recovery in viscosity required about 24 hours. Based on this report, it was thought that there may be some complicated mechanisms involved in the gelation process. However a likely explanation for this observation is simply that the visible-adapted state (assuming it was even entirely achieved with the available light intensity) is different from the dark-adapted state. The extent of gelation will be higher in the dark-adapted state because it is 100% *trans*, as opposed to about 70% *trans* (dependent on the wavelength of visible light used). The observed slow recovery time was probably due to the slow thermal reaction that returned the gel to the dark-adapted state.

It is likely that the rate of the photoreaction is the limiting step in gelation, in optically thin samples. This rate is affected by the incident light intensity and the wavelength. In optically thick samples, mass transfer can be thought of as limiting. If the sample were mixed, the photoconversion and thus gel-sol transition would be faster.

4.6 Solute diffusion

4.6.1. Measured in aqueous solvent

Measurements of solute diffusivity through the gel are also helpful for characterizing the gel structure and assessing appropriateness for several end-use applications. A series of poly(ethylene glycols) of varying sizes was chosen as the primary probes. Their diffusivities were measured in very dilute solutions (0.03 wt% or 0.06 wt% PEG) in deuterium oxide, and compared to literature values.

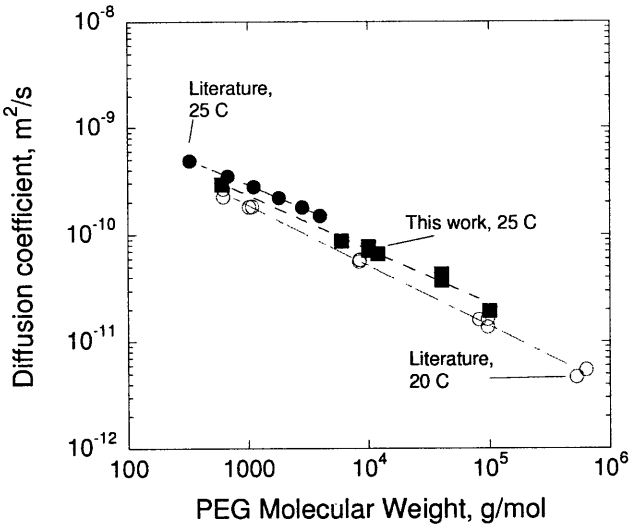

Figure 4-49 Diffusivities of PEG in deuterium oxide. Literature values in circles; this work in squares. Solid circles, measured at 25 C, taken from Johansson et al [77]. Hollow circles, measured at 20 C, taken from Colsenet et al and le Feunteun et al [64, 73, 76]. Measurements in this work are done at 25 C, and a diffusion time of approximately 500 ms. Power law line drawn through all series. Exponents: 0.47, 0.51 and 0.56 for literature 25 C, this work and literature 20 C series, respectively.

The literature values bound the measurements described here (Figure 4-49), giving confidence in the calibration and technique employed. The star PEO with a MW of 10,000 falls on the line with the other polymers, despite being nonlinear.

The diffusivity varies as

$$D \sim MW^{-\upsilon'} \tag{4.20}$$

where MW is the molecular weight of the polymer. υ' is taken from the exponent of the lines in Figure 4-49, and is equal to 0.51 ± 0.06. This corresponds well to the Zimm model exponent of 0.5; the Zimm model results from adding hydrodynamic interactions to the Rouse bead-spring model of a polymer chain. To the extent that the hydrodynamic radius, root mean squared (r.m.s.) radius of gyration and r.m.s. end to end to displacement are proportional to each other, this is also the Flory exponent υ:

$$R_f \sim N^{\upsilon} l \tag{4.21}$$

where R_f is the r.m.s end to end displacement, N is the number of bonds in the chain and l is the bond length. A Flory exponent of 0.5 corresponds to an unperturbed polymer, or the theta condition [105]. To a first approximation, assuming an equivalence between υ and υ' is not unreasonable in dilute solutions

[106]. When doing quantitative calculations, the appropriate bond length for PAA is the carbon-carbon bond length of 0.154 nm. For PEG the r.m.s. value of two carbon-oxygen lengths and one carbon-carbon length is required [107].

4.6.2. Measured in azoTAB-HMPAA gels and solutions

Based on the review of the published literature, it was anticipated that solute diffusion might respond to changing levels of crosslinking and finally gelation. Different extents of crosslinking were sampled by measuring diffusion at different azoTAB concentrations with a fixed HMPAA concentration and further by switching between the dark and UV photostationary states. Some results are given in Figure 4-50 and Table 4-3.

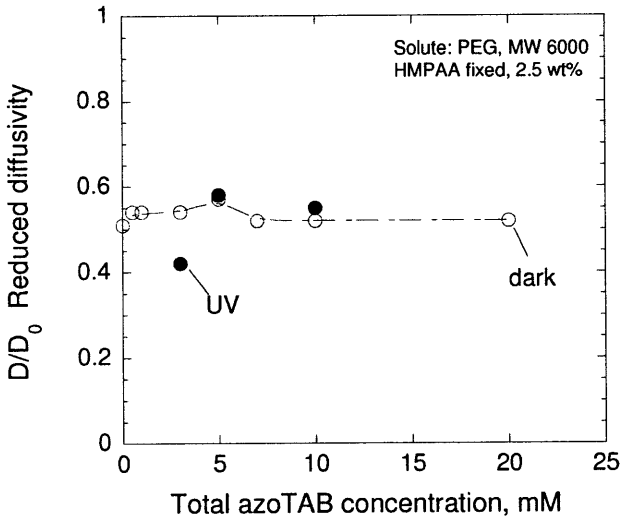

Figure 4-50 Diffusivity of PEG MW 6000, scaled against its diffusivity in neat solvent. Surfactant concentration and photostationary state have no obvious impact. The hydrodynamic radius of this solute is 2.3 nm. Measured at diffusion times ranging from 100 to 3000 ms; this time has no effect on the diffusivity. Some values are therefore averages of several measurements.

Table 4-3 Diffusivities of various solutes in neat solvent, and reduced diffusivities in 2.5wt% HMPAA solutions and azoTAB-HMPAA mixtures, in dark- and UV-adapted states. Measurement in polymer-only solution not always available. Also given is the hydrodynamic radius.

Solute, MW	$D_0, m^2/s$	R_H, nm	[azoTAB], mM	D/D_0, no azoTAB	D/D_0, dark, with azoTAB	D/D_0, UV, with azoTAB
Dimethylformamide, 73	$9.98*10^{-10}$		3.85		0.88	0.87
Star PEO: 10,000	$7.74*10^{-11}$	2.7	10	0.47	0.48	0.48
PEG: 12,000	$6.61*10^{-11}$	3.0	5	0.39	0.46	0.47
PEG: 40,000	$3.76*10^{-11}$	5.3	10		0.34	0.34

While the extent of gelation changes dramatically across the different measurements shown in Figure 4-50, it has no obvious effect on the diffusion of solutes with a molecular weight of 40,000 or less. This suggests that the mesh size is always greater than the largest solute hydrodynamic diameter, 10 nm.

A schematic of the mesh in a semi-dilute polymer solution is given in Figure 4-51.

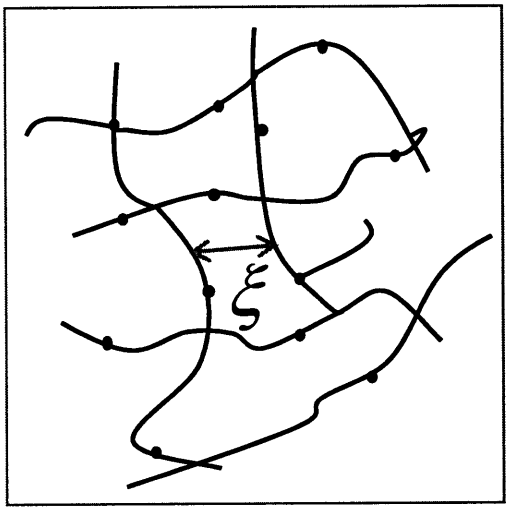

Figure 4-51 Polymer mesh in semi-dilute solution. ξ is the characteristic length of the mesh. Potential crosslinking sites are shown in red. If that crosslinking can substantially reduce ξ, it would be expected to hinder solute diffusion. Alternately, crosslinking could cause the polymer clusters to constrict upon themselves, leaving large solvent voids that are available for solute transport.

Through a supplementary SANS experiment, the mesh size in HMPAA solution was estimated to be 16 nm, which is indeed larger than the largest solute above. Alternately, the mesh dimensions can be estimated through use of scaling laws [71, 108]:

$$\xi = R_g \left(\frac{C^*}{C} \right)^{3/4} \tag{4.22}$$

where C^* is the overlap concentration, C is the polymer concentration, and the radius of gyration R_g was found using Equation (4.12). The resulting estimate for 2.5 wt% HMPAA is about 10 nm, so the SANS estimate is of plausible magnitude. In the absence of additional crosslinking induced by the surfactants, the HMPAA solution can be expected to impose an obstruction effect on the solutes, but little size-specific sieving would be in effect for the solutes presented above.

However, micellar crosslinking should somehow distort this mesh. The average HMPAA coil consists of 3470 repeat units, 3% of which are hydrophobically modified. There are thus about 32 repeat units between potential crosslinking sites, or a contour length of about 10 nm. The actual displacement between neighboring side chains will be rather less than this. If a substantial number of side chains (red spots in Figure 4-51) associate with each other via micelles, the mesh size may effectively be reduced. The mesh size could alternately also be increased, as some larger voids are created as the polymer coils crosslink with each other.

Based on these results, a larger solute was introduced in an attempt to detect any sieving effect. This was PEO with a molecular weight of 100,000, which has a hydrodynamic radius of about 10.4 nm. A solute with this size should be more sensitive to changes in the mesh structure. The resulting Stejskal-Tanner curves are given in Figure 4-52:

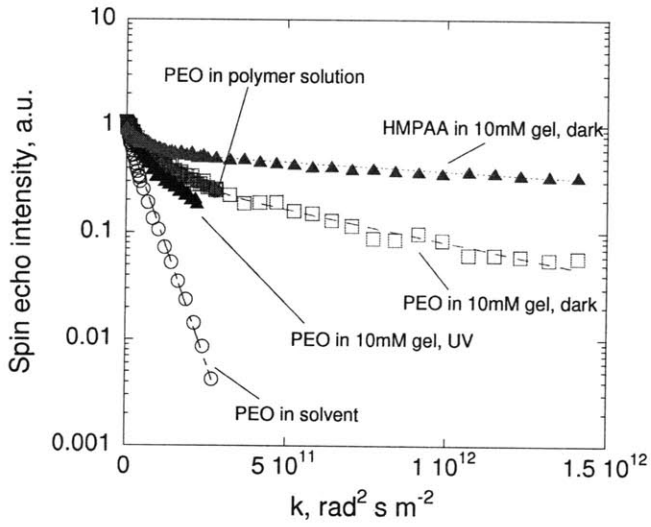

Figure 4-52 Stejskal-Tanner plots for PEO, MW 100,000. Faster signal decay with increasing 'k' indicates faster diffusion. Hollow squares: PEO in 10 mM azoTAB/2.5 wt% HMPAA gel, dark state. Solid triangles: PEO in same gel, but UV state. Solid circles, obscured by dark gel series: PEO in 2.5 wt% HMPAA, no azoTAB. Hollow circles: PEO in neat solvent. Triangles: HMPAA in dark gel, for comparison. All broken lines are best fits to two-component model, except PEO in solvent which is a simple linear regression for one component. Diffusion times used range from 500 ms to 2500 ms.

The results are difficult to interpret. The Stejskal-Tanner plot for PEO in solvent is linear, indicating simple translation with a single diffusion coefficient. The diffusivity in 2.5 wt% HMPAA solution is much slower than in neat solvent, but there is also curvature in the plot. There are multiple diffusion coefficients for PEO present in the polymer solutions, implying that some of the solute is becoming entangled with the HMPAA. The results do not appreciably change when 10 mM *trans* azoTAB is added to form a dark-adapted gel. However the diffusivity of PEO increases after irradiation with UV light. It is unclear why disrupting any micellar crosslinks with UV light would have an impact on solute diffusion,

when the creation of those crosslinks via the addition of surfactant had little effect. Either the presence of *cis* azoTAB somehow led to larger voids in the gel structure, or the apparent effect is a result of measurement error.

The use of other large solutes was attempted in order to elucidate these mechanisms. These solutes included latex beads and globular proteins such as albumin, myoglobin and hemoglobin. Unfortunately none of these probes provided a sharp enough proton NMR peak for observation using the available NMR probe.

For these gels to be effective in sieving more moderately sized molecules or particles, it was hypothesized that an increase in potential crosslinking sites was required. A higher density of hydrophobic side chains could allow for a more substantial difference in the mesh size between the gel and solution states.

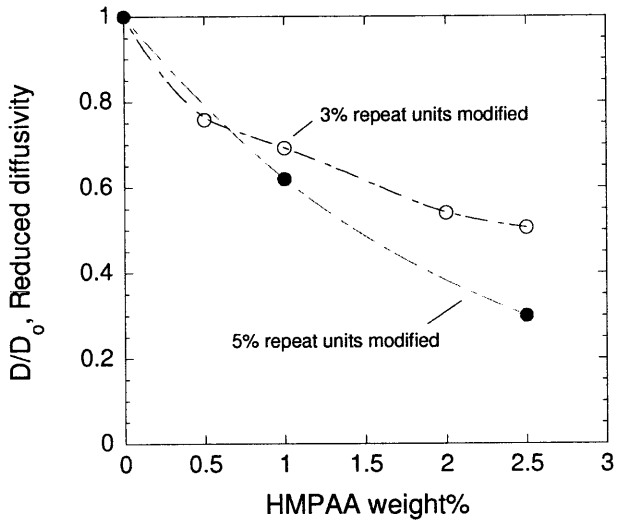

Figure 4-53 Diffusivity of PEG MW 6000 in HMPAA solutions of different concentrations and different levels of hydrophobic modification. The diffusivity is more attenuated in HMPAA with 5% modification (250-5) as compared to the polymer with 3% modification (250-3) otherwise used throughout this work. Lines drawn to guide the eye.

An initial test of this idea is presented in Figure 4-53. In the absence of any surfactant, an increase in the hydrophobic modification rate of the PAA results in lowered PEG diffusivity. At any given concentration, the HMPAA with the higher extent of modification results in more viscous samples. This thickening is a result of enhanced inter-polymer crosslinking due to side chain aggregates. In principle the crosslinking could be further enhanced in a light-sensitive manner through use of azoTAB, but exploration of azoTAB in mixture with HMPAA of various substitution ratios was left out of the scope of this work. In any case, a sieving mechanism is not wholly necessary for the light-activated modulation of

solute transport; small hydrophobic molecules should be immobilized in the gel state as compared to the solution due to solubilisation by the crosslinking micelles.

4.6.3. Dependence on solute size and polymer concentration

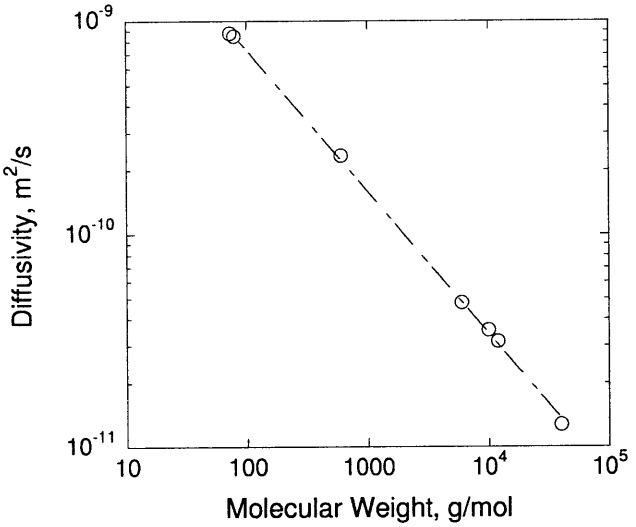

Figure 4-54 Dependence of probe diffusivity on probe molecular weight, measured in dark-adapted azoTAB-HMPAA gels. Includes PEG 600, 6000, 10000, 12000 and 40000, as well as small molecules pyridine and dimethylformamide. Line indicates power law fit.

In azoTAB-HMPAA gels with a polymer content of 2.5 wt%, the probe diffusivity was found to scale as $D \propto MW^{-0.67}$. Exponents of 0.5 and 1 would correspond to Zimm and Rouse chain dynamics respectively, while an exponent of 2 would be expected in a reptation regime. The gel is not concentrated enough for the reptation model to apply, wherein the diffusing polymer can be thought of as being restricted to a tube. A result intermediate to the Zimm and Rouse values is fairly typical in semi-dilute polymer solutions.

A wide variety of models have been suggested for solute transport in polymer solutions and gels [70]. These are either based on the hydrodynamic drag acting on the solute, the free volume available for transport, or the increase in path length due to obstructions. The drag and obstruction models have also been combined, to account for both effects. Some relations have also been derived that include size-exclusion effects due to the relative sizes of solute and mesh. The Ogston model was used to describe the diffusion of solutes through the gel matrix of this work. In the Ogston model, the gel is treated as randomly oriented impenetrable fibers which present an obstruction to the diffusing solute.

The Ogston model is stated as

$$\frac{D}{D_0} = \exp\left[-\phi_p^{0.5}\frac{r_s+\rho}{\rho}\right] \tag{4.23}$$

where ρ is the fiber radius. The hydrodynamic radius of the solute measured in dilute solution was used as r_s, as is suggested for PEG [70].

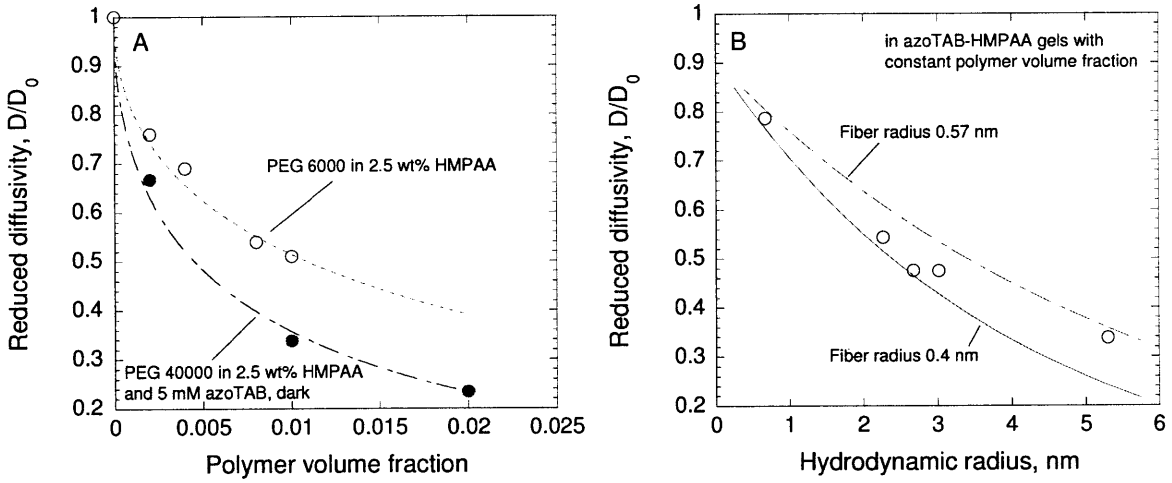

Figure 4-55 Measured PEG diffusivities in comparison with predictions of Ogston model. A: Effect of changing volume fraction. Hollow markers, PEG with MW 6000 diffusing in HMPAA solutions. Solid markers, PEG with MW 40000 diffusing in azoTAB-HMPAA gels. Broken line is from Ogston model, with a different fiber radius used in the two cases. B: Effect of changing the solute radius. Solutes used are PEG 600, 6000, 10000, 12000 and 40000. Hydrodynamic radius is used as the solute radius. Lines are from Ogston model, using the different radii found from gel series in panel A.

Data were collected using PEG with weights of 6000 and 40,000 across a range of polymer volume fractions. The PEG 6000 data were collected in the absence of surfactant, while the larger solute was placed in azoTAB-HMPAA gels. The relationship between solute diffusivity and volume fraction matches the Ogston model fairly well. However the best fit value of the fiber radius was different in the two cases; fiber radii of 0.4 nm and 0.57 nm resulted from using PEG 6000 and 40,000, respectively. This difference is not thought to be due to the presence or absence of surfactant, as the diffusivity of PEG 6000 was not found to be sensitive to the presence of polymer in at least one polymer concentration. Therefore there may be some solute size dependence that the Ogston model is not capturing. As seen in Figure 4-55B, the model treatment of the solute size is less satisfactory. Nonetheless these trends were used to estimate the reduction in free micelle diffusivity due to the polymer obstacles, in an earlier section. This estimate may have some error due to electrostatic interactions being ignored.

At these low polymer volume fractions, it is likely that obstruction is a major mechanism for the reduction of solute diffusivity. The Ogston scaling of solute diffusivity against polymer fraction appears appropriate, though there are other behaviors here which are not well described by that model.

4.7 Discussion

An array of NMR techniques has been used to characterize the structure of the gels and solutions formed by azoTAB and HMPAA under different light conditions. These measurements have been used to estimate the level of surfactant-polymer binding through observation of both surfactant and polymer, as well as the level of micelle formation, and the ensuing growth of polymer clusters and networks. Also obtained were estimates of the polymer mesh size, and indications of the stability of different aggregates as inferred by the exchange rate of components into and out of those aggregates. In order to build a coherent understanding of the structures present under various light conditions, all of these measurements must be reconciled with each other and with rheological measurements [47] and SANS measurements [50].

This was done under the framework of the tree model of gelation. The gels in this work are crosslinked by physical interactions, leading to crosslinks with finite lifetimes. In general, this will lead to 'weak' gels, in comparison to stronger chemically crosslinked networks. Physical gels are not expected to have the sharp sol-gel transitions seen in chemical gels [71], and require special theoretical attention as developed for HMPs by Rubinstein and Semenov [109-114] and Tanaka [115-122]. Nonetheless, physical crosslinking bears a resemblance to the vulcanization process, and so the tree model of vulcanization as presented by Flory was used as a general guide [105].

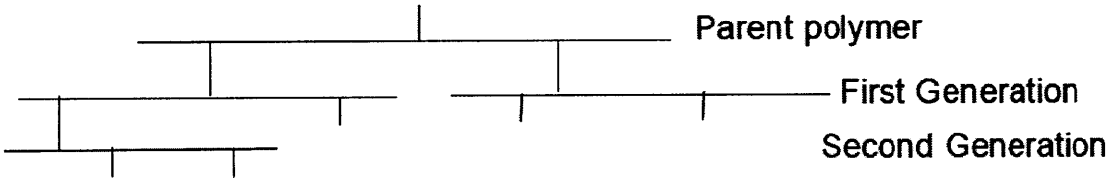

Figure 4-56 Tree model of gelation. Individual polymer coils are represented by the horizontal lines. Crosslinks or potential crosslinks are denoted by the vertical lines. See text for discussion. Based on treatment by Flory [105].

A gel can be defined in many different ways. There are rheological definitions, whereby a gel is formed when the storage modulus exceeds the loss modulus, or when the loss modulus is constant over a wide

range of frequencies. In this work, a gel is defined as a crosslinked network that is much larger than the individual polymer coils; this network extends indefinitely across the volume in which it's found. The tree in Figure 4-56 was used to find the conditions necessary to form an infinite network. Each polymer coil has some number f of sites where crosslinks may form, such as the hydrophobic grafts in this work. In the Figure, $f = 3$. The probability that any given side chain is involved in an active crosslink is p. Neglecting intra-polymer aggregation and assuming that each crosslink only includes one hydrophobic graft from each of two polymer coils, the number of polymer coils connected to the parent coil is pf. The number of as yet unaccounted side chains in the first generation is $pf(f-1)$. Applying the same assumptions as before, there are then $p^2 f(f-1)$ members of the second generation. In order for the network to extend indefinitely, there must be at least as many members in the second generation as the first. Applying this condition, the critical point for gelation p_c is

$$p_c = \frac{1}{f-1} \tag{4.24}$$

Once the fraction of side chains that participate in interpolymer crosslinks exceeds this critical point, a gel will have formed.

On a weight averaged basis, the original HMPAA coils have 3470 repeat units, and about 104 side chains per coil. The critical point p_c is thus about 1%, so the fraction of active side chains should be roughly on that order as the clusters grow to maximum size and the viscosity rises. Correspondingly, there must be enough surfactant micelles available to host these side chains, and each micelle must on average host side chains from at least two polymer coils. As seen in Figure 4-24, even at the lowest azoTAB concentrations, the fraction of side chains that are somehow associated with the surfactants easily exceeds 1%. This is true in both the dark and UV photostationary states. It is doubtful that all of those side chains are actively engaged in crosslinking; in fact they cannot be or else there would be no difference in cluster size or viscosity between the dark and UV states.

The concentration of surfactant present in micelles was estimated by use of surfactant chemical shifts, and was presented in Figure 4-20. These values were converted to the concentration of micelles by dividing by the aggregation number; N_{agg} was chosen to be 70 on the basis of the SANS results [50]. As expected, the number density of viable micelles is the limiting factor in gelation:

Table 4-4 Micelle and side chain populations as estimated from chemical shift data of both surfactant and polymer. Dark state only. Total side chain concentration is 8.65 mM. "Associated" side chain concentration is the fraction identified as interacting with either surfactant micelles or with bound monomeric surfactant.

[azoTAB], mM	[micelles], mM	[micelles]/[total side chains]	[side chains associated with azoTAB]/[micelles]	[side chains associated with azoTAB]/[azoTAB]	[micelles]/[polymer coils]
0	0.00	0.00			0.00
0.5	0.00	0.00		1.00	0.00
1	0.01	0.00			0.09
3	0.04	0.00	47.62	0.36	0.43
5	0.06	0.01	31.85	0.32	0.77
7	0.09	0.01	25.30	0.28	1.12
10	0.14	0.02	19.40	0.22	1.63
20	0.28	0.03	13.15	0.18	3.35

If each micelle were on average hosting two side chains, then from 5 mM azoTAB and above there are enough micelles to allow for 1% of the side chains to be actively crosslinking (see third column of Table 4-4). This figure is reasonable in the context of the dark state viscosity and cluster size measurements; both are strongly elevated at 5 mM.

It is also clear that not all of the side chains that are associated with the surfactant are actually participating in micelles, so Figure 4-24 must be interpreted with caution. It is simply implausible that at 3 mM azoTAB, there are nearly 50 side chains in each surfactant micelle (fourth column). The 1:1 ratio of azoTAB and azoTAB-associated side chains at 0.5 mM (fifth column) strongly suggests that upto 0.5 mM, each surfactant molecule binds to the polymer at its own side chain. This ratio decreases rapidly beyond 0.5 mM, indicating that the surfactant is forming micelles above 0.5 mM and that the polymer side chains are a minority component in the micelles. In principle, the estimate of the bound azoTAB concentration in Figure 4-20 could be subtracted from the concentration of side chains associated with surfactant, thus yielding the concentration of side chains in micelles and the micellar composition. Unfortunately the data are too noisy and uncertain for this calculation to be meaningful, though the number of side chains per micelle may be on the order of 3-4.

The micellar and side chain populations in the UV system suggest the exact same scenario as the dark state, but yet there is a substantial difference in cluster size and rheology between the two light conditions. Surfactant micelles are forming in the UV state at the same overall azoTAB concentration as in the dark. Side chains are interacting with those micelles at about the same rate. From the lack of effective crosslinking, it can be inferred that the *cis* micelles are smaller than the *trans*, and less stable. The size effect is consistent with SANS measurements (Figure 4-17). These smaller *cis* micelles may be

incorporating polymer side chains, but they would be less likely to simultaneously accommodate two side chains from different polymer coils for long enough to have any crosslinking effect.

The fact that *cis* surfactants are able to form well-formed micelles at all is noteworthy, as they tend to form pre-micellar discs in aqueous solution. The polymer side chains must be important for *cis* micelle formation; the side chain likely provides a substrate around which the *cis* surfactants can condense. This substrate may also relieve some of the packing constraints inherent in the formation of aggregates by *cis* azoTAB.

In consideration of all these results, the schematic in Figure 4-16 appears to best explain the structure of these polymer-surfactant mixtures under dark and UV conditions.

4.8 Conclusions

NMR chemical shift and diffusion measurements have been successfully used to describe the molecular scale architecture of photosensitive gels in both gel and sol states. The size of the growing gel network was directly observed by quantifying its diffusivity, and these data were found to correlate very well with viscosity measurements. Polymer diffusion can thus provide the bridge between molecular and macroscopic observations. Chemical shift data were used to estimate the extent of surfactant-polymer binding and micelle formation; these are consistent with gelation theory. The combination of NMR, SANS and rheology data were used to suggest a different mechanism of reversible gelation than what was inferred without the benefit of NMR measurements. The kinetics of the gel-sol transition were followed using NMR chemical shift measurements; the extent of gelation appears to respond quickly to changes in the isomer composition. These changes are in turn controlled by the photon flux through the material. An accurate kinetic model for this reaction is therefore important, and the model for unmixed volumes described in Chapter 2 was found to be adequate. This model predicts that concentration gradients will result from uneven absorption of light throughout the sample, and NMR spectra were used to detect these gradients. The range of discoveries made here demonstrate the power of NMR measurements in elucidating structures and processes in colloidal and polymeric systems.

4.9 Works cited

1. Pelton, R.H. and P. Chibante, *Preparation of Aqueous Lattices with N-Isopropylacrylamide.* Colloids and Surfaces, 1986. 20(3): p. 247-256.
2. Pelton, R., *Temperature-Sensitive Aqueous Microgels.* Advances in Colloid and Interface Science, 2000. 85(1): p. 1-33.
3. Wang, K.L., J.H. Burban, and E.L. Cussler, *Hydrogels as Separation Agents.* Advances in Polymer Science, 1993. 110: p. 67-79.
4. Katchalsky, A., *Rapid Swelling and Deswelling of Reversible Gels of Polymeric Acids by Ionization.* Experientia, 1949. **5**(8): p. 319-320.
5. Philippova, O.E., D. Hourdet, R. Audebert, and A.R. Khokhlov, *Ph-Responsive Gels of Hydrophobically Modified Poly(Acrylic Acid).* Macromolecules, 1997. **30**(26): p. 8278-8285.
6. Brannonpeppas, L. and N.A. Peppas, *Solute and Penetrant Diffusion in Swellable Polymers .9. The Mechanisms of Drug Release from Ph-Sensitive Swelling-Controlled Systems.* Journal of Controlled Release, 1989. **8**(3): p. 267-274.
7. Mamada, A., T. Tanaka, D. Kungwatchakun, and M. Irie, *Photoinduced Phase-Transition of Gels.* Macromolecules, 1990. **23**(5): p. 1517-1519.
8. Mudiyanselage, T.K. and D.C. Neckers, *Photochromic Superabsorbent Polymers.* Soft Matter, 2008. **4**(4): p. 768-774.
9. Irie, M., *Stimuli-Responsive Poly(N-Isopropylacrylamide) - Photoinduced and Chemical-Induced Phase-Transitions.* Advances in Polymer Science, 1993. **110**: p. 49-65.
10. Suzuki, A., H. Suzuki, O. Sakashita, and H. Sakuyama, *Phase-Transition in Polymer Gels Due to Local Heating by Illumination of Light.* Phase Transitions, 1994. **47**(3-4): p. 161-181.
11. Schild, H.G., *Poly (N-Isopropylacrylamide) - Experiment, Theory and Application.* Progress in Polymer Science, 1992. **17**(2): p. 163-249.
12. Tanaka, T., *Collapse of Gels and Critical Endpoint.* Physical Review Letters, 1978. **40**(12): p. 820-823.
13. Thalberg, K., B. Lindman, and G. Karlstrom, *Phase-Diagram of a System of Cationic Surfactant and Anionic Polyelectrolyte - Tetradecyltrimethylammonium Bromide Hyaluronan Water.* Journal of Physical Chemistry, 1990. **94**(10): p. 4289-4295.
14. Nagarajan, R., *Thermodynamics of Nonionic Polymer-Micelle Association.* Colloids and Surfaces, 1985. **13**: p. 1-17.
15. Bai, G.Y., L. Santos, M. Nichifor, A. Lopes, and M. Bastos, *Thermodynamics of the Interaction between a Hydrophobically Modified Polyelectrolyte and Sodium Dodecyl Sulfate in Aqueous Solution.* Journal of Physical Chemistry B, 2004. **108**(1): p. 405-413.
16. Bai, G.Y., M. Nichifor, A. Lopes, and M. Bastos, *Thermodynamic Characterization of the Interaction Behavior of a Hydrophobically Modified Polyelectrolyte and Oppositely Charged Surfactants in Aqueous Solution: Effect of Surfactant Alkyl Chain Length.* Journal of Physical Chemistry B, 2005. **109**(1): p. 518-525.
17. Hansson, P., *A Fluorescence Study of Divalent and Monovalent Cationic Surfactants Interacting with Anionic Polyelectrolytes.* Langmuir, 2001. **17**(14): p. 4161-4166.
18. Hansson, P., *Self-Assembly of Ionic Surfactants in Polyelectrolyte Solutions: A Model for Mixtures of Opposite Charge.* Langmuir, 2001. **17**(14): p. 4167-4180.
19. Wang, C. and K.C. Tam, *New Insights on the Interaction Mechanism within Oppositely Charged Polymer/Surfactant Systems.* Langmuir, 2002. **18**(17): p. 6484-6490.
20. Plucktaveesak, N., A.J. Konop, and R.H. Colby, *Viscosity of Polyelectrolyte Solutions with Oppositely Charged Surfactant.* Journal of Physical Chemistry B, 2003. **107**(32): p. 8166-8171.

21. Leung, P.S., E.D. Goddard, C. Han, and C.J. Glinka, *A Study of Polycation Anionic-Surfactant Systems.* Colloids and Surfaces, 1985. **13**(1): p. 47-62.
22. Bakshi, M.S., I. Kaur, R. Sood, and K. Singh, *Nmr Studies of Mixed Cationic Surfactants with Similar Tails and Dissimilar Bulky Head Groups.* Colloid and Polymer Science, 2003. **281**(8): p. 771-776.
23. Johan Fundin, P.H., Wyn Brown and Ida Lidegran, *Poly(Acrylic Acid)-Cetyltrimethylammonium Bromide Interactions Studied Using Dynamic and Static Light Scattering and Time-Resolved Fluorescence Quenching.* Macromolecules, 1997. **30**: p. 1118-1126.
24. Hansson, P. and M. Almgren, *Polyelectrolyte-Induced Micelle Formation of Ionic Surfactants and Binary Surfactant Mixtures Studied by Time-Resolved Fluorescence Quenching.* Journal of Physical Chemistry, 1995. **99**(45): p. 16684-16693.
25. Goddard, E.D., *Polymer Surfactant Interaction .1. Uncharged Water-Soluble Polymers and Charged Surfactants.* Colloids and Surfaces, 1986. **19**(2-3): p. 255-300.
26. Proietti, N., M.E. Amato, G. Masci, and A.L. Segre, *Polyelectrolyte/Surfactant Interaction: An Nmr Characterization.* Macromolecules, 2002. **35**(11): p. 4365-4372.
27. Kaur, M.S.B.a.I., *Surfactant-Polymer Aggregates of Mixed Cationic Micelles and Anionic Polyelectrolytes: A Surfactant Head Group Contribution.* Progr Colloid Polym Sci, 2003. **122**: p. 37-46.
28. Hayakawa, K. and J.C.T. Kwak, *Surfactant Poly-Electrolyte Interactions .1. Binding of Dodecyltrimethylammonium Ions by Sodium Dextran Sulfate and Sodium Poly(Styrenesulfonate) in Aqueous-Solution in the Presence of Sodium-Chloride.* Journal of Physical Chemistry, 1982. **86**(19): p. 3866-3870.
29. Hayakawa, K., J.P. Santerre, and J.C.T. Kwak, *Study of Surfactant Poly-Electrolyte Interactions - Binding of Dodecyldecyltrimethylammonium and Tetradecyltrimethylammonium Bromide by Some Carboxylic Poly-Electrolytes.* Macromolecules, 1983. **16**(10): p. 1642-1645.
30. Abuin, E.B. and J.C. Scaiano, *Exploratory-Study of the Effect of Poly-Electrolyte Surfactant Aggregates on Photochemical Behavior.* Journal of the American Chemical Society, 1984. **106**(21): p. 6274-6283.
31. Lim, P.F.C., L.Y. Chee, S.B. Chen, and B.H. Chen, *Study of Interaction between Cetyltrimethylammonium Bromide and Poly(Acrylic Acid) by Rheological Measurements.* Journal of Physical Chemistry B, 2003. **107**(26): p. 6491-6496.
32. Thalberg, K., J. Vanstam, C. Lindblad, M. Almgren, and B. Lindman, *Time-Resolved Fluorescence and Self-Diffusion Studies in Systems of a Cationic Surfactant and an Anionic Polyelectrolyte.* Journal of Physical Chemistry, 1991. **95**(22): p. 8975-8982.
33. Konop, A.J. and R.H. Colby, *Role of Condensed Counterions in the Thermodynamics of Surfactant Micelle Formation with and without Oppositely Charged Polyelectrolytes.* Langmuir, 1999. **15**(1): p. 58-65.
34. Tanford, *The Hydrophobic Effect: Formation of Micelles and Biological Membranes.* 1980: Wiley.
35. Almgren, P.H.a.M., *Interaction of Cntab with Sodium (Carboxymethyl)Cellulose: Effect of Polyion Linear Charge Density on Binding Isotherms and Surfactant Aggregation Number.* J Phys Chem, 1996. **100**: p. 9038-9046.
36. Zana, O.A.a.R., *Effect of Temperature on the Interactions between Neutral Polymers and a Cationic and a Nonionic Surfactant in Aqueous Solutions.* Langmuir, 1994. **10**: p. 4048-4052.
37. Francoise Winnik, M.W.a.S.T., *Interaction of Hydroxypropylcellulose with Aqueous Surfactants: Fluorscence Probe Studies and a Look at Pyrene-Labeled Polymer.* J Phys Chem, 1987. **91**: p. 594-597.
38. Tian, Q., X. Zhao, X.Z. Tang, and Y.X. Zhang, *Hydrophobic Association and Temperature and Ph Sensitivity of Hydrophobically Modified Poly(N-Isopropylacrylamide/Acrylic Acid) Gels.* Journal of Applied Polymer Science, 2003. **87**(14): p. 2406-2413.

39. Shashkina, Y.A., Y.D. Zaroslov, V.A. Smirnov, O.E. Philippova, A.R. Khokhlov, et al., *Hydrophobic Aggregation in Aqueous Solutions of Hydrophobically Modified Polyacrylamide in the Vicinity of Overlap Concentration.* Polymer, 2003. **44**(8): p. 2289-2293.
40. Karlson, L., K. Thuresson, and B. Lindman, *Cyclodextrins in Hydrophobically Modified Poly(Ethylene Glycol) Solutions: Inhibition of Polymer-Polymer Associations.* Langmuir, 2002. **18**(23): p. 9028-9034.
41. Tanaka, R., J. Meadows, G.O. Phillips, and P.A. Williams, *Viscometric and Spectroscopic Studies on the Solution Behavior of Hydrophobically Modified Cellulosic Polymers.* Carbohydrate Polymers, 1990. **12**(4): p. 443-459.
42. Wang, K.T., I. Iliopoulos, and R. Audebert, *Viscometric Behavior of Hydrophobically Modified Poly(Sodium Acrylate),*Polymer Bulletin, 1988. **20**(6): p. 577-582.
43. Magny, B., F. Lafuma, and I. Iliopoulos, *Determination of Microstructure of Hydrophobically Modified Water-Soluble Polymers by C-13 Nmr,* Polymer, 1992. **33**(15): p. 3151-3154.
44. Gudeman, L.F. and N.A. Peppas, *Ph-Sensitive Membranes from Poly(Vinyl Alcohol) Poly(Acrylic Acid) Interpenetrating Networks.* Journal of Membrane Science, 1995. **107**(3): p. 239-248.
45. Magny, B., I. Iliopoulos, R. Zana, and R. Audebert, *Mixed Micelles Formed by Cationic Surfactants and Anionic Hydrophobically-Modified Polyelectrolytes,*Langmuir, 1994. **10**(9): p. 3180-3187.
46. Magny, B., I. Iliopoulos, R. Audebert, L. Piculell, and B. Lindman, *Interactions between Hydrophobically Modified Polymers and Surfactants,*in *Trends in Colloid and Interface Science Vi*, C. Helm, M. Losche, and H. Mohwald, Editors. 1992. p. 118-121.
47. Lee, C.T., K.A. Smith, and T.A. Hatton, *Photoreversible Viscosity Changes and Gelation in Mixtures of Hydrophobically Modified Polyelectrolytes and Photosensitive Surfactants.* Macromolecules, 2004. **37**(14): p. 5397-5405.
48. Hayashita, T., T. Kurosawa, T. Miyata, K. Tanaka, and M. Igawa, *Effect of Structural Variation within Cationic Azo-Surfactant Upon Photoresponsive Function in Aqueous Solution.* Colloid and Polymer Science, 1994. **272**(12): p. 1611-1619.
49. Kronberg, B., *Surfactant Mixtures.* Current Opinion in Colloid & Interface Science, 1997. **2**(5): p. 456-463.
50. C. Ted Lee, J., Kenneth A. Smith and T. Alan Hatton, *Small-Angle Neutron Scattering Study of the Micellization of PhotosensitiveSurfactants in Solution and in the Presence of a Hydrophobically ModifiedPolyelectrolyte.* Langmuir, 2009. **25**: p. 13784–13794.
51. Deshmukh, S., L. Bromberg, K.A. Smith, and T.A. Hatton, *Photoresponsive Behavior of Amphiphilic Copolymers of Azobenzene and N,N-Dimethylacrylamide in Aqueous Solutions.* Langmuir, 2009. **25**(6): p. 3459-3466.
52. Pouliquen, G., I. Porcar, C. Tribet, and C. Amiel, *Photoresponsive Thickening in Polyamphiphile-Based Physical Gels: The Examples of Micelle, Protein and Cyclodextrin Cross-Linkers*, in *Polymer Gels: Fundamentals and Applications*, H.B. Bohidar, P. Dubin, and Y. Osada, Editors. 2003. p. 262-288.
53. Ruchmann, J., S. Fouilloux, and C. Tribet, *Light-Responsive Hydrophobic Association of Surfactants with Azobenzene-Modified Polymers.* Soft Matter, 2008. **4**(10): p. 2098-2108.
54. Irie, M., Y. Hirano, S. Hashimoto, and K. Hayashi, *Photoresponsive Polymers .2. Reversible Solution Viscosity Change of Polyamides Having Azobenzene Residues in the Main Chain.* Macromolecules, 1981. **14**(2): p. 262-267.
55. Irie, M. and W. Schnabel, *Photoresponsive Polymers - on the Dynamics of Conformational-Changes of Polyamides with Backbone Azobenzene Groups.* Macromolecules, 1981. **14**(5): p. 1246-1249.
56. Takahashi, M., T. Okuhara, T. Yokohari, and K. Kobayashi, *Effect of Packing on Orientation and Cis-Trans Isomerization of Azobenzene Chromophore in Langmuir-Blodgett Film.* Journal of Colloid and Interface Science, 2006. **296**(1): p. 212-219.

57. Muller, N., *Kinetics of Micelle Dissociation by Temperature-Jump Techniques: A Reinterpretation.* J Phys Chem, 1972. **76**: p. 3017-3020.
58. Klaveness, T.M. and P. Ruoff, *Kinetics of the Cross-Linking of Polyacrylamide with Cr(Iii): Analysis of Possible Mechanisms.* J. Phys. Chem., 1994. **98**: p. 10119-10123.
59. Klaveness, T.M., P. Ruoff, and J. Kolnes, *Kinetics of the Cross-Linking of Poly(Acrylamide) with Cr(Iii). 3. Rheological Measurements of the Gelation.* J. Phys. Chem., 1995. **99**: p. 8255-8259.
60. Nijenhuis, K.T., *Viscoelastic Properties of Thermoreversible Gels*, in *Physical Networks: Polymers and Gels*, W. Burchard and S.B. Ross-Murphy, Editors. 1990, Elsevier: New York. p. 15-33.
61. Allain, C. and L. Salome, *Gelation of Semidilute Polymer Solutions by Ion Complexation: Critical Behavior of the Rheological Properties Versus Cross-Link Concentration.* Macromolecules, 1990. **23**: p. 981-987.
62. Hansen, E.W. and T. Lund, *Gelation of Xanthan by Trivalent Chromic Ions Monitored by 1h Nmr Relaxation: A Preliminary Study.* J. Phys. Chem., 1991. **95**: p. 341-344.
63. Terech, P., *Kinetics of Aggregation in a Steroid Derivative Cyclohexane Gelifying System,*Journal of Colloid and Interface Science, 1985. **107**(1): p. 244-255.
64. Le Feunteun, S. and F. Mariette, *Pfg-Nmr Techniques Provide a New Tool for Continuous Investigation of the Evolution of the Casein Gel Microstructure after Renneting.* Macromolecules, 2008. **41**: p. 2071-2078.
65. Hansen, E., A. Bouzga, B. Sommer, and P.O. Kvernberg, *Crosslinking of Pva and Glutaraldehyde in Water Monitored by Viscosity and Pulse Field Gradient Nmr: A Comparative Study.* Polymers for Advanced Technologies, 2000. **11**: p. 185-191.
66. Brand, T., S. Richter, and S. Berger, *Diffusion Nmr as a New Method for the Determination of the Gel Point of Gelatin.* Journal of Physical Chemistry B, 2006. **110**(32): p. 15853-15857.
67. Iliopoulos, I. and I. Furo, *Nmr Study of the Association of Anionic Surfactants with an Anionic Polyelectrolyte Hydrophobically Modified with Perfluorinated Side Chains.* Langmuir, 2001. **17**(26): p. 8049-8054.
68. Petit-Agnely, F. and I. Iliopoulos, *Aggregation Mechanism of Amphiphilic Associating Polymers Studied by F-19 and C-13 Nuclear Magnetic Resonance?* Journal of Physical Chemistry B, 1999. **103**(23): p. 4803-4808.
69. Blanshard, A.H.M.a.J.M., *Diffusion in Gels.* Polymer, 1982. **23**: p. 1012-1026.
70. Amsden, B., *Solute Diffusion within Hydrogels. Mechanisms and Models.* Macromolecules, 1998. **31**(23): p. 8382-8395.
71. deGennes, P., *Scaling Concepts in Polymer Physics.* 1979, Ithaca: Cornell UP.
72. Matsukawa, S. and I. Ando, *Study of Self-Diffusion of Molecules in a Polymer Gel by Pulsed-Gradient Spin-Echo 1h Nmr. 2. Intermolecular Hydrogen-Bond Interaction between the Probe Polymer and Network Polymer in N,N-Dimethylacrylamide-Acrylic Acid Copolymer Gel Systems.* Macromolecules, 1997. **30**: p. 8310-8313.
73. Colsenet, F., O. Soderman, and F. Mariette, *Effect of Casein Concentration in Suspensions and Gels on Poly(Ethylene Glycol)S Nmr Self-Diffusion Measurements.* Macromolecules, 2005. **38**: p. 9171-9179.
74. Colsenet, R., F. Mariette, and M. Cambert, *Nmr Relaxation and Water Self-Diffusion Studies in Whey Protein Solutions and Gels.* J. Agric. Food. Chem, 2005. **53**: p. 6784-6790.
75. Colsenet, R., O. Soderman, and F. Mariette, *Pulsed Field Gradient Nmr Study of Poly(Ethylene Glycol) Diffusion in Whey Protein Solutions and Gels.* Macromolecules, 2006. **39**: p. 1053-1059.
76. Feunteun, S. and F. Mariette, *Impact of Casein Gel Microstructure on Self-Diffusion Coefficient of Molecular Probes Measured by 1h Pfg-Nmr.* J. Agric. Food. Chem, 2007. **2007**: p. 10764-10772.
77. Johansson, L., U. Skantze, and J.-E. Lofroth, *Diffusion and Interaction in Gels and Solutions. 2. Experimental Results on the Obstruction Effect.* Macromolecules, 1991. **24**: p. 6019-6023.

78. Kwak, S. and M. Lafleur, *Nmr Self-Diffusion of Molecular and Macromolecular Species in Dextran Solutions and Gels.* Macromolecules, 2003. **36**: p. 3189-3195.
79. Gibbs, S. and C.S. Johnson, *Pulsed Field Gradient Nmr Study of Probe Motion in Polyacrylamide Gels.* Macromolecules, 1991. **24**: p. 6110-6113.
80. Ho, A.K., L. Bromberg, A.J. O'Connor, J.M. Perera, G.W. Stevens, et al., *Solute Diffusion in Associative Copolymer Solutions.* Langmuir, 2001. **17**: p. 3538-3544.
81. Ohtsuka, A. and T. Watanabe, *The Network Structure of Gellan Gum Hydrogels Based on the Structural Parameters by the Analysis of the Restricted Diffusion of Water.* Carbohydrate Polymers, 1996. **30**(2-3): p. 135-140.
82. Yamane, Y., I. Ando, F. Buchholz, A. Reinhardt, and S. Schlick, *Detection of Spatial Inhomogeneity in Poly(Acrylic Acid) Gels by Measuring Time-Dependent Diffusion Coefficients of a Probe in Nmr Experiments: Effect of the Degree of Cross-Linking and Degree of Swelling.* Macromolecules, 2004. **37**: p. 9841-9849.
83. Peppas, N.A. and S.L. Wright, *Solute Diffusion in Poly(Vinyl Alcohol) Poly(Acrylic Acid) Interpenetrating Networks.* Macromolecules, 1996. **29**(27): p. 8798-8804.
84. Pelta, M.D., H. Barjat, G.A. Morris, A.L. Davis, and S.J. Hammond, *Pulse Sequences for High-Resolution Diffusion-Ordered Spectroscopy (Hr-Dosy).* Magnetic Resonance in Chemistry, 1998. **36**(10): p. 706-714.
85. Soderman, O. and P. Stilbs, *Nmr-Studies of Complex Surfactant Systems,*Progress in Nuclear Magnetic Resonance Spectroscopy, 1994. **26**: p. 445-482.
86. Price, *Pulsed-Field Gradient Nuclear Magnetic Resonance as a Tool for Studying Translational Diffusion: Part Ii. Experimental Aspects.* Concepts in Magnetic Resonance, 1998. **10**: p. 197-237.
87. Wu, D.H., A.D. Chen, and C.S. Johnson, *An Improved Diffusion-Ordered Spectroscopy Experiment Incorporating Bipolar-Gradient Pulses,*Journal of Magnetic Resonance Series A, 1995. **115**(2): p. 260-264.
88. Stilbs, P., *Fourier Transform Pulsed-Gradient Spin-Echo Studies of Molecular Diffusion.* Progress in Nuclear Magnetic Resonance Spectroscopy, 1987. **19**: p. 1-45.
89. Petiaud, Q.-T.P.a.R., *Spectres Rmn Des Polymeres 1h-13c.* Vol. 1. 1980, London: Heyden.
90. Quang Tho Pham, R.P.a.H.W., *Proton and Carbon Nmr Spectra of Polymers.* 1991, New York: Wiley.
91. Mallion, J.A.N.F.G.a.R.B., *Aromaticity and Ring Currents.* Chem. Rev., 2001. **101**: p. 1349-1383.
92. Petit, F., I. Iliopoulos, and R. Audebert, *Aggregation of Associating Polymers Studied by F-19 Nmr.* Polymer, 1998. **39**(3): p. 751-753.
93. Gerig, J.T., *Fluorine Nmr of Proteins,*Progress in Nuclear Magnetic Resonance Spectroscopy, 1994. **26**: p. 293-370.
94. Nilsson, S., K. Thuresson, B. Lindman, and B. Nystrom, *Associations in Mixtures of Hydrophobically Modified Polymer and Surfactant in Dilute and Semidilute Aqueous Solutions. A Rheology and Pfg Nmr Self-Diffusion Investigation.* Macromolecules, 2000. **33**(26): p. 9641-9649.
95. Cussler, E.L., *Diffusion: Mass Transfer in Fluid Systems.* 1984: Cambridge University Press.
96. Reith, D., B. Muller, F. Muller-Plathe, and S. Wiegand, *How Does the Chain Extension of Poly (Acrylic Acid) Scale in Aqueous Solution? A Combined Study with Light Scattering and Computer Simulation.* Journal of Chemical Physics, 2002. **116**(20): p. 9100-9106.
97. Akcasu, A.Z. and C.C. Han, *Molecular-Weight and Temperature-Dependence of Polymer Dimensions in Solution.* Macromolecules, 1979. **12**(2): p. 276-280.
98. Tanford, *Physical Chemistry of Macromolecules.* 1961, New York: Wiley.
99. Kirkwood, J.G. and J. Riseman, *The Intrinsic Viscosities and Diffusion Constants of Flexible Macromolecules in Solution.* Journal of Chemical Physics, 1948. **16**(6): p. 565-573.
100. Teraoka, *Polymer Solutions: An Introduction to Physical Properties.* 2002, 2002: Wiley.

101. Kuhn, T. and H. Schwalbe, *Monitoring the Kinetics of Ion-Dependent Protein Folding by Time-Resolved Nmr Spectroscopy at Atomic Resolution.* Journal of the American Chemical Society, 2000. **122**(26): p. 6169-6174.
102. Derome, A., *Modern Nmr Techniques for Chemistry Research.* 1987.
103. Aniansson, E.A.G., S.N. Wall, M. Almgren, H. Hoffman, I. Kielmann, et al., *Theory of the Kinetics of Micellar Equilibria and Quantitative Interpretation of Chemical Relaxation Studies of Micellar Solutions of Ionic Surfactants.* Journal of Physical Chemistry, 1976. **80**: p. 905-922.
104. C. Groth, M.N., K. Holmberg, J. R. Kanicky and D.O. Shah, *Kinetics of the Self-Assembly of Gemini Surfactants.* Journal of Surfactants and Detergents, 2004. **7**: p. 247-255.
105. Flory, P.J., *Principles of Polymer Chemistry.* 1953, Ithaca: Cornell University Press.
106. Augeì , S., P.-O. Schmit, C.A. Crutchfield, M.T. Islam, D.J. Harris, et al., *Nmr Measure of Translational Diffusion and Fractal Dimension. Application to Molecular Mass Measurement.* The Journal of Physical Chemistry B, 2009. **113**(7): p. 1914-1918.
107. Mark, J.E. and P.J. Flory, *The Configuration of the Polyoxyethylene Chain.* Journal of the American Chemical Society, 1965. **87**: p. 1415-1423.
108. Biehl, R., X. Guo, R.K. Prud'homme, M. Monkenbusch, J. Allgeier, et al., *Diffusion of Compact Macromolecules through Polymer Meshes: Mesh Dynamics and Probe Dynamics.* Physica B: Condensed Matter, 2004. **350**(1-3): p. 76-78.
109. Dobrynin, A.V. and M. Rubinstein, *Hydrophobic Polyelectrolytes.* Macromolecules, 1999. **32**(3): p. 915-922.
110. Rubinstein, M. and A. Dobrynin, *Associations Leading to Formation of Reversible Networks and Gels.* Current Opinion in Colloid & Interface Science, 1999. **4**: p. 83-87.
111. Rubinstein, M. and A. Semenov, *Thermoreversible Gelation in Solutions of Associating Polymers. 2. Linear Dynamics.* Macromolecules, 1998. **31**: p. 1386-1397.
112. Rubinstein, M. and A.N. Semenov, *Dynamics of Entangled Solutions of Associating Polymers.* Macromolecules, 2001. **34**(4): p. 1058-1068.
113. Semenov, A. and M. Rubinstein, *Thermoreversible Gelation in Solutions of Associative Polymers 1. Statics.* Macromolecules, 1998. **31**: p. 1373-1385.
114. Semenov, A.N. and M. Rubinstein, *Dynamics of Entangled Associating Polymers with Large Aggregates.* Macromolecules, 2002. **35**(12): p. 4821-4837.
115. Tanaka, F., *Polymer-Surfactant Interaction in Thermoreversible Gels.* Macromolecules, 1998. **31**(2): p. 384-393.
116. Tanaka, F., *Intramolecular Micelles and Intermolecular Crosslinks in Thermoreversible Gels of Associating Polymers.* Journal of Non-Crystalline Solids, 2002. **307**: p. 688-697.
117. Tanaka, F., *Phase Formation of Associating Polymers: Gelation, Phase Separation and Microphase Formation.* Advances in Colloid and Interface Science, 1996. **63**: p. 23-40.
118. Tanaka, F., *Thermoreversible Gelation of Associating Polymers.* Physica A, 1998. **257**(1-4): p. 245-255.
119. Tanaka, F., *Elastically Effective Chains in Transient Gels with Multiple Junctions.* Macromolecules, 1996. **29**: p. 7571-7580.
120. Tanaka, F. and M. Ishida, *Microphase Formation in Mixtures of Associating Polymers.* Macromolecules, 1997. **30**(6): p. 1836-1844.
121. Tanaka, F. and M. Ishida, *Thermoreversible Gelation with Two-Component Networks.* Macromolecules, 1999. **32**: p. 1271-1283.
122. Tanaka, F. and W. Stockmayer, *Thermoreversible Gelation with Junctions of Variable Multiplicity.* Macromolecules, 1994. **27**: p. 3943-3954.

Chapter 5

Photoresponsive Vesicles

5.1 Introduction

Surfactants are able to self-assemble into a wide variety of structures, including spherical micelles, reverse micelles, rod-like micelles, unilamellar and multilamellar vesicles, and planar bilayers. These structures have attracted attention in a variety of fields, including biology and medicine. Closed bilayer structures bear a resemblance to naturally occurring cell membranes, so artificially produced bilayers have been used to mimic those membranes. There is indeed speculation that the self-assembly of vesicles was an important step in the origins of life, as these compartments provided an environment that was separated from the surroundings and also one that might have facilitated biologically useful reactions [1]. Vesicles have also been used for drug delivery [2-6]. Hydrophilic drugs can be stored within the aqueous cavity of the vesicle; the stored materials permeate slowly through the bilayer wall so they remain encapsulated until released. Hydrophobic chemicals are stored within the bilayer. Vesicles have also been proposed for removing contaminants from aqueous streams [7]. Self-assembled vesicles are also used as a soft template for more permanent hollow silica nanoparticles [8-11]; the desired size and shape of the final nanoparticles are tuned by adjusting the surfactant system.

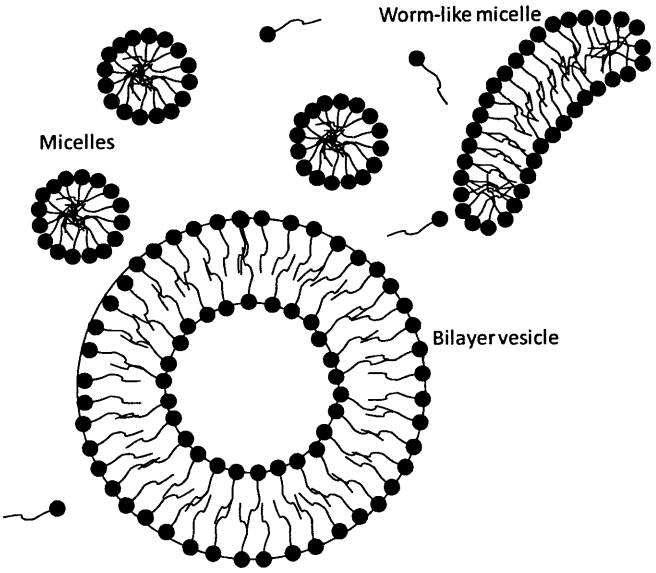

Figure 5-1 Various structures that may result from self-assembly of surfactants. The hydrophobic domains formed by the surfactant tail groups is generally described as being liquidlike. Some water may penetrate

some distance into what is drawn as the hydrophobic core; this region is called the Palisade layer. Not shown are any counterions of the surfactant molecules.

The ability to reversibly alter self-assembled structures between different shapes, or to disrupt self-assembly entirely, would be beneficial to many of these possible applications. For example, an external stimulus that triggered the formation or disruption of vesicles could be used to load and discharge the drug or pollutants localized within the vesicles. The external stimulus could also be used to create a multitude of soft templates from a single chemical system. Micelle to vesicle transitions have been reported to be initiated by changes in temperature [12-15], pressure [16], or the addition of some other chemical [17].

For some applications, light may be a more advantageous stimulus because it is less invasive and is easily spatially controlled. There are some prior examples of light-sensitive vesicles in the literature. Veronese et al have demonstrated surfactants that are synthesized through a photoreaction; these surfactants then assemble into vesicles [18]. Such a mechanism may be relevant to the origin of life, but the process is irreversible, limiting further applications. Conversely, Eastoe et al have shown that vesicles formed by photodestructible surfactants are destroyed upon irradiation [19], but this is also an irreversible process. Uda et al have developed a system wherein vesicles fuse together to form larger vesicles upon irradiation, though the reverse would be a slow thermal process [20]. Sakai et al made truly photo-reversible vesicles from a mixture of an azoTAB-like surfactant and sodium dodecylbenzenesulfonate (SDBS) [21]; vesicles were present in the dark- and visible-adapted states, but were disrupted in the UV-state. The exact nature of the structures in the UV state was not clear, but glucose that had been taken up by the vesicles was released upon UV irradiation.

The present work describes an attempt to extend this field by using the azoTAB surfactant to create a series of self-assembled shapes that are photoswitchable. This was done by exploring mixtures of azoTAB with sodium octyl sulfate (SOS) under different irradiation conditions.

5.2 Background

5.2.1. Geometric constraints

The foundations of the current theoretical understanding of self-assembly are largely due to Tanford [22] and Israelachvili et al [23]. The hydrophobic effect, which favors the removal of hydrophobic materials from the aqueous environment, is a major component of the change in free energy associated with moving a surfactant molecule from the bulk solution to a micelle or vesicle. This was described in Chapter 1.

There are also two effects to consider at the colloidal surface. One is the electrostatic or steric repulsion between the headgroups of different surfactant molecules; this repulsion would tend to increase the surface area per molecule within the colloid. The other effect is an interfacial tension due to any remaining contact between the surrounding water and the hydrophobic core of the colloid. This tension would tend to drive the headgroups closer together to reduce this unfavorable contact, and thus decrease the surface area per molecule. The overall free energy is minimized at some optimum area per molecule, a_0.

This consideration of free energies leads to an understanding of why aggregates form, as well as the critical micelle concentration (CMC), but it does not give any insight on why rod-like micelles, vesicles and planar bilayers sometimes form instead of spheres. A simple set of criteria derived from geometric packing constraints was described by Israelachvili to predict and explain the appearance of these different structures [23]. Briefly, if a micelle is spherical, then the number of surfactant molecules within it (the aggregation number N_{agg}) will be

$$N_{agg} = \frac{4\pi R^3}{3v} \tag{5.1}$$

where v is the volume of the hydrophobic tail, and R is the micellar radius. The aggregation number can also be written as

$$N_{agg} = \frac{4\pi R^2}{a} \tag{5.2}$$

where a is the surface area per molecule. Combining these expressions results in the following geometric relationship:

$$\frac{v}{Ra} = \frac{1}{3} \tag{5.3}$$

It is assumed that the balance between the competing attractive and repulsive forces at the surface constrains the surface area a to being approximately equivalent to the optimal surface area a_0. The radius R cannot be larger than the fully extended length of the surfactant tail, so a further constraint is that $R \leq l_c$, where l_c is some critical length that is on the order of the fully extended length. Applying these two constraints, it is apparent that spherical micelles are only possible if

$$\frac{v}{a_o l_c} \leq \frac{1}{3} \tag{5.4}$$

where the term $v / a_o l_c$ is known as the packing parameter. When the analogous analysis is carried out for rod-like micelles, it can be shown that these shapes require that

$$\frac{1}{3} \leq \frac{v}{a_o l_c} \leq \frac{1}{2} \tag{5.5}$$

and for vesicles,

$$\frac{1}{2} \leq \frac{v}{a_o l_c} \leq 1 \tag{5.6}$$

These criteria are summarized in Figure 5-2, taken from Israelachvili's text [24].

Lipid	Critical packing parameter $v/a_o l_c$	Critical packing shape	Structures formed
Single-chained lipids (surfactants) with large head-group areas: *SDS in low salt*	< 1/3	Cone 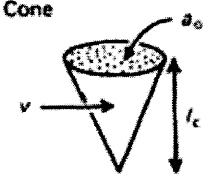	Spherical micelles 
Single-chained lipids with small head-group areas: *SDS and CTAB in high salt, nonionic lipids*	1/3-1/2	Truncated cone 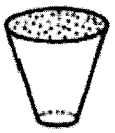	Cylindrical micelles 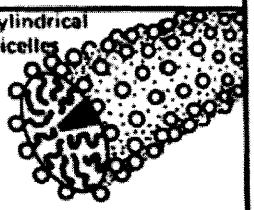
Double-chained lipids with large head-group areas, fluid chains: *Phosphatidyl choline (lecithin), phosphatidyl serine, phosphatidyl glycerol, phosphatidyl inositol, phosphatidic acid, sphingomyelin, DGDG*, dihexadecyl phosphate, dialkyl dimethyl ammonium salts*	1/2-1	Truncated cone 	Flexible bilayers, vesicles 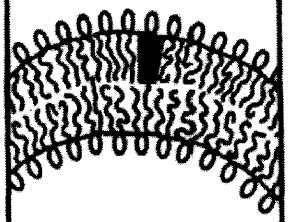
Double-chained lipids with small head-group areas, anionic lipids in high salt, saturated frozen chains: *phosphatidyl ethanolamine, phosphatidyl serine + Ca^{2+}*	~1	Cylinder 	Planar bilayers 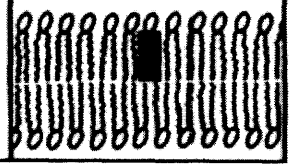

Figure 5-2 Summary of the different self-assembled structures that may be expected at different values of the packing parameter. Taken directly from [24].

For surfactants with single alkyl tails, Tanford provided expressions for the tail length and volume, in nm and nm^3 respectively:

$$l_c \leq l_{\max} = 0.154 + 0.1265n \tag{5.7}$$

$$v = 0.0274 + 0.0269n \tag{5.8}$$

where n is the number of carbons in the tail alkyl chain. There are subtleties in predicting the surface area a; it can be affected by the solution ionic strength or even the nature of the surfactant tail [25].

The usage of these geometric concepts has been common in the literature, and it has often been qualitatively successful.

5.2.2. Vesicles

Most common single-tailed surfactants tend to form various types of micelles, instead of vesicles. This observation is consistent with the geometric criteria presented above. An increase in the tail volume would be predicted to favor vesicle formation; this could be accomplished by using double-tailed surfactants. Indeed, naturally occurring bilayer membranes are comprised of double-tailed phospholipids. Bangham et al first found in 1964 that phospholipids could be used to create vesicles in-vitro; these structures are generally called liposomes. However, liposomes are not thermodynamically stable. High energy methods like sonication are required to prepare the vesicular solutions, and over the course of months the phospholipids form some multilamellar structure or crystalline precipitates [26].

More recently it has been found that mixtures of commonly available single-tailed cationic and anionic surfactants can spontaneously form vesicles. Dubbed 'catanionic' mixtures, this concept was most notably reported by Kaler et al [27]. Due to electrostatic attraction, the oppositely charged headgroups form ion pairs. The result is effectively a double-tailed surfactant, with a larger tail volume v than either original surfactant, as well as a compact surface area a due to the attractive attractions between the headgroups. Many different surfactant pairs have been found to result in vesicles at certain overall concentrations and mixing ratios, including: cetyl trimethylammonium tosylate (CTAT) and SDBS [27], cetyltrimethylammonium bromide (CTAB) and sodium octyl sulfate (SOS) [28-31], dodecyltrimethylammonium chloride (DTAC) and SDBS [32], among many others. Double-chained surfactants [33, 34] and gemini surfactants [35] have also been used as one of the surfactants in the mixture. In many cases, the counterions of the original surfactants are still present in solution ('excess salt'). If the original counterions were simply H^+ and OH^-, these of course combine to form water and the solution is called salt-free. These latter mixtures are sometimes distinguished with the name 'ion-pair amphiphiles' [4]. The presence or absence of counterions may cause systems to behave differently, due to the electrostatic screening effect of counterions.

Vesicles formed in catanionic mixtures have been shown to be stable for months, even years, and may be thought of as equilibrium structures [36]. Marques et al prepared equivalent solutions through very different paths, and found that unilamellar vesicles were present in each [36]. The vesicle size distribution was somewhat path dependent, but a short period of sonication caused each sample to become

apparently identical, despite different preparation methods prior to the sonication. It was suggested that different preparation methods result in the solutions being kinetically trapped in metastable states very near the global equilibrium, with a short period of sonication bringing about thermodynamically stable vesicles.

Many authors have constructed phase diagrams for the ternary mixtures (cationic surfactant, anionic surfactant and water). The phase diagrams typically resemble the generic example drawn by Bramer et al, Figure 5-3:

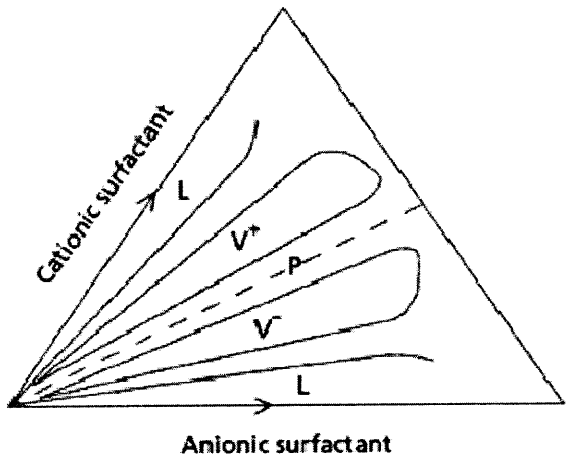

Figure 5-3 Typical phase diagram in catanionic mixtures. L denotes the isotropic micellar phase. P denotes precipitate formation. V^+ and V^- denote positively and negatively charged vesicles, respectively. Broken line marks equimolar mixtures of the two surfactants. Taken from Bramer et al [4].

The example phase diagram was drawn to be symmetric, though an asymmetry may be expected if the tail lengths of the two surfactants differ [26].

Aggregates may form in catanionic mixtures at concentrations well below the CMC of either surfactant alone. At some overall concentration, the nature of the structures formed is a function of the mixing ratio of the two surfactants. When the concentration of one surfactant is much higher than that of the other, an isotropic micellar phase results. These micelles need not be spherical, but may also be globular or worm-like [4]. The micelles typically grow as the mixing ratio approaches equimolarity, until vesicles form. Different systems show different behavior in the transition region between micellar and vesicular phases; there may be phase separation and precipitation, or a coexistence of micelles and vesicles. There is also a region of precipitate formation in equimolar and nearly equimolar solutions; the oppositely charged surfactants neutralize each other and form crystals.

The stability of catanionic vesicles has been further explored. Each surfactant on its own will assemble into colloids of a preferred curvature, based on the optimal surface area per molecule and packing constraints. This typically results in some sort of micelle, whether it be spherical or cylindrical. A vesicle presents a different radius of curvature from those micelles; in fact the two monolayers of the vesicle have opposite radii. These differences in curvature are due to the mixing of the surfactants; some mixture of the two will have a different equilibrium curvature from either surfactant alone. Further, the two opposing monolayers in the vesicle must have different compositions, to allow each to have differing curvatures [37]. If the bending energy of the bilayer is high, then vesicles can be expected to be stabilised by the energy cost of taking on any other curvature [29]. Even if the bending energy is low, vesicles can be stabilised against growth by fusion by repulsive undulations [29].

5.3 Choice of surfactant system

Sodium octyl sulfate was chosen as the anionic surfactant to pair with azoTAB for several reasons. Mixtures of SOS and other trimethylammonium halide surfactants have been well characterized before, providing a guide to this work. Also, the tail lengths in the system were considered. The fully extended length of SOS is about 1.2 nm, as is that of *cis* azoTAB. The length of fully extended *trans* azoTAB is about 1.9 nm. Therefore the transition from *trans* to *cis* azoTAB would bring about a change from a surfactant pair with mismatched tail lengths to a pair with matched tail lengths. This could have interesting implications for the resulting structures, as the relative lengths of the tails have been reported to have an impact on the resulting colloids [4].

The CMCs of the surfactants also differ. As found in Chapter 2, the CMC of *trans* CMC is about 3.3 mM in deuterium oxide, and between 4 and 5 mM in water. It was not possible to isolate samples of 100% *cis* azoTAB, nor was it possible to observe the CMC in the UV adapted state with 97% *cis*. However, the CMC of the *cis* is somewhere above 12 mM, if there is indeed a proper CMC in that system. The CMC of SOS in water is about 133 mM [38].

The mixture of azoTAB and SOS has multiple components: *trans* azoTAB, *cis* azoTAB, SOS, the sulfate and bromide counterions and water. The ability to use light to change the composition of any sample adds to degree of flexibility not present in traditional catanionic mixtures.

5.4 Experimental section

5.4.1. Materials

The azoTAB surfactant, described in Chapter 1, was synthesized following the procedure of Hayashita et al [39]. Sodium octyl sulfate was used as received from Fluka. Solutions were made in both de-ionised water, obtained from a Millipore Milli-Q system, and deuterium oxide, obtained from Cambridge Isotopes.

5.4.2. Sample preparation

Most samples were prepared such that the total concentration of surfactant was 20 mM. This was done by preparing a 20 mM stock solution of azoTAB and a 20 mM stock solution of SOS, and then mixing them at the desired mixing ratio. The stock solutions were individually sonicated before being mixed together. Due to the different molecular weights of the two surfactants, the total weight fraction of surfactant was not constant. A 20 mM solution of azoTAB in deuterium oxide has a surfactant wt% of 0.76, while 20 mM SOS is 0.42 wt% surfactant. The corresponding weight percentages in water are 0.83% and 0.46%. These are within the concentration range normally used for vesicle studies. Any solution with azoTAB was kept in the dark, when not being intentionally irradiated.

Other mixtures were prepared at higher or lower total concentrations, as described in the text.

Initial observations were made after only gentle vortex mixing of the mixed solutions. Samples were then centrifuged for at least 30 minutes, to cause any precipitates to sediment out. Centrifugation was also used to cause dust particles to sediment out, in order to allow a dust-free solution to be obtained for light scattering studies. Sonication was also applied, but was not found to have any obvious impact on visual appearance, or NMR results.

5.4.3. Irradiation

UV irradiation was done with a Dymax BlueWave 200 lamp, described in Chapter 2. At a distance of one inch from the lightguide, the irradiance was 110-140 mW/cm^2. The kinetics models developed in Chapter 2 were used to guide the required irradiation times; the light was applied from different directions to ensure spatially even conversion. About 30 minutes of UV irradiation was used. Visible irradiation was done with an argon ion laser meant for light scattering studies, producing 514 nm light. The irradiation was continued until the scattering rate and the hydrodynamic radius from the dynamic light scattering experiment stabilised, indicating a photostationary state was achieved. About 15 minutes was sufficient. Measurements were made within one hour of the exposure to UV or visible light. Samples were loaded in

either 5 mm borosilicate NMR tubes when doing NMR experiments, or borosilicate light scattering tubes for all other experiments.

The argon ion laser was found to have no heating effect on the solutions. Prolonged exposure to UV light from the Dymax lamp did cause moderate heating, so the irradiation was done in short increments to prevent the temperature from rising. When this was not practically possible (as with the sample for cryo-TEM), the sample was allowed to cool for 30 minutes before further preparation.

5.4.4. NMR methods

One-dimensional and diffusion NMR experiments were performed largely as detailed in Chapter 3. 12-20 scans were sufficient for a good signal/noise ratio in the one-dimensional experiments; this required 3-5 minutes of scanning time. Sample volumes were 0.6 to 0.7 mL. For diffusion measurements, 16 scans were done to complete the suggested phase cycling routine for the BPP-LED sequence [40]. The gradient strength was varied from 0.02 T/m to as high as 0.49 T/m; the variation in gradient strength was used to do the Stejskal-Tanner analysis (see Chapter 3). The pulse width δ was 2 ms, and the time T was usually 500 ms, resulting in a diffusion time Δ of 502.2 ms. For simplicity, this is described as a diffusion time of 500 ms in the text. Diffusion times of 10, 50 and 100 ms were also used, in order to detect any dependence of the observed diffusion coefficients on diffusion time.

5.4.5. Dynamic light scattering

Measurements were made at 90° with an argon ion laser and the Brookhaven BI-200SM system. The autocorrelation function was fit by the Brookhaven software to find the diffusion coefficients, and then the Stokes-Einstein equation was used by the software to find the hydrodynamic diameter. The CONTIN method was used for the fit; the results from other models (NNLS) were largely consistent with the CONTIN. The minimum sample volume was 1.5 mL.

The sample tubes were soaked in sulfuric acid, then rinsed in water and methanol, in order to remove any dust, before the addition of sample.

Supplementary experiments were done at a variety of scattering angles: 45, 60, 65, 70, 90, 110 and 135 degrees for a 20 mM surfactant solution in water, with a SOS/azoTAB molar mixing ratio of 30/70. No angular dependence was observed.

This argon ion laser itself caused photoreaction of azoTAB; it was in fact used to bring about the visible photostationary state. It could therefore only be used to characterize the visible-adapted state of azoTAB, or the transition to this state. A second DLS instrument, the Dynapro Titan TC, was used to characterize

solutions without perturbing them; the wavelength of this instrument was 830 nm. This wavelength does not cause isomerisation of azoTAB at any detectable rate. The Dynapro is located at the Biophysical Instrumentation Facility. The sample size was 45 μL, and the path length 3 mm.

5.4.6. Cryo-transmission electron microscopy (cryo-TEM)

Cryo-TEM was used to image self-assembled structures that were too small (sub-micron) to view directly with an optical microscope. Samples were prepared and irradiated as described above. Samples were about 2-3 days old at the time of observation by TEM. Some samples were kept in the dark, while others were irradiated with visible at 514 nm or UV. The preparation for TEM was done within 1 hour of irradiation. This preparation was fully automated. A sample of a few microliters was taken from the solution, under conditions of nearly 100% relative humidity to avoid evaporation. This sample was put onto a lacy carbon grid, and blotted to remove any excess. This was then plunged into liquid ethane to vitrify the sample; the cooling rate was about 10^5 cal/s. This process required 5 s. The vitrified samples where then transferred to the electron microscope (JEOL 1200TEM) under liquid nitrogen.

5.4.7. Optical microscopy

The Zeiss Axiovert 200 system was used for the observation of relatively larger structures. 10x, 20x, 50x and 100x magnification was available, as was polarized light.

5.5 Results

5.5.1. Visual observation, light microscopy and turbidity

A series of 20 mM SOS/azoTAB mixtures were prepared in water, and kept in the dark-adapted state such that the azoTAB was entirely *trans*. After gentle vortex mixing to prepare the mixture, the samples were visually observed. At molar mixing ratios of 0/100 through 30/70 SOS/azoTAB, clear yellow solutions resulted, which would be consistent with the isotropic micellar phase that might be expected. Mixing ratios of 34/66 and 40/60 SOS/azoTAB yielded slightly cloudy and very cloudy samples respectively, while precipitate was apparent from 50/50 to 80/20 SOS/azoTAB. 90/10 was turbid. 100/0 was clear and colorless, consistent with a simple liquid with no aggregates.

As expected, equimolar mixtures resulted in phase separation. It was also apparent that the phase diagram in this system was asymmetric, with the anionic-rich side being dominated by phase separation.

In traditional catanionic mixtures, a slight bluish tinge is apparent in solutions with vesicles, due to light scattering. The strong yellow color of azoTAB solutions prevented any blue color from being detected, but turbidity was taken as a possible sign of large aggregates. However, turbidity could also be an indication of precipitate that remained suspended in solution. The samples were centrifuged, to remove any precipitate. A summary of the visual observations on the resulting samples is given below:

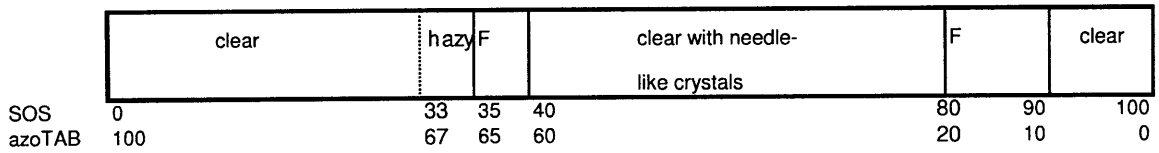

Figure 5-4 Visual observations at a total concentration of 20 mM surfactant, and different SOS/azoTAB mixing ratios. After centrifugation. Samples kept in the dark, so azoTAB is at 100% *trans*. Essentially the same observations were made in both deuterium oxide and water, see text. Clear samples were found at mixing ratios from 0/100 to 32.5/67.5 SOS/azoTAB, and again at 100/0. Hazy samples resulted at 33/67 and 34/66, but with no apparent precipitate. 'F' denotes the appearance of fuzzy/fluffy precipates, seen at 35/65, 40/60, 80/20 and 90/10. From 35/65 to 70/30, there was a definite phase separation with a clear liquid above needle-like crystals.

In the composition range around the equimolar point, crystals were apparent after centrifugation (and in some cases, before). The crystals continued growing for several weeks, signaling some slow dynamics in the system. After a full year however, no crystals were visible in any of the other samples. On either side of the crystal-forming region were samples with precipitates of fuzzy appearance. On the azoTAB-rich side, this was followed by a turbid region with no obvious precipitates. Finally, the extrema of the phase diagram correspond to clear solutions.

When repeated in deuterium oxide, an identical phase diagram resulted. Any solvent effect between deuterium oxide and water did not appear to be very strong. If there was any difference, it was that the 33/67 and 34/66 azoTAB/SOS samples were more obviously turbid in deuterium oxide than in water.

In trying to detect possible vesicles, the turbid and 'fuzzy' parts on the azoTAB-rich side of the phase diagram were of most interest, and these samples were examined under a light microscope. Under polarizers, the 'fuzzy' samples showed 'maltese cross' patterns (Figure 5-5). These patterns are indicative of large multilamellar 'onion' structures [36, 41]. However, nothing could be observed by light microscope in the clear or turbid solutions. This indicated that there were no micron-scale structures in these samples.

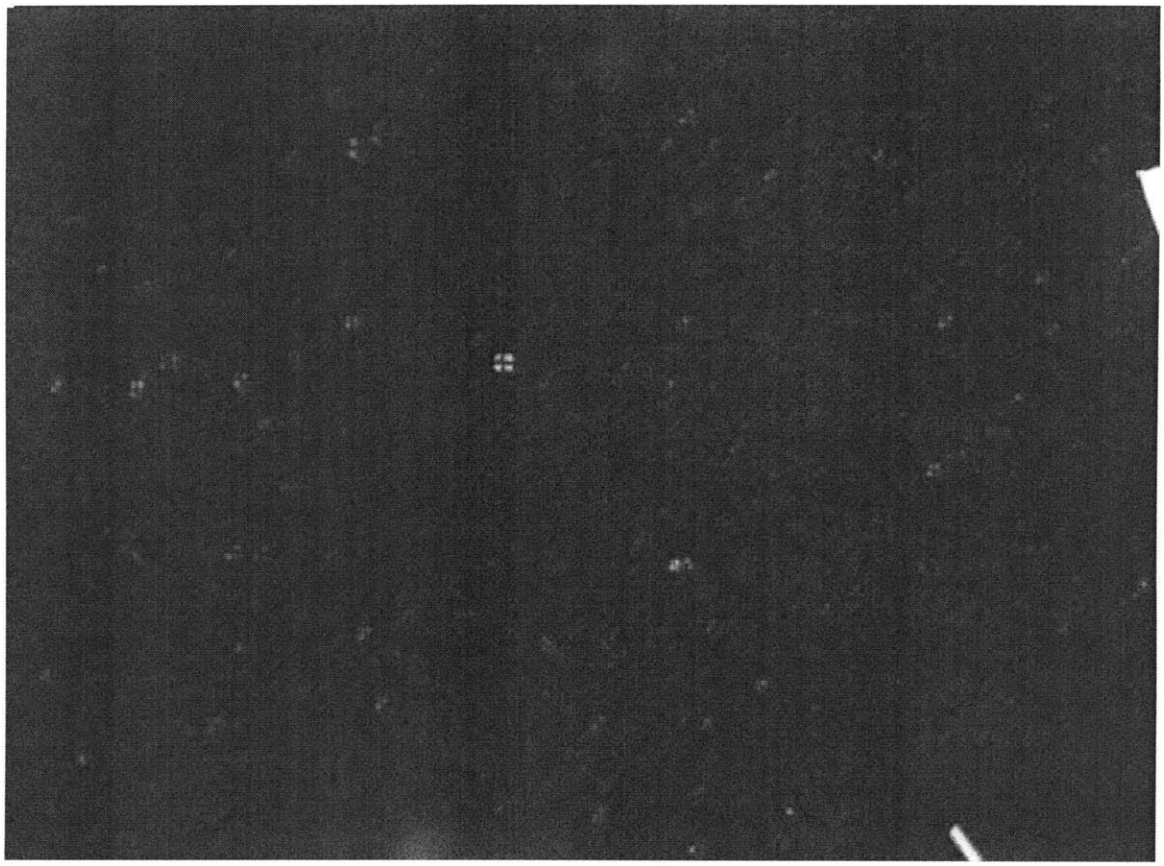

Figure 5-5 20 mM SOS/azoTAB mixture in water at a molar mixing ratio of 40/60. Observed at 20x magnification under polarized light. Maltese cross patterns indicate multilamellar structures. Visually under no magnification, these samples contained fuzzy-looking precipitates.

The observations discussed so far were all with azoTAB in the dark-adapted state, meaning that all of the azoTAB was existing as the *trans* isomer. When exposed to visible light from an argon ion laser from the light scattering apparatus, the appearance of the 34/66 azoTAB/SOS sample became much more strongly turbid in both water and deuterium oxide. In the visible-photostationary state, about 80-90% of the azoTAB existed as the *trans* isomer. Upon UV irradiation (resulting in 3-4% *trans*), the sample became clearer. These changes in turbidity were observed by following the light scattering rate of the solutions at 90°.

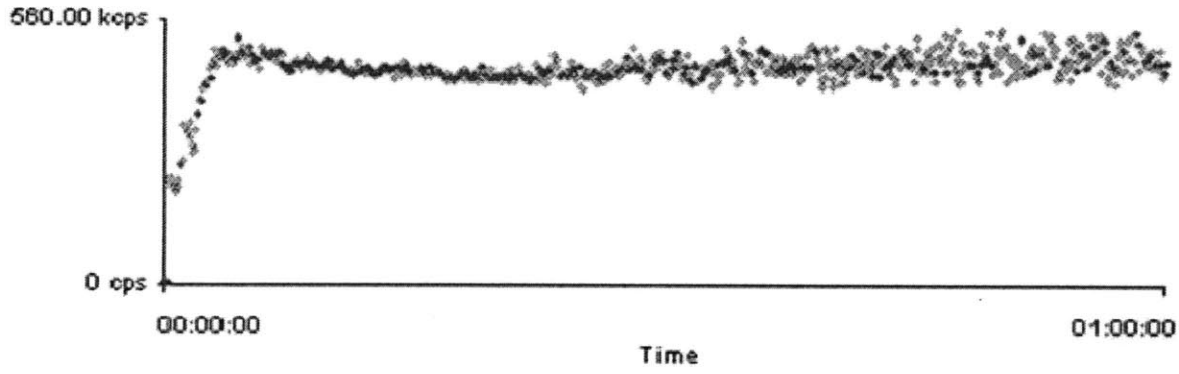

Figure 5-6 Change in scattering rate over time, under visible (514 nm) irradiation. The laser for light scattering is used to simultaneously perturb the sample, and observe it. 20 mM 34/66 azoTAB/SOS solution, initially dark-adapted (100% of azoTAB is *trans*). Experiment proceeded for one hour. Solvent was water. Laser power: 0.5 W. Scattering rate in counts/s should be regarded as an arbitrary unit.

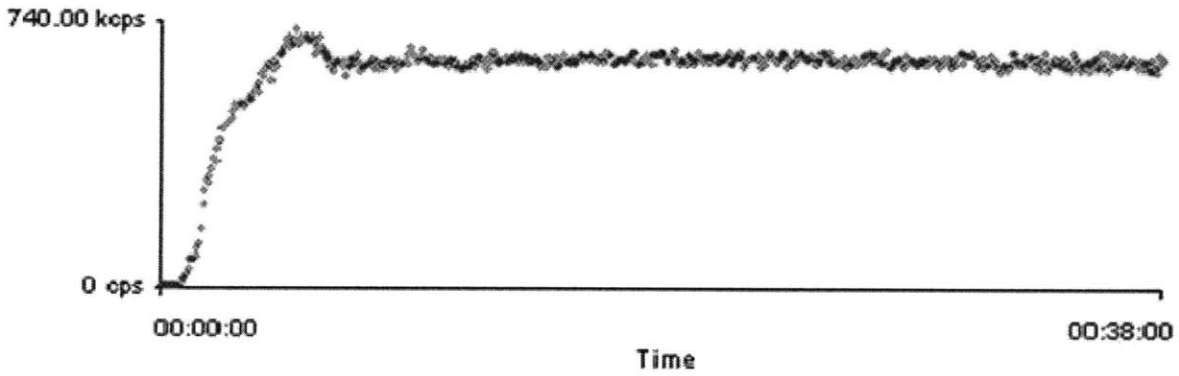

Figure 5-7 Same experiment and sample as Figure 5-6, but with the initial condition being the UV photostationary state (3-4% of the azoTAB is *cis*)

From these scattering rate histories, it is apparent that some major change in aggregate structure was induced by the argon ion laser. This change took place on the time scale of minutes. The solution was much more strongly scattering in the visible-adapted state, than the dark- or UV-states. This provided an initial evidence of some photoreversible effect.

In addition, the 20 mM samples with a molar mixing ratio of 34/66 and 33/67 SOS/azoTAB were noticeably more viscous than those at other compositions. This effect was not quantified, but provided further evidence for the formation of large aggregates.

5.5.2. Dynamic light scattering

Two different DLS instruments were used, in order to find the hydrodynamic radii of whatever aggregates were present in the various samples. One, with a 514 nm argon ion light source, could only be used to

characterize the visible-adapted state of the solutions because that 514 nm light itself converted the azoTAB to the visible state. The other used 830 nm light, and therefore did not perturb the azoTAB. This latter system was used to observe the dark-adapted samples.

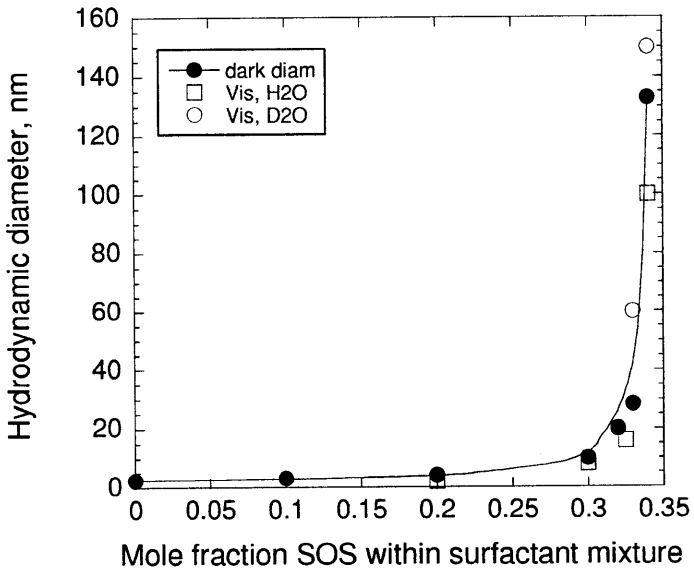

Figure 5-8 Mean hydrodynamic diameter of aggregates in 20 mM SOS/azoTAB aqueous solutions. Solid markers: dark-adapted state (azoTAB is fully *trans*). Hollow markers: visible state (azoTAB is 80-90% *trans*). Circles: in deuterium oxide solvent. Squares: in water solvent. Line drawn to guide the eye.

The azoTAB rich side of the phase diagram was studied, up to the point where multilamellar aggregates formed. Based on the previously observed CMCs, the azoTAB-only solutions are expected to contain micelles at this concentration. It appears that there is some micellar growth as SOS is added to the mixture. The hydrodynamic diameter is about 2.4-3 nm at mixing ratios of 0/100 or 10/90 azoTAB/SOS, consistent with simple micelles. There is then a fairly rapid transition to some much larger structure.

There is no strong difference here between dark-adapted and visible-adapted states, despite the strong difference in turbidity rate that was previously observed. Somewhat erratic results were obtained in the UV state; these are not reported.

Some caution must be used in interpreting the hydrodynamic dimensions, as some of the aggregates may not be spherical. There may also be significant polydispersity in any vesicle system.

In order to detect the concentration at which aggregation begins at the 34/66 mixing ratio, samples were prepared for DLS at overall concentrations of 0.1, 1 and 5 mM. In Figure 5-9 it can be seen that no aggregates were detected at 0.1 mM, but colloids were present at 1 mM and 5 mM. These colloids were

about the same size as those seen at 20 mM. The onset of aggregation is therefore between 0.1 and 1 mM, which is below the CMC of either surfactant alone.

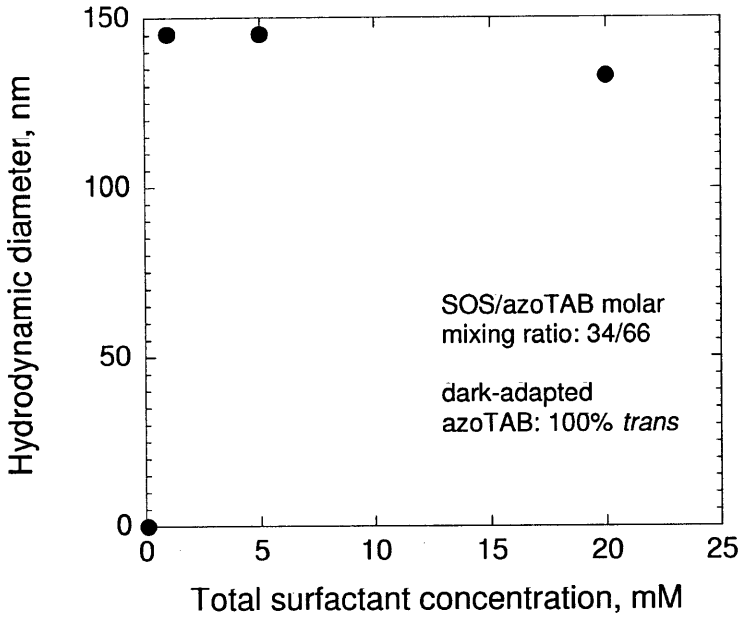

Figure 5-9 Hydrodynamic diameter from DLS measurements, over fixed composition but varying overall surfactant concentration. Measured in the dark-adapted state.

5.5.3. NMR

The widths of the peaks in an NMR spectrum can provide some qualitative indication of aggregate formation, as discussed in Chapter 3. Linewidths are related to the relaxation rates of the nuclei which are excited by the initial radiofrequency pulse of the one-dimensional NMR experiment. Relaxation pathways include interactions with other nuclei on the same molecule, as well as interactions with nuclei on surrounding molecules. A surfactant molecule that maintains close contact with other surfactant molecules will therefore have nuclei that relax more quickly than a surfactant that is free in the bulk solution. As shown in Chapter 3, NMR peaks are broader in micellar solutions, than below the CMC.

The same principle was used in the catanionic mixtures of this Chapter. NMR spectra in the azoTAB-rich region were collected under the different light conditions, at a fixed total surfactant concentration of 20 mM. Some key spectra are presented below. All NMR studies were done in deuterium oxide.

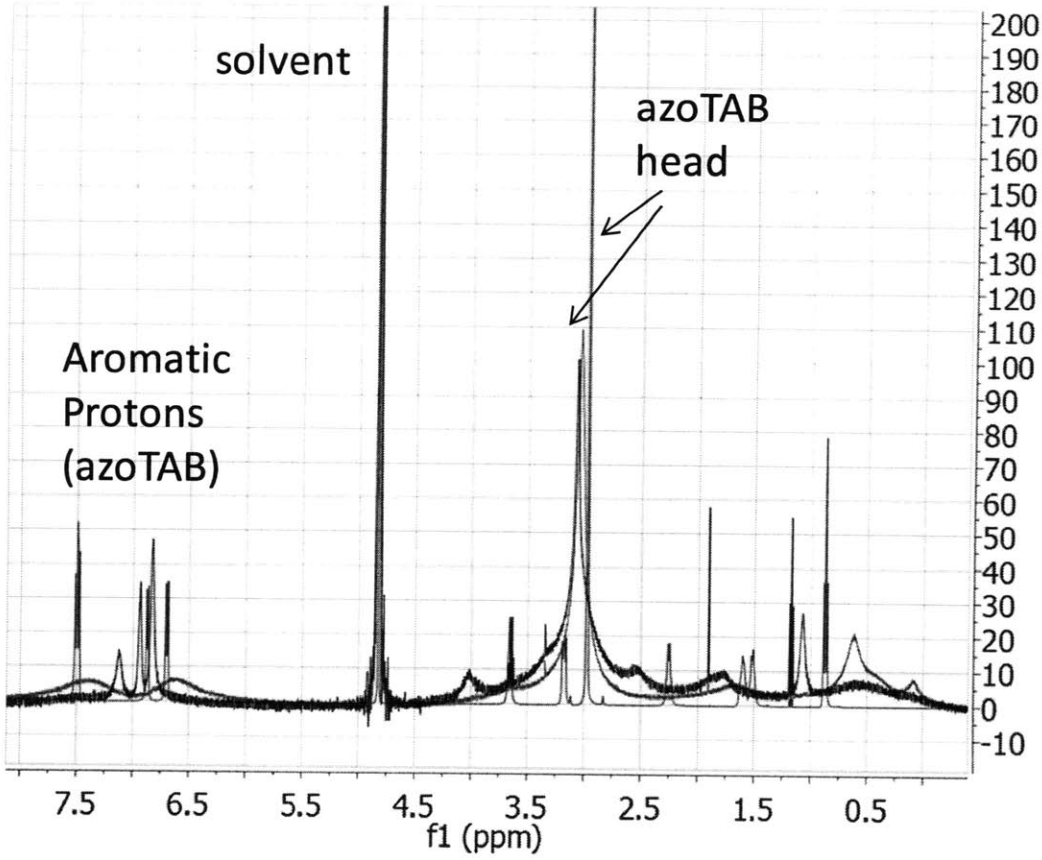

Figure 5-10 Proton NMR spectra. Red: 20 mM azoTAB, dark-adapted state (fully *trans*). Micelles expected. Green: 20 mM, azoTAB/SOS mixture, 34/66 molar mixing ratio, dark-adapted. Blue: 20 mM 34/66 mixture, visible-adapted (80-90% of azoTAB is *trans*). See text.

Simple micelles are expected in a dark-adapted azoTAB sample of 20 mM; the resulting NMR spectrum has well-defined peaks for each nucleus (red). The peak linewidths are a little broader than in a sample below the CMC, but are still identifiable. The peaks become rather more broad as SOS is added to the mixture. The most extreme example is at a molar mixing ratio of 34/66 SOS/azoTAB. This sample was faintly turbid in the dark state, and strongly turbid in the visible state. The NMR spectrum in the dark state of the 34/66 mixture shows very broad peaks (green), to the point that it becomes difficult to identify many peaks. The 34/66 mixture under visible light (blue) shows those peaks becoming even broader to the point that some essentially disappear, but some sharp new peaks also appear. These sharp peaks are likely due to the 10-20% *cis* azoTAB that is present in the visible state. As discussed in Chapter 3, the *cis* azoTAB is less likely to participate in any aggregates, so it would tend to exhibit more narrow linewidths.

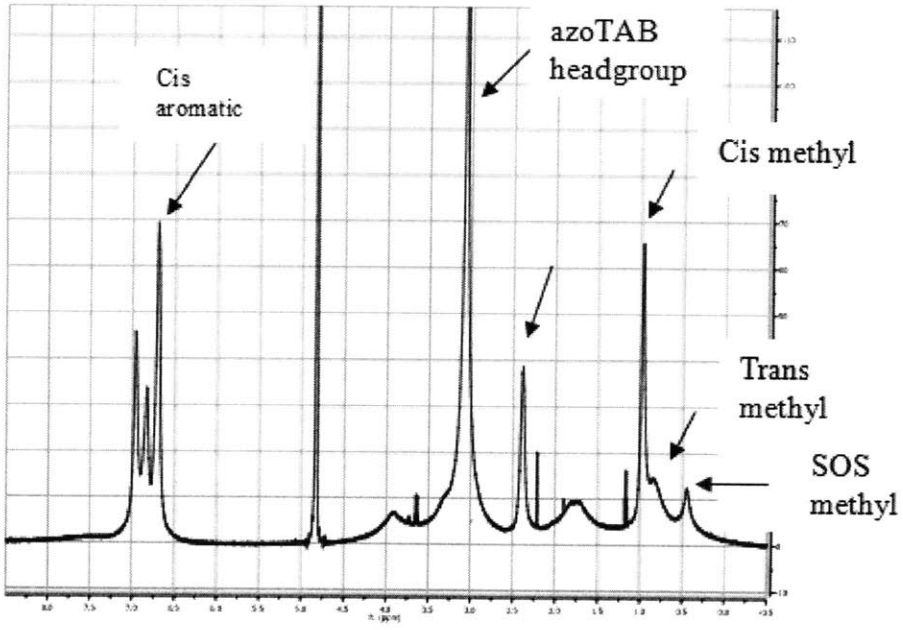

Figure 5-11 NMR spectrum of 20 mM, 34/66 azoTAB/SOS mixture, under UV light. 3-4% of azoTAB is *cis*.

This trend continues in the UV-adapted sample; peaks assigned to the *cis* surfactant are fairly narrow, in comparison to the peaks of SOS and those of the residual *trans*.

It was possible to measure the FWHM (full width at half maximum) linewidth of the azoTAB headgroup proton peak, in the dark state over different mixing ratios. It was found that this measure varied with the mixing ratio in a similar fashion to the hydrodynamic radius from DLS measurements. This correspondence adds further evidence to the growth of aggregates as the SOS/azoTAB mixing ratio approaches equimolarity.

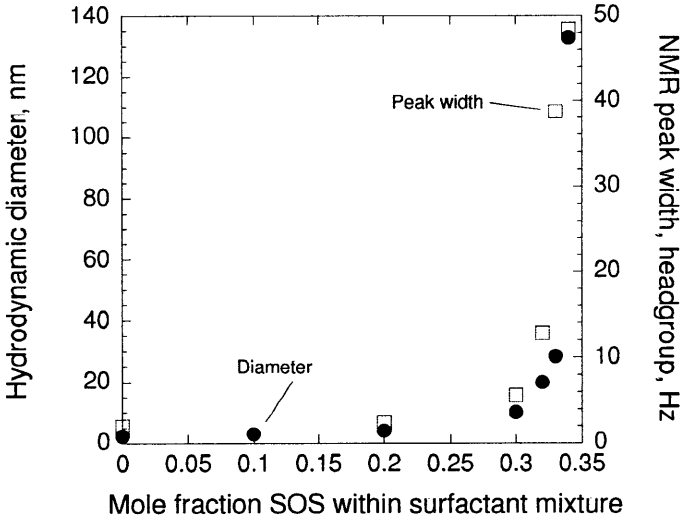

Figure 5-12 In dark-adapted SOS/azoTAB mixtures, total concentration 20 mM. Hydrodynamic diameter from DLS, and NMR peak width from the headgroup protons.

NMR was also used to measure the diffusion coefficients of the surfactants in SOS/azoTAB aqueous mixtures.

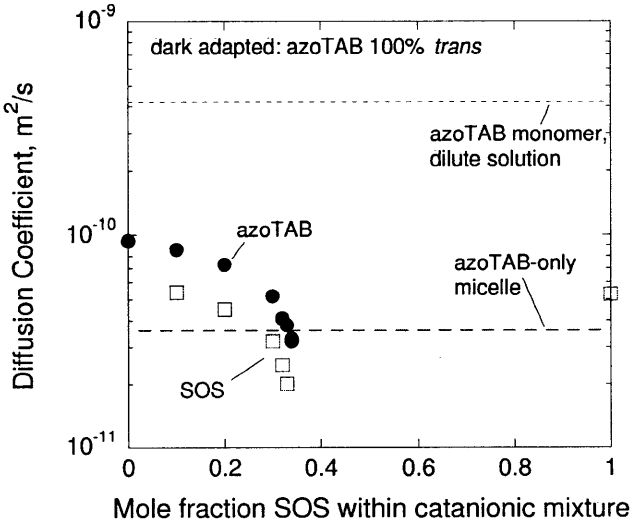

Figure 5-13 NMR diffusion results, dark-adapted SOS/azoTAB mixtures, total surfactant concentration: 20 mM. Diffusivity of azoTAB in solid markers; SOS in hollow. Aggregate formation and growth is indicated by decrease in diffusivity. Shown for reference is the diffusivity of azoTAB monomer, measured in dilute azoTAB-only solutions, and the diffusivity of an azoTAB-only micelle.

In the dark state, the observed diffusion coefficient of both *trans* azoTAB and SOS decreased as the SOS/azoTAB mixing ratio was increased from 0/100 to 34/66, at a fixed total concentration of 20 mM

(Figure 5-13). For reference, the diffusivities of azoTAB monomers and micelles are also shown, as described in Chapter 3. The observed diffusivities are number-weighted averages of the diffusion coefficients of the different aggregation states which may be present: monomer, dimer, micelles, small vesicles, large vesicles, etc. For simplicity, it is assumed that there are only two possible states: monomer and some aggregate. In this case, the observed diffusivity can be related to the surfactant population in each state:

$$D_{obs}^{i} = y_{mon}^{i} D_{mon}^{i} + y_{agg}^{i} D_{agg} \tag{5.9}$$

where i refers to the surfactant being considered, D_{mon}^{i} is the diffusivity of that surfactant in the monomer form, D_{agg} is the diffusivity of the aggregate (valid for either surfactant), y_{mon}^{i} is the fraction of surfactant i that exists in the monomer form, and y_{agg}^{i} is the fraction of that surfactant that is found in the aggregate.

Some assumptions must be made in order to apply Equation (5.9), because D_{agg} and the mole fractions y are not known a priori. One interesting feature of Figure 5-13 is that the observed diffusivity of SOS is lower than that of azoTAB. This could be a sign that there are multiple types of aggregates present, with different compositions. However, working within the assumption that there is only one type of aggregate, this deviation between azoTAB and SOS could also indicate that there is excess azoTAB existing as monomer. It is further assumed that the minority component, SOS, essentially exists only in aggregates, as the overall concentration (20 mM) is well above the critical aggregation concentration (0.1 – 1 mM). With these assumptions, D_{agg} can be set equal to D_{obs}^{SOS}. To test these assumptions, and to check for consistency with the DLS results, the resulting values of D_{agg} are then converted to hydrodynamic diameters by using the Stokes-Einstein equation (see Chapters 3 or 4).

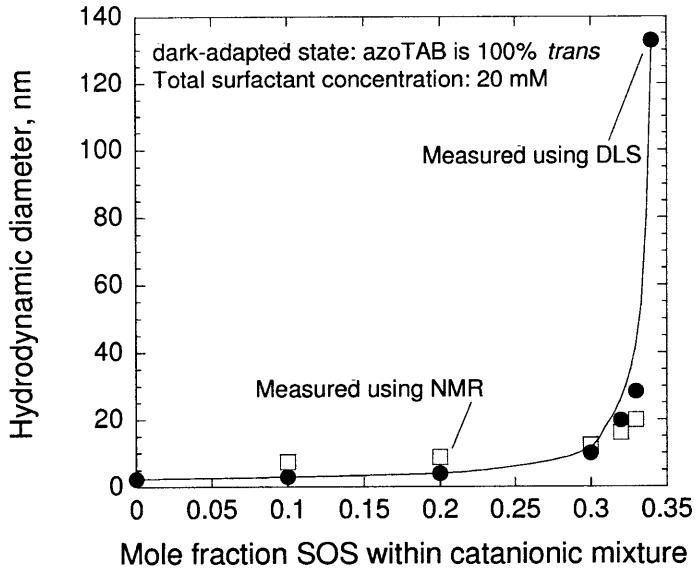

Figure 5-14 Hydrodynamic diameter of aggregates in SOS/azoTAB mixtures, measured using DLS and NMR. NMR: hollow symbols. DLS: solid. Dark-adapted samples only; total surfactant concentration fixed at 20 mM. NMR results are based on the observed diffusivity of SOS. NMR peaks for SOS could not be resolved at the 34/66 mixing ratio.

As can be seen in Figure 5-14, there is only a rough qualitative agreement between the DLS and NMR methods for estimating the hydrodynamic dimensions of the colloids. Both methods do indicate growth of the aggregates as the mixing ratio approaches equimolarity from the cationic-rich side. The DLS results are taken as being more reliable in this case, because it requires no assumptions to be made about the monomer/aggregate portioning of the surfactants.

To the extent that results could be obtained in the visible state (Figure 5-15), the diffusivities of SOS and *trans* azoTAB were similar to those in the dark state. However, the *cis* azoTAB diffusion was much higher than either. This suggests that the 10-20% of the azoTAB that is *cis* is much less likely than the *trans* to participate in aggregates. Such a result is to be expected, as *cis* azoTAB is known to be more hydrophilic, and poor at packing into micelles (Chapter 3).

The peaks in the UV state (only examined at a mixing ratio of 34/66) were so broad that only the *cis* azoTAB signal could be followed. This was still relatively high, though lower than the *cis* diffusivity in the visible state. This suggests either some aggregate growth from the visible state to the UV state at 34/66, or that the *cis* is more likely to participate in aggregates when in the UV state than the visible state.

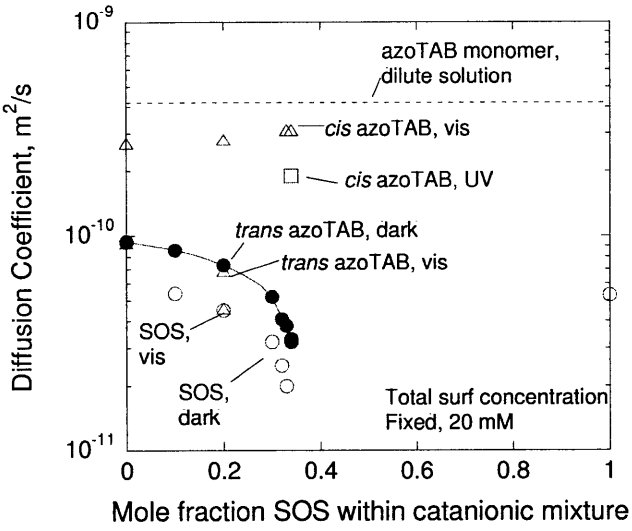

Figure 5-15 Diffusion coefficients of SOS, *trans* azoTAB and *cis* azoTAB under dark-adapted (azoTAB is 100% *trans*), visible-adapted (azoTAB is 80-90% *trans*) and UV-adapted (azoTAB is 3-4% *trans*) conditions. Shown at different compositions on the cationic rich side, but at a fixed total surfactant concentration of 20 mM. UV measurement was only attempted at one mixing ratio, and was only possible for the *cis* azoTAB. Peak broadness prevented analysis of the SOS peaks. Visible measurements were also not possible for SOS at many mixing ratios due to peak broadness or overlap.

5.5.4. Cryo-TEM

Cryo-TEM provided some more conclusive evidence as to the structures formed under different conditions. Samples at a mixing ratio of 34/66 SOS/azoTAB were examined. In the dark state, there was evidence of disc-like structures. The edge-projections of these discs are clearly visible. The discs appear to be about 50 nm in diameter. Some very large objects are also visible; these are not thought to be equilibrium structures.

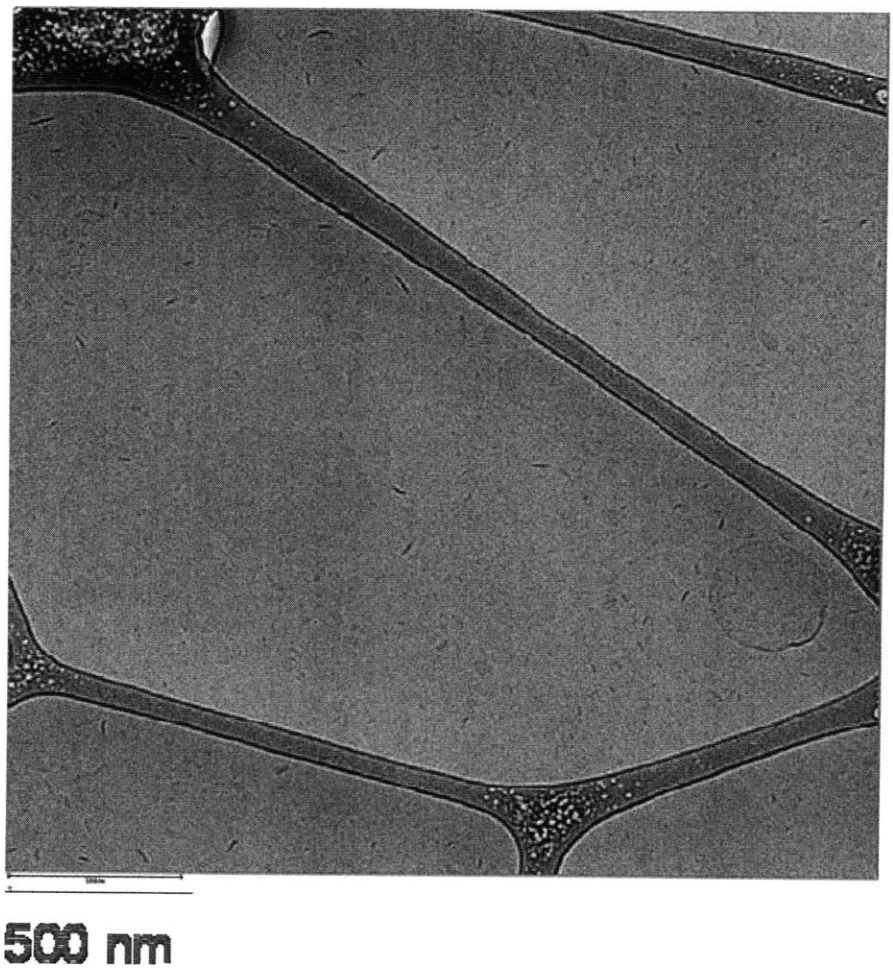

Figure 5-16 Cryo-TEM image of dark-adapted 20 mM 34/66 SOS/azoTAB sample. Edge projections of discs are visible.

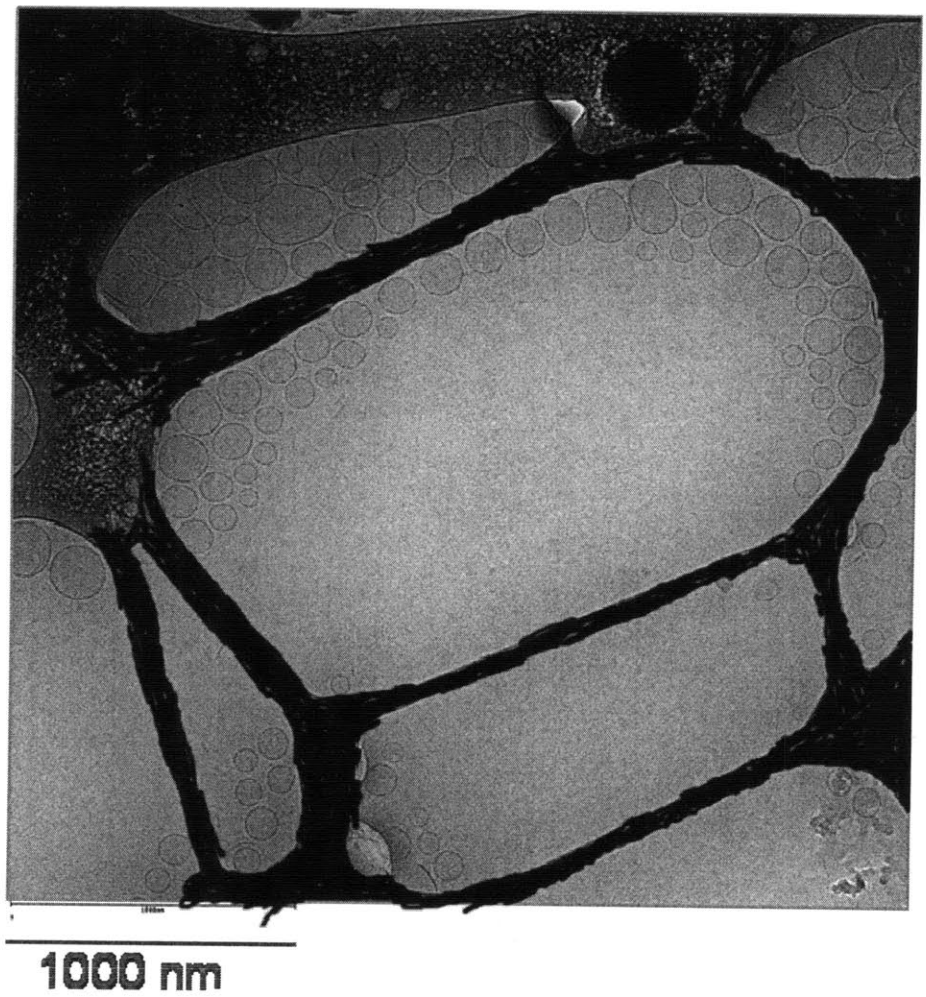

Figure 5-17 Cryo-TEM image of 34/66 SOS/azoTAB sample, under visible irradiation. Closed unilamellar vesicles are visible. Note that the scale bar is different from that in the previous image.

Under visible irradiation, these discs appear to close into closed unilamellar vesicles. The mean diameter was 148 nm. Under UV irradiation, there appear to be a lower number of somewhat smaller vesicles; the mean diameter is 86 nm.

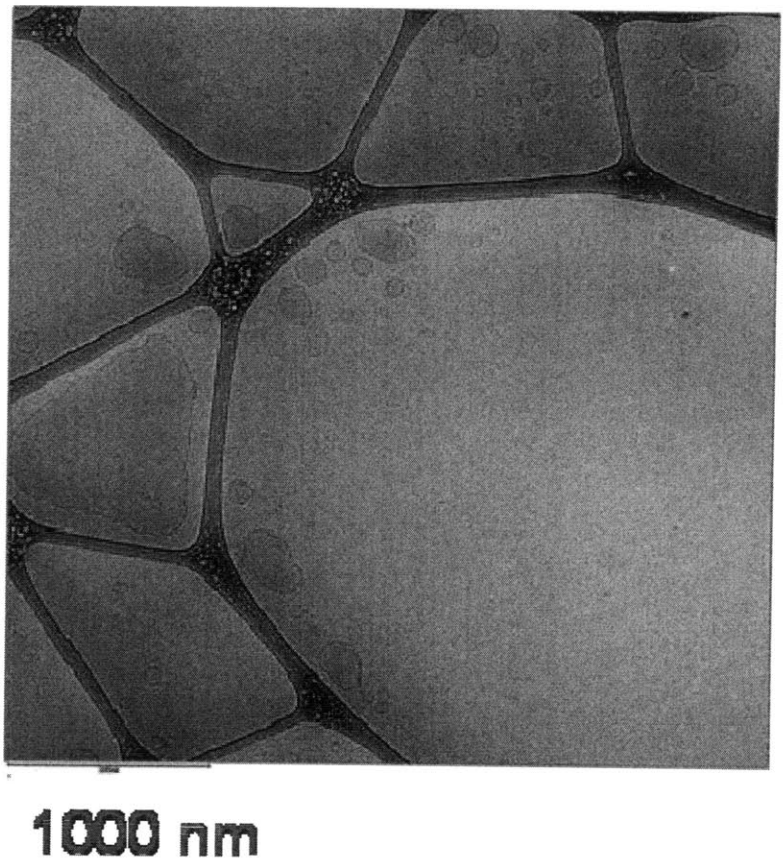

Figure 5-18 Cyro-TEM image of 34/66 SOS/azoTAB mixture under UV irradiation. Smaller closed vesicles are visible, along with some large non-equilibrium structures. Note that the scale bar is different from that in the previous images.

The size distributions of the vesicles were manually measured from the micrographs, and are presented below. The polydispersity of the vesicle sizes is apparent, as is a log-normal distribution of those sizes.

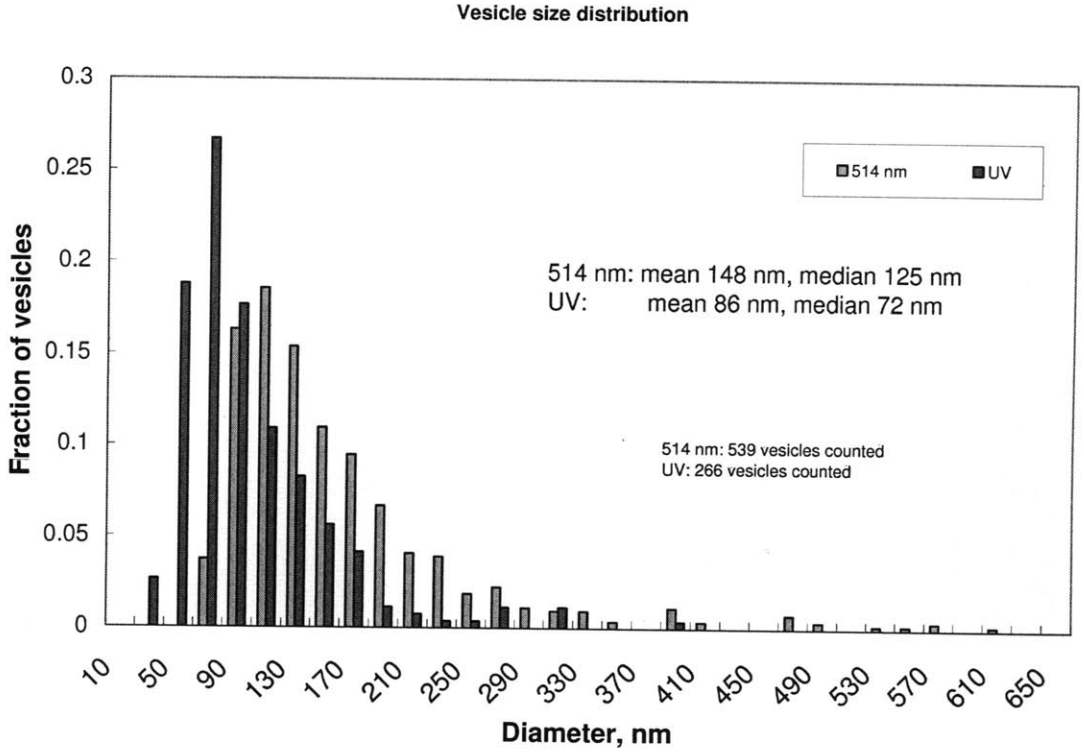

Figure 5-19 Size distribution of vesicles in visible and UV-adapted state, as observed in cryo-TEM micrographs.

5.6 Discussion

Several experimental techniques suggested that there was some growth from micelles to larger micelles or vesicles, and finally large multilamellar structures, as the SOS/azoTAB mixing ratio was increased at a fixed total molar concentration of surfactant. This was expected, based on the phase diagrams reported in the literature for other similar, but not light-sensitive, systems. The 34/66 SOS/azoTAB mixing ratio the highest before multilamellar onion-like structures were observed, so this composition was studied in further detail. The TEM images showed that nanodiscs were formed in the dark-adapted state. This was an unexpected result, as discs are very rarely observed as equilibrium objects. The edge is energetically unfavorable, so discs tend to fuse into vesicles; discs are observed as a transition structure between micelles and vesicles [42]. Discs have been reported at least twice in catanionic systems; Jung et al reported them in mixtures of CTAB and a perfluorinated sodium octanoate [43]. Zemb et al reported them in a salt-free catanionic mixture, and attributed the disc formation in part to the absence of salt (counterions) [44]. The interpretation of Jung may also apply to the results here; it was suggested that the trimethylammonium bromide surfactant preferred high curvature interfaces, and thus stabilised the edges.

The flat faces of the disc would then be composed of some mixture of the two surfactants that favors a planar bilayer. Fewer discs appeared as the mixing ratio was changed towards the sodium octanoate-rich side; there was relatively less CTAB present to stabilise the edge of the discs.

Upon irradiation with visible light, well-formed vesicles appeared. It is possible that this was brought about by a simple change in the mixing ratio and total concentration. NMR results suggested that the *cis* isomer of azoTAB preferred existing as monomer in the bulk solution. If the *cis* played no role in the aggregate formation at all, then the result should be similar to that seen in a solution of 6.8 mM SOS and 11.9 mM *trans* azoTAB. Such a solution was prepared, and under an optical microscope, flocculated clumps of vesicles were observed. This result indicates that the conversion to the visible-adapted state moved the 20 mM 34/66 sample to a region of the phase diagram where vesicles are preferred. Physically, it can be reasoned that there is a reduction in the amount of the excess *trans* azoTAB available to stabilise the edges. Without this excess, the discs join and bend into vesicles.

Upon irradiation with UV light, a small number of smaller vesicles were imaged by TEM. The reduction in number density and size was also suggested by the light scattering rate. The lower number density was expected, as the *cis* azoTAB is known to be poor at packing into aggregates due to its kinked shape. Aggregate formation in *cis*-rich samples is therefore difficult. However, the *cis*-azoTAB did participate in the vesicles, as the measured zeta-potential indicated the presence of positively-charged particles.

The discs seen in the dark samples may well be equilibrium structures, as the visual appearance of the samples was similar after one year. The sample still became more turbid upon visible irradiation, suggesting that the disc-vesicle transition was still taking place. However, it is unclear to what extent the visible-state and UV-state vesicles are stable structures. Metastable aggregates may persist in these systems for months, and it is not practically possible to irradiate a sample for months to verify whether the structures are changing over that time span. This is however not relevant to any practical applications, where the photo-triggered structure changes are likely not needed to persist for months.

5.7 Conclusions

A photosensitive system of colloids has been demonstrated. A solution can be switched from including nanodiscs, vesicles, or a small number of small vesicles, based on the wavelength and duration of irradiation. A system with this variety of colloids, accessible simply by use of light, is novel.

5.8 Works cited

1. Walde, P., *Surfactant Assemblies and Their Various Possible Roles for the Origin(S) of Life.* Origins of Life and Evolution of the Biosphere, 2006. **36**(2): p. 109-150.
2. Gregoriadis, G., A.T. Florence, and H.M. Patel, *Liposomes in Drug Delivery.* Drug Targeting and Delivery Series, V. 2. 1993, Singapore: Harwood Academic Pub.
3. Gregoriadis, G., *Engineering Liposomes for Drug Delivery: Progress and Problems.* Trends in Biotechnology, 1995. **13**(12): p. 527-537.
4. Bramer, T., N. Dew, and K. Edsman, *Pharmaceutical Applications for Catanionic Mixtures.* Journal of Pharmacy and Pharmacology, 2007. **59**(10): p. 1319-1334.
5. Langer, R., *New Methods of Drug Delivery.* Science, 1990. **249**(4976): p. 1527-1533.
6. Barry, B.W., *Novel Mechanisms and Devices to Enable Successful Transdermal Drug Delivery.* European Journal of Pharmaceutical Sciences, 2001. **14**(2): p. 101-114.
7. Kondo, Y., M. Abe, K. Ogino, H. Uchiyama, J.F. Scamehorn, et al., *Solubilization of 2-Phenylethanol in Surfactant Vesicles and Micelles.* Langmuir, 1993. **9**(4): p. 899-902.
8. Lootens, D., C. Vautrin, H. Van Damme, and T. Zemb, *Facetted Hollow Silica Vesicles Made by Templating Catanionic Surfactant Vesicles.* Journal of Materials Chemistry, 2003. **13**: p. 2072-2074.
9. Kepczynski, M., F. Ganachaud, and P. Hémery, *Silicone Nanocapsules from Catanionic Vesicle Templates.* Advanced Materials, 2004. **16**(20): p. 1861-1863.
10. Liu, J., S. Hartono, Y.G. Jin, G.Q. Lu, and S.Z. Qiao, *A Facile Vesicle Template Route to Multi-Shelled Mesoporous Silica Hollow Nanospheres.* Journal of Materials Chemistry, 2010. **20**: p. 4595-4601.
11. Hentze, H.P., S.R. Raghavan, C.A. McKelvey, and E.W. Kaler, *Silica Hollow Spheres by Templating of Catanionic Vesicles.* Langmuir, 2003. **19**(4): p. 1069-1074.
12. Silva, B.F.B., E.F. Marques, and U. Olsson, *Unusual Vesicle-Micelle Transitions in a Salt-Free Catanionic Surfactant: Temperature and Concentration Effects.* Langmuir, 2008. **24**(19): p. 10746-10754.
13. Bryskhe, K., S. Bulut, and U. Olsson, *Vesicle Formation from Temperature Jumps in a Nonionic Surfactant System.* The Journal of Physical Chemistry B, 2005. **109**(19): p. 9265-9274.
14. Li, H.G., S.A. Wieczorek, X. Xin, T. Kalwarczyk, N. Ziebacz, et al., *Phase Transition in Salt-Free Catanionic Surfactant Mixtures Induced by Temperature.* Langmuir. **26**(1): p. 34-40.
15. Yin, H., J. Huang, Y. Lin, Y. Zhang, S. Qiu, et al., *Heating-Induced Micelle to Vesicle Transition in the Cationicâ''Anionic Surfactant Systems:Â€‰ Comprehensive Study and Understanding.* The Journal of Physical Chemistry B, 2005. **109**(9): p. 4104-4110.
16. Li, W., J. Zhang, Y. Zhao, M. Hou, B. Han, et al., *Reversible Switching of a Micelle-to-Vesicle Transition by Compressed Co2.* Chemistry – A European Journal. **16**(4): p. 1296-1305.
17. Yin, H.Q., S. Lei, S.B. Zhu, J.B. Huang, and J.P. Ye, *Micelle-to-Vesicle Transition Induced by Organic Additives in Catanionic Surfactant Systems.* Chemistry-a European Journal, 2006. **12**(10): p. 2825-2835.
18. Veronese, A., N. Berclaz, and P.L. Luisi, *Photoinduced Formation of Bilayer Vesicles.* The Journal of Physical Chemistry B, 1998. **102**(37): p. 7078-7080.
19. Eastoe, J., A. Vesperinas, A.C. Donnewirth, P. Wyatt, I. Grillo, et al., *Photodestructible Vesicles.* Langmuir, 2006. **22**(3): p. 851-853.
20. Uda, R.M., D. Yamashita, Y. Sakurai, and K. Kimura, *Photoinduced Increase in Vesicle Size and Role of Photoresponsive Malachite Green Leuconitrile Derivative in Vesicle Fusion.* Langmuir, 2007. **23**(15): p. 7936-7941.
21. Sakai, H., A. Matsumura, S. Yokoyama, T. Saji, and M. Abe, *Photochemical Switching of Vesicle Formation Using an Azobenzene-Modified Surfactant.* Journal of Physical Chemistry B, 1999. **103**(49): p. 10737-10740.

22. Tanford, *The Hydrophobic Effect: Formation of Micelles and Biological Membranes.* 1980: Wiley.
23. Israelachvili, J., D.J. Mitchell, and B.W. Ninham, *Theory of Self-Assembly of Hydrocarbon Amphiphiles into Micelles and Bilayers.* Journal of the Chemical Society-Faraday Transactions 2, 1976. **72**: p. 1525-1568.
24. Israelachvili, J., *Intermolecular and Surface Forces.* 1992, Academic Press.
25. Nagarajan, R., *Molecular Packing Parameter and Surfactant Self-Assembly:Â€‰ the Neglected Role of the Surfactant Tailâ€* Langmuir, 2001. **18**(1): p. 31-38.
26. Gradzielski, M., *Vesicles and Vesicle Gels - Structure and Dynamics of Formation.* Journal of Physics: Condensed Matter, 2003. **15**: p. R655-R697.
27. Kaler, E.W., A.K. Murthy, B.E. Rodriguez, and J.A.N. Zasadzinski, *Spontaneous Vesicle Formation in Aqueous Mixtures of Single-Tailed Surfactants.* Science, 1989. **245**(4924): p. 1371-1374.
28. Yatcilla, M.T., K.L. Herrington, L.L. Brasher, E.W. Kaler, S. Chiruvolu, et al., *Phase Behavior of Aqueous Mixtures of Cetyltrimethylammonium Bromide (Ctab) and Sodium Octyl Sulfate (Sos).* Journal of Physical Chemistry, 1996. **100**(14): p. 5874-5879.
29. Jung, H.T., B. Coldren, J.A. Zasadzinski, D.J. Iampietro, and E.W. Kaler, *The Origins of Stability of Spontaneous Vesicles.* Proceedings of the National Academy of Sciences of the United States of America, 2001. **98**(4): p. 1353-1357.
30. Brasher, L.L., K.L. Herrington, and E.W. Kaler, *Electrostatic Effects on the Phase-Behavior of Aqueous Cetyltrimethylammonium Bromide and Sodium Octyl Sulfate Mixtures with Added Sodium-Bromide.* Langmuir, 1995. **11**(11): p. 4267-4277.
31. O'Connor, A.J., T.A. Hatton, and A. Bose, *Dynamics of Micelle-Vesicle Transitions in Aqueous Anionic/Cationic Surfactant Mixtures.* Langmuir, 1997. **13**(26): p. 6931-6940.
32. Soderman, O., K.L. Herrington, E.W. Kaler, and D.D. Miller, *Transition from Micelles to Vesicles in Aqueous Mixtures of Anionic and Cationic Surfactants.* Langmuir, 1997. **13**(21): p. 5531-5538.
33. Marques, E.F., O. Regev, A. Khan, M.D. Miguel, and B. Lindman, *Vesicle Formation and General Phase Behavior in the Catanionic Mixture Sds-Ddab-Water. The Anionic-Rich Side.* Journal of Physical Chemistry B, 1998. **102**(35): p. 6746-6758.
34. Marques, E.F., O. Regev, A. Khan, M.D. Miguel, and B. Lindman, *Vesicle Formation and General Phase Behavior in the Catanionic Mixture Sds-Ddab-Water. The Cationic-Rich Side.* Journal of Physical Chemistry B, 1999. **103**(39): p. 8353-8363.
35. Engberts, J. and J. Kevelam, *Formation and Stability of Micelles and Vesicles.* Current Opinion in Colloid & Interface Science, 1996. **1**(6): p. 779-789.
36. Marques, E.F., *Size and Stability of Catanionic Vesicles:Â€‰ Effects of Formation Path, Sonication, and Aging.* Langmuir, 2000. **16**(11): p. 4798-4807.
37. Safran, S.A., P. Pincus, and D. Andelman, *Theory of Spontaneous Vesicle Formation in Surfactant Mixtures.* Science, 1990. **248**(4953): p. 354-356.
38. Holmberg, K., B. Jonsson, B. Kronberg, and B. Lindman, *Surfactants and Polymers in Aqueous Solution.* 2002, Chichester: Wiley.
39. Hayashita, T., T. Kurosawa, T. Miyata, K. Tanaka, and M. Igawa, *Effect of Structural Variation within Cationic Azo-Surfactant Upon Photoresponsive Function in Aqueous Solution.* Colloid and Polymer Science, 1994. **272**(12): p. 1611-1619.
40. Wu, D.H., A.D. Chen, and C.S. Johnson, *An Improved Diffusion-Ordered Spectroscopy Experiment Incorporating Bipolar-Gradient Pulses,*Journal of Magnetic Resonance Series A, 1995. **115**(2): p. 260-264.
41. Hao, J.C., W.M. Liu, G.Y. Xu, and L.Q. Zheng, *Vesicles from Salt-Free Cationic and Anionic Surfactant Solutions.* Langmuir, 2003. **19**(26): p. 10635-10640.

42. Xia, Y., I. Goldmints, P.W. Johnson, T.A. Hatton, and A. Bose, *Temporal Evolution of Microstructures in Aqueous Ctab/Sos and Ctab/Hdbs Solutions.* Langmuir, 2002. **18**(10): p. 3822-3828.
43. Jung, H.T., S.Y. Lee, E.W. Kaler, B. Coldren, and J.A. Zasadzinski, *Gaussian Curvature and the Equilibrium among Bilayer Cylinders, Spheres, and Discs.* Proceedings of the National Academy of Sciences of the United States of America, 2002. **99**(24): p. 15318-15322.
44. Zemb, T., M. Dubois, B. Deme, and T. Gulik-Krzywicki, *Self-Assembly of Flat Nanodiscs in Salt-Free Catanionic Surfactant Solutions.* Science, 1999. **283**(5403): p. 816-819.

Chapter 6

Conclusions and Future Work

6.1 Summary of research

A photosensitive surfactant, azoTAB, was synthesized as described in the literature, and its photoreactivity and aggregation behavior were characterized extensively. The two photoswitchable isomers of azoTAB, *cis* and *trans*, were known to have different tendencies to form aggregates. Methods were devised for measuring the isomeric composition of any given sample, and the photostationary state of azoTAB was found for a variety of different irradiation wavelengths. UV irradiation led to *cis*-rich samples, with very little residual *trans*. Visible irradiation led to *trans*-rich samples, though relatively long wavelengths (500 nm+) are required for the *cis* content to go below 15%. The photoreaction rate was measured at different conditions (concentration, intensity). Simple models were developed to describe the reaction as well, based on the Beer-Lambert Law. These models predicted that at higher concentrations of azoTAB in water, the rate of mixing within the solution would strongly limit the extent of reaction in optically thick samples. This prediction was borne out by experiment. For well-mixed samples, the experimentally measured reaction rate agreed very well with the model for a well-mixed sample. Poorly mixed samples showed much slower overall reaction rates than well-mixed samples. These observations are due to the decreasing photon flux along the path length; azoTAB in regions of low photon flux will have react slowly. However, mixing will expose all azoTAB molecules to the same average irradiance. In the absence of mixing, there would be high conversion at low path lengths and low conversion at longer path lengths. It was also possible to use NMR to directly find evidence for these composition gradients. Aggregation of azoTAB into micelles or surfactant-polymer gels was not found to affect the reaction rate. Using these results, it is possible to design an azoTAB system with the desired isomerisation response to irradiation. For a given intensity of UV irradiation, path length, and azoTAB concentration, the rate of reaction can be predicted.

A variety of methods were used to detect and characterize the formation of micelles in azoTAB solutions. These included fluorescence and NMR spectroscopy. Studies were done at a multitude of concentrations and isomeric compositions. The size of micelles in the dark state was found; it is larger than would be expected if the micelle were perfectly spherical. This was consistent with SANS results reported in the

literature. These methods were also used to detect the onset of aggregation at the critical micelle concentration (CMC), as well as the population of surfactant in the monomer and micellar states. Pre-micellar aggregates were also detected. The CMC was found as a function of isomeric composition. Such information at intermediate isomer compositions was not previously reported for azoTAB. As expected, the CMC was higher in *cis*-rich samples. By applying some simple thermodynamic modeling, it was found that the *trans* and *cis* azoTAB engaged in non-ideal mixing within micelles, when both isomers were present. The theory was used to predict the isomer composition of the micelles themselves, and there was a qualitative agreement with experimental estimates based on diffusion measurements. As micelles have a range of possible applications, such as the solubilisation of pollutants, providing a nanoscale site for certain reactions, or as crosslinking sites for polymers, this research makes it possible to predict the prevalence and nature of micelles under different concentrations and irradiation conditions.

Mixtures of azoTAB and an oppositely charged hydrophobically modified polymer, HMPAA, were then characterized. There had previously been a proof of principle demonstration that a gel-sol transition could be reversibly triggered by irradiation. This had been done using rheology, which does not give direct information about the molecular scale interactions that are present. NMR methods were used to confirm that azoTAB forms micelles in the presence of HMPAA, and that these micelles interact with the hydrophobic side chains of the polymer. Unexpectedly, it was found that micelles were as likely to form in both *trans* rich and *cis* rich samples. Despite this, the micelles in the *cis* rich samples were poor at crosslinking the polymer, so UV samples formed solutions, or weaker gels than those in the dark samples. NMR diffusion was used to estimate the degree of binding of surfactant to polymer; the *cis* was somewhat less likely to be bound to the HMPAA than the *trans*. Diffusion measurements on the polymer itself were illuminating; these were used to demonstrate entanglements in semidilute polymer solutions without surfactant, and then gelation as surfactant was added to form crosslinking sites. The gelation was apparent through growth of crosslinked polymer clusters, as inferred from a rapidly decreasing polymer diffusivity. This cluster growth was in strong agreement with rheological results, thus providing a key link between molecular scale observations and macroscopic rheological measurements.

The diffusion of various solutes in the gel matrix was studied. For the gels and solutes studied here, there was no change in the sieving effect upon the gel-sol transition. It was estimated that the diffusion of larger solutes might be affected by this transition.

The photoresponsive surfactant azoTAB was mixed with a common oppositely charged surfactant, sodium octyl sulfate. Such mixtures of oppositely charged surfactants are known to result in the spontaneous formation of vesicles, when mixed at certain concentrations and compositions. The phase

diagram was explored for this system, and a rich variety of structures was detected, including micelles, nanodiscs, unilamellar vesicles and multilamellar 'onions'. At a certain concentration and SOS/azoTAB composition, light was used to reversibly switch between nanodiscs, large vesicles, and a sparse solution of smaller vesicles.

6.2 Future work

Further experiments could be done to allow the design of specific applications. Given that many possible applications of light-sensitive gels require the diffusivity of solutes to be sensitive to the extent of gelation, the azoTAB-HMPAA system could be altered such that the mesh sizes in the gel are smaller. This could be accomplished by changing the polymer concentration and the percentage of polymer repeat units that are hydrophobically modified.

The transition from micelle-to-monomer or gel-to-solution has been well characterized using UV light, but the kinetics of the reverse transitions using visible light were not quantitatively studied. This was due to a lack of a suitably powerful visible light source with an appropriately sized area of uniform irradiation. In principle, this could be done with the argon ion laser and appropriate optics tools.

It would be of great interest to use simple mean field models to predict the size distribution of the polymer clusters in the gel, and then relate that to the viscosity or modulus of the material. This would then provide a solid framework for understanding the relationship between polymer diffusivity and rheology.

If a diffusion-specific NMR probe is available, many further interesting experiments could be done by studying the diffusivity of the polymer in surfactant-polymer mixtures. Here, a proof of principle has been given that polymer diffusivity can be related to entanglements and cluster growth. However, such measurements were not done dynamically, at different irradiation times, in order to follow cluster growth or destruction with light over time. Such an experiment would require irradiation of the sample *in-situ* in the NMR spectrometer, which presents something of a challenge. In particular, the optical depth of the azoTAB samples would tend to prevent the spatially even gels that would be required for easily interpreted diffusion results. It may be possible to use NMR tube inserts to reduce the path length of the light, to allow for more homogeneous gelation.

The understanding of gelation in surfactant-polymer systems would be advanced by including the thermodynamics of the surfactant-polymer interactions. Tools such as titration calorimetry could be utilized. Fluorescence lifetime experiments could also be used to provide an additional indication of micellar size and aggregation number.

Inasmuch as the light-generated composition gradients in optically thick samples are of interest, the experiments presented here for detecting such gradients could be extended by use of NMR imaging experiments. Using an MRI-like probe, the NMR chemical shift could be measured as a function of spatial position. The gradients could thus be directly seen.